Universitat de València
(ESTUDI GENERAL)

DEPARTAMENT DE FÍSICA ATÒMICA
MOLECULAR I NUCLEAR

UNIVERSITAT DE VALÈNCIA

DETERMINATION OF THE b QUARK MASS AT THE M_Z SCALE WITH THE DELPHI DETECTOR AT LEP

UNIVERSITAT DE VALÈNCIA
TESI DOCTORAL
MARÍA JOSÉ COSTA MEZQUITA
Gener de 2003

En JUAN ANTONIO FUSTER VERDÚ, Professor d'investigació del C.S.I.C.,

CERTIFICA :

Que la present memòria DETERMINATION OF THE b QUARK MASS AT THE M_Z SCALE WITH THE DELPHI DETECTOR AT LEP ha estat realitzada sota la meua direcció en el Departament de Física Atòmica, Molecular i Nuclear de la Universitat de València per Na María José Costa Mezquita i constitueix la seua tesi per a optar al grau de doctor en Física per la Universitat de València.

I per tal que conste, en compliment a la legislació vigent, signe el present certificat a Burjassot a 8 de gener de 2003.

Dr. Juan Antonio Fuster Verdú

Vist i plau el tutor: Dr. Ramón Cases Ruiz.

A Pepe.

Agraïments

Sense dubte, la realització d'aquest treball no hagués estat possible sense l'ajuda, col·laboració i motivació de moltes persones, cadascuna en distints aspectes però totes elles necessàries. És per això que m'agradaria dedicar a totes elles les primeres línies d'aquest escrit.

En primer lloc he d'agrair a Dr. Joan Fuster l'oferiment d'aquest tema d'investigació, a pesar de la meua primera resistència als canvis, el transmetre'm els seus coneiximents de QCD i per la seua direcció i seguiment del que ha acabant sent la meua tesi doctoral.

A Dr. Antonio Ferrer per donar-me a conèixer l'IFIC, donant-me així l'oportunitat d'encetar aquest camí de l'investigació, i per recolçar-me i aconsejar-me quan l'he necessitat.

A Dr. Philip Bambade per la seua col·laboració contínua i interés mostrat en aquest treball, per indicar la manera de millorar l'anàlisi i per les llargues sessions de discussió, inclús a distància.

Aquest treball no havera anat enlloc si no fos pels càlculs teòrics realitzats per Dr. Arcadi Santamaría i Dr. German Rodrigo. A ambdòs els he d'agrair la seua ajuda i col·laboració en aquest anàlisi.

A Dr. Salvador Martí per estar en qualsevol moment disposat a resoldre dubtes, estigués on fos, des de l'aspecte més general i conceptual al més concret i tècnic de l'anàlisi. Gràcies per fer eixe esforç de memòria i tenir-ho tot tan clar a pesar del temps.

A Dra. Susana Cabrera per ajudar-me en l'inici d'aquest treball mostrant-me el que s'havia fet fins al moment.

Al grup de QCD de DELPHI per totes les suggerències realitzades durant les setmanes DELPHI. Especialment a Dr. Klaus Hamacher i Dr. Uwe Flagmeyer per ensenyar-me tot el que sé sobre tunings de generadors, per la seua paciència i el temps que m'han dedicat.

Vull agrair també a Dr. Günther Dissertori el compartir obertament la seua experiència en aquest tipus de mesura.

A Dr. Tobjörn Sjöstrand per les seues explicacions i discussions sobre com els efectes de massa estan implementats en el generador de PYTHIA.

A Dr. Jorge Portoles i Dr. Markus Eidemüller per l'ajuda prestada en l'enteniment de les masses dels quarks i mesures a baixa energia.

Per supost no puc oblidar-me de Pablo Tortosa, amb qui he compartit les alegries i desgràcies d'aquest treball des del principi. Per escoltar els problemes que em sorgien i tractar de trobar una solució, per totes les hores de dicussió que hem tingut sobre cada pas de l'anàlisi i per les seues aportacions i idees noves.

A Marcel, amic i company de despatx, per soportar-me més hores que ningú al dia i per aconseguir que foren més divertides. A Arantza per intentar transmetre'm la seua creativitat i il·lusió i per fer agradables els meus curts exilis en Ginebra. Als meus companys de viatje, Emiliano, Paco, Santi, Mari Carmen, Farida, Gabriela, Marcel, Pablo, Arantza, José Enrique, Sergio, Juande i Esteban, per compartir aquesta experiència amb mi. A Kiko, que es va escapar, però que sempre ha estat a l'abast.

A tota la resta de l'IFIC, en especial al grup de silici, amb els que primer vaig treballar i dels que tant vaig apendre en el seu moment, a Javier, Kiko, Pepe, Pablo, Luis, Marcel, Rosario, Rosa i Paco, per compartir hores de laboratori i de test beam. A Carmen i Jose Enrique per mimar-me i fer-me més senzilla la caracterització de detectors. A Carlos i Gabriela per estar molt a prop del meu despatx i poder desfogar-me amb ells.

Als meus amics de la muntanya, Pablo, Luis, Juanba, Mari Carmen, Ascen, Francis, Marc i Pepe per proporcionar-me la màxima desconnexió d'aquest treball. Als amics incodicionals, Pilar, Alícia, Bàrbara, Eva, Alma, per poder contar sempre amb ells. A l'artista Alícia en especial perquè seua és la portada d'aquest manuscrit.

Als meus pares i al meu germà Carles per l'interés i el recolçament que mostren en tot el que faig.

Al meu amic per sempre Pepe. Per ser el millor company de vida i de treball, per escoltar-me, motivar-me, ajudar-me, renegar-me i compartir-ho tot amb mi.

Abstract

A new and precise measurement of the b quark mass at the M_Z scale, $m_b(M_Z)$, has been obtained using the complete dataset collected by the DELPHI experiment at the Z^0 peak from 1994 to 2000.

The normalized three-jet rate of b quarks with respect to light ($\ell \equiv u, d, s$) quarks, $R_3^{b\ell}$, defined using the DURHAM and CAMBRIDGE jet finding algorithms, has been measured. The observable was compared with next-to-leading order massive calculation in order to extract $m_b(M_Z)$ assuming α_s universality or to extract the ratio α_s^b/α_s^ℓ taking as an input the b quark mass determined with low energy data.

The result obtained with CAMBRIDGE is the most precise and the measured running mass is:

$$m_b(M_Z) = 2.96^{+0.17}_{-0.18}\ (\mathrm{stat}) \pm 0.19\ (\mathrm{had}) \pm 0.14\ (\mathrm{exp}) \pm 0.12\ (\mathrm{theo})\ \mathrm{GeV/c^2} \quad (1)$$

which has a total uncertainty of $^{+310}_{-320}$ MeV$/c^2$. It is compatible with other determinations performed at the M_Z energy scale and it agrees with the running predicted by QCD when compared with the low energy determinations.

The measured observable was also compared with theoretical calculations in terms of the b pole mass, allowing then to extract this mass,

$$M_b = 4.26^{+0.22}_{-0.23}\ (\mathrm{stat})^{+0.30}_{-0.31}\ (\mathrm{syst}) \pm 0.44\ (\mathrm{theo})\ \mathrm{GeV/c^2} \quad (2)$$

which is compatible with the results obtained at threshold.

If the value $m_b(m_b) = 4.24 \pm 0.11$ GeV$/c^2$ is taken as an input to the theoretical predictions, the ratio α^b/α_s^ℓ is found to be,

$$\alpha_s^b/\alpha_s^\ell = 0.996 \pm 0.004\ (\mathrm{stat}) \pm 0.006\ (\mathrm{syst}) \pm 0.003\ (\mathrm{theo}) \quad (3)$$

which verifies α_s flavour independence with a precision of 8‰.

The increase in statistics and the better understanding of the hadronization process, flavour tagging and the gluon splitting process led to a reduction of both statistical and systematic uncertainties, representing a substantial improvement compared to previous measurements.

Resum

Les dades recollides pel detector DELPHI en el pic del Z^0 entre 1994 i 2000 s'han emprat per a obtenir una nova mesura de la massa del quark b a l'escala M_Z, $m_b(M_Z)$, molt precisa.

S'ha mesurat la secció eficaç normalitzada de producció de tres jets en esdeveniments iniciats per quarks b respecte a aquells iniciats per quarks lleugers ($\ell \equiv u, d, s$), $R_3^{b\ell}$, definida amb els algoritmes de reconstrucció de jets DURHAM i CAMBRIDGE. La mesura d'aquest observable s'ha comparat amb càlculs next-to-leading order, que tenen en compte l'efecte de massa, per tal d'extraure $m_b(M_Z)$ assumint universalitat de α_s o, alternativament, per tal d'extraure el quocient α_s^b/α_s^ℓ prenent la massa del quark b obtinguda a partir de dades de baixa energia.

El resultat obtingut amb CAMBRIDGE és el més precís i el valor obtingut per a la massa running és,

$$m_b(M_Z) = 2.96^{+0.17}_{-0.18}\ (\text{estad}) \pm 0.19\ (\text{had}) \pm 0.14\ (\text{exp}) \pm 0.12\ (\text{teo})\ \text{GeV/c}^2 \tag{4}$$

que té un error total de $^{+310}_{-320}$ MeV/c^2. És compatible amb altres mesures realitzades a l'escala d'energia M_Z i, quan es compara amb les determinacions realitzades a baixa energia, està d'acord amb l'evolució amb l'escala predita per QCD.

L'observable mesurat s'ha comparat també amb els càlculs teòrics en termes de la massa pol, permetent així extraure aquesta massa,

$$M_b = 4.26^{+0.22}_{-0.23}\ (\text{estad})^{+0.30}_{-0.31}\ (\text{sist}) \pm 0.44\ (\text{teo})\ \text{GeV/c}^2 \tag{5}$$

sent el resultat compatible amb els obtinguts al llindar de producció.

A partir de les prediccions teòriques per a una massa $m_b(m_b) = 4.24 \pm 0.11$ GeV/c^2, es troba que el quocient α^b/α_s^ℓ val,

$$\alpha_s^b/\alpha_s^\ell = 0.996 \pm 0.004\ (\text{estad}) \pm 0.006\ (\text{syst}) \pm 0.003\ (\text{theo}) \tag{6}$$

verificant així la independència de sabor de α_s amb una precisió de 8‰.

Gràcies a l'augment en estadística i a una millor comprensió del procés d'hadronització, de les tècniques d'identificació de sabor i del procés $g \to q\overline{q}$, s'ha reduït tant l'error estadístic com el sistemàtic, suposant una millora important respecte a les mesures prèvies.

Contents

Introduction

The theoretical framework describing the observed electroweak and strong interactions among elementary particles is known as the Standard Model (SM). This model has been extremely successful predicting and explaining the observed phenomena with very high precision.

The SM has two basic components, which will be described in Chapter 1:

- The electroweak theory: It combines the electromagnetic and weak interactions in a unified gauge theory.
- Quantum Chromodynamics (QCD): It is the gauge theory of strong interactions among quarks and gluons.

There is a set of free parameters in the SM that need to be determined experimentally, as couplings and masses. Once this is done, physical observables can be calculated as a perturbative expansion in the coupling constants. Different kind of divergences appear in these computations. In order to avoid the UV divergences the theory needs to be renormalized. This means that masses and couplings have to be redefined in order to absorb the infinities appearing in the calculations. There are different ways to make these redenitions and each defines a renormalization scheme.

The renormalization procedure leads to a dependence of the renormalized couplings and masses with the scale of the process under consideration, known as the running of these quantities. For the case of QCD, we have the running of the strong coupling constant, α_s, and of quark masses. The exact dependence with the energy scale is determined by the specific renormalization scheme. In our case, the $\overline{\mathrm{MS}}$ scheme will be used.

In this scheme, the strong coupling constant is predicted to decrease as the energy scale increases. This is in agreement with what it is observed in nature: qualitatively, when two quarks are close together, the force is relatively weak (asymptotic freedom) but when they move further apart the force becomes much stronger (confinement). As the distance increases the force also increases and at some distance it becomes energetically favourable to create new quark and antiquark pairs, which combine to form hadrons. During this process of hadron formation (hadronization) perturbation theory fails due to the increase of α_s and we enter in a nonperturbative regime. Different methods based on QCD have been developed to explain the hadronization process.

The construction of accelerators in the multi-GeV range has been crucial for the development of the theory of strong interactions. In particular, electron-positron colliders present an ideal environment for precise tests of QCD because the hadronic activity is limited to the final state. This makes the study of hadronic events much simpler from both theoretical and experimental points of view. This work is based on data taken at the LEP accelerator (1989-2000), which is the largest and most energetic e^+e^- collider ever built.

The CM energy of the first period of LEP, at the Z^0 peak ($\sqrt{s} = 91.2$ GeV), is much higher than the previous e^+e^- colliders as PETRA, PEP or TRISTAN. The e^+e^- hadronic processes can be described by a perturbative stage followed by the nonperturbative hadronization process. Perturbative QCD predicts corrections which evolve as $1/\log\sqrt{s}$ [1] while nonperturbative effects are expected to scale with $1/\sqrt{s}$ [2]. Therefore, at the high energy of LEP, perturbative QCD can be tested with higher precision. Furthermore, the cross section at the energy of the Z^0 resonance is much larger than for any of the previous accelerators.

Several million hadronic Z^0 decays have been collected in the four detectors installed at LEP and have allowed precision measurements of the strong coupling constant and its flavour independence. Quark masses are also free parameters of the SM and their origin is still an unsolved puzzle. It becomes then essential to determine them experimentally. The heaviest quark produced at LEP is the b quark. Although at such high energy, b mass effects are expected to be negligible for inclusive observables, as they go like $m_b^2/m_Z^2 \leq 0.3\%$, for more exclusive observables as jet rates they can have sizeable effects.

Due to high statistics collected at LEP, b mass effects have to be taken into account when measuring α_s from event shapes observables. For some observables the correction due to the b quark mass was found to be as large as 15% [3]. In order to verify α_s universality it is also essential to consider b mass effects. If they are not taken into account when the ratio α_s^b/α_s^ℓ ($\ell \equiv uds$) is measured from event shape observables, the result obtained is not compatible with unity. In [4] a shift of order 5 to 7% was found for α_s^b/α_s^ℓ if b mass effects were neglected.

The fact that there are some observables sensitive to the b quark mass effect at the Z^0 energy suggested that they could be used to measure the b quark mass assuming α_s flavour independence [5, 6].

Determinations of the b quark mass from measurements performed at threshold, where the contribution of nonperturbative effects is large, have been available for a long time. A measurement performed at high energy becomes interesting since it implies an independent determination of the quark mass and, for the case of the renormalized running mass mentioned above, it also allows to test the evolution with the energy scale predicted by QCD.

The first measurement of the running b quark mass at the M_Z scale, $m_b(M_Z)$, was performed in 1998 with the DELPHI detector at LEP with a precision of about 500 MeV/c^2 [7] by measuring the three-jet rate for b over ℓ quark events ($R_3^{b\ell}$), with jets reconstructed with the DURHAM algorithm [8], and comparing it with the NLO massive calculation of [9]. Measurements of the b quark mass have also been performed by SLD, ALEPH and OPAL leading to compatible results [10–12]. A shift with respect to the mass measured at threshold was observed and the difference agreed with the energy scale evolution predicted by QCD.

The aim of this thesis is to improve the measurement performed by DELPHI and to obtain a more precise determination of $m_b(M_Z)$. The main sources of error in the DELPHI determination of [7] were coming from uncertainties on the hadronization process and on the theoretical predictions for $R_3^{b\ell}$. The theoretical error was reduced when the CAMBRIDGE algorithm [13] was used for jet reconstruction instead of DURHAM [14]. In the presented thesis the main motivation was to reduce the hadronization uncertainty and, once this was accoplished, other sources of error, not considered before, had to be taken into account. These are for instance the uncertainties associated with the heavy quark gluon splitting rates and the quark mass parameters of the generators.

The same observable, $R_3^{b\ell}$, was used in this analysis and jets were reconstructed with two jet clustering algorithms, DURHAM and CAMBRIDGE. The data collected by DELPHI at the Z^0 peak from 1994 to 2000 was analysed, increasing the data sample with respect to the previous analysis.

The flavour tagging methods developed by the DELPHI Collaboration were used to isolate the b and ℓ quark initiated events. These techniques are based on the properties on B hadrons that distinguish them from other particles, as their long lifetime, large mass, high decay multiplicity and leptonic branching rate. The main discriminative variable is built from the measurements of the charged track impact parameters and therefore the silicon vertex detector of DELPHI is essential for this analysis.

The jet clustering algorithm is applied to all tracks (charged and neutrals) to get the $R_3^{b\ell}$ observable at detector level. A sample of simulated events (including physic processes, detector and reconstruction effects) is used to correct for detector effects and the tagging procedure to bring the observable to hadron level. The effect of the heavy quark gluon splitting rates of the simulated data on this correction was found to be important and therefore the Monte Carlo simulation was reweighted in order to have the measured rates.

In order to correct for the hadronization process the string and cluster phenomenological models, implemented in the PYTHIA [15] and HERWIG [16] generators respectively, were used. Both generators have a set of parameters that are relevant in the fragmentation process and that need to be tuned to the observed data at hadron level. A DELPHI tuning was already available for PYTHIA 6.131 [17] and a tuning of HERWIG 6.1 was done as part of the present work.

Compared to the versions of the generators used in the previous DELPHI measurement, JETSET 7.3 and HERWIG 5.8, big improvements have been made in both generator to model the observed b mass effects.

The uncertainties due to the hadronization process constitute one of the dominant sources of error on $m_b(M_Z)$ and that is why they have been studied in detail in this thesis. The measurement was then performed in a restricted region of the phase space where the two hadronization models give similar predictions. A study to understand the way the b quark mass parameters of the generator were entering in the different stages was also done in order to constrain these parameters. The uncertainty associated to them was found to be the dominant source of error in our determination of $m_b(M_Z)$. This is the first time that this source of uncertainty is considered.

Once the observable is corrected to parton level a comparison with the NLO massive calculations of [9,14] allowed to extract the b quark mass. Alternatively, the ratio α_s^b/α_s^ℓ was measured taking the b quark mass obtained from low energy data as input.

This thesis is divided in the following parts: Chapter 1 contains an introduction to the Standard Model, with special emphasys on the QCD theory of strong interactions. The particular case of e^+e^- annihilations and the effect of the b quark mass in these processes is discussed. The LEP collider and the DELPHI detector are introduced in Chapter 2. A description of the Monte Carlo generators (PYTHIA and HERWIG) and the tuning of the second one are given in Chapter 3. In Chapter 4 the hadronization correction of the observable used to measure the b mass and its different sources of uncertainties are obtained. The analysis procedure used to measure the $R_3^{b\ell}$ observable is described in Chapter 5 and in Chapter 6 the measured observable is compared with the theoretical calculations to extract the b quark mass or test α_s flavour independence. The last part gives the conclusions of this analysis.

Introducció

El marc teòric que descriu les interaccions electro-febles i fortes observades entre partícules elementals es coneix amb el nom de Model Estàndar (SM). Aquest model ha predit i explicat extraordinàriament tots els fenòmens observats amb molt alta precisió.

El SM té dos components bàsiques, les quals es descriuran al Capítol 1:

- La teoria electro-feble: Combina les interaccions electromagnètiques i febles en una teoria gauge unificada.
- Cromodinàmica Quàntica (QCD): És la teoria gauge de la interacció forta entre quarks i gluons.

Hi ha un conjunt de paràmetres lliures en el SM que cal determinar experimentalment, com ara les constants d'acoblament i les masses dels fermions. Una vegada determinats, els observables físics es poden calcular com una expansió pertorbativa en les constants d'acoblament. En aquests càlculs apareixen distints tipus de divergències. Per tal d'evitar les divergències UV, cal renormalitzar la teoria, és a dir, cal redefinir les masses i les constants d'acoblament de manera que els infinits queden absorbits. Hi ha distintes maneres de fer aquestes redefinicions i cadascuna d'elles és el que s'anomena esquema de renormalització.

El procés de renormalització implica una dependència de les constants d'acoblament i masses renormalitzades amb l'escala d'energia del procés en qüestió, coneguda com el *running* d'aquestes quantitats. Per al cas de QCD, tenim el *running* de la constant d'acoblament forta, α_s, i de les masses dels quarks. La dependència exacta amb l'escala d'energia ve determinada per l'esquema de renormalització emprat. En el nostre cas utilitzarem l'esquema $\overline{\mathrm{MS}}$.

En aquest esquema es prediu que la constant d'acoblament forta decreix en augmentar l'escala d'energia del procés. Aquest comportament està d'acord amb el que s'observa en la natura: qualitativament, quan dos quarks es troben a prop, la força entre ells és relativament feble (llibertat asimptòtica), però quan s'allunyen la força es torna molt més forta (confinament). En augmentar la distància la força augmenta i a certa distància resulta energèticament favorable crear noves parelles de quarks i antiquarks, els quals es combinen formant hadrons. Durant aquest procés de formació d'hadrons (hadronització) la teoria pertorbativa deixa de ser vàlida degut a l'augment de α_s i s'entra en un règim no pertorbatiu. S'han desenvolupat distints mètodes basats en QCD per tal d'explicar el procés d'hadronització.

La construcció d'acceleradors en el rang d'energia d'uns quants GeV ha sigut crucial per al desenvolupament de la teoria de les interaccions fortes. En particular, els col·lisionadors electró-positró presenten un entorn ideal per tal de realitzar comprovacions de QCD amb gran precisió. Com que en les aniquilacions e^+e^- l'activitat hadrònica està limitada exclusivament a l'estat final, l'estudi d'esdeveniments hadrònics resulta molt més sencill des del punt de vista teòric i experimental. Aquest treball es basa en les dades preses a l'accelerador LEP (1989-2000), que és el col·lisionador e^+e^- més gran i més energètic que s'ha construït mai.

L'energia en CM del primer període de LEP, al pic del Z^0 ($\sqrt{s} = 91.2$ GeV), és molt més alta que la dels acceleradors e^+e^- anteriors, com ara PETRA, PEP o TRISTAN. Els processos hadrònics en les aniquilacions e^+e^- es poden descriure com a una fase pertorbativa seguida del procés no pertorbatiu d'hadronització. Les correccions predites per la teoria pertorbativa evolucionen amb l'energia de la forma $1/\log\sqrt{s}$ [1] mentre que les no pertorbatives ho fan com $1/\sqrt{s}$ [2]. Per tant, a l'alta energia de LEP, es pot verificar la teoria de QCD pertorbativa amb major precisió. A més, la secció eficaç en la resonància del Z^0 és molt més gran que la de qualsevol dels acceleradors anteriors.

Els quatre detectors de instal·lats en LEP han recollit uns quants milions de desintegracions hadròniques del Z^0, permetent així mesures d'alta precisió de la constant d'acoblament forta i de la seua independència amb el sabor de l'esdeveniment. Les masses dels quarks són també paràmetres lliures en el SM i el seu origen és encara una de les qüestions sense resoldre, de manera que resulta fonamental determinar-les experimentalment. El quark més pesat produït en LEP és el quark b. Tot i que a l'alta energia de LEP s'espera que els efectes de massa del quark b siguen menyspreables per a observables inclusius, ja que van com a $m_b^2/m_Z^2 \leq 0.3\%$, poden donar efectes apreciables en observables més exclusius com ara seccions eficaces de jets.

Degut a l'alta estadística recollida en LEP, els efectes de massa del quark b s'han de tenir en compte en mesures de α_s realitzades a partir d'observables de forma. Per a alguns d'aquests observables es va trobar que la correcció deguda als efectes de massa del quark b eren tan grans com un 15% [3]. Per tal de verificar universalitat de α_s, és imprescindible considerar els efectes de massa del b. Si no es tenen en compte quan es mesura el quocient α_s^b/α_s^ℓ ($\ell \equiv uds$), el resultat obtingut no és compatible amb la unitat. En [4] es va observar un desplaçament de l'ordre de 5 a 7% en α_s^b/α_s^ℓ si es menyspreaven els efectes de massa del b.

El fet de que hi ha observables sensibles a la massa del quark b a l'energia del Z^0 va suggerir que aquests prodrien emprar-se per tal de mesurar la massa del quark b assumint independència de sabor de α_s [5,6].

Determinacions de la massa del quark b realitzades en el llindar de producció, on la contribució dels efectes no pertorbatius és gran, existeixen des de fa temps. Una possible mesura a altes energies resulta interessant ja que significa una determinació completament independent de la massa del quark i, per al cas de la massa renormalitzada *running*, una comprovació de l'evolució amb l'escala d'energia predita per QCD.

La primera mesura de la massa *running* del quark b a l'escala M_Z, $m_b(M_Z)$, es van realitzar en 1998 amb el detector Delphi de LEP, assolint una precisió d'uns 500 MeV/c^2 [7]. Es va mesurar la secció eficaç normalitzada de producció de tres jets d'esdeveniments iniciats per quarks b respecte a aquells iniciats per quarks ℓ ($R_3^{b\ell}$), amb jets reconstruïts amb l'algoritme de Durham [8], i el resultat es va comparar amb els càlculs NLO amb efectes de massa de [9]. Sld, Aleph i Opal han realitzat també mesures de la massa del quark

b obtenint resultats compatibles amb els de DELPHI [10–12]. La diferència entre la massa mesurada i l'obtinguda en el llindar de producció del b estava d'acord amb l'evolució amb l'escala d'energia predita per QCD.

L'objectiu d'aquesta tesi és millorar la mesura realitzada per DELPHI i obtenir una determinació més precisa de $m_b(M_Z)$. Les fonts principals d'error en la determinació de DELPHI de [7] provenien d'incerteses en el procés d'hadronització i en les prediccions teòriques de $R_3^{b\ell}$. L'error teòric es va reduir en emprar l'algoritme de CAMBRIDGE [13] per tal de reconstruir els jets, en comptes del de DURHAM [14]. En aquesta tesi la motivació principal fou reduir l'error d'hadronització i, una vegada aconseguit, van haver de considerar-se altres fonts d'incertesa. Aquestes són per exemple les incerteses associades amb la secció eficaç de conversió de gluons en parelles de quarks pesats i les incerteses en els paràmetres de massa dels quarks en els generadors.

En aquest anàlisi es mesura el mateix observable, $R_3^{b\ell}$, reconstruint jets amb els algoritmes de DURHAM i CAMBRIDGE. S'analitzen les dades recollides per DELPHI en el pic del Z^0 des de 1994 a 2000, augmentant així la mostra de dades respecte a la mesura anterior.

Per tal de distingir entre els esdeveniments iniciats per quarks b i ℓ s'utilitzen els mètodes d'identificació de sabor desenvolupats per la Col·laboració DELPHI. Aquestes tècniques es basen en les propietats dels hadrons B que els diferencien d'altres partícules, com ara la vida mitja llarga, massa gran, alta multiplicitat de partícules provinents de les seues desintegracions i l'existència de leptons en els seus productes de desintegració. La principal variable de discriminació es construeix a partir de les mesures dels paràmetres d'impacte de les traces carregades, de manera que el detector de vèrtex de DELPHI és fonamental en aquest anàlisi.

L'algoritme de reconstrucció de jets s'aplica a totes les traçes (carregades i neutres) per tal d'obtenir l'observable $R_3^{b\ell}$ a nivell de detector. S'empra una mostra d'esdeveniments simulats (que inclou els processos físics i els efectes de detector i reconstrucció) per tal de corregir per efectes de detector i pel procés d'identificació de sabor, duent així l'observable a nivell d'hadrons. S'ha observat que l'efecte de la secció eficaç del procés de gluons convertits en parelles de quarks pesats en la mostra simulada és important. Per tant, la mostra del Monte Carlo es va repesar per tal de tenir les seccions eficaces mesurades.

Per tal de corregir pel procés d'hadronització, es van utilitzar els models fenomenològics de cordes i cúmuls, implementats en els generadors PYTHIA [15] i HERWIG [16] respectivament. Ambdòs generadors tenen una sèrie de paràmetres que són relevants en el procés de fragmentació i que s'han d'ajustar per tal de reproduir les dades observades a nivell d'hadrons. Per al cas de PYTHIA 6.131, s'havia realitzat ja un ajust a les dades de DELPHI [17], mentre que per al cas de HERWIG 6.1 l'ajust forma part d'aquest treball.

En aquestes versions dels generadors cal destacar una millora important en la modelització dels efectes de massa del quark b, respecte a les versions utilitzades en la mesura anterior de DELPHI, JETSET 7.3 i HERWIG 5.8.

Les incerteses degudes al procés d'hadronització constitueixen una de les fonts dominants d'error en $m_b(M_Z)$ i és per aquest motiu que s'han estudiat detalladament en aquesta tesi. Així doncs, la mesura es va realitzar en una regió restringida de l'espai fàsic on els dos models de fragmentació donen prediccions similars. Es va fer també un estudi per tal de compendre la manera en què els paràmetres de massa del quark b entraven en les distintes fases del generador amb l'objectiu de fitar els seus valors. La incertesa associada amb aquests paràmetres va acabar sent l'error dominant en la determinació de $m_b(M_Z)$. És la primera vegada que es considera aquesta font d'error en la mesura de la massa del quark b.

Una vegada corregit l'observable a nivell de partons, es va comparar amb els càlculs NLO amb efectes de massa de [9, 79] per tal d'extraure la massa del quark b. Alternativament, es va mesurar el quocient α_s^b/α_s^ℓ, prenent la massa del quark b obtinguda amb dades de baixa energia en els càlculs teòrics.

Aquesta tesi està dividida en les segënts parts: El Capítol 1 conté una introducció al Model Estàndar, emfatitzant en la teoria de les interaccions fortes, QCD. Es discutix després el cas particular de les aniquilacions e^+e^- i l'efecte produït per la massa del quark b en aquests processos. El col·lisionador LEP i el detector DELPHI es descriuen al Capítol 2. Els generadors PYTHIA i HERWIG i l'ajust dels paràmetres del segon es descriuen en el Capítol 3. Al Capítol 4 s'obté la correcció d'hadronització de l'observable utilitzat per tal de mesurar la massa del quark b, així com les seues diferents fonts d'error. El procediment d'anàlisi utilitzat per tal de mesurar l'observable $R_3^{b\ell}$ es descriu al Capítol 5 i en el Capítol 6 es compara l'observable mesurat amb els càlculs teòrics per tal d'extraure la massa del quark b o verificar la independència de sabor de α_s. Finalment, es donen les conclusions d'aquest anàlisi.

Chapter 1

Theoretical framework

This chapter is devoted to describe the theoretical aspects related with the results presented in this thesis. It starts by an introduction of the Standard Model of elementary particles: the theories of electroweak and strong interactions. During this overview special emphasis is made on the origin of masses and the concept of running couplings and quark masses.

The application of the theory of strong interactions to e^+e^- annihilations is shown next. Perturbative calculations and nonperturbative models used to describe the process $e^+e^- \to$ hadrons are presented. Quark mass effects in these processes are then discussed. Quark masses are first defined and a review of different quark mass determinations is reported. Observables sensitive to the b quark mass at high energy are then presented. Next-to-leading order (NLO) massive calculations for the three-jet rate of Z^0 hadronic decays, which is the one used in this thesis to determine the b quark mass, are then described.

Finally, a discussion about why the Standard Model is not believed to be the ultimate theory is made.

1.1 The Standard Model

The present Standard Model (SM) of elementary particles and their fundamental interactions provides a very elegant theoretical framework which predicts extremely well all known particle physics phenomena from microscopic scales of order 10^{-19} m up to the cosmological distances of order 10^{25} m. However, not all aspects of the model have been experimentally established, in particular the Higgs Mechanism. Furthermore, the SM is expected to fail at short distances.

In the early 1960's, particle physicists described nature in terms of four different forces, characterized by different ranges and strengths: the strong force with a range of 10^{-15} m, the weak force, responsible for radioactive decays, with a range of 10^{-17} m and the electromagnetic and gravity forces, both having infinite ranges.

The SM describes all interactions except gravity in the language of quantum gauge field theories. Moreover, it combines the weak and electromagnetic forces in a single electroweak gauge theory.

There are two types of elementary particles [1] (see table 1.1):

- Fermions (matter particles): They are spin-1/2 particles and are classified into leptons and quarks, which are organized in three families with identical properties except for mass and flavour quantum number. These are:

$$\begin{bmatrix} \nu_e & u \\ e^- & d \end{bmatrix} \quad \begin{bmatrix} \nu_\mu & c \\ \mu^- & s \end{bmatrix} \quad \begin{bmatrix} \nu_\tau & t \\ \tau^- & b \end{bmatrix} \tag{1.1}$$

  plus the corresponding antiparticles.

  Quarks have an additional quantum number, the colour, which can be of three types. Colour is not seen in nature and therefore quarks need to be confined into the experimentally observed colourless matter particles, the hadrons. These are classified into baryons, fermions made of three quarks, and mesons, bosons made of one quark and one antiquark.

  The particles of the first generation form the ordinary matter and particles from the other two families rapidly decay via the weak forces to the quarks and leptons of the first family.

- Bosons (intermediate interaction particles): Apart from gravitational interactions, all interactions in particle physics are known to be mediated by the exchange of an elementary particle that is a boson of spin-1. The massless photon, γ, is the exchanged particle in the electromagnetic interactions, the eight massless gluons mediate the strong interactions among quarks and the three massive weak bosons, $W^\pm$ and Z, are the corresponding intermediate bosons of the weak interactions.

Fermions	**Generations**			Q_f	T_3^f	s
	1st	2nd	3rd			
Leptons	ν_e	ν_μ	ν_τ	0	+1/2	1/2
	e^-	μ^-	τ^-	-1	-1/2	1/2
Quarks	u	c	t	+2/3	+1/2	1/2
	d	s	b	-1/3	-1/2	1/2

Bosons	Q_f	T_3^f	s
γ	0	0	1
W^+	+1	+1	1
Z	0	0	1
W^-	-1	-1	1
g	0	0	1

Table 1.1: Elementary particles of the Standard Model and some of the quantum numbers assigned (charge, weak isospin and spin).

The first elementary particle discovered was the electron, which was found in 1897 by Thomson [18]. In 1930 Pauli postulated the existence of the neutrino as the cause of the missing energy and angular momentum observed in β decay, 23 years later the ν_e was found in experiments at nuclear reactors [19]. The muon was discovered in 1936 by analyzing cosmic rays [20] and in 1962 the ν_μ neutrino was also found in pion decays [21].

[1] Elementary particles are understood as the point-like constituents of matter with no known substructure up to the present limits of $10^{-18} - 10^{-19}$ m.

The up, down and strange quarks were seen in deep inelastic electron- and neutrino-nucleon scattering experiments [22]. In 1974, the J/Ψ was observed and interpreted as a $c\bar{c}$ bound state [23] and in 1976 mesons with a single charm quark were also found [24].

The first particle of the third family of fermions found was the τ lepton in 1975 at SLAC [25]. The discovery of the Υ at FNAL in 1979 was interpreted as the bound state of a new bottom quark [26]. The top quark was discovered at FNAL in 1994 [27]. The ν_τ was finally directly observed in the DONUT detector at FNAL in 2000 [28].

The large disparity on the measured matter particle masses is one of the unsolved fundamental questions of the SM and it is known as the hierarchy problem. They go from nearly massless neutrinos, 0.5 MeV/c^2 electrons, a few MeV/c^2 u and d quarks to around 200 GeV/c^2 for the top.

Regarding the intermediate boson particles, all of them have also been discovered. Starting with the γ, it was discovered when the photoelectric effect was interpreted theoretically in 1905 [29]. Gluons were discovered in 1979 at DESY as hadron jets in e^+e^- annihilations at high energy [31]. The $W^\pm$ and Z bosons were found at the CERN $p\bar{p}$ collider in 1983 [30], representing a drastic confirmation of the theory.

1.1.1 Theoretical formulation

Concerning the theoretical formulation of the SM, it is based on the gauge symmetry group $SU(3)_C \otimes SU(2)_L \otimes U(1)_Y$ [2] of unitary gauge transformations. This gauge group includes the symmetry group of strong interactions, $SU(3)_C$, and the symmetry group of electroweak interactions, $SU(2)_L \otimes U(1)_Y$. The group symmetry of electromagnetic interactions, $U(1)_{QED}$, appears in the SM as a subgroup of $SU(2)_L \otimes U(1)_Y$ and it is in this sense that weak and electromagnetic interactions are said to be unified.

The theory of strong interactions based on the colour group $SU(3)_C$ is called Quantum Chromodynamics (QCD) [32]. The gauge theory of the electroweak interactions based on the symmetry group $SU(2)_L \otimes U(1)_Y$ is known as the Glashow-Salam-Weinberg theory [33]. The eight gluons are the gauge bosons of $SU(3)_C$ and the γ, $W^\pm$ and Z particles are the four gauge bosons of $SU(2)_L \otimes U(1)_Y$.

The fact that the weak gauge bosons are massive particles indicates that $SU(2)_L \otimes U(1)_Y$ is not a symmetry of the vacuum. In contrast, the photon being massless reflects that $U(1)_{QED}$ is a good symmetry of the vacuum. Therefore there is an Spontaneous Symmetry

[2] $U(1)$ is the group of complex numbers with unit modulus.
$SU(2)$ is the group of 2×2 unitary matrices, i.e. $U^+U = UU^+ = 1$, with det $U = 1$. Any element of $SU(2)$ can be written in terms of 3 generators, $\vec{\sigma}/2$, and 3 real parameters, $\vec{\theta}$, as $U = e^{i\vec{\theta}\vec{\sigma}/2}$. $\vec{\sigma}$ are the Pauli matrices, which are traceless and satisfy $[\sigma_i, \sigma_j] = 2i\epsilon_{ijk}\sigma_k$, where ϵ_{ijk} is totally antisymmetric and its elements are the structure constants of $SU(2)$.
$SU(3)$ is the group of 3×3 unitary matrices with unit determinant. Any element of $SU(3)$ can be written in terms of 8 generators, $\lambda_\alpha/2$, and a set of 8 real parameters θ_α as $U = e^{i\theta^\alpha \lambda_\alpha/2}$. The generators are 3×3 hermitian matrices and are given by the so-called Gell-Mann matrices, λ_α, and satisfy $[\lambda_\alpha, \lambda_\beta] = i f_{\alpha\beta\gamma}\lambda_\gamma$, where $f_{\alpha\beta\gamma}$ is totally antisymmetric and its elements are the structure constants of $SU(3)$.

Breaking (SSB) [3] of the electroweak group to the electromagnetic subgroup:

$$SU(3)_C \otimes SU(2)_L \otimes U(1)_Y \overset{\text{SSB}}{\longrightarrow} SU(3)_C \otimes U(1)_{QED} \tag{1.2}$$

In the SM this SSB is implemented by the so-called Higgs Mechanism which generates the masses of the weak gauge bosons, fermion masses and mixings and gives rise to the appearance of a new particle, the Higgs boson, which is predicted to be scalar and electrically neutral.

1.2 The theory of electroweak interactions

We will concentrate here on the gauge theory of electroweak interactions and leave the QCD theory for Section 1.3.

The symmetry $G = SU(2)_L \otimes U(1)_Y$ is required to be a local symmetry of the electroweak Lagrangian. $SU(2)_L$ is the weak isospin group which acts only on left handed fermions [4] and $U(1)_Y$ is the weak hypercharge group. The $SU(2)_L \otimes U(1)_Y$ has then four generators, the three generators of $SU(2)_L$, $T_i = \sigma_i/2$ (i = 1,2,3), and the generator of $U(1)_Y$, $Y/2$.

The left handed fermions transform as doublets of $SU(2)_L$ while the right handed fields transform as singlets. For each family of fermions we have then,

$$\begin{bmatrix} \nu_l & q_u \\ l^- & q_d \end{bmatrix} \equiv \begin{pmatrix} \nu_l \\ l^- \end{pmatrix}_L , \quad \begin{pmatrix} q_u \\ q_d \end{pmatrix}_L , \quad l_R^- , \quad (q_u)_R , \quad (q_d)_R \tag{1.3}$$

The SM electroweak Lagrangian is build following the same steps as in any gauge theory. Starting from the free Lagrangian, $\sum_{f=l,q} i\overline{f}\gamma^\mu \partial_\mu f$ (f denoting any fermion field), the requirement of invariance under local G transformations, implies replacing the fermion derivatives by the corresponding covariant ones,

$$D_\mu f = \left(\partial_\mu - ig\vec{T} \cdot \vec{W}_\mu - ig' \frac{Y}{2} B_\mu \right) f \tag{1.4}$$

being the number of the introduced gauge boson fields ($\vec{W}_\mu$ and B_μ) equal to the number of generators, which is the number needed to describe the $W^\pm$, Z and γ. The coupling constants g and g' correspond to $SU(2)_L$ and $U(1)_Y$ respectively.

[3] In the language of Quantum Field Theory a system is said to possess a symmetry that is spontaneously broken if the Lagrangian describing the dynamics of the system is invariant under these symmetry transformations but the vacuum of the theory is not.

[4] The left-handed and right-handed fields are defined using the chirality operator $\gamma_5 = i\gamma_0\gamma_1\gamma_2\gamma_3$ as,

$$f_L = \frac{1}{2}(1 - \gamma_5)f; \; f_R = \frac{1}{2}(1 + \gamma_5)f$$

The four γ_μ matrices are given by:

$$\gamma_0 = \begin{pmatrix} 1 & 0 \\ 0 & -1 \end{pmatrix} \quad \gamma_i = \begin{pmatrix} 0 & \sigma_i \\ -\sigma_i & 0 \end{pmatrix}$$

being σ_i the Pauli matrices and 1 and 0 denoting, respectively, the 2×2 unit and zero matrices.

The resulting fermionic Lagrangian,

$$\mathcal{L}_f = \sum_{f=l,q} \overline{f} i\gamma^\mu D_\mu f \tag{1.5}$$

contains the kinetic and fermion interactions terms. But, in order to get the total Lagrangian one must add an extra piece $\mathcal{L}_G$ with the gauge boson kinetic terms and the gauge boson self-interaction terms,

$$\mathcal{L}_G = -\frac{1}{4}W^i_{\mu\nu}W^{\mu\nu}_i - \frac{1}{4}B_{\mu\nu}B^{\mu\nu} + \mathcal{L}_{GF} + \mathcal{L}_{FP} \tag{1.6}$$

being $\mathcal{L}_{GF}$ and $\mathcal{L}_{FP}$ the gauge fixing and Faddeev Popov Lagrangians respectively that are needed in order to quantize the gauge theory, which will be omitted, and the field strength tensors are given by,

$$\begin{aligned} W^i_{\mu\nu} &= \partial_\mu W^i_\nu - \partial_\nu W^i_\mu + g\epsilon^{ijk}W^j_\mu W^k_\nu \\ B_{\mu\nu} &= \partial_\mu B_\nu - \partial_\nu B_\mu \end{aligned} \tag{1.7}$$

Due to the non-abelian property of $SU(2)_L$, $\mathcal{L}_G$ contains the cubic and quartic self interactions among the gauge fields.

The physical gauge bosons $W^\pm_\mu$, Z_μ and A_μ are obtained from the electroweak interaction eigenstates by,

$$\begin{aligned} W^\pm_\mu &= \frac{1}{\sqrt{2}}(W^1_\mu \mp iW^2_\mu) \\ Z_\mu &= \cos\theta_w W^3_\mu - \sin\theta_w B_\mu \\ A_\mu &= \sin\theta_w W^3_\mu + \cos\theta_w B_\mu \end{aligned} \tag{1.8}$$

where θ_w defines the rotation in the neutral sector. The relations among the various couplings are obtained by identifying the interactions terms of A_μ with those of QED. Thus one gets,

$$\begin{aligned} g &= \frac{e}{\sin\theta_w} \qquad g' = \frac{e}{\cos\theta_w} \\ Q &= T_3 + \frac{Y}{2} \end{aligned} \tag{1.9}$$

The Lagrangian $\mathcal{L}_f + \mathcal{L}_G$ only contains massless fields and no mass terms, neither for the gauge bosons nor for the fermions, can be added without breaking the gauge symmetry.

The needed gauge boson masses must be generated preserving the gauge symmetry. The spontaneous breaking of the $SU(2)_L \otimes U(1)_Y$ and the Higgs Mechanism provide this mass generation.

The idea is to add a piece to the Lagrangian, $\mathcal{L}_{SBS}$, in such a way that the gauge symmetry is preserved but the ground state (vacuum) of the system does not possess such a symmetry and instead has the $U(1)_{QED}$ symmetry. In other words, the new Lagrangian should have a degenerate set of states with minimal energy, which transforms under G as the members of a given multiplet. When one of these states is arbitrarily selected as the ground state of the system, the symmetry becomes spontaneously broken.

The simplest choice is to add a new system Φ and the following $\mathcal{L}_{SBS}$,

$$\begin{aligned}\mathcal{L}_{SBS} &= (D_\mu\Phi)^\dagger(D^\mu\Phi) - V(\Phi)\\ V(\Phi) &= -\mu^2\Phi^\dagger\Phi + \lambda(\Phi^\dagger\Phi)^2 \;;\; \lambda > 0 \text{ and } -\mu^2 < 0\end{aligned}$$

with,

$$\begin{aligned}\Phi &= \begin{pmatrix}\phi^+\\ \phi_0\end{pmatrix}\\ D_\mu\Phi &= (\partial_\mu - \frac{1}{2}ig\vec{\sigma}\cdot\vec{W}_\mu - \frac{1}{2}ig'B_\mu)\Phi\end{aligned}$$

Φ is an $SU(2)_L$ doublet of complex scalar fields with hypercharge $Y(\Phi) = 1$. There is an infinite set of degenerate states with minimum energy,

$$| < 0|\Phi|0 > | = \begin{pmatrix}0\\ \frac{v}{\sqrt{2}}\end{pmatrix} \;;\; \text{arbitrary } arg\ \Phi \;;\; v \equiv \sqrt{\frac{\mu^2}{\lambda}} \tag{1.10}$$

All of them are $SU(2)_L \otimes U(1)_Y$ non-symmetric and $U(1)_{QED}$ symmetric. The breaking $SU(2)_L \otimes U(1)_Y \to U(1)_{QED}$ occurs once a particular vacuum is chosen.

It is important to note that one more degree of freedom than needed is introduced into the theory. Φ is a complex doublet and therefore it has four real components. Three of them provide the necessary longitudinal degrees of freedom in order to convert the massless $W^\pm$ and Z to massive fields and the fourth component translates into an extra massive scalar particle, the Higgs boson.

As it will be shown, the $\mathcal{L}_{SBS}$ provides the masses for the gauge bosons, M_W and M_Z, but to generate the fermion masses an additional piece needs to be added to the Lagrangian. Since a scalar doublet has been introduced into the model, we can write the following gauge invariant fermion-scalar coupling, the so-called Yukawa Lagrangian,

$$\mathcal{L}_{YW} = \lambda_e\bar{l}_L\Phi e_R + \lambda_u\bar{q}_L\widetilde{\Phi}u_R + \lambda_d\bar{q}_L\Phi d_R + \ h.c. + 2^{nd} \text{ and } 3^{rd} \text{ families} \tag{1.11}$$

where,

$$l_L = \begin{pmatrix}\nu\\ e\end{pmatrix}_L \;;\; q_L = \begin{pmatrix}u\\ d\end{pmatrix}_L \;;\; \widetilde{\Phi} = i\sigma_2\Phi^* = \begin{pmatrix}\phi_0^*\\ -\phi^-\end{pmatrix} \tag{1.12}$$

The full Lagrangian of the SM electroweak theory, $SU(2)_L \otimes U(1)_Y$ gauge invariant, is then:

$$\mathcal{L}_{EW} = \mathcal{L}_f + \mathcal{L}_G + \mathcal{L}_{SBS} + \mathcal{L}_{YW} \tag{1.13}$$

In order to get the particle masses, the non-symmetric vacuum must be first fixed. The simplest choice is chosen, that is the one of Eq. (1.10) with $arg\ \Phi = 0$. The physical spectrum is then build by making small oscillations around the vacuum,

$$\Phi(x) = \exp\left(i\frac{\vec{\xi}(x)\vec{\sigma}}{v}\right)\begin{pmatrix}0\\ \frac{v+H(x)}{\sqrt{2}}\end{pmatrix} \tag{1.14}$$

where $\vec{\xi}(x)$ and $H(x)$ are real fields. The local $SU(2)_L$ invariance of the Lagrangian allows us to rotate away any dependence on $\vec{\xi}(x)$. If we finally rotate the weak eigenstates to the mass eigenstates, we get,

$$\begin{aligned} (D_\mu\Phi')^\dagger(D^\mu\Phi') &= \left(\frac{g^2v^2}{4}\right)W_\mu^+W^{\mu-} + \frac{1}{2}\left(\frac{(g^2+g'^2)v^2}{4}\right)Z_\mu Z^\mu + ... \\ V(\Phi') &= \frac{1}{2}(2\mu^2)H^2 + ... \\ \mathcal{L}_{YW} &= \left(\lambda_e\frac{v}{\sqrt{2}}\right)\bar{e}'_L e'_R + \left(\lambda_u\frac{v}{\sqrt{2}}\right)\bar{u}'_L u'_R + \left(\lambda_d\frac{v}{\sqrt{2}}\right)\bar{d}'_L d'_R + ... \end{aligned} \tag{1.15}$$

and get finally:

$$\begin{aligned} M_W &= \frac{gv}{2}\ ;\ M_Z = \frac{\sqrt{g^2+g'^2}v}{2} \\ M_H &= \sqrt{2}\mu \\ m_e &= \lambda_e\frac{v}{\sqrt{2}}\ ;\ m_u = \lambda_u\frac{v}{\sqrt{2}}\ ;\ m_d = \lambda_d\frac{v}{\sqrt{2}}\ ;... \end{aligned} \tag{1.16}$$

If $\mathcal{L}_{SBS}$ and $\mathcal{L}_{YW}$, after the Higgs mechanism, are rewritten in terms of the physical scalar fields then the mass, the kinetic and interaction terms for the Higgs sector are found to be,

$$\mathcal{L}_{SBS} + \mathcal{L}_{YW} \to \mathcal{L}_H^{\rm free} + \mathcal{L}_H^{\rm int} + ... \tag{1.17}$$

where

$$\begin{aligned} \mathcal{L}_H^{\rm free} &= \frac{1}{2}\partial_\mu H\partial^\mu H - \frac{1}{2}M_H^2H^2 \\ \mathcal{L}_H^{\rm int} &= -\frac{M_H^2}{2v}H^3 - \frac{M_H^2}{8v^2}H^4 - \frac{m_f}{v}\bar{f}Hf + M_W^2W_\mu^+W^{\mu-}\left(1+\frac{2}{v}H+\frac{1}{v^2}H^2\right) \\ &+\frac{1}{2}M_Z^2Z_\mu Z^\mu\left(1+\frac{2}{v}H+\frac{1}{v^2}H^2\right) \end{aligned} \tag{1.18}$$

The following consequences are derived from the equations above:

- All masses are given in terms of the v parameter and the couplings g, g', λ_l ($l = e, \mu, \tau$) and λ_q ($q = u, d, s, c, b, t$).

- The interaction of the Higgs field with fermions and gauge bosons are proportional to the gauge couplings and to the corresponding particle masses:

$$f\bar{f}H\ :\ -i\frac{g}{2}\frac{m_f}{M_W}\ ;\quad W_\mu^+W_\nu^-H\ :\ igM_Wg_{\mu\nu}\ ;\quad Z_\mu Z_\nu H\ :\ \frac{ig}{c_w}M_Zg_{\mu\nu} \tag{1.19}$$

- The $W^{\pm}$ and Z masses can be predicted by using the relation $G_F/\sqrt{2} = g^2/(8M_W^2)$ obtained from the V-A theory [5] and Eq. (1.10), taking as input the measured θ_w, the fine structure constant α and G_F,

$$\begin{aligned} M_W &= \left(\frac{\pi\alpha}{G_F\sqrt{2}}\right)^{1/2}\frac{1}{\sin\theta_W} = 78\ \mathrm{GeV}/c^2, \quad M_Z = \frac{M_W}{\cos\theta_W} = 89\ \mathrm{GeV}/c^2 \qquad (1.20) \\ v &= (\sqrt{2}G_F)^{-1/2} = 246\ \mathrm{GeV} \end{aligned}$$

  The discovery of the $W^{\pm}$ and Z gauge bosons at the CERN SPS collider in 1983 [30], with $M_W = 81 \pm 2$ GeV/c^2 and $M_Z = 93 \pm 3$ GeV/c^2, may be considered as the first experimental evidence of the SSB phenomenon.

- The Higgs mass M_H (or the Higgs self coupling λ) and all fermion masses (or the λ_l and λ_q Yukawa parameters) are completely undetermined in the SM.

  The Higgs particle has not been found in the experiments so far. Experimentally, a lower bound for the Higgs mass of 114.4 GeV/c^2 with 95% C.L. has been set by the four LEP Collaborations via searches on the LEP data at energies $\sqrt{s} \leq 209$ GeV [34]. From fits to precise electroweak data, $M_H < 193$ GeV/c^2 with 95% C.L. [35]. Theoretically the Higgs is expected to have a mass below 1 TeV in order for perturbation theory to be valid up to very high energy. If the Higgs mass is higher, nonperturbative techniques are required, the Higgs self-interactions become strong and new physics phenomena may appear in the $\mathcal{O}$(TeV) range. This range of energy will be reached at the Tevatron and LHC accelerators.

1.3 The theory of strong interactions

1.3.1 The quark model

The discovery of the K^0 in 1947 [36] led to a new quantum number, the strangeness S, which appeared to be conserved by the strong interactions but not by the weak interactions. The conservation of S suggested that the strong interaction should have a larger symmetry than $SU(2)$: Gell-Mann and Ne'eman in 1961 proposed the $SU(3)$ symmetry group (sometimes called the flavour symmetry group) [37]. All mesons and baryons with the same spin and parity were then grouped into irreducible representations of $SU(3)$. Each particle is labelled by its (T_3, Y) quantum numbers and fits into one of the elements of this representations. This was the so-called *Eightfold Way* classification of hadrons.

In 1964 Gell-Mann and Zweig [38] proposed the existence of new particles, named quarks, in order for them to correspond to the lowest irreducible representation, i.e. the triplet, of $SU(3)$, which was not filled by any of the observed hadrons. By taking these three quarks as

[5] Before the Glashow-Salam-Weinberg electroweak theory was established, the V-A theory was proposed as the theory of electroweak interactions in 1958 by Feynman and Gell-Mann in order to explain the non-parity conservation of these interactions. This theory described well the phenomenology of weak interactions until the discovery of neutral currents in 1973. The V-A theory it is not predictive at high energies and it can only be used as an effective theory at low energies.

the elements of this fundamental representation one could build the whole spectra of hadrons. This led to the prediction of the u, d and s quarks and its corresponding antiparticles.

This description of hadrons in terms of quarks was called the $SU(3)$ *Quark Model.* Mesons appeared then as composite states of a quark and an antiquark and baryons as states made of three quarks. But the $SU(3)$ flavour symmetry is note an exact symmetry, since the members of a multiplet have different masses. The Quark Model was spectacularly confirmed by the discovery at Brookhaven Laboratory (BNL) of the Ω^- particle at the predicted mass.

However, the Quark Model presented some failures that indicated that this was not the proper model for strong interactions. The most famous one is the so-called *paradox of the* Δ^{++}. This particle is made of three quarks with identical quantum numbers and therefore its wave function is apparently totally symmetric, in contradiction with Pauli's Principle. This led to the hypothesis by Gell-Mann that quarks have an additional quantum number called colour. Each quark has $N_C = 3$ different colours and, since this property of colour is not observed in nature, hadrons are composed of quarks in such a way that are colourless. In the group theory language this is accomplished by requiring the hadrons to be in the singlet representations of the colour group, $SU(3)_C$.

The concept of colour is supported experimentally, as for example by the observation of hadrons like Ω^- and Δ^{++}. Other evidences for colour come from the measurement of the ratio of e^+e^- total hadronic cross section to the cross section for the production of a pair of point-like and charge-one objects such muons, the hadronic decay of the τ lepton and the $\pi^0 \to \gamma\gamma$ decay [39].

1.3.2 The QCD Lagrangian

Quantum Chromodynamics is the gauge theory for strong interactions. It is based on the gauge symmetry of strong interactions, i.e. the local colour transformations which leave the Lagrangian invariant. The gauge symmetry group generated by these colour transformations is the non-abelian Lie group $SU(3)_C$, where C refers to colour and 3 to the three possible colour states of quarks. The gluons are the eight gauge boson particles associated to this gauge symmetry, there are as much as $SU(3)$ generators, and they are interpreted as the mediators of the strong interactions among quarks.

The QCD Lagrangian is built by applying the gauge principle, i.e. the global symmetry $SU(3)_C$ of the Lagrangian for strong interactions is promoted to local by introducing the eight gluon fields, as it was done in Section 1.2 for the case of the electroweak Lagrangian.

The Lagrangian density describing the interaction of spin-$\frac{1}{2}$ quarks of mass m_f and massless spin-1 gluons, can be then written as,

$$\mathcal{L}_{QCD} \equiv -\frac{1}{4} G_a^{\mu\nu} G^a_{\mu\nu} + \sum_f \bar{q}_f \left(i\gamma^\mu D_\mu - m_f \right) q_f \tag{1.21}$$

where the gauge and ghost field terms have been suppressed [6]. $q_f \equiv (q_f^1, q_f^2, q_f^3)$ where q_f^α denotes a quark field of colour α and flavour f and D_μ is the covariant derivative. The field

[6] In order to properly quantize the QCD Lagrangian, one needs to add to the Lagrangian the so-called gauge fixing and Fadeev-Popov terms.

strength tensor $G_a^{\mu\nu}$ depends on the gluon fields G_a^μ by,

$$G_a^{\mu\nu}(x) = \partial^\mu G_a^\nu - \partial^\nu G_a^\mu + g_s f^{abc} G_b^\mu G_c^\nu \tag{1.22}$$

where the indices a, b and c denote the eight elements of the gluon field octet of QCD and f^{abc} are the structure constants of $SU(3)_C$.

The covariant derivative is given by,

$$(D_\mu)_{ab} = \partial_\mu \delta_{ab} + i g_s (t^A G_\mu^A)_{ab} \tag{1.23}$$

being t^A the $SU(3)_C$ generators which have the following commutation relation,

$$[t^A, t^B] = i f^{ABC} t^C \tag{1.24}$$

A representation for the generators is provided by the eight Gell-Mann matrices λ^A, which are hermitean and traceless, $t^A = \lambda^A/2$.

By convention, the normalization of the $SU(N)$ matrices is chosen to be,

$$\mathrm{Tr}\ (t^A t^B) = T_F \delta^{AB}, \quad T_F = \frac{1}{2} \tag{1.25}$$

With this choice, the colour matrices obey the following relations,

$$\sum_A t^A_{ab} t^A_{bc} = C_F \delta_{ac}, \quad C_F = \frac{N^2-1}{2N} \tag{1.26}$$

$$\sum_{A,B} f^{ABC} f^{ABD} = C_A \delta^{CD}, \quad C_A = N \tag{1.27}$$

Therefore, for the particular case of $N = 3$, the colour factors are,

$$C_F = \frac{4}{3}, \quad C_A = 3 \tag{1.28}$$

The Lagrangian of Eq. (1.21) can be decomposed in the following way,

$$\begin{aligned} \mathcal{L}_{QCD} \;\; = \;\; & -\frac{1}{4}(\partial^\mu G_a^\nu - \partial^\nu G_a^\mu)(\partial_\mu G^a_\nu - \partial_\nu G^a_\mu) + \sum_f \bar{q}_f^\alpha \left(i\gamma^\mu \partial_\mu - m_f\right) q_f^\alpha \\ & + g_s G_a^\mu \sum_f \bar{q}_f^\alpha \gamma_\mu \left(\frac{\lambda^a}{2}\right)_{\alpha\beta} q_f^\beta \\ & -\frac{g_s}{2} f^{abc} (\partial^\mu G_a^\nu - \partial^\nu G_a^\mu) G^b_\mu G^c_\nu - \frac{g_s^2}{4} f^{abc} f_{ade} G_b^\mu G_c^\nu G^d_\mu G^e_\nu \end{aligned} \tag{1.29}$$

The first line contains the kinetic terms for the different fields, which give rise to the corresponding propagators. The colour interaction between quarks and gluons is given by the second line, involving the $SU(3)_C$ matrices λ^a. In the last line, the $G_a^{\mu\nu} G^a_{\mu\nu}$ term generates the cubic and quartic gluon self-interactions, which appear as a consequence of the non-abelian

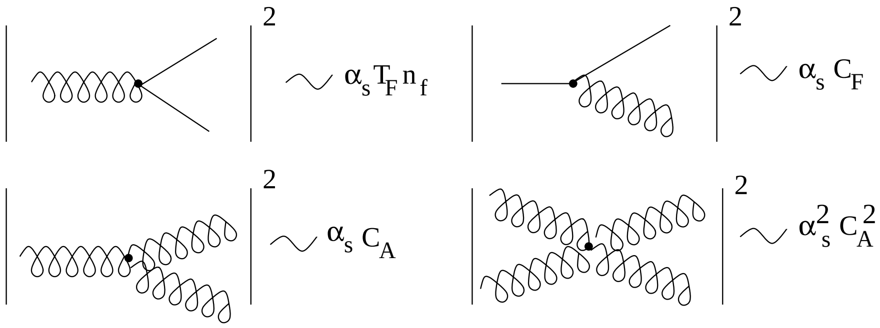

Figure 1.1: The four interaction vertices of QCD.

character of the colour group. All interactions are given in terms of a single universal coupling g_s. The strong coupling constant is defined as $\alpha_s = g_s^2/4\pi$, in analogy with the fine structure constant of QED.

Figure 1.1 shows the four possible interaction vertices of QCD. The probability of all these processes to occur depends on α_s and on the colour factors of Eqs. (1.25) and (1.28). The amplitude-squared corresponding to the radiation of a gluon from a quark diagram is proportional to C_F, that corresponding to the gluon splitting into a $q\overline{q}$ pair is proportional to T_F, and those corresponding to the non-abelian processes $g \to gg$ and $g \to ggg$ are proportional to C_A and C_A^2 respectively. Since C_F is smaller than C_A, quarks have a lower probability of emitting gluons than gluons.

The development of the QCD theory has always been linked to the advances on the experimental observations. In the late 1960's experiments at SLAC directed high energy electrons on proton and nuclear targets. The distributions in energy and angle of the electrons scattered in inelastic collisions suggested that electrons interact via photon exchange with charged point-like objects, which were called partons. Further deep inelastic experiments showed that the charged partons (quarks) carry only half of the proton momentum, giving indirect evidence for neutral partonic gluons.

The predicted gluons were discovered later in 1979 at the PETRA e^+e^- collider [31]. These collisions form an intermediate virtual photon state which may decay in a pair of quarks. The coloured quarks create many quark-antiquark pairs from the vacuum and arrange themselves into a set of colourless hadrons moving approximately in the directions of the original quarks, which are called jets. This is the process called *hadronization* of quarks into hadrons. However, before this occurs quarks can radiate gluons. If the gluon is radiated in a large enough angle to be distinguished, a separate jet is formed from the gluon. Three-jet event topologies were found, as expected from events containing a gluon. Experiments at higher energies, as those of the LEP collider, observe this gluon radiation even clearer (see figure 1.2). Studies in e^+e^- and hadron collisions have verified the expected QCD structure of the quark-gluon couplings and their interference patterns. For instance, three-jet events have been used to measure the strong coupling constant and the spin of the gluon. The colour group factors have also been determined by measuring event shape variables and jet rates.

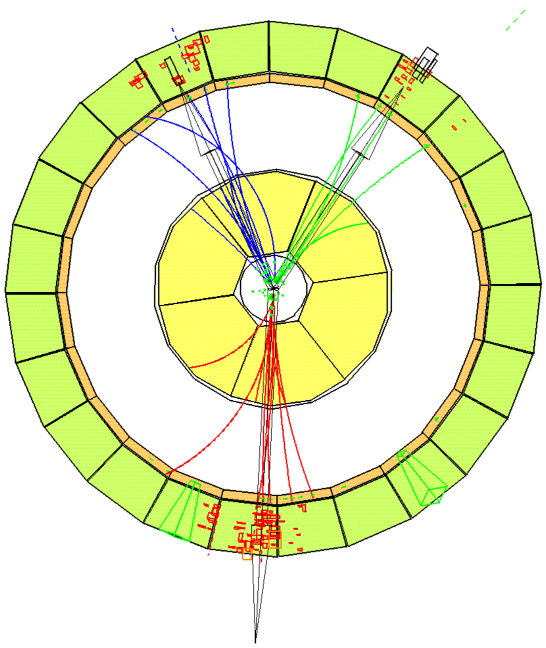

Figure 1.2: A three-jet event from the DELPHI experiment at LEP e^+e^- collider. It corresponds to a $e^+e^- \to b\bar{b}g$ event.

1.3.3 Regularization and renormalization

It is observed experimentally that the strength of the strong forces changes with the scale: the interaction is very strong at low energies (confinement) but quarks are nearly free particles at high energies (asymptotic freedom). However, the QCD Lagrangian involves a single parameter g_s and we cannot understand both energy regimes with a single constant.

In this section we will see that in order to compute loop diagrams the strong coupling constant and quark masses are made to depend on the energy scale of the process under consideration. This redefinition of α_s, found to solve a computational problem, is consistent with the two energy regimes observed in nature, as it will be shown.

The computation of perturbative corrections to the tree-level results involves divergent loop integrals, known as ultraviolet (UV) divergences. The strategy to deal with these divergences is the following:

- Identify an appropriate way of getting finite results with physical meaning from a priori meaningless divergent quantities. This is called the *regularization* of infinite integrals.
- Absorb the divergent terms into a redefinition of the original fields or parameters (couplings and masses). This step is usually called *renormalization*.
- Make sure the procedure is consistent, by checking that the physical results do not depend on the regularization prescription.

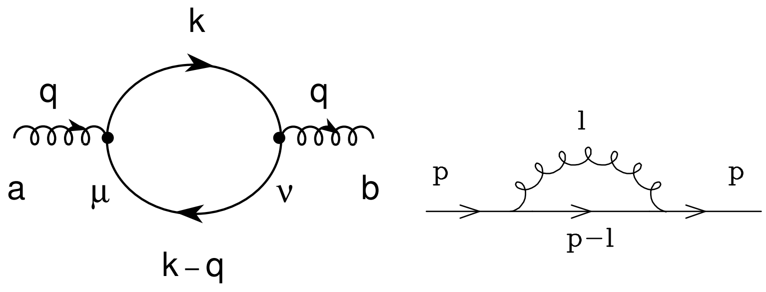

Figure 1.3: (Left) Gluon self-energy diagram. (Right) Quark self-energy diagram.

A Quantum Field Theory is called renormalizable if all ultraviolet (UV) divergences can be reabsorbed through a redefinition of the original fields and parameters. It has been proved that any gauge theory is renormalizable and therefore QCD can also be renormalized [40].

Regularization

As an example let's consider the self-energy gluon loop of figure 1.3. Using the Feynman rules one gets an integral in the momentum space of the form:

$$\int \frac{d^4k}{(2\pi)^4} \frac{k^\alpha (k-q)^\beta}{k^2 (k-q)^2} \tag{1.30}$$

which is clearly divergent [$\sim \int d^4k (1/k^2) = \infty$]. Different ways to get around this divergence exist. The methods are based on introducing a regularizing parameter such that the integral is well defined. One possibility is to introduce a cut-off M so that only momentum scales smaller than M are integrated. Another method consists on performing the calculation in $D = 4 + 2\epsilon$ dimensions with $\epsilon \neq 0$. This is called *dimensional regularization* [41] [7]. The resulting integral is then well defined,

$$\int \frac{d^Dk}{(2\pi)^D} \frac{k^\alpha (k-q)^\beta}{k^2 (k-q)^2} = \frac{-i}{6(4\pi)^2} \left(\frac{-q^2}{4\pi}\right)^\epsilon \Gamma(-\epsilon) \left(1 - \frac{5}{3}\epsilon\right) \left\{\frac{q^2 g^{\alpha\beta}}{2(1+\epsilon)} + q^\alpha q^\beta\right\} \tag{1.31}$$

where,

$$\Gamma(-\epsilon) = -\frac{1}{\epsilon} - \gamma_E + \mathcal{O}(\epsilon^2) \qquad \gamma_E = 0.577215\ldots \tag{1.32}$$

so the divergence appears at $\epsilon = 0$ through the pole of the Gamma function.

Since the momentum-transfer q^2 ($Q^2 = -q^2$) has dimensions, it is convenient to introduce an arbitrary energy scale μ (usually called the renormalization scale),

$$\mu^{2\epsilon} \left(\frac{-q^2}{4\pi\mu^2}\right)^\epsilon \Gamma(-\epsilon) = -\mu^{2\epsilon} \left\{\frac{1}{\epsilon} + \gamma_E - \log 4\pi + \log\left(-q^2/\mu^2\right) + \mathcal{O}(\epsilon)\right\} \tag{1.33}$$

[7] Dimensional regularization has many advantages because it preserves the gauge symmetry of QCD and therefore simplifies a lot the calculations.

so that one has a dimensionless quantity $(-q^2/\mu^2)$ inside the logarithm.

The contribution of the self-energy loop diagram can be then split into two parts: A meaningless divergent piece and a finite term including the q^2 dependence. This separation is ambiguous, since the finite q^2 independent contributions can be splitted in different ways, each of them defining a *scheme*. Both pieces are μ dependent but the sum does not depend on the scale μ.

For example, in the MS scheme [42] (Minimal Subtraction) one subtracts only the divergent $1/\epsilon$ term. A modification of this scheme is the $\overline{\text{MS}}$ scheme [43] (Modified Minimal Subtraction) in which the $\gamma_E - \log(4\pi)$ factor is also included in the divergent part. The $\overline{\text{MS}}$ scheme will be used from now on.

Renormalization

The divergent corrections generated by quantum loops can be reabsorbed by a redefinition of the coupling and quark masses. As an example, the gluon self-energy diagram of figure 1.3 (left) leads to the redefinition of the strong coupling constant while the one of the quark self-energy of figure 1.3 (right) leads to the quark mass renormalization. All ultraviolet divergent contributions to all possible scattering processes should be eliminated through the same redefinitions.

The renormalized quantities depend then on the arbitrary μ scale and on the chosen renormalization scheme. The prediction of the theoretical calculations for different observables depend on the renormalized quantities and therefore they can be determined experimentally.

Renormalization group equations

Let R be a dimensionless physical observable that depends on a single energy scale Q. Since the renormalization procedure introduces an additional energy scale, μ, R depends on the ratio Q^2/μ^2 and on the renormalized coupling α_s and quark masses m, which also depend on μ. However, since the μ scale is completely arbitrary, it cannot be related to any physical observable and hence physical observables should be invariant under the change of variables $(\mu,\alpha_s(\mu),m(\mu)) \to (\mu',\alpha_s(\mu'),m(\mu'))$, i.e.,

$$\mu^2 \frac{d}{d\mu^2} R(Q^2/\mu^2, \alpha_s(\mu), m(\mu)/Q) = \left(\mu^2 \frac{\partial}{\partial \mu^2} + \beta(\alpha_s) \frac{\partial}{\partial \alpha_s} - \gamma(\alpha_s) m \frac{\partial}{\partial m} \right) R = 0 \tag{1.34}$$

which defines two renormalization group coefficients, the β function and the mass anomalous dimension γ,

$$\beta(\alpha_s) = \mu^2 \frac{\partial \alpha_s}{\partial \mu^2} \tag{1.35}$$

$$\gamma(\alpha_s) = -\mu^2 \frac{1}{m} \frac{\partial m}{\partial \mu^2} \tag{1.36}$$

The solutions of these two differential equations lead to two fundamental properties of QCD: running coupling, $\alpha_s(Q^2)$, and running masses, $m(Q^2)$.

- **The running of the coupling constant**:

The value of the strong coupling constant changes with the energy scale of the process under consideration, Q^2. The running is determined by the renormalization group equation (RGE),

$$Q^2 \frac{\partial \alpha_s}{\partial Q^2} = \beta(\alpha_s) \tag{1.37}$$

which has been calculated from Eq. (1.35) after separation of variables, integration and derivation with respect to Q^2.

In QCD, the β function has the perturbative expansion [44],

$$\beta(\alpha_s) = -\beta_0\alpha_s^2 - \beta_1\alpha_s^3 - \beta_2\alpha_s^4 - \beta_3\alpha_s^5 + \mathcal{O}(\alpha_s^6) \tag{1.38}$$

where

$$\begin{aligned}
\beta_0 &= \frac{1}{4\pi}\left(11 - \frac{2}{3}n_f\right) \\
\beta_1 &= \frac{1}{4\pi}\left(102 - \frac{38}{3}n_f\right) \\
\beta_2 &= \frac{1}{4\pi}\left(\frac{2857}{2} - \frac{5033}{18}n_f + \frac{325}{54}n_f^2\right) \\
\beta_3 &= \frac{1}{4\pi}\left[\left(\frac{149753}{6} + 3564\zeta_3\right) - \left(\frac{1078361}{162} + \frac{6508}{27}\zeta_3\right)n_f \right. \\
&\quad \left. + \left(\frac{50065}{162} + \frac{6472}{81}\zeta_3\right)n_f^2 + \frac{1093}{729}n_f^3\right]
\end{aligned} \tag{1.39}$$

being n_f is the number of active flavours and ζ is the Riemann zeta function ($\zeta_3 = 1.202056903\ldots$).

A very important property of QCD is derived from the β_0 coefficient which is positive as long as $n_f \leq 16$, causing α_s to decrease with increasing Q^2 [8]. Therefore QCD has indeed the required property of asymptotic freedom, meaning that quarks and gluons behave at very short distances like free particles. At low energy scales, the strong coupling constant grows, suggesting that coloured objects will eventually be confined in colourless compounds (hadrons).

In Ref. [45] the renormalization group equation (1.37) was solved considering 4-loop expression for the β function and the result is:

$$\begin{aligned}
\alpha_s(Q^2) &= \frac{1}{\beta_0 L} - \frac{\beta_1 \log L}{\beta_0^3 L^2} + \frac{1}{\beta_0^3 L^3}\left[\frac{\beta_1^2}{\beta_0^2}\left(\log^2 L - \log L - 1\right) + \frac{\beta_2}{\beta_0}\right] \\
&+ \frac{1}{\beta_0^4 L^4}\left[\frac{\beta_1^3}{\beta_0^3}\left(-\log^3 L + \frac{5}{2}\log^2 L + 2\log L - \frac{1}{2}\right) - 3\frac{\beta_1\beta_2}{\beta_0^2}\log L + \frac{\beta_3}{2\beta_0}\right] \\
&+ \mathcal{O}\left(\frac{1}{L^5}\right)
\end{aligned} \tag{1.40}$$

[8] The gluonic self-interactions introduce the positive contribution to β_0. Only non-abelian gauge theories, where the intermediate gauge bosons are self-interacting particles, have this positive contribution.

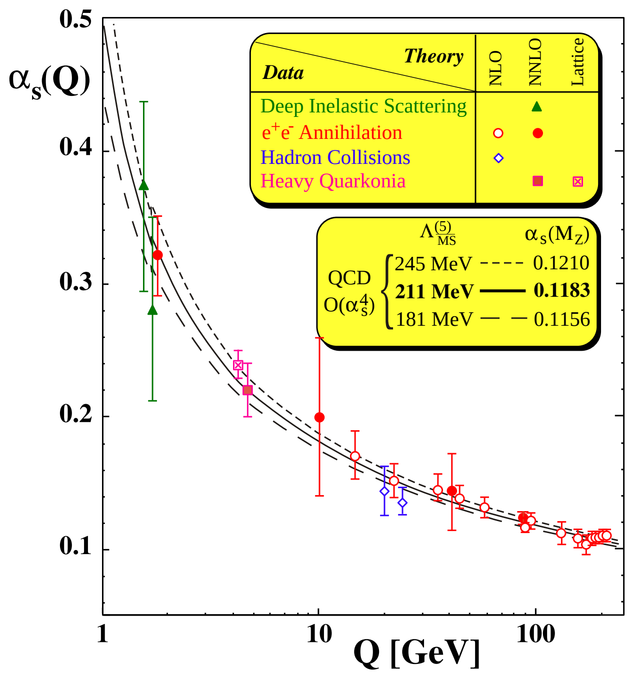

Figure 1.4: α_s determinations at different energies compared with the running predicted by QCD.

expressed in powers of $L = \log\left(Q^2/\Lambda^2_{\overline{\mathrm{MS}}}\right)$, where $\Lambda_{\overline{\mathrm{MS}}}$ is the constant of integration that depends in general on the renormalization scheme and on the number of active flavours. This constant is also denoted by Λ_{QCD}.

When $Q^2 \gg \Lambda^2_{\overline{\mathrm{MS}}}$, $\alpha_s(Q^2) \to 0$, so asymptotic freedom is recovered. At lower energies the running coupling gets larger and for $Q^2 \to \Lambda_{\overline{\mathrm{MS}}}$, $\alpha_s(Q^2) \to \infty$ indicating that the perturbative expansion cannot be applied at very small scales where nonperturbative effects become important.

The measurements of α_s at different processes and at different scales provide a crucial test of QCD. Figure 1.4 shows the results of some of the measurements as a function of the energy scale. The agreement with the QCD predicted running of α_s is very good.

- **The running of the quark mass**:

  The energy scale dependence of the quark mass is regulated by the γ function,

$$Q^2 \frac{\partial m}{\partial Q^2} = -\gamma(\alpha_s) m(Q^2) \tag{1.41}$$

  A perturbative expression for the mass anomalous dimension γ has been derived [46–48]:

$$\gamma(\alpha_s) = \gamma_0 \alpha_s + \gamma_1 \alpha_s^2 + \gamma_2 \alpha_s^3 + \gamma_3 \alpha_s^4 + \mathcal{O}(\alpha_s^5) \tag{1.42}$$

being,

$$\begin{aligned}
\gamma_0 &= \frac{1}{\pi} \qquad (1.43)\\
\gamma_1 &= \frac{1}{16\pi}\left[\frac{202}{3}-\frac{20}{9}n_f\right]\\
\gamma_2 &= \frac{1}{64\pi}\left[1249+\left(-\frac{2216}{27}-\frac{160}{3}\zeta_3\right)n_f-\frac{140}{81}n_f^2\right]\\
\gamma_3 &= \frac{1}{256\pi}\left[\frac{4603055}{162}+\frac{135680}{27}\zeta_3-8800\zeta_5+\left(-\frac{91723}{27}-\frac{34192}{9}\zeta_3+880\zeta_4+\frac{18400}{9}\zeta_5\right)n_f\right.\\
&\quad\left.+\left(\frac{5242}{243}+\frac{800}{9}\zeta_3-\frac{160}{3}\zeta_4\right)n_f^2+\left(-\frac{332}{246}+\frac{64}{27}\zeta_3\right)n_f^3\right]
\end{aligned}$$

where $\zeta_4 = 1.0823232\ldots$ and $\zeta_5 = 1.0369277\ldots$.

The solution of Eq. (1.41) is,

$$\begin{aligned}
m(Q^2) &= m(\mu^2)\exp\left[-\int_{\mu^2}^{Q^2}\frac{dQ^2}{Q^2}\gamma(\alpha_s(Q^2))\right] \qquad (1.44)\\
&= m(\mu^2)\exp\left[-\int_{\alpha_s(\mu^2)}^{\alpha_s(Q^2)}\frac{\gamma(\alpha_s)}{\beta(\alpha_s)}d\alpha_s\right]
\end{aligned}$$

Since $\gamma(\alpha_s)/\beta(\alpha_s)$ is positive, quark masses are smaller at higher energies. A 4-loop expansion for the running of the quark masses $m(Q^2)$ in the $\overline{\mathrm{MS}}$ scheme is given in Ref. [48].

1.4 QCD in e^+e^- annihilations

Electron-positron collisions provide one of the cleanest environments in which to study QCD. The key process is the annihilation of the e^+e^- pair into a virtual photon or Z^0 boson, which will subsequently decay to a $q\overline{q}$ pair. This process can be divided into four steps which involve different energy scales (see figure 1.5):

1. the actual e^+e^- annihilation into a $q\overline{q}$ pair via an intermediate boson, γ or Z^0, ($Q \sim \sqrt{s}$),

2. gluon radiation off quarks and gluon splitting into $q\overline{q}$ pairs, leading to the so-called parton shower ($\sqrt{s} > Q >$ few GeV),

3. the hadronization process, which refers to the transition of quarks and gluons into hadrons ($Q \sim$ few GeV),

4. and the decay of the unstable hadrons.

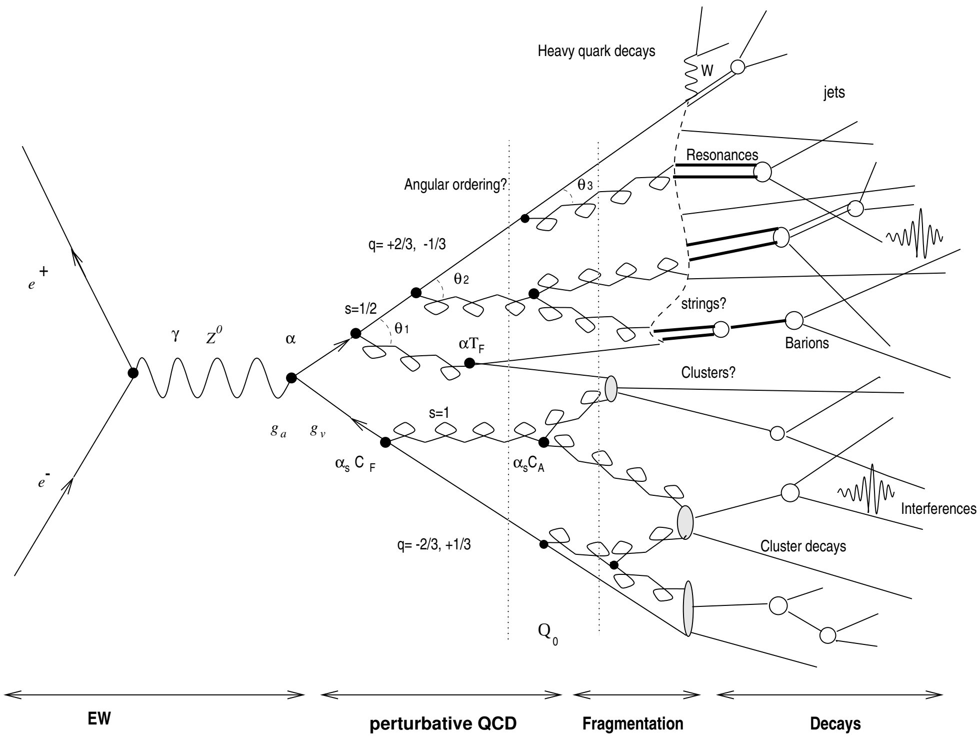

Figure 1.5: Schematic representation of an e^+e^- annihilation process into hadrons.

The first step is well described by the electroweak theory, for the parton shower phase perturbative QCD can be applied while the hadronization process is a nonperturbative effect. Hadron decays can be explained again by the electroweak and QCD theory. The main input here comes from the experimentally determined branching ratios. Particles produced at this last stage are the only ones observed by the detectors and the reconstruction of the primary hard process is done from these final particles.

The following sections will concentrate on the second and third steps. Two approaches to the modeling of perturbative QCD exist (see Sections 1.4.1, 1.4.2 and 1.4.3):

- Matrix Element (ME): Feynman diagrams are calculated order by order. In principle, this is the correct approach since it takes into account exact kinematics and the full interference and helicity structure. The problem here is that calculations become increasingly difficult as long as higher orders are considered. In fact, calculations have only been carried up to $\mathcal{O}(\alpha_s^2)$, insufficient to account for event structures.

- Parton Shower (PS): An arbitrary number of branchings of one parton into two (or more) may be put together, to yield to a description of multijet events, with no explicit upper limit on the number of partons involved. This is possible because instead of the full ME expressions, approximations derived by simplifying the kinematics and the interference and helicity structure are used. Parton showers are expected to give a good description of the substructure of jets, but in principle this approach has no predictive power for the rate of well separated jets.

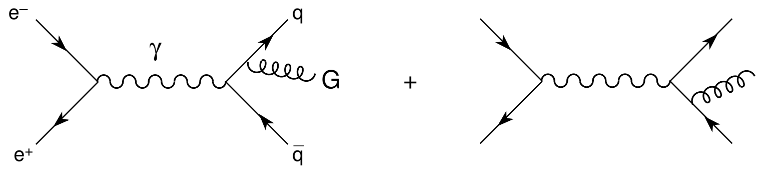

Figure 1.6: Feynman diagrams for real gluon bremsstrahlung corrections to $e^+e^- \to q\bar{q}$.

Concerning the third step, i.e. the hadronization process, although it is given by QCD, it cannot be calculated perturbatively and therefore phenomenological models have to be invoked. Some of them will be described in Section 1.4.4.

1.4.1 Cross section of $e^+e^- \to$ hadrons

The total production of hadrons, i.e. the inclusive $\sigma(e^+e^- \to \text{hadrons})$, can be calculated without considering the hadronization process (since the probability to hadronize is just one due to the confinement assumption),

$$\sigma(e^+e^- \to \text{hadrons}) = \sigma(e^+e^- \to q\bar{q} + q\bar{q}g + q\bar{q}gg + \dots) \tag{1.45}$$

At lowest order, the total hadronic cross section is obtained by summing over all kinematically accessible flavours and colours of $q\overline{q}$ pairs. Real and virtual gluon corrections to this process will generate higher-order contributions to the perturbation series. Instead of the absolute production cross section for $q\overline{q}$ pairs, its ratio to the muon pair production cross section is usually considered. Assuming massless quarks, at lowest order and at energies far below the Z^0 peak, i.e. $\sqrt{s} \ll M_Z$,

$$R = \frac{\sigma(e^+e^- \to \text{hadrons})}{\sigma(e^+e^- \to \mu^+\mu^-)} = \frac{\sum_q \sigma(e^+e^- \to q\overline{q})}{\sigma(e^+e^- \to \mu^+\mu^-)} = 3\sum_q Q_q^2 \tag{1.46}$$

where the factor 3 comes from the sum over quark colours, Q_q is the electric charge of the quark and the sum extends to all flavours that can be produced at the given energy. On the Z^0 resonance, the analogous quantity is the ratio of the partial decay widths of the Z^0 to hadrons and muon pairs:

$$R_Z = \frac{\Gamma(Z \to \text{hadrons})}{\Gamma(Z \to \mu^+\mu^-)} = \frac{3\sum_q(a_q^2 + v_q^2)}{a_\mu^2 + v_\mu^2} \tag{1.47}$$

v_f and a_f being the vector and axial couplings of the fermions ($f = q, \mu$) to the Z^0.

The strong interaction enters when calculating the $\mathcal{O}(\alpha_s)$ corrections to the total hadronic cross section, which has two contributions: the radiation of real and virtual gluons (the Feynman diagrams are shown in figures 1.6 and 1.7 respectively). The differential cross section for the real gluon emission process, $e^+e^- \to q\overline{q}g$, is found to be,

$$\frac{1}{\sigma_0}\frac{d^2\sigma}{dx_1 dx_2} = C_F \frac{\alpha_s}{2\pi}\frac{x_1^2 + x_2^2}{(1-x_1)(1-x_2)} \tag{1.48}$$

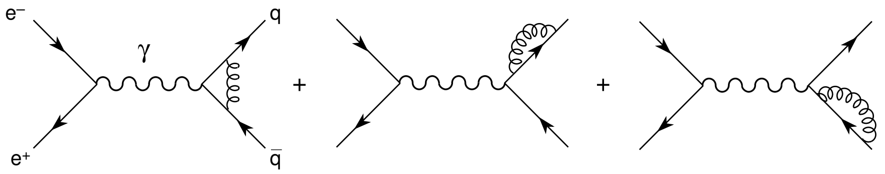

Figure 1.7: Feynman diagrams for 1-loop virtual gluonic corrections to $e^+e^- \to q\overline{q}$.

where σ_0 is the tree-level total cross section for $e^+e^- \to q\overline{q}$ and $x_i = 2E_i/\sqrt{s}$ $(i = 1, 2)$ represents the energy fraction taken by the quark or antiquark (the energy fraction taken by the gluon, x_3, is related through $x_1 + x_2 + x_3 = 2$).

Eq. (1.48) diverges when x_1 or x_2 tend to 1. These are called infrared (IR) divergences and they can be caused by the following kinematical configurations,

- Collinear gluon: The four-momentum of the gluon is parallel to that of either the quark or the antiquark. This divergence would be absent if either the gluon or the quark had a mass.
- Soft gluon: The gluon energy is small compared to $\sqrt{s}$, i.e. $E_g/\sqrt{s} \to 0$.

In order to obtain the total cross section, the differential cross section of Eq. (1.48) has to be integrated over the phase space, which includes the regions of singularities. In addition to this integration the diagrams involving the virtual gluons among the quarks of figure 1.7 have to be added. These diagrams, apart from the already mentioned ultraviolet divergences, which must be renormalized, also have infrared divergences. It can be shown [49] that these divergences exactly cancel the divergences of the differential cross section of Eq. (1.48), leading to a finite total cross section [9]. The QCD correction factor to the R ratio of Eqs. (1.46) and (1.47) takes the form,

$$K_{QCD} = 1 + \frac{\alpha_s}{\pi} + \mathcal{O}(\alpha_s^2) \tag{1.49}$$

1.4.2 Jet cross sections

It is interesting to measure more exclusive observables than the total hadronic cross section as distributions of final state quarks and gluons. However, due to confinement, hadrons are observed instead in the final state of a reaction. These hadrons are observed as a concentration of energy and particles around the direction of the original parton (quark or gluon). This spray of particles is qualitatively called a jet.

One thinks of a jet then as consisting of the fragmented products of a single off-shell parton that was produced in the annihilation by a short distance process. However, it is not completely straightforward to define precisely how many jets are present in a given

[9] The cancellation of the infrared singularities between the real and virtual diagrams is a general result: The Block-Nordsieck [50] and Kinoshita-Lee-Nauenberg [51] theorems state that for inclusive enough cross sections both the soft and collinear infrared divergences cancel.

final state and what their momenta and energies are. The physical problem is that the fragmented products from an energetic parton are not completely collimated and, due to quantum interference, a given hadron can be a product of more than one parton at once. A precise definition of jet is then needed in order to classify a final state of hadrons (experimentally) or quarks and gluons (theoretically) according to the number of jets it contains. Such definition should have the following requirements:

- the same definition should be applicable to real experiment data, i.e. the observed particles, and to partons that appear in perturbative calculations,
- infrared safe, i.e. insensitive to the emission of arbitrarily soft and collinear particles in order to avoid the IR singularities appearing in the perturbative calculations for massless partons,
- a close correspondence between the results obtained theoretically at parton and experimentally at hadron level, i.e. small hadronization corrections,
- good theoretical properties as reduced renormalization scale dependence in fixed order calculations, which is an indication that missing higher order contributions do not change significantly the fixed order predictions, and resummability of large terms to all orders in perturbation theory.

Various jet algorithms have been proposed and they can be divided in two types: cone and clustering algorithms. Cone algorithms are usually used to define jets in hadron collisions. In this case the jet is defined as those particles that have their momentum within a cone of a given angle. Clustering algorithms have been instead widely used in e^+e^- annihilations. They start by finding pairs of particles that are close in phase space and merging them together to form new pseudo-particles. This continues iteratively until the event consists of a a few well separated pseudo-particles, which are the resulting jets. There are different ways to define the closeness in phase space, the way to recombine the particles and the clustering ordering and therefore different clustering algorithms are available.

We will concentrate here on three of the most commonly used in e^+e^- experiments: the JADE [136], DURHAM [8] and CAMBRIDGE [13] algorithms.

The JADE algorithm was the earliest of the three and established the method of successive binary clustering. For all pairs of final state particles (i, j), a test variable y_{ij} is defined (see table 1.2). The minimum of all y_{ij} is compared with the so-called jet resolution parameter, y_c. If it is smaller, the two particles are recombined into a new pseudo-particle with four momentum $p_k = p_i + p_j$. The algorithm can be applied to the new group of pseudo-particles until all pairs satisfy $y_{ij} > y_c$. The number of jets in the event is the number of pseudo-particles that are left at the end. In perturbative theoretical calculations, this procedure leads to infrared-safe quantities because one excludes the regions of phase space that cause trouble.

The JADE algorithm was found to be not quite optimal from the theoretical and experimental point of view, which arise from the fact that its resolution criterion is approximately the invariant mass of the pair of pseudo-particles, $M_{ij}^2 \approx 2E_iE_j(1-\cos\theta_{ij}) > y_c s$. The effect is that particles at wide angles can be combined into the same jet, leading to theoretical

Algorithm	Resolution	Ordering	Recombination
JADE	$y_{ij} = \frac{2E_iE_j(1-\cos\theta_{ij})}{s}$	$v_{ij} = y_{ij}$	$p_k = p_i + p_j$
DURHAM	$y_{ij} = \frac{2\cdot\min(E_i^2,E_j^2)\cdot(1-\cos\theta_{ij})}{s}$	$v_{ij} = y_{ij}$	$p_k = p_i + p_j$
CAMBRIDGE	$y_{ij} = \frac{2\cdot\min(E_i^2,E_j^2)\cdot(1-\cos\theta_{ij})}{s}$	$v_{ij} = 2\cdot(1-\cos\theta_{ij})$	$p_k = p_i + p_j$

Table 1.2: Definition of the jet resolution variable y_{ij}, ordering variable and recombination procedure of the JADE, DURHAM and CAMBRIDGE jet finders. s is the total energy of the event, $p_i \equiv (E_i, \vec{p}_i)$ and θ_{ij} is the angle between $\vec{p}_i$ and $\vec{p}_j$.

predictions with large higher order corrections that cannot be resummed [53] and to the possibility of "ghost jets" (jets in directions where no particles are observed).

To overcome these problems the DURHAM algorithm was proposed [8]. In this new algorithm, the invariant mass test variable is replaced by a quantity which, when the angle between the particles is small, is the minimum of the relative transverse momentum (see table 1.2).

The CAMBRIDGE algorithm was introduced to cure some defects of the DURHAM algorithm at low y_c, with a better understanding of the processes involving soft gluon radiation, allowing to explore regions of smaller y_c [13]. It uses the same recombination procedure and test variable than DURHAM but with the new ingredients of angular ordering and *soft freezing*.

The selection of the first pair of particles to be compared with the resolution parameter is now done according to the ordering variable $v_{ij} = 2(1 - \cos\theta_{ij})$ (see table 1.2). Then, for the pair of particles with the smallest v_{ij}, one computes y_{ij} and if $y_{ij} < y_c$ the two particles are recombined. If not, the *soft freezing* mechanism comes into the game by considering the softer particle a resolved jet and by bringing back the other one to the binary procedure.

In the DURHAM algorithm one can always define a transition value of y_c, $y^{n\leftarrow n+1}$, in which an $(n+1)$-jet configuration event becomes an n-jet event. Furthermore, the number of jets is monotonically decreasing for increasing y_c. However, in CAMBRIDGE, this property is lost due to the fact that the sequence of clustering depends on the external y_c and in some circumstances certain jet topologies are not present for a specific event.

The general expression for a fraction of n-jet events takes the form,

$$R_n(s, y_c) = \left(\frac{\alpha_s(s)}{\pi}\right)^{n-2} \sum_{j=0} C_j^{(n)}(y_c) \left(\frac{\alpha_s(s)}{\pi}\right)^j \tag{1.50}$$

with $\sum_n R_n = 1$. The coefficients $C_j^{(n)}(y_c)$ depend on the jet clustering algorithm used.

Higher order $\alpha_s(\mu^2)^j \log^k(s/\mu^2)$ terms have been summed into $\alpha_s(s)$ but the coefficients $C_j^{(n)}(y_c)$ still contain $\log^k(y_c)$ terms. At low values of y_c, the infrared divergence reappears and the perturbative series becomes unreliable.

1.4.3 Parton shower

The fixed order perturbative calculations described in the previous sections get very complicated already at next-to-next-to-leading order (NNLO) and a different approach is then needed to describe multi-parton final states. Different methods have been developed which resum to all orders in α_s contributions to the cross section that become large in the region close to the kinematical limit (i.e. in which soft or collinear emissions occur).

The parton shower approach is derived within the framework of one of these methods, the *leading logarithm approximation* (LLA), where only the leading terms in the perturbative expansion are kept and resummed to all orders in α_s. Different schemes have been devised for taking into account some subleading corrections such as the MLLA [54,55] (M stands for modified), DLLA [56] (D for double) or NLLA [57] (N for next-to-).

The LLA can be formulated in terms of a probabilistic picture, suitable for event generation. The approach is based on simplifications in kinematical variables and therefore predictions for hard, wide-angle, parton emissions are limited.

Most parton showers algorithms are based on an iterative use of the branchings $q \to qg$, $g \to gg$ and $g \to q\bar{q}$ and a probabilistic picture is used to describe them. The probability $\mathcal{P}$ that a branching $1 \to 23$ will take place during a small change $dt = dQ^2_{evol}/Q^2_{evol}$ of the evolution parameter $t = \log(Q^2_{evol}/\Lambda^2)$ is given by the Altarelli-Parisi equations, which at leading order are,

$$\frac{d\mathcal{P}_{1\to 23}}{dt} = \int dz \frac{\alpha_s(Q^2)}{2\pi} P_{1\to 23}(z) \tag{1.51}$$

where $P_{1\to 23}(z)$ are the DGLAP or Altarelli-Parisi splitting kernels [58],

$$\begin{aligned} P_{q\to qg}(z) &= C_F \frac{1+z^2}{1-z} \\ P_{g\to gg}(z) &= 2C_A \frac{[1-z(1-z)]^2}{z(1-z)} \\ P_{g\to q\bar{q}}(z) &= T_F\left[z^2+(1-z)^2\right] \end{aligned} \tag{1.52}$$

and z specifies the sharing of four-momentum between the daughters, with daughter 2 taking the fraction z and the 3 daughter 1-z. The Q^2 scale of α_s doesn't need to agree with the evolution scale Q^2_{evol}. Flavour and energy conservation has to be maintained as an additional requirement and this is accomplished in the Monte Carlo programs at each branching.

A cut-off needs to be introduced on the range of the z integral in the Altarilli-Parisi equations in order to avoid the singular regions corresponding to excessive production of very soft gluons. This is usually achieved by introducing an effective gluon mass (usually denoted by $Q_0/2$ in the Monte Carlo programs).

The t parameter is regarded as a dimensionless evolution parameter, so the parton shower starts with the maximum virtuality $t = t_{max}$ and successively decreases at each branching. The shower stops at some fixed t_0, corresponding to a scale Q_0^2 around 1-2 GeV, where perturbative QCD is no longer valid.

The probability that a parton starting from a maximum virtuality t will reach the fixed lower cut-off t_0 without branching is the so-called Sudakov form factor,

$$S_1(t) = \exp\left(-\int_{t_0}^{t} dt' \int_{z_{min}(t')}^{z_{max}(t')} dz \frac{\alpha_s(Q^2)}{2\pi} P_{1\to 23}(z)\right) \tag{1.53}$$

Since the Sudakov form factors only depend on t, many Monte Carlo programs pretabulate them for each parton flavour at the beginning of the run.

The probability that no branching occurs from t_{max} to t, $\mathcal{P}_{\text{no}-\text{emission}}(t_{max}, t)$, is then just $S_1(t_{max})/S_1(t)$. With R a random number uniformly distributed between 0 and 1, the t value for a branching may be found to be by solving the equation,

$$\mathcal{P}_{\text{no}-\text{emission}}(t_{max}, t) = \mathrm{R} = \frac{S_1(t_{max})}{S_1(t)} \tag{1.54}$$

The products 2 and 3 may be allowed to branch in their turn, and so on. As already mentioned, the branching of a given parton is stopped whenever the evolution parameter is below t_0, i.e. when an $\mathrm{R} < S_1(t_{max})$ is chosen.

Different Monte Carlo programs based on the parton shower approach are available. They mainly differ on the interpretation of t (or Q^2_{evol}), Q^2 and z and some also include sub-leading logarithmic approximations.

1.4.4 Hadronization

The transition from partons (free states at small distances) to hadrons (confined states at large distances), the so-called hadronization or fragmentation process, cannot be explained by perturbative QCD, due to the very low energy scale involved in this transition which makes α_s too large.

Nonperturbative calculations are very complicated; Lattice QCD calculations can be used to predict some static hadronic properties such as masses and decay constants. For dynamical processes, like hadronization, phenomenological models are used instead. All these models implement hadronization as a probabilistic and iterative procedure and depend on effective parameters that cannot be calculated from the QCD Lagrangian but have to be adjusted. Two of the most commonly used in e^+e^- annihilations will be described here: the string and cluster models (implemented in PYTHIA [15] and HERWIG [16] Monte Carlo generators respectively).

- **String fragmentation** The basic idea of the string model [59, 60] is that the confinement potential of QCD corresponds to a colour flux tube, called a string, which is stretched between the partons in a singlet state. This tube has a transverse dimension of typical hadronic sizes (1 fm) and a constant tension of $k = 1$ GeV/fm. The $q\overline{q}$

pair corresponds to the ends of the string while the emitted gluons can be regarded as energy-momentum carrying kinks of the string [61].

If the potential energy stored in the string is high enough to create a $q'\overline{q}'$ pair from the vacuum the string will split into two independent pieces. This is then repeated for the resulting strings until only string pieces of hadron sizes are left. At the end of the process a set of hadrons are formed which move approximately along a straight line connecting the original quarks.

The generation of the $q'\overline{q}'$ pairs that leads to string breakups is governed by a quantum mechanical tunneling probability,

$$\exp\left(-\frac{\pi m_T^2}{k}\right) = \exp\left(-\frac{\pi m^2}{k}\right)\exp\left(-\frac{\pi p_T^2}{k}\right) \tag{1.55}$$

where m_T is the common transverse mass of the q' and $\overline{q}'$. This expression leads to a flavour independent Gaussian spectrum for the transverse momentum of $q'\overline{q}'$ pairs and a suppression of heavy quark production so that charm and heavier quarks are not expected to be produced.

The hadron transverse momentum is obtained as the sum of the transverse momenta of its constituent quarks. The energy of the hadron is given by the fragmentation function $f(z)$, being z the fraction of the quark energy carried by the fragmented hadron. If one requires that the fragmentation process should be the same whether it starts from the q end or the $\overline{q}$ one, there's only one possible function [62]: the Lund symmetric fragmentation function,

$$f(z) \propto \frac{(1-z)^a}{z}\exp\left(\frac{-bm_T^2}{z}\right) \tag{1.56}$$

with two free parameters, a and b, being m_T now the hadron transverse mass. For heavy quarks, this function predicts a harder spectrum than observed in data. The Bowler [63] and Peterson [64] fragmentation functions are some of the alternative. The former is given by,

$$f(z) \propto \frac{1}{z^{1+r_Q bm_Q^2}} z^a \left(\frac{1-z}{z}\right)^a \exp\left(\frac{-bm_T^2}{z}\right) \tag{1.57}$$

being r_Q a parameter chosen so to extrapolate smoothly between this form and the Lund symmetric one. The Peterson fragmentation function is given by,

$$f(z) \propto \frac{1}{z\left(1-\frac{1}{z}-\frac{\epsilon_Q}{1-z}\right)^2} \tag{1.58}$$

where ϵ_Q is a free parameter, expected to scale between flavours like $\epsilon_Q \propto 1/m_Q^2$.

- **Cluster fragmentation**

The cluster fragmentation model is based on the preconfinement property of perturbative QCD [65]. At the end of the parton shower, all gluons are split into a $q\overline{q}$ pair.

Colour singlet clusters are formed by quarks and antiquarks. Finally, hadrons are formed from the cluster decays. A cluster is assumed to decay into two hadrons unless it is too light (in which case it decays into just one hadron) or too heavy (it decays then into two clusters which decay further into hadrons).

1.5 Quark mass effects in e^+e^- annihilations

At LEP1 energy, $\sqrt{s} = M_Z$, the heaviest quark flavour produced is the bottom. Depending on the observable under study, the b quark mass can have a sizeable contribution within the experimental precision and therefore needs to be taken into account on the perturbative calculations [6].

The aim of this thesis is the determination of the b quark mass at the M_Z energy scale and therefore this section is devoted to the presentation of observables that are sensitive to b quark mass effects at the Z^0 peak energy and to a brief description of how the perturbative calculations taking mass effects into account were done for this kind of observables. But first a definition of quark masses will be given and an overview of the results obtained for the b quark mass at low energy will be done, with a brief description of the techniques used for this purpose.

1.5.1 Quark mass definition

In the SM all fermion masses are free parameters and their origin, although linked to the spontaneous symmetry breaking mechanism, is still an unresolved puzzle.

All free parameters of the SM model need to be determined experimentally and accurate knowledge of all of them is important for two main reasons: First, in order to improve the precision of the SM predictions for all processes. Second, they are not a random set of numbers, there are different patterns which could lead towards a fundamental theory which predicts some (if not all) of these parameters.

Most of these parameters are in the fermion sector so, in order to progress, the problem of fermion masses has to be attacked. There are theories beyond the SM, as Grand Unified Theories (GUT) and Supersymmetry (SUSY), that predict some relationship among fermion masses at the unification scale, $M_{\mathrm{GUT}} \sim 10^{16}$ GeV. For instance, the $SU(5)$ model predicts that at that scale the fermion Yukawa couplings (or fermion masses) are related as $\lambda_b = \lambda_\tau$, $\lambda_s = \lambda_\mu$ and $\lambda_d = \lambda_e$ while $SO(10)$ predicts unification of the third family, i.e. $\lambda_t = \lambda_b = \lambda_\tau = \lambda_{\nu_\tau}$. Therefore, a good determination of quark masses, in particular of the b quark, could be an important constraint on models beyond the SM, once the predicted mass is evolved, using the RGE's, from the unification scale to the scale at which the mass has been measured .

Focusing on the b quark, there are many processes predicted by the SM which are very sensitive to the b quark mass and therefore the uncertainty on this mass limits the precision reached in other parameters. As an example, the rate for inclusive semileptonic $b \to ul\overline{\nu}$, used to determine the CKM matrix element $|V_{ub}|$, is proportional to m_b^5. Another example is the rate for inclusive $b \to cl\overline{\nu}$ used to determine $|V_{cb}|$, which also has some sensitivity with m_b. In fact, determinations of the b quark mass have been performed recently by CLEO, Babar and Delphi Collaborations by measuring the lepton and hadronic moments for the inclusive decays $B \to X_c l \overline{\nu}$ and the γ energy moments in $B \to X_s \gamma$ decays [66]. There are other processes, not yet observed, as the branching ratio of the Higgs into $b\overline{b}$ which are also affected by the b quark mass value [71]. It is then clear than all efforts made to determine the b quark mass are worth it.

First, it is essential to clarify how a quark mass can be defined. For leptons it is clear than the physical mass corresponds to the pole of the propagator. Masses of charged leptons are well measured experimentally and neutrino masses are also bounded. The situation gets more complicated for quarks because they are confined inside hadrons and are not observed as free particles in nature. Therefore, it is not trivial to define the mass of a quark and, once this is done, they cannot be directly measured but can only be determined indirectly through their influence on hadron properties.

Quark masses need to be then properly defined with a chosen convention. The value of the quark mass must then always make reference to the particular theoretical framework that is used to define it. The perturbative pole mass, M_q, and the running mass, $m_q(\mu)$, are the two most commonly used quark mass definitions.

- Pole mass, M_q: It is defined as the pole of the renormalized quark propagator. It is a perturbative definition since the pole of the propagator can only be defined order by order in perturbation theory. It is gauge and scheme independent but it is very sensitive to nonperturbative effects.

  The pole mass can be used in perturbation theory but, in contrast to the pole mass in QED, the quark pole mass is not a physical parameter. The nonperturbative corrections to the quark self-energy give an ambiguity to the physical position of the pole of the quark propagator. In Ref. [67] it was shown that any perturbation series that relates a physical quantity to the pole mass has an intrinsic ambiguity of order $\Lambda_{\rm QCD}$. Since the pole mass can only be determined by its relation to a physical quantity, this translates into an ambiguity of the same order in the definition of the pole mass itself. This type of ambiguity is known as an *infrared renormalon.*

- Running mass, $m_q(\mu)$: It corresponds to the renormalized mass in the $\overline{\rm MS}$ scheme. Quark masses are just additional couplings in the QCD Lagrangian that need to be renormalized and therefore one gets scale dependent running quark masses (see Section 1.3.3).

  The renormalization scale μ is typically chosen to be of the same order as the characteristic energy scale Q of the process under study, since perturbation theory typically contains terms proportional to $\alpha_s^m(\mu)\log^m(Q/\mu)$, which are otherwise large. It is important to stress that the $\overline{\rm MS}$ running mass is not a useful quantity when renormalized at a scale $\mu < M_q$ [68].

Both mass definitions are related to each other. At $\mathcal{O}(\alpha_s)$ the relationship is given by [69],

$$M_b^2 = m_b^2(\mu)\left[1 + \frac{2\alpha_s(\mu)}{\pi}\left(\frac{4}{3} - \log\frac{m_b^2(\mu)}{\mu^2}\right)\right] \qquad (1.59)$$

This relationship has been computed up to three loops in Ref. [70]. Physics should be independent on the mass definition used but at a fixed order in perturbation theory there is a dependence on the mass definition as well as on the renormalization scale μ.

1.5.2 Quark masses determinations

Quark masses have been measured using different methods. Recent values of the $\overline{\mathrm{MS}}$ running mass are summarized in table 1.3. The c, b and t quark masses are given at the quark mass scale itself while for the other quarks a reference scale of 2 GeV has been selected.

Quark	$m_q(\mu)$ GeV/c^2
u	0.0034 ± 0.0006 [72]
d	0.0061 ± 0.0008 [72]
s	0.105 ± 0.020 [73]
c	1.19 ± 0.11 [74]
b	4.24 ± 0.11 [75]
t	165 ± 5 [76]

Table 1.3: Values of $\overline{\mathrm{MS}}$ running quark masses at a scale of 2 GeV for uds quarks and at the quark mass scale for c, b and t quarks.

The QCD Lagrangian has a chiral symmetry in the limit that quark masses vanish [10]. This symmetry is spontaneously broken by dynamical chiral symmetry breaking at a scale Λ_χ of around 1 GeV [77] and explicitly broken by the quark masses. Therefore, a quark is considered heavy if its mass is greater than Λ_χ (c, b and t quarks are then heavy) and light if it is smaller (u, d and s quarks are light).

For the bottom quark mass, which is the interest of this thesis, different nonperturbative techniques have been used to measure it at low energies. These are:

- **Effective field theories (EFT)**:

  The EFT approach allows to separate the short-distance physics associated with the b quark mass from the long-distance QCD dynamics. The leading order Lagrangian corresponds to the heavy mass limit [11]. Corrections to this limit are incorporated by non-renormalizable operators, suppressed by powers of $1/M_b$.

[10] In the case of massless quarks, the QCD Lagrangian can be written as two independent quark sectors,

$$\mathcal{L}_{\mathrm{QCD}} \equiv -\frac{1}{4} G_a^{\mu\nu} G^a_{\mu\nu} + i\,\bar{q}_L \gamma^\mu D_\mu q_L + i\,\bar{q}_R \gamma^\mu D_\mu q_R$$

where q denotes the flavour (and colour) vector $q^T = (u, d, \ldots)$, and L, R stand for the left- and right-handed components of the quarks ($q_L = \frac{1}{2}(1-\gamma_5)q$ and $q_R = \frac{1}{2}(1+\gamma_5)q$). Thus, the two quark chiralities live in separate flavour spaces (gluon interactions do not change the chirality). In this case, the QCD Lagrangian has the large symmetry $SU_L(N) \otimes SU_R(N) \otimes U_L(1) \otimes U_R(1)$, with N is the number of flavours.

[11] Limit of QCD in which the b quark mass is much larger than the QCD scale, i.e. $\frac{\Lambda_{\mathrm{QCD}}}{M_b} \to 0$. Therefore the physics that occurs at a distance $1/M_b$ can be separated from the physics of confinement, which occurs at a much larger distance scale $1/\Lambda_{\mathrm{QCD}}$. The hadronic physics is then irrelevant in this limit and the process is determined by short-distance physics.

Since the EFT is only applied to the b quark, the Lagrangian is given by $\mathcal{L}_{eff} = \mathcal{L}_{\rm heavy} + \mathcal{L}_{\rm light}$, where $\mathcal{L}_{\rm heavy}$ is the effective Lagrangian for b quarks and $\mathcal{L}_{\rm light}$ is the QCD Lagrangian for the gluons and light quarks.

The Heavy quark effective theory (HQET) and Non-relativistic QCD (NRQCD) are effective field theories that differ on the form of $\mathcal{L}_{\rm heavy}$.

- **HQET**:

  This theory is constructed by splitting the momentum of a heavy quark into a "large" piece, which scales like M_q, and a "small" piece, which scales like $\Lambda_{\rm QCD}$,

  $$p_q^\mu = M_q v^\mu + k^\mu \tag{1.60}$$

  where M_q is usually chosen to be the pole mass, but could be any mass parameter that differs from the meson mass by a term of order $\Lambda_{\rm QCD}$. The HQET Lagrangian is defined as an expansion in powers of $k^\mu/M_q \sim \Lambda_{\rm QCD}/M_q$. This expansion has been studied up to order $1/M_q^2$. At order $1/M_q$ it leads to the following relationship between the b quark pole mass and the meson mass,

  $$\begin{aligned} m_B &= M_b + \bar\Lambda - \frac{\lambda_1 + 3\lambda_2}{2M_b} + \ldots \\ m_{B^*} &= M_b + \bar\Lambda - \frac{\lambda_1 - \lambda_2}{2M_b} + \ldots . \end{aligned} \tag{1.61}$$

  where $\bar\Lambda$ corresponds to the energy of the light constituents (light quarks and gluons) of the meson and λ_1 and λ_2 are matrix elements of the quark kinetic energy and chromomagnetic moment operators.

  HQET gives also predictions for the inclusive decay rates of B hadrons in terms of the b quark mass.

- **NRQCD**:

  Bound states of a heavy quark and antiquark, such as the Υ or J/ψ, are non-relativistic systems in the heavy quark limit. NRQCD is the effective theory describing these systems.

  Since the physics of a non-relativistic bound state is very different from that of a single heavy quark interacting with the light components, the relevant expansion parameter in NRQCD is the heavy quark velocity v instead of $1/M_q$.

- **Lattice**:

  The space-time is replaced by a finite, discrete lattice of points. The lattice QCD Lagrangian contains then discrete differences replacing the derivatives of the QCD continuum.

  In order to determine quark masses, an appropriate set of physical quantities (usually hadronic masses) are computed using lattice QCD for different input values of the quark masses. The quark masses are found as those that best reproduce the set of physical quantities. The obtained masses are lattice bare masses and they need to be related with the renormalized masses in some renormalization scheme, such as $\overline{\mathrm{MS}}$.

The precision reached for quark masses is limited to the available computing resources. Another limitation is that calculations cannot be performed for three light quark flavours. Results are available for zero ($n_f = 0$, quenched approximation) and two light flavours. In the last years there has been a considerable progress in reducing systematic uncertainties.

- **QCD sum rules**:

  QCD sum rules have been successfully applied for extracting c and b quark masses from experimental data on the charmonium and bottomium systems. The fundamental quantity in these investigations is the vacuum polarization function $\Pi(q^2)$. The experimental cross section $e^+e^- \to q\overline{q}$ can be related to the imaginary part of $\Pi(q^2)$ via the optical theorem,

  $$R(s) = \frac{1}{Q_q^2}\frac{\sigma(e^+e^- \to q\overline{q})}{\sigma(e^+e^- \to \mu^+\mu^-)} = 12\pi \mathrm{Im}\Pi(s+i\epsilon) \tag{1.62}$$

  Using a dispersion relation, the moments $\mathcal{M}_n$ of $\Pi(s)$ can be expressed by integrals over the spectral density $R(s)$,

  $$\mathcal{M}_n = \frac{12\pi^2}{n!}\left(4M_q^2\frac{d}{ds}\right)^n \Pi(s)|_{s=0} = \left(4M_q^2\right)^n \int_0^\infty ds\frac{R(s)}{s^{n+1}} \tag{1.63}$$

  being M_q the pole mass. The moments can either be calculated theoretically in renormalization group improved perturbation theory or can be obtained from experimental data. This is how hadronic quantities like masses and decay widths get related to QCD parameters as α_s and quark masses.

The b quark mass has been extracted using the above techniques from the $b\overline{b}$ and B systems. NRQCD, QCD sum rules and lattice are the methods used to measure the b quark mass from the Υ system while HQET and lattice QCD are used to extract it from the B system. A value for each method has been estimated in Ref. [75] and they are shown in table 1.4. The best estimate of the b quark mass obtained in Ref. [75] from all these values is $m_b(m_b) = 4.24 \pm 0.11$ GeV/c^2.

For light quarks, chiral symmetry considerations can be used to fix quark mass ratios, which are independent of renormalization conventions. A relation between the physical meson masses (π, K and η) and light quark masses is extracted leading to the ratios of light quark masses [78],

$$\frac{m_u}{m_d} = 0.553 \pm 0.043 \qquad \frac{m_s}{m_d} = 18.9 \pm 0.8 \tag{1.64}$$

The absolute values of light quark masses have to be determined using methods that go beyond chiral perturbation theory, such as QCD sum rules or lattice. The up and down quark masses of table 1.3 have been fixed by using the ratio of Eq. (1.64) and the estimate of $m_u(2\text{ GeV}) + m_d(2\text{ GeV}) = 9.5 \pm 1.4$ MeV/c^2 from QCD sum rules [72].

System	Method	$m_b(m_b)$ GeV/c^2
Υ	NRQCD	4.23 ± 0.11
	Sum Rules	4.20 ± 0.10
	Lattice QCD	4.26 ± 0.11
B	HQET	4.31 ± 0.13
	HQET	$4.22 \pm 0.09 \pm \mathcal{O}(\alpha_s^2)$
	Lattice QCD	4.26 ± 0.09

Table 1.4: Results of the b quark mass determinations with the different techniques available from the Υ and B systems [75]. The error associated with each value includes theoretical and statistical uncertainties.

The strange quark mass has been extracted from the hadronic τ decays using QCD perturbation theory, since the relevant scale, m_τ, is high enough. In Ref. [73] it was determined to be $m_s(m_\tau) = 121.7 \pm 17.2$ MeV/c^2. Other methods to determine the s quark mass have been used, an average value of $m_s(2 \text{ GeV}) = 105 \pm 20$ MeV/c^2 was found in Ref. [73].

For the c quark one of the latest determinations give $m_c(m_c) = 1.19 \pm 0.11$ GeV/c^2 [74]. The top quark mass given in table 1.3 corresponds to the one measured at Fermilab [76], $M_t = 174.3 \pm 5.1$ GeV/c^2, assuming that the measured mass is the pole mass.

1.5.3 Motivations to measure the b quark mass at high energy

The b quark mass is a fundamental parameter in the SM and therefore it is important to have as many as possible independent determinations of it, i.e. with different conditions, physical observables and theoretical calculations.

All determinations of the b quark mass described in previous section were performed at the production threshold taking as an input the known spectra of hadronic bound states or the measured moments of the B decay products spectra.

A determination of the b quark mass at LEP energy, $\sqrt{s} \sim M_Z$, using jet rates becomes then very interesting since it represents a direct and independent measurement of this free parameter of the SM at an energy scale far from threshold. In the case of the running mass, it allows to test the evolution with the scale predicted by QCD, when the value obtained at M_Z is compared with the results obtained at threshold. Other motivations are the test of GUT and SUSY theories, which predict some relations among fermion masses at the unification scale, as mentioned in Section 1.5.1. Since large part of the b mass running from the production threshold to the unification scale occurs at the M_Z scale, $m_b(M_Z)$ is a basic input parameter to test this kind of theories.

1.5.4 Sensitivity to the quark mass at high energy in e^+e^- annihilations

The radiation of gluons by quarks does not only depend on the strong coupling constant but also on the mass of the emitting quark. A finite mass, apart from reducing the phase space available for gluon emission, has the effect of reducing the QCD radiation. The differential cross section of Eq. (1.48), considering a quark mass of m_q, gets modified to,

$$\frac{1}{\sigma_0}\frac{d^2\sigma}{dx_1 dx_2} = C_F\frac{\alpha_s}{2\pi}\left[\frac{x_1^2+x_2^2}{(1-x_1)(1-x_2)} - \frac{4m_q^2}{s}\left(\frac{1}{1-x_1}+\frac{1}{1-x_2}\right)\right.$$
$$\left. -\frac{2m_q^2}{s}\left(\frac{1}{(1-x_1)^2}+\frac{1}{(1-x_2)^2}\right) - \frac{4m_q^4}{s^2}\left(\frac{1}{1-x_1}+\frac{1}{1-x_2}\right)^2\right] \tag{1.65}$$

where all terms dependent on the mass are subtracted implying a suppression of gluon radiation. Since $1 - x_i \geq m_q^2/s$ ($i = 1, 2$), the collinear singularity disappears for $m_q \neq 0$. The soft singularity however is still present. Another interesting feature derived from the above equation is that the cross section is suppressed for gluons approximately collinear with the heavy quark ($\theta \leq 2m_q/\sqrt{s}$). This is known as the *dead cone* effect.

At LEP energies, the heaviest quark produced is the bottom but, even for this case, b mass effects are negligible for inclusive observables since they are suppressed by $m_b^2/M_Z^2 \leq 0.3\%$. However, for more exclusive observables, like jet cross sections, mass effects can be enhanced considerably for small enough values of the jet resolution parameter, y_c, as they go like $m_b^2/M_Z^2/y_c$ [6]. In addition, mass effects could also be enhanced by logarithms of the mass due to the phase space restriction (for example, the ratio of the phase space for two quarks and a gluon for b quarks over massless quarks is $1 + 8(m_b/M_Z)^2\log(m_b/M_Z) \sim 3\%$ for $m_b =$ 3 GeV/c^2 and about 7% for $m_b = 5$ GeV/c^2) [6].

1.5.5 NLO computations with massive quarks

NLO calculations taking mass effects into account have been performed for the ratios of b over light ℓ quark events for some infrared-safe observables of event shape type and the three-jet rate [9, 14, 79, 80]. They allow to either test α_s flavour independence, taking the b quark mass extracted from independent measurements performed at low energies, or, assuming α_s universality, measure the b quark mass.

We will concentrate on the computations performed on the three-jet rate for the DURHAM and CAMBRIDGE jet clustering algorithms, since those are the ones used for the results presented in this thesis. Details of the calculations can be found in [9, 14]. The observable used to quantify the b mass effect is in this case,

$$R_3^{b\ell} = \frac{\Gamma_{3j}^b(y_c)/\Gamma^b}{\Gamma_{3j}^\ell(y_c)/\Gamma^\ell} \tag{1.66}$$

being $\Gamma_{3j}^q(y_c)$ and Γ^q, respectively, the three-jet and total decay widths of the Z^0 into $q\bar{q}$, where $q = (b$ or $\ell \equiv uds)$. All light quarks are considered massless in the calculations. The flavour q of the hadronic event is defined as that of the quarks coupled to the Z^0 and therefore events of the type $Z^0 \to \ell\bar{\ell}g \to \ell\bar{\ell}b\bar{b}$, where the radiated gluon has splitted into a pair of b quarks, will contribute to the denominator of Eq. (1.66). This definition of the event flavour allows to cancel large logarithms of the b quark mass appearing in the theoretical calculations.

The definition of the observable as a double ratio presents theoretical and experimental advantages. The normalization to total rates, $\Gamma^q_{3j}(y_c)/\Gamma^q$, is important from the theoretical point of view because most of the electroweak corrections cancel. The ratio between the b and ℓ normalized cross sections allows a partial cancelation of those corrections which are similar for b and ℓ quark events, as hadronization and detector corrections.

From the definitions of the jet clustering algorithms of Section 1.4.2, the cross section of e^+e^- annihilations into three jets at LO is the same for both DURHAM and CAMBRIDGE algorithms, since only three-parton final state configurations contribute at LO to this cross section.

At NLO the three-jet cross section receives contributions from the one-loop corrected three-parton final states and from the four-parton processes, where two of the four partons are combined in order to produce a three-jet final state. The UV divergences found in the calculation of the three-parton contribution at the one-loop level are removed by the renormalization of the parameters of the QCD Lagrangian. A mixed renormalization scheme was used, the $\overline{\mathrm{MS}}$ scheme for the strong coupling constant and the on-shell (pole) definition for the quark mass. IR singularities coming from three- and four-parton final states are canceled analytically using the phase-space slicing method [81]. The remaining finite pieces from both three- and four-parton processes are integrated numerically over the three-jet phase space defined by the jet algorithm.

At the end, the double ratio of Eq. (1.66) can be written as an expansion in α_s,

$$R_3^{b\ell} = 1 + \frac{\alpha_s(\mu)}{\pi} a_0(y_c) + r_b \left(b_0(r_b, y_c) + \frac{\alpha_s(\mu)}{\pi} b_1(r_b, y_c) \right) \tag{1.67}$$

where $r_b = M_b^2/s$ and $s = M_Z^2$ at the Z^0 peak.

Note that $R_3^{b\ell}$ is not unity for a vanishing b quark mass due to the triangle one-loop diagrams [82], which give a small non-zero contribution even in the case of massless b quarks, taken into account by the function a_0. The size of this effect is about 2‰ in $R_3^{b\ell}$.

The functions b_0 and b_1 depend on the jet clustering algorithm and describe the quark mass effect at LO and NLO in α_s respectively.

Eq. (1.67) can be re-expressed in terms of the running mass $m_b(\mu)$ by using the relationship of Eq. (1.59),

$$R_3^{b\ell} = 1 + \frac{\alpha_s(\mu)}{\pi} a_0(y_c) + \overline{r}_b \left(b_0(\overline{r}_b, y_c) + \frac{\alpha_s(\mu)}{\pi} \overline{b}_1(\overline{r}_b, y_c, \mu) \right) \tag{1.68}$$

being now $\overline{r}_b(\mu) = m_b^2(\mu)/M_Z^2$ and the function $\overline{b}_1$ is related to b_0 and b_1 like,

$$\overline{b}_1(\overline{r}_b, y_c, \mu) = b_1(\overline{r}_b, y_c) + 2 b_0(\overline{r}_b, y_c) \left(\frac{4}{3} - \log \overline{r}_b + \log \frac{\mu^2}{M_Z^2} \right) \tag{1.69}$$

At the perturbative level both equations (1.67) and (1.68) are equivalent but, since different higher order terms are neglected in each case, they lead to slightly different results. Furthermore, both have a residual dependence with the scale μ; in Eq. (1.67) it comes from the dependence in $\alpha_s(\mu)$ and in Eq. (1.68), apart from entering in $\alpha_s(\mu)$, it also comes from the incomplete cancellation of the μ dependence between $m_b(\mu)$ and the logarithms of μ

appearing in Eq. (1.69). All these dependences are used to estimate uncertainties due to higher order missing terms.

Figure 1.8 shows the $R_3^{b\ell}$ as a function of y_c obtained at NLO for a running mass $m_b(M_Z)$ = 3 GeV/c^2 using Eq. (1.68) and for a pole mass of $M_b = 5$ GeV/c^2 using Eq. (1.67). The LO results are also shown for comparison for these two values of the b mass (note from Eq. (1.59) that the difference between the pole and running mass is a NLO effect). The NLO predictions for $R_3^{b\ell}$ are only valid for that region of y_c in which events are reconstructed mostly to two or three jets, with a small contribution of four jets events. For small values of y_c the perturbative calculations are not expected to be correct and higher order computations would be needed in order to take into account n-parton ($n > 4$) final states too. Several things can be observed from figure 1.8, where the $R_3^{b\ell}$ dependence with y_c is shown for a y_c range in which the perturbative calculations are valid:

- $R_3^{b\ell}$ decreases for smaller y_c values.
- For small values of the y_c the mass effect is of the order of 5% which with the LEP precision can be observed.
- For the case of CAMBRIDGE the NLO corrections when the parameterization in terms of the running mass is used are much smaller than when $R_3^{b\ell}$ is written in terms of the pole mass. This means that the LO calculations for the value of the running mass takes into account the bulk of the NLO corrections. This suggests that the higher order corrections to the result obtained when the parameterization in terms of the running mass is used might be smaller. For the DURHAM algorithm the size of the NLO corrections are about the same in both parameterizations.

In order to obtain $m_b(M_Z)$ from a measured value of $R_3^{b\ell}$ at a given y_c there are two possibilities:

- Method 1: Use Eq. (1.67) to extract a value for the pole mass, M_b, for an arbitrary value of μ. Then use Eq. (1.59) at $\mu = M_b$ to obtain $m_b(M_b)$ and use the RGE to go from $\mu = M_b$ to $\mu = M_Z$ to get $m_b(M_Z)$.
- Method 2: Use Eq. (1.68) to obtain, for an arbitrary scale μ, the running mass at that scale, $m_b(\mu)$. Then use the RGE to evolve from that scale to M_Z to finally get $m_b(M_Z)$.

Notice that since our observable is $\mathcal{O}(\alpha_s)$, to be consistent, the 1-loop renormalization group equations should be used:

$$\alpha_s(\mu) = \frac{\alpha_s(M_Z)}{K}, \qquad m_b(\mu) = m_b(M_Z) K^{-\gamma_0/\beta_0} \tag{1.70}$$

being $K = 1 + \alpha_s(M_Z)\beta_0 \log(\mu^2/M_Z^2)$ and β_0 and γ_0 those given in Eqs. (1.40) and (1.44).

Figure 1.9 shows, for the two jet clusterings algorithms, the results obtained for $m_b(M_Z)$ for each of the two methods as a function of the value used for μ/M_Z. For the case of DURHAM

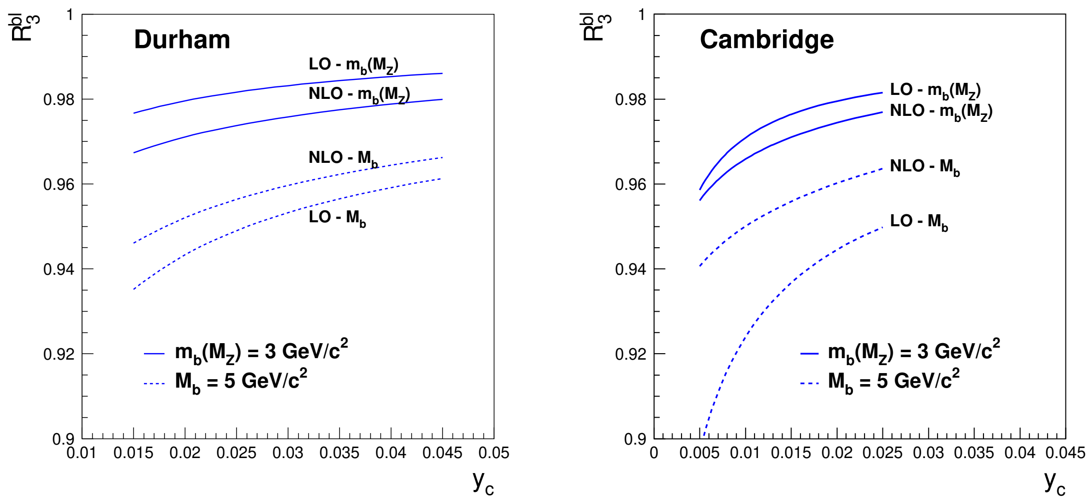

Figure 1.8: $R_3^{b\ell}$ as a function of y_c predicted for DURHAM (left) and CAMBRIDGE (right) for the NLO order results obtained for a running mass $m_b(M_Z) = 3$ GeV/c^2 using Eq. (1.67) and for a pole mass of $M_b = 5$ GeV/c^2 using Eq. (1.68). The LO results are also shown for comparison. In both cases, $\mu = M_Z$ and $\alpha_s(M_Z) = 0.1183$.

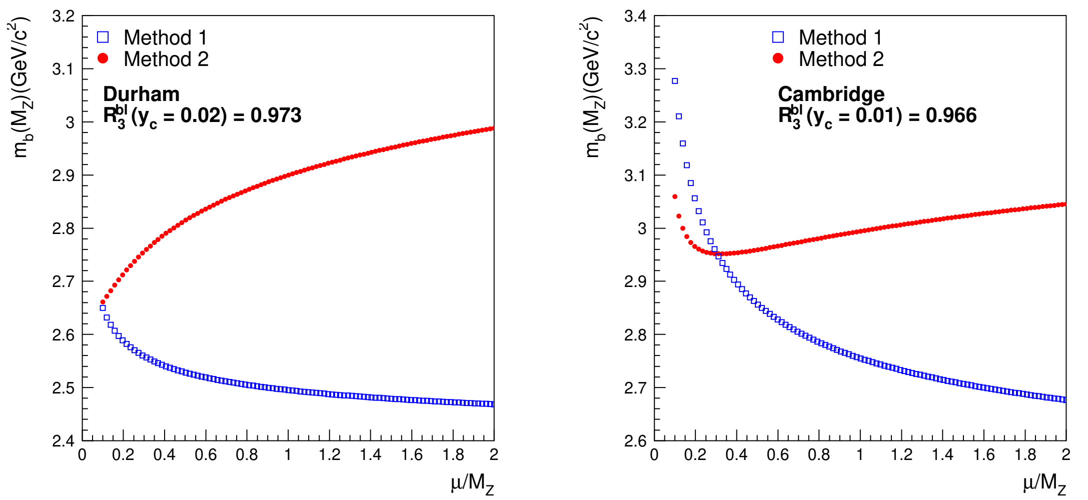

Figure 1.9: Results obtained, for a given value of $R_3^{b\ell}$ at a given y_c, for $m_b(M_Z)$ as a function μ/M_Z for the two methods. The plot on the left are obtained with DURHAM and CAMBRIDGE is the algorithm used on the right plot.

the results correspond to an input of $R_3^{b\ell}(y_c = 0.02) = 0.973$ while for CAMBRIDGE the input is $R_3^{b\ell}(y_c = 0.01) = 0.966$.

We have adopted the convention of giving the final result for $m_b(M_Z)$ as the mean of the results obtained by the two methods at $\mu = M_Z$. We considered that the theoretical uncertainty has three contributions:

- μ dependence: It is evaluated using the second method and it is given as half of the difference between the results obtained for a variation of the arbitrary scale μ from $\mu_{\max}$ to $\mu_{\min}$,

$$\sigma_\mu = \left(m_b(M_Z)_{\mu=\mu_{\max}} - m_b(M_Z)_{\mu=\mu_{\min}} \right)/2 \tag{1.71}$$

- Mass ambiguity: It is calculated as half of the difference of the results obtained with method 1 and 2 for the same scale $\mu = M_Z$,

$$\sigma_{\text{mass}} = \left(m_b(M_Z)_{\text{Method1}} - m_b(M_Z)_{\text{Method2}} \right)/2 \tag{1.72}$$

- α_s uncertainty: The uncertainty on $\alpha_s(M_Z)$ is propagated to the extracted $m_b(M_Z)$.

The total theoretical uncertainty will be then given by $\sigma_{\text{theo}} = \sqrt{\sigma_\mu^2 + \sigma_{\text{mass}}^2 + \sigma_{\alpha_s}^2}$.

1.6 Is the Standard Model the ultimate theory?

The SM theoretical framework has been able to accommodate all the present knowledge on electroweak and strong interactions and it has passed very precise tests. In spite of its success, it leaves some questions unanswered and there are still some parts in the scalar sector which remain untested. Some examples of why the SM is not believed to be the ultimate fundamental theory are listed below:

- The Higgs mechanism is believed to be incomplete. It predicts the existence of a scalar particle but not its mass. This particle has not yet been found.

- The origin of CP violation in the SM is also not completely well understood. Violation of CP in the electroweak interactions is given by a single phase in the CKM matrix which describes well the results obtained in present laboratory experiments. But the experimental evidence that in the universe matter dominates over antimatter gives a hint to some other source of CP violation.

  In the strong interactions no evidence for CP violation has been found. However, the SM has another phase, θ, that governs the strength of CP violation induced by nonperturbative effects in QCD. Experimentally this parameter is constrained to be very small and the unexplained smallness of it is called the strong CP problem.

- Within the SM the three gauge coupling constants don't get precisely unified at a single point when they are evolved in energy [12]. An exact unification requires new particles, as those predicted by the minimal supersymmetric extension of the SM. If coupling unification is true, then physics is described by a more fundamental theory above the scale of unification, 10^{16} GeV, as Grand Unified Theories (GUT) or superstring theory.

- The SM doesn't include gravity and at some energy scale gravity will become relevant and will need to be included in the theoretical description.

- There are too many free parameters in the SM Lagrangian, not predicted within the model and that can only be given by experiments. Four of them are in the gauge and scalar sector: g, g', μ^2 and λ (or alternatively, $\alpha = e^2/4\pi$, θ_w, M_W and M_H, or one can also choose α, M_Z, G_F and M_H).

  A larger number of free parameters is present in the Yukawa sector: 9 fermion masses (or the 9 corresponding Yukawa couplings) and those of the quark-mixing matrix (not discussed here), which are 3 angles and 1 phase.

  If the QCD coupling constant, $\alpha_s(M_Z)$, is also added, the $SU(3)_C \otimes SU(2)_L \otimes U(1)_Y$ Lagrangian is determined by 18 free parameters. If one considers also a possible CP-violating θ term in the strong Lagrangian, then 19 parameters are needed.

- Fermion masses and the elements of the CKM matrix are governed by Yukawa couplings of fermions to the Higgs field. The observed hierarchies among quark fermion masses and mixing parameters suggests the appearance of new physics. Many models have been proposed in order to understand the observed pattern of fermion masses and mixings, as extended gauge or global symmetries in the context of GUT or string theory or the possibility of fermion compositeness.

  This thesis provides an experimental determination of the mass of a fermion, the b quark, not predicted within the SM. Measurements of this parameter are essential for the predictive power of the SM and can be used to test alternative theories in which fermion masses are predicted.

- Many other questions remain unsolved within the SM, as: Is the proton stable? There are three families and three colours, is the number 3 magic?

Hopefully the coming experiments, as the LHC, will help to clarify these aspects.

[12] As explained in Section 1.3.3 for the case of QCD, in order to deal with the infinities appearing in the perturbative calculations, the coupling constants of the gauge theories are made to depend on the energy scale of the process.

Chapter 2

Experimental apparatus

The experimental setup used to obtain the results of the present thesis is described in this chapter. A brief description of the LEP e^+e^- collider is done first. Then the main characteristics of the DELPHI detector are given since this analysis is based on the data collected by this detector.

2.1 The LEP accelerator

LEP (Large Electron Positron) is an e^+e^- collider which operated at CERN (European Laboratory for Particle Physics) from August 1989 until November 2000. It is the largest accelerator ever built, with a circumference of about 27 km situated about 100 m underground between Switzerland and France (see figure 2.1).

LEP has four interaction points surrounded by the particle detectors: ALEPH [83], DELPHI [84, 85], L3 [86] and OPAL [87], that have been optimized differently to study various physics aspects of e^+e^- annihilations.

Concerning the LEP energy, two phases can be distinguish:

- **LEP1**: Until October 1995, the center of mass energy was around 91 GeV, so to produce the Z^0 resonance.

- **LEP2**: In October 1995, the energy was increased in order to study the W^+W^- ($\sqrt{s}$ = 161 GeV) and Z^0Z^0 ($\sqrt{s}$ = 183 GeV) production, reaching the maximum energy of $\sqrt{s}$ = 209 GeV in the year 2000. During this period searches for new particles, in particular the Higgs boson and supersymmetric particles, became very active.

During the second phase, LEP also ran at the LEP1 Z^0 energy for calibration purposes. In the analysis of this thesis, only data taken at the Z^0 peak has been used, in particular data from the 1994 and 1995 years and the calibration runs of LEP2.

Electrons and positrons are injected into the LEP ring with an energy of 20 GeV, after going through several accelerators. Radio frequency (RF) cavities accelerate the beams to the desired energy. Dipole magnets are used to keep them in the circular orbit. Near the interaction points, the particles are focussed by quadrupole and sextupole magnets in order to reduce the beam size and reach the highest possible luminosity.

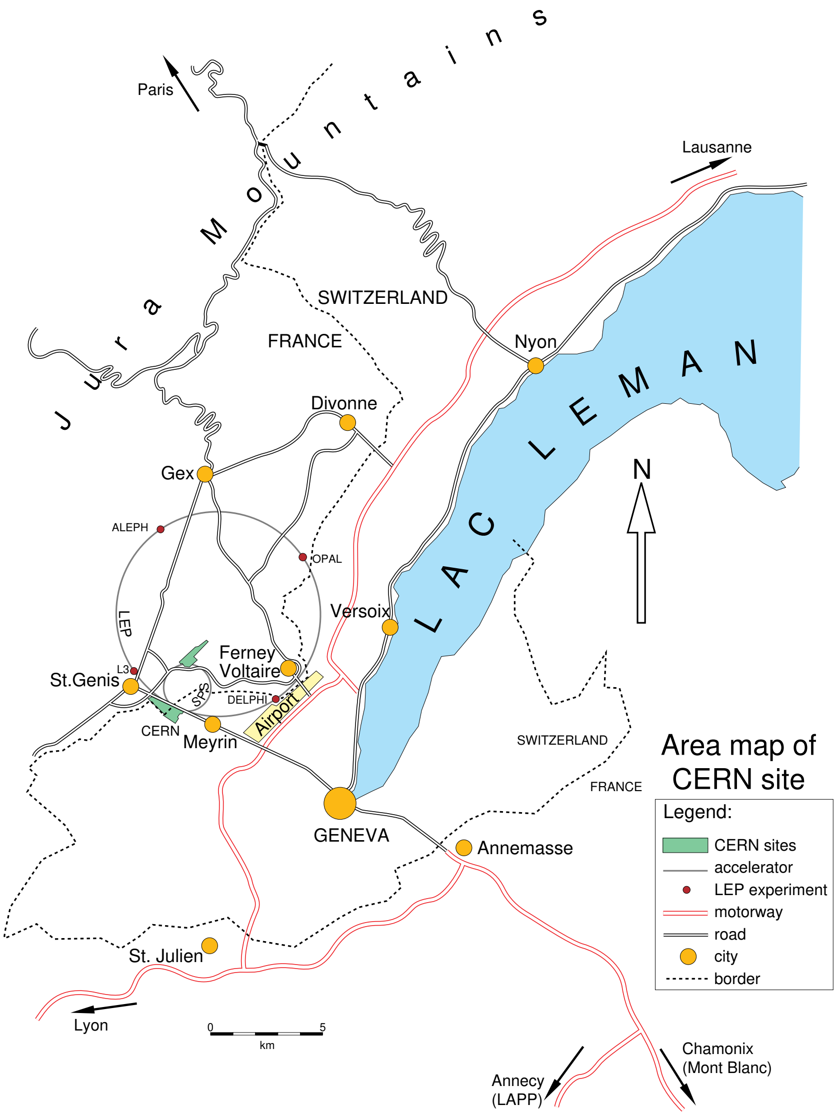

Figure 2.1: Location of the LEP accelerator.

The luminosity, $\mathcal{L}$, is a fundamental parameter of an accelerator and it is defined as the proportional factor between the rate of events of a given process and its cross section,

$$R = \mathcal{L}\sigma \tag{2.1}$$

The Luminosity depends on the machine parameters in the following way,

$$\mathcal{L} = \frac{N_{e^-} N_{e^+} k f}{4\pi \sigma_x \sigma_y} \tag{2.2}$$

where N_{e^-} and N_{e^+} are respectively the number of electrons and positrons per bunch, k the number of bunches in the ring (4 or 8) and f the LEP revolution frequency (11.25 KHz). The beam dimensions in the plane transverse to the beam direction are given by σ_x (50 μm) and σ_y (10 μm). The nominal LEP luminosity is then of about 10^{31} cm^{-2}s^{-1}.

For more details of the LEP machine see [88].

2.2 The DELPHI detector

The DELPHI (DEtector with Lepton, Photon and Hadron Identification) detector is one of the four detectors installed at the LEP collider. It is designed to provide high granularity over a 4π solid angle. Special features of the detector are the powerful particle identification and tracking system.

Cartesian and cylindrical coordinate systems are usually used within the detector: the z axis is along the electron direction, the x axis points towards the center of LEP and the y axis points upwards. The polar angle, θ, is defined with respect to the z axis and the azimuthal angle ϕ and the radial coordinate $R = \sqrt{x^2 + y^2}$ are defined in the xy plane.

A view of the detector can be seen in figure 2.2. The detector is about 10 m long with a diameter of 9 m and it weights 3500 tons. The whole detector can be divided in two parts:

- Barrel: is the central cylindrical section and covers the angular region $40° \leq \theta \leq 140°$.
- Forward: it consists of two endcaps covering the small θ region.

A superconductive solenoid provides a highly uniform magnetic field of 1.23 T parallel to the z axis throughout the central tracking volume, allowing the determination of the momentum of charged particles with high precision.

An overview of the DELPHI subdetectors is given below. Detailed descriptions can be found in [84, 85].

2.2.1 The tracking system

The tracker detectors are responsible of reconstructing the track trajectories for charged particles. They are the nearest detectors to the collision point (except for the muon chambers) so tracks are the least affected by the material. They are distributed in both barrel and forward regions.

They allow the measurement of:

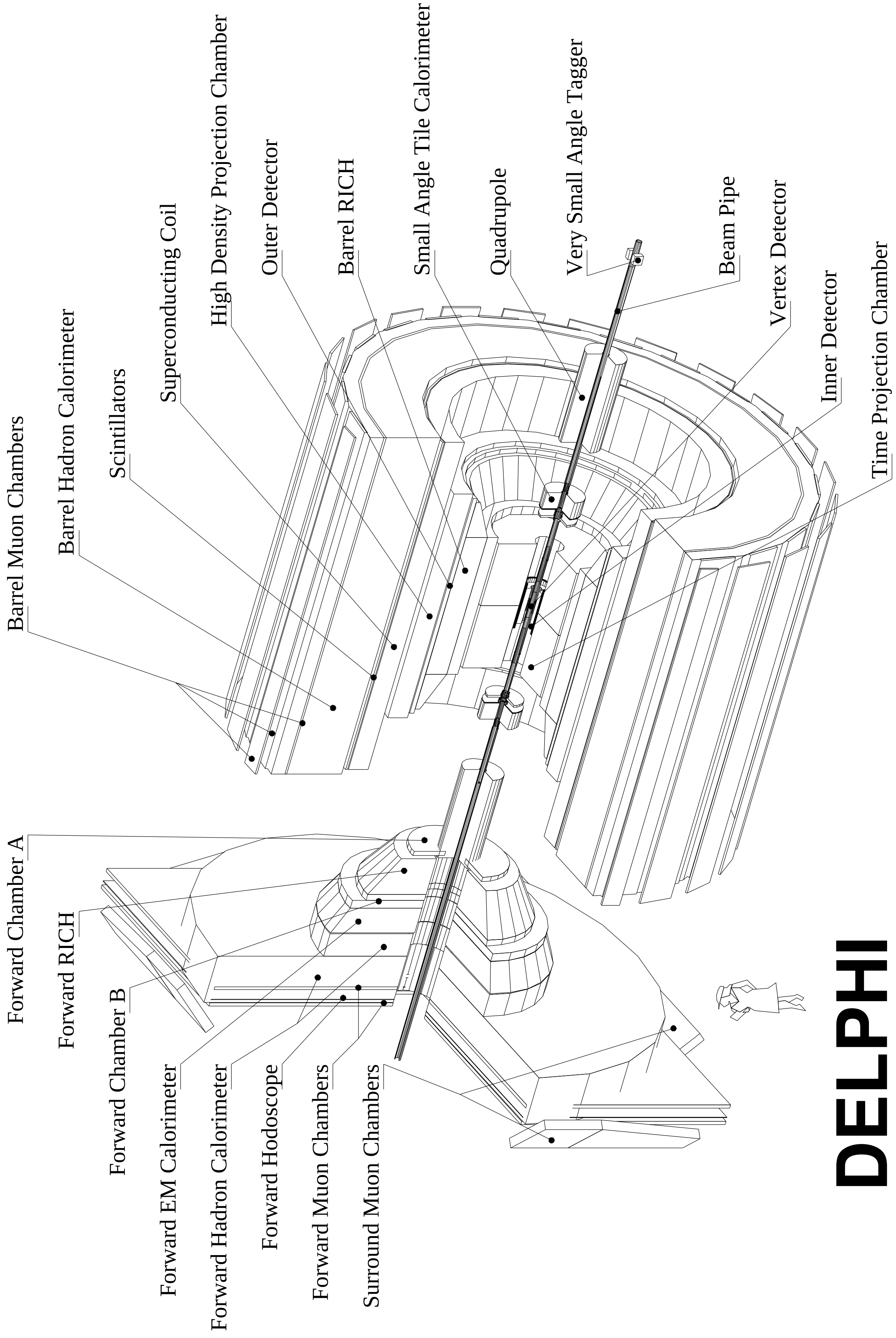

Figure 2.2: General view of the DELPHI detector: the barrel region and one of the endcaps are shown.

- the momentum of charged particles with a precision of $\sigma(1/p) = 0.00057$ (GeV/c)$^{-1}$ for the barrel region and $\sigma(1/p) = 0.00131$ (GeV/c)$^{-1}$ for the forward.
- the impact parameter of such tracks, essential for b tagging, with a resolution of:

$$\sigma_{ip-R\phi} = 20 \oplus \frac{60}{p\sin^{3/2}\theta}\ \mu\text{m} \tag{2.3}$$

$$\sigma_{ip-Rz} = 39 \oplus \frac{71}{p}\ \mu\text{m}\ (80^\circ < \theta < 90^\circ)$$

$$\sigma_{ip-Rz} = 96 \oplus \frac{151}{p}\ \mu\text{m}\ (45^\circ < \theta < 55^\circ)$$

  where the constant and a momentum dependent terms correspond respectively to the intrinsic resolution and to the multiple scattering contributions.

The following subdetectors constitute the DELPHI tracking system:

- **The Vertex Detector (VD) [89, 90]:**

  It is the closest detector to the interaction point. It is made of three coaxial cylindrical layers of AC coupled silicon strip detectors at average radii of 6.3, 9.0 and 10.9 cm. Particles with a polar angles $44^\circ \leq \theta \leq 136^\circ$ cross all three layers of the VD.

  In 1994, the closer and outer layers were equipped with double-sided silicon detectors with orthogonal strips, allowing to measure both the $R\phi$ and z coordinates, with a resolution of about 8 μm in $R\phi$ and of 9 μm in z for the case of tracks perpendicular to the modules.

  Due to the high precision achieved it allows to reconstruct the primary and secondary vertex generated by the short lived particles.

- **The Inner Detector (ID):**

  It is a tracker and trigger detector. It goes from a radii of 12 cm to 28 cm. It consists of two parts: the jet chamber and the trigger layers.

  The jet chamber is a drift chamber located in the inner part of the ID (up to 23 cm in radii). It is made of 24 azimuthal sectors, each consisting in 24 sense wires measuring the drift time.

  The trigger layers surround the jet chamber. Before 1995 it consisted of 5 cylindrical Multiwire Proportional Chambers (MWPC) layers with 192 signal wires per layer for the $R\phi$ measurements and with 192 circular cathode strips giving the z measurement. At the beginning of 1995, it was changed to 5 cylindrical layers of straw tube detectors (192 tubes per layer) having the same functionality as the previous MWPC layers but the z measurement was no longer done.

  Before the modifications of 1995, the precisions were $\sigma(R\phi) = 50$ μm, $\sigma(\phi) = 1.5$ mrad and $\sigma(z)$ varying between 0.5 and 1 mm, depending on θ. After the modifications, the precisions achieved were $\sigma(R\phi) = 40$ μm and $\sigma(\phi) = 0.89$ mrad.

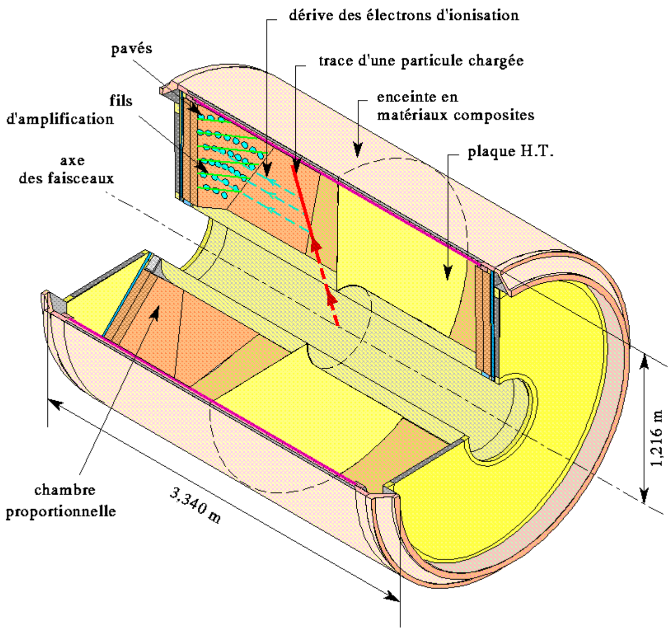

Figure 2.3: Schematic view of the DELPHI TPC.

- **Time Projection Chamber (TPC):**

  The TPC is the main tracker device of DELPHI (see figure 2.3). It also contributes in the charged particle identification by measuring dE/dx. It is situated in the radii range of 35 cm to 111 cm and has an angular coverage of $44° \leq \theta \leq 136°$. It consists of two cylindric drift chambers separated by a high voltage plane producing an electric field of 150 V/cm. When a charged particle goes through, the electrons produced by the ionization of the gas derive towards the end plates, where the readout chambers are located. Each of this two planes are divided in 6 azimuthal sectors containing a MWPC. The final resolution obtained is of 250 μm in $R\phi$ and 880 μm in z.

- **The Outer Detector (OD):**

  Due to its large distance from the interaction point (radii from 197 cm to 206 cm), the OD detector significantly improves the momentum resolution of the high energetic particles with small curvature trajectories. It consists of 5 layers of drift tubes. The resolution in $R\phi$ is 110 μm and 3.5 cm in z.

- **The Forward Chamber (FCA and FCB):**

  The two Forward Chambers (FCA and FCB) are installed in the two endcaps of the DELPHI detector and are made of drift chambers.

  The first one, FCA, is located right after the TPC, at a distance $|z| = 160$ cm, covering the angular region $11° \leq \theta \leq 32°$ and $148° \leq \theta \leq 169°$. Each endcap region is made of 3 modules rotated by 120° with respect to each other. The precision achieved is of $\sigma(x) = 290$ μm, $\sigma(y) = 240$ μm, $\sigma(\theta) = 8.5$ mrad and $\sigma(\phi)$ averaged over θ is 24 mrad.

The FCB is located at a distance $|z| = 275$ cm from the interaction point and covering the angular region $11° \leq \theta \leq 36°$ and $144° \leq \theta \leq 169°$. It consists of 12 wire readout planes, divided into 3 groups of 4 planes. Again, the groups are rotated 120° to each other. The precision reached is in this case $\sigma(x, y) = 150$ μm, $\sigma(\theta) = 3.5$ mrad and $\sigma(\phi) = 4.0/\sin\theta$ mrad.

- **The Muon Chambers (MUC = MUB+MUF+SMC):**

  The MUC are the DELPHI subdetectors which are the farthest from the collision point. They are drift chambers detectors and are crucial for the μ identification, since muons are the only charged particles that can traverse the lead and iron of the calorimeters practically unaffected. They are divided in three parts: the barrel (MUB), which covers the angular region $53.0° \leq \theta \leq 88.5°$ and $91.5° \leq \theta \leq 127.0°$, the forward (MUF), covering $20° \leq \theta \leq 42°$ and $138° \leq \theta \leq 160°$, and the surrounding chambers (SMC), based on limited streamer tubes which were installed in 1994 outside the endcaps to fill the gap between the barrel and forward regions and improve the hermeticity of the detector.

2.2.2 Calorimetry

Calorimeters are responsible of measuring the energy of both, charged and neutral, particles. The energy measurement is based on the total absorption of the incident particle through a series of inelastic collisions degrading its energy. Calorimeters contain then a large amount of high density material, where particles loose their energy in the production of showers of secondary particles. Sampling calorimeters combine the passive high density material with and active one, which can reconstruct the position and energy of the original particle from the shower produced.

The DELPHI detector has two kinds of calorimeters:

- Electromagnetic: Electron and photon identification is provided primarily by the electromagnetic calorimeter. It is composed of a barrel calorimeter, the HPC, a forward calorimeter, the FEMC, and two very forward calorimeters, the STIC and the VSAT. The latest two are mainly used for luminosity measurements.

- Hadronic: In order to measure the charged and neutral hadrons energy, DELPHI contains the HCAL (Hadron CALorimeter) subdetector.

A brief description of all of them is done below.

- **The High Density Projection Chamber (HPC):**

  It is the barrel electromagnetic calorimeter and is installed in a cylindrical layer outside the OD and inside the magnetic field. It consists of 144 independent modules arranged in 6 concentric rings around z. Each module combines lead with drift chambers. The relative energy precision obtained is:

$$\frac{\sigma(E)}{E} = 0.043 \oplus \frac{0.32}{\sqrt{E}} \tag{2.4}$$

with E expressed in GeV. It also reconstructs the shower with an angular resolution of $\sigma(\theta) = 1.0$ mrad and $\sigma(\phi) = 3.1$ mrad.

- **The Forward Electromagnetic Calorimeter (FEMC):**

  They are installed in the two endcap regions at a distance $|z| = 284$ cm and each consists of 4532 blocks of lead-glass. The Cherenkov light emitted by the charged particles of the electromagnetic shower is read out by photomultipliers. The relative precision obtained in the energy is,

$$\frac{\sigma(E)}{E} = 0.03 \oplus \frac{0.12}{\sqrt{E}} \oplus \frac{0.11}{E} \tag{2.5}$$

  where E is expressed in GeV.

- **Hadron Calorimeter (HCAL):**

  It is divided in a barrel region (HAB) and two forward regions (HAF), covering almost the whole solid angle. It is a sampling gas detector incorporated in the magnet yoke, mainly made of iron. The energy resolution reached is,

$$\frac{\sigma(E)}{E} = 0.21 \oplus \frac{1.12}{\sqrt{E}} \tag{2.6}$$

  being E expressed in GeV.

2.2.3 Luminosity measurement

The luminosity is measured by counting the number of events of the process $e^+e^- \to e^+e^-$ (Bhabha scattering) at small angles, since it has a clear experimental signature, high statistics and a theoretically well known cross section.

Before 1994, the absolute luminosity was measured using the SAT detector [91, 92] and the VSAT was used to measure the relative luminosity at different energies [93]. In 1994 the SAT was replaced by a new calorimeter, the STIC.

- **Very Small Angle Tagger (VSAT)**: It is composed of two calorimeters and it is also designed to measure the contamination of electrons and X rays. It covers the angular region between 5 and 7 mrad and it is located at a distance $|z| = 7.7$ m.

- **The Small angle TIle Calorimeter (STIC)**: The STIC is a sampling lead-scintillator calorimeter formed by two cylindrical detectors placed on either side of the interaction point at a distance of 2.2 m, covering the angular region 29 mrad $\leq \theta \leq$ 185 mrad.

2.2.4 Scintillators

In order to achieve complete hermeticity for high energy photon detection, additional scintillators were installed in the cable regions (between the barrel and each endcap, and between the HPC modules), the HERmiticy detectors (HER). In addition DELPHI has in the barrel part the Time Of Flight (TOF) and in the forward part the HOrizontal Flight tagger (HOF). The scintillator counters are also used for fast trigger and cosmic radiation identification.

- **HER**: They are lead-scintillator counters installed to cover the holes of the electromagnetic calorimeter at $\theta = 90°$, at a region around $\theta = 40°$ and $140°$ and at some ϕ cracks.

- **TOF**: It consists of a single layer of plastic scintillators located in the barrel region and parallel to the beam axis. Each scintillator is read by a photomultiplier at each end. It covers the angular region $41° \leq \theta \leq 139°$ but it has a dead zone of 6 cm around $\theta = 90°$. It has an efficiency of 98% to detect photons crossing the inefficient ϕ regions of the HPC. It has a temporal resolution of ~ 4 ns.

- **HOF**: It consists of two planes of 10×10 m^2 in each endcap: HOFa and HOFc (in forward and backward endcaps). Each of them has 4 quadrants with 28 scintillator counters per quadrant. It has a temporal resolution of ~ 5 ns.

2.2.5 Cherenkov detectors

Charge particles traversing a dielectric medium faster than the speed of light in that medium produce a cone of Cherenkov light. The emission angle, θ_c, depends on the mass, m, and the momentum, p, according to the relation $\cos\theta_c = 1/n\sqrt{1 + m^2/p^2}$, where n is the refractive index of the radiator medium. The number of photons emitted per unit length is proportional to $\sin^2\theta_c$. The number of photons associated to a track and their Cherenkov angles are the input used to identify the particle mass (taking the p from the measurement performed by the tracker system). The fact that particles below the Cherenkov threshold do not emit light is also used for the identification.

The DELPHI RICH detector is a Cherenkov detector that allows to distinguish among pions, kaons and protons. It contains two radiators of different refractive indices. The liquid radiator is used for particle identification of momentum from 0.7 to 8 GeV/c and the gas radiator is used from 2.5 to 25 GeV/c.

The full solid angle coverage is provided by two independent detectors, one in the endcap region (Forward RICH) and one in the barrel region (Barrel RICH).

2.3 The DELPHI simulation

In order to correct the measured data by detector effects, like resolution and acceptance, a simulation program is used. For the case of the DELPHI detector, this program is called DELSIM [94] and it consists on the simulation of the following processes:

1. Generation of the primary physics process. An external program is used to generate this part. For the case of hadronic events, JETSET 7.3 has been used.

2. Tracking the particles through the DELPHI detector, interacting with the different materials. This includes a simulation of energy losses, multiple scattering and the following secondary processes: photoelectric effect, emission of delta rays, bremsstrahlung, annihilation of positrons, pair production, Compton scattering, weak decays and nuclear interactions.

3. Generation of the detector response and the output electric signals.

For the case of hadronic events, a tuning of the simulation is done in order to reproduce the measured data.

Once the simulated data is produced by DELSIM, it is stored in the same format as real data and the same analysis chain is applied for both sets of the data, real and simulated.

Chapter 3

Tuning of the QCD generators

This chapter is devoted to present the results obtained for the tuning of one of the QCD generators, HERWIG, to the DELPHI hadronic data. First, a brief description of the parton shower and hadronization process (generally described in Sections 1.4.3 and 1.4.4) of the PYTHIA and HERWIG QCD generators is done, making emphasis on the modeling of mass effects. Some more detail is given in the HERWIG description in order to describe the parameters affecting the hadronization process that need to be tuned. Then, an attempt to determine the parameters of HERWIG that lead to an optimal description of the observed hadronic event shapes, charged particle inclusive distributions, information on identified particles, the mean charged multiplicity for b events and the B hadron scaled energy distributions is presented.

3.1 The QCD Monte Carlo generators

Experiments observe hadrons rather than partons due to confinement. Therefore, in order to compare the measured observables at hadron level with the predictions given by the theoretical perturbative calculations at parton level, QCD Monte Carlo generators are used. They provide a full simulation of the process we are interested in, $e^+e^- \to Z^0 \to$ hadrons, by keeping the information of the intermediate steps, as before and after the hadronization process. The first part of the QCD process, i.e. gluon radiation off quarks and gluons and gluon splitting, is described by a perturbative parton shower approach (see Section 1.4.3). The formation of hadrons from the final partons cannot be given by perturbation theory, due to the increase of the strong coupling constant at small momentum transfer, and a phenomenological model is used in the generator to describe the hadronization process (see Section 1.4.4).

Different phenomenological models of the fragmentation process exist but the most frequently used are the string and cluster models which are implemented, respectively, in the PYTHIA [15] and HERWIG [16] generators. The parton shower of each generator is also different.

A precise modeling of the hadronic final state properties is required by many precision measurements performed at LEP, such as the determination of α_s from event shapes, the b quark mass measurement from R_3^{bl} or event shapes and the determination of the Z^0 mass and width. There are several free parameters in the generators that need to be tuned in order to reproduce the observed data.

The versions of the generators used in the analysis presented in this thesis are PYTHIA 6.131 and HERWIG 6.1. A tuning of PYTHIA to DELPHI data was already done in Ref. [17] for previous versions, JETSET 7.3/7.4. This tuning was checked to be valid for the version of PYTHIA considered in this analysis. For the case of HERWIG, a DELPHI tuning was already available for version 5.8 [17]. Since important improvements, mainly in the b sector, were done in version 6.1, a tuning to this version has been done in this work following the method developed in Ref. [17].

A description of the parton shower and hadronization process of PYTHIA and HERWIG follows. It is important to note that both Monte Carlo programs are continuously in progress. This means that what it is written below is valid for versions PYTHIA 6.131 and HERWIG 6.1 (unless explicitly stated) but could not hold for previous or more recent versions of the generators.

3.1.1 PYTHIA

- **Parton Shower**:

  The PYTHIA parton shower is based on the LLA approximation described in Section 1.4.3. It consists on an evolution in the squared virtual mass m^2 of a parton, i.e. Q^2_{evol} $= m_1^2$ in the branching $1 \to 2+3$. Therefore emissions are ordered in decreasing mass of the radiating parton. The z variable is defined as the energy fraction in the CM frame of the event, that is $E_2 = zE_1$ and $E_3 = (1-z)E_1$.

  The values for m^2 and z are given by the Sudakov form factors and the splitting kernels of Eqs. (1.53) and (1.51) respectively for each branching of the shower. The kinematics of the parton shower is built taken into account effective masses for all partons (quarks and gluons), which are given by:

  $$m_{\mathrm{eff}-g} = \frac{1}{2}Q_0 \qquad m_{\mathrm{eff}-q} = \sqrt{M_q^2 + \frac{1}{4}Q_0^2} \tag{3.1}$$

  being M_q the so-called kinematical quark mass parameter and Q_0 a cut-off parameter.

  These effective masses constrain the allowed values of m^2 and z^2 for each branching. They also determine the end of the parton shower since a parton cannot branch if its mass is smaller than that of the lightest pair of allowed decay products, i.e. $m_{\mathrm{min}-g} =$ $2\ m_{\mathrm{eff}-g} = Q_0$ and $m_{\mathrm{min}-q} = m_{\mathrm{eff}-q} + m_{\mathrm{eff}-g} \geq Q_0$. If a parton cannot branch further it is put on the mass shell, i.e. gluons are made massless and quarks masses are set to the M_q parameter.

  The argument Q^2 of α_s used in each branching of the shower is an approximation of the squared transverse momentum of the daughter partons 2 and 3 with respect to the mother 1 direction, $p_\perp^2 \approx z(1-z)m_1^2$.

  Coherence effects are taken into account by angular ordering, i.e. by vetoing emissions that don't correspond to decreasing opening angles between the radiated partons [1].

[1] Gluon radiation in the parton shower should be coherent. However, models beyond the LLA are needed

The parton shower is corrected in PYTHIA in order to agree with the $\mathcal{O}(\alpha_s)$ ME prediction. In the process $e^+e^- \to q\overline{q}$ the emission probability of the first quark and antiquark is corrected to the ME result. However, subsequent emissions have no corrections and only the splitting kernels are used [2].

One of the main improvements of the version of PYTHIA used in this analysis, 6.131, is that the matching procedure takes into account quark mass effects. A detailed description of how this technically works is given in Ref. [97] and [96]. For the process $e^+e^- \to q\overline{q}g$, the $\mathcal{O}(\alpha_s)$ ME probability of gluon emission off a quark was given in Eq. (1.66). In Ref. [97] an equivalent expression was derived for the parton shower probability. The ratio between the ME and parton shower probabilities is used as an acceptance factor inside the shower evolution in order to correct the first emission [3].

- **Hadronization**:

The model used in PYTHIA for the transition of quarks into hadrons is by default the string model described in Section 1.4.4 [4].

The generation of the quark pairs needed for the string breakup is determined by the probabilities to produce the different possible flavours. The quantum mechanical tunnellig mechanism implies a flavour independent Gaussian spectrum for the transverse momentum of the quark pairs and a suppression of heavy quark production. But, since the predicted flavour suppressions are in terms of quark masses and these are difficult to assign, the suppression of $s\overline{s}$ production is left as a free parameter in the program and no heavier flavours can be produced.

The meson production is given by the relative probabilities that a given quark pair combination forms a specific meson. The tunnelling mechanism can also explain the production of baryons and the program contains three different scenarios: diquark, simple popcorn and advanced popcorn which are explained in Ref. [15].

The transverse momenta of the produced hadrons are determined from the p_t values of their constituent quarks, which are defined by the tunnelling process, which implies a Gaussian p_t^2 distribution controlled by the standard deviation σ_q parameter.

Concerning the fraction of energy taken by the produced hadrons, in the DELPHI setup

to reproduce the observed gluon interference (the next simplest approximation, MLLA, already explains a number of these effects). Due to the non-abelian nature of QCD, the overall result of this interference is angular ordering of gluon radiation [95], which constrains the angles between the radiator and the radiated gluon to decrease as the evolution proceeds to lower scales.

[2]More recent versions of PYTHIA include some ME correction for the first and subsequent branchings [96].

[3]In major regions of the phase space this ratio is greater than unity and a technical solution was applied in PYTHIA 6.131 by rescaling the z variable in order to bring it below 1. An alternative and more elegant algorithm is used in more recent versions of PYTHIA ($\geq$ 6.153). The evolution in this case is performed in terms of the variable $Q^2_{evol} = m^2 - (m^2)_{\text{on shell}}$ rather than $Q^2_{evol} = m^2$, then the gluon radiation off heavy quarks in the parton shower is overestimated instead of underestimated and a suppression factor can then be used [96].

[4]The independent fragmentation model [98] is left as an option in the program.

of PYTHIA [5] the Lund symmetric fragmentation function is used for the case of light quarks and the Peterson function for c and b quarks. Other fragmentation functions are also available in the program as for instance the Bowler function.

3.1.2 HERWIG

- Parton shower:

  The evolution of the parton shower is based on the coherent parton branching formalism, an extension of the LLA. It accounts for leading and sub-leading logarithmic terms arising from soft and collinear gluon emission. The evolution variable explicitly involves angles and therefore angular ordering is automatically incorporated.

  For a parton branching $1 \to 23$, $Q^2_{evol} = E_1^2 \xi_{23}$, where E_1 is the energy of the branching parton and $\xi_{23} = 2(p_2 p_3)/(E_2 E_3)$. For massless quarks, $\xi_{23} = 1 - \cos\theta_{23}$, being θ_{23} the opening angle between the decay products. Thus, ordering in Q^2_{evol} corresponds to ordering in angles. The distribution of ξ is determined then by the Sudakov form factors. The z variable is defined as $z = E_2/E_1$ and its value is chosen according to the leading order Altarelli-Parisi splitting functions. As in PYTHIA, in each branching the scale Q of α_s is chosen as the relative transverse momentum of the two daughter partons.

  The end of the parton shower is implemented in the following way: For each parton of mass m_i there is a cut-off of the form $Q_i = m_i + Q_0$ and showering from any parton stops when a value of ξ below Q_i^2/E_i^2 is selected for the next branching. The condition $\xi > Q_i^2/E_i^2$ corresponds to the dead cone effect for heavy quarks.

  The parton masses are not defined during the evolution stage. At the end of the parton shower partons are put on mass-shell or given a small non-zero mass in the case of gluons. By moving backwards towards the shower initiators all parton virtual masses are constructed. The quark mass parameters should be thought as effective masses. For massive quarks, the mass of the quark modifies the angular-ordered phase space. In the soft limit, the emission pattern off heavy quarks is similar to that from light quarks at large angles but it is smoothly suppressed at small angles.

  The HERWIG parton showers are performed in the soft or collinear approximation and emission is entirely suppressed inside the so-called dead zones, corresponding to hard and/or large-angle parton radiation. According to the exact ME, the radiation in the dead zones is suppressed but it is not completely absent. Therefore, some ME corrections need to be applied to the HERWIG standard parton shower in order to get a full description of the physical phase space.

  The radiation in the dead zones is generated according to the exact first-order ME (*hard correction*). The shower in the already populated region of phase space is corrected by the use of the exact $\mathcal{O}(\alpha_s)$ amplitude any time a branching is the hardest so far (*soft correction*). By the hardest so far we mean the radiation of a parton whose transverse

[5] By DELPHI setup I mean the conditions in which the tuning of the PYTHIA generator was done in Ref. [17].

momentum relative to the splitting one is larger than all those previously emitted. This is not always the first emission since angular ordering does not necessarily imply ordering in transverse momentum.

This method to match the parton shower to the ME is quite different to the one described before for PYTHIA, where the parton shower probability is applied over the whole phase space and the first-order amplitude is used only to correct the first emission.

- Hadronization:

  The fragmentation model used is the so-called cluster model based on the preconfinement property of perturbative QCD to form colour-neutral clusters which decay into the observed hadrons. This model was briefly described in Section 1.4.4, some more details are given here.

  First of all, after the perturbative parton shower, all outgoing gluons are split nonperturbatively into light quark-antiquark pairs. A unique colour flow is generated for each final state, so that each final state quark is colour-connected to an antiquark, forming then a colour-singlet cluster. The mass and spatial size distributions of these clusters peak at low values. Once the clusters are formed, they are fragmented into hadrons. Depending on the cluster mass we have the following situations:

  - $M_{\mathrm{cluster}} < M_{\mathrm{min}}$: If a cluster is too light to decay into two hadrons, it is taken as the lightest single hadron of its flavour. Its mass is shifted to the appropriate value by an exchange of four-momentum with the neighboring cluster.
  - $M_{\mathrm{min}} \leq M_{\mathrm{cluster}} \leq M_{\mathrm{max}}$: The cluster decays into a pair of hadrons. Given a cluster of flavour $f_1\overline{f_2}$, a pair $f\overline{f}$ is randomly generated among u, d, s, the six corresponding diquark and c flavours, so that $f_1\overline{f_2} \to f_1\overline{f} + f\overline{f_2}$. The decay products are selected randomly from tables of hadrons of those flavours and they are accepted in proportion to the density of states for that channel. Particle production is modified by changing the weights for the individual hadron types.

    If the cluster does not contain quarks coming from the perturbative stage it decays isotropically into the pair of hadrons [6]. If instead, the cluster contains a perturbative quark the event remembers its direction. Thus, the hadron carrying its flavour continues in the same direction (in the cluster CM frame) than the quark. This hardens the spectrum of heavy hadrons since all heavy quarks come from the perturbative phase.
  - $M_{\mathrm{cluster}} > M_{\mathrm{max}}$: The cluster is fragmented using an iterative fission model until the masses of the product clusters are below the fission threshold, M_{max}. In the fission model the produced flavour f is limited to u, d or s and the product clusters move in the directions of the original constituents in their CM frame, being the fission mechanism similar to the string fragmentation.

[6] Perturbative quarks are all quarks except those produced in the nonperturbative gluon splittings produced at the end of the parton shower.

The minimum mass requiered by a cluster so that it can decay into a pair of hadrons, $M_{\min}$, is given by the hadron masses. The fission threshold mass, $M_{\max}$, is controled by two parameters: CLMAX and CLPOW, so that,

$$M_{\max}^{\mathrm{CLPOW}} = \mathrm{CLMAX}^{\mathrm{CLPOW}} + (m_1 + m_2)^{\mathrm{CLPOW}} \tag{3.2}$$

where m_1 and m_2 are the effective quark mass parameters of the quarks forming the cluster.

3.2 Tuning of HERWIG

In the following sections the tuning of the HERWIG parameters that are relevant in the hadronization process will be described. The goal is to find the set of parameters that give the best global description of the hadronic event shapes, jet rates and charged particle inclusive distributions measured by DELPHI, the identified particle spectra from all LEP experiments and some other measured distributions for b events.

3.2.1 Tuning procedure

The tuning procedure is based on a simultaneous fit of the Monte Carlo parameters to physical observables, taking correlations between parameters into account. For a detailed description of the tuning procedure see [17, 99]. The fit consists on the minimization of the variable:

$$\chi^2(\vec{p}) = \sum_{\text{observables}} \sum_{\text{bins}} \left(\frac{X_{meas} - X_{MC}(\vec{p})}{\sigma_{meas}} \right)^2 \tag{3.3}$$

The sum extends over all bins of all physical observables included in the fit, X_{meas} represents the measured value, being σ_{meas} its total error and $X_{MC}(\vec{p})$ the Monte Carlo prediction of bin X for the parameter setting $\vec{p}$.

In order to perform the fit, the Monte Carlo prediction for each bin X of each observable needs to be known for any parameter setting $\vec{p}$. A quadratic approximation is used:

$$X_{MC}(p_1, p_2, ..., p_n) = A_0 + \sum_{i=1}^{n} B_i p_i + \sum_{i=1}^{n} C_i p_i^2 + \sum_{i=1}^{n-1} \sum_{j=i+1}^{n} D_{ij} p_i p_j + ... \tag{3.4}$$

The coefficients A_0, B_i, C_i and D_{ij} are extracted from a systematic parameter variation by applying a singular value decomposition [100].

So, the steps to follow to get the Monte Carlo tuned to the data are the following:

1. Determine the number of parameters to tune and which ones among all tunable parameters available in the Monte Carlo.

2. Determine the measured physical observable distributions to be used in the fit. These distributions have to be sensitive to the variation of the selected parameters.

3. Find an appropriate variation range of each of the chosen parameters so that the coefficients of the Taylor expansion (3.4) can be determined.

4. Minimize the $\chi^2(\vec{p})$ of Eq. (3.3) and obtain the set of parameters that better reproduce the data.

5. Generate a sample of events with the best parameter settings and compare the obtained observable distributions with the measured ones.

In the next sections the results for each of these steps are shown.

3.2.2 Selection of the parameters to tune

From previous tunings done for older versions of HERWIG using LEP1 data [17, 99], the important parameters that need to be tuned are the following:

- Parton shower:

  QCDLAM: Λ_{QCD}. At high momentum fractions, it can be identified with the fundamental 5-flavour QCD scale $\Lambda^{(5)}_{\overline{\mathrm{MS}}}$ [101].

  RMASS(13): Effective gluon mass used to set the parton shower cut-off for gluons and in the gluon splitting into $q\overline{q}$ pairs during the hadronization phase. Therefore, it must be at least twice the lightest quark mass.

- Fragmentation parameters:

  CLMAX and CLPOW: As it was mentioned in Section 3.1, these are the parameters controlling the splitting of high mass clusters.

  PSPLT(1) and PSPLT(2): These parameters determine the mass distribution of the cluster products in the cluster splitting. The masses of these products are generated uniformly in M^{PSPLT}.

  CLSMR(1) and CLSMR(2): As shown in Section 3.1, in the decay of a cluster containing a quark from the perturbative phase into hadrons, CLSMR tells us up to what extend the hadron and the constituent quark directions are aligned. A Gaussian smearing is applied to the quark momentum by CLSMR. Increasing CLSMR decorrelates the cluster decay from the initial quark direction.

  DECWT: The weight for the decuplet baryon production.

With respect to older versions, PSPLT and CLSMR are now two-dimensional arrays, with the first element controlling clusters that do not contain a b quark and the second those that do. This allows to tune the b fragmentation independently of other flavours.

Our first attempt was to fit the 9 parameters described above to the data. A variation range has to be selected for each of the 9 chosen parameters and then a number of Monte Carlo sets with different parameter settings within those ranges has to be generated so the coefficients of Eq. (3.4) can be determined.

Table 3.1 shows the selected ranges for each parameter in the last column. They have been chosen taking into account the restrictions one has in the HERWIG Monte Carlo. In the same table the default values used for HERWIG are also shown, as well as the result obtained by ALEPH [7] and OPAL [102] experiments after applying alternative tuning methods.

Parameter	Default	ALEPH	OPAL	DELPHI range
QCDLAM	0.180	0.190	default	[0.14, 0.2]
RMASS(13)	0.750	0.780	default	[0.67, 0.96]
CLMAX	3.350	3.380	default	[2.9,3.85]
CLSMR(1)	0.000	0.570	0.400	[0,1]
CLSMR(2)	0.000	default	default	[0,1]
DECWT	1.000	0.720	0.70	[0.5,1]
PSPLT(1)	1.000	0.944	default	[0.65, 1.25]
PSPLT(2)	1.000	0.338	0.330	[0.15, 0.55]
CLPOW	2.000	default	default	[1, 2]

Table 3.1: List of the parameters to be tuned. The HERWIG default values are shown in the second column and the tuning results obtained by the ALEPH and OPAL experiments are in the third and fourth column. The last column shows the variation range selected for each of the parameters for the DELPHI tuning.

A hundred Monte Carlo sets with 300,000 events each and with different parameter settings within the selected ranges were generated. For n parameters to tune, the number of coefficients in Eq. (3.4) to be determined for each observable bin is $N(n) = \frac{1}{2}(n(n+3)+2)$. Therefore, at least $N(n)$ different sets should be generated. In Ref. [103] it was considered that the number of generated sets should be $N \simeq 1.5 \times N(n)$ in order to avoid numerical problems. In our case, for $n = 9$, $N \simeq 83$ and therefore a hundred sets is more than enough.

3.2.3 Selection of the physical observable distributions

The choice of the sample of observable distributions that should be used in the fit is not trivial. It is clear that the best way to proceed is to use observables that show the strongest dependence with the parameters to tune and that are the least correlated, to keep the influence of statistical errors as small as possible.

Fourteen different sets containing observables of event shape type, jet rates and inclusive single particle distributions have been constructed, these are shown in table 3.2. The definitions of the different variables are given in appendix A. The data distributions measured by DELPHI in Ref. [17] are the ones used.

Since parameters that have to do with clusters containing a b quark (CLSMR(2) and PSPLT(2)) have to be tuned, some observables sensitive to the variation of these two parameters need to be added to the sample. The following observables have then been introduced:

- Charged multiplicity for $b\bar{b}$ events: N_{ch}^{b} measured by OPAL [104].

[7] The results shown for the ALEPH experiment have not been published.

Observable	1	2	3	4	5	6	7	8	9	10	11	12	13	14
1-thrust	x		x	x	x	x	x	x	x	x	x	x	x	x
$D_2^{Jade} \equiv y_{32}^{Jade}$				x								x		x
$D_3^{Jade} \equiv y_{43}^{Jade}$				x								x		
$D_4^{Jade} \equiv y_{54}^{Jade}$				x								x		
$D_2^{Durham} \equiv y_{32}^{Durham}$	x	x	x		x	x	x	x	x	x	x	x	x	x
$D_3^{Durham} \equiv y_{43}^{Durham}$	x	x	x		x		x	x	x	x	x	x	x	x
$D_4^{Durham} \equiv y_{54}^{Durham}$	x	x	x		x	x		x	x	x	x	x	x	x
sphericity		x										x		
aplanarity										x		x	x	x
planarity	x	x	x	x	x	x	x	x		x	x	x	x	x
major	x	x	x	x	x	x	x		x	x	x	x	x	x
minor	x	x	x	x	x	x	x		x	x	x	x	x	x
EEC											x	x	x	x
N_{ch}	x	x	x	x		x	x	x	x	x	x	x	x	x
$p_t^{in}(t)$	x	x	x	x	x	x	x	x	x	x	x	x	x	x
$p_t^{out}(t)$	x	x	x	x	x	x	x	x	x	x	x	x	x	x
$p_t^{in}(s)$												x		
$p_t^{out}(s)$												x		
$y(t)$			x									x		
$y(s)$												x		
x_p	x	x	x	x	x	x	x	x	x	x	x	x	x	x

Table 3.2: The fourteen different sets containing different event shapes, differential jet rates and inclusive particle distributions.

- Scaled energy of B hadrons: $x_E^b = 2E_{B-\mathrm{hadron}}/E_{CM}$, for two cases:
  - Leading B mesons [8]: Measured by ALEPH [105].
  - Weakly decaying B hadrons: Measured by SLD [106].

The identified particle spectra for π^0, η, η', K^0, K^+, ρ^0, ω^0, ϕ^0, $K^{*\pm}$, f_2, p, Λ^0, Ξ^-, Σ^* measured at LEP (all references can be found in Ref. [17]) have also been used.

From all these observables, $3 \times 14 = 42$ different samples have been constructed in the following way:

$$
\begin{aligned}
A_i &= \mathrm{Set}_i + N_{ch}^b + x_E^b(\mathrm{ALEPH}) \\
B_i &= \mathrm{Set}_i + N_{ch}^b + x_E^b(\mathrm{ALEPH}) + \text{particle spectra} \\
C_i &= \mathrm{Set}_i + N_{ch}^b + x_E^b(\mathrm{SLD}) + \text{particle spectra}
\end{aligned}
\tag{3.5}
$$

where $i = 1, 14$ and Set_i refers to set i of table 3.2.

[8] Leading B meson refers to the first B meson produced after the fragmentation process.

3.2.4 The best DELPHI tuning

So far, the parameters to tune and their variation ranges have been chosen as well as several samples of physical observables to which to fit. Before making any of the 42 fits it is important to check that, for each observable, the 100 Monte Carlo predictions with 100 different parameter settings are around the measured distribution. Figure 3.1 shows for four of the observables their measured distribution and the 100 Monte Carlo predictions, indicating that the selected parameter ranges are appropriate.

In none of the 42 fits the CLSMR(2) parameter was well determined and therefore it was fixed to its default value, 0, which means that the hadron is aligned to the perturbative quark of the decayed cluster (see Section 3.1.2) and therefore the b fragmentation is made harder. The tuned DECWT parameter was out of the selected range for all fits performed. So we tried fixing it to the tuned value of ALEPH, which was 0.72 (see table 3.1), for all sets of sample type A, and fitted the rest of parameters.

Figures 3.2 and 3.3 show the results obtained for each parameter for the different fits performed. By looking at all these plots we can conclude the following:

- For a given sample, all sets give very similar tuned parameters with the exception of set number 8, which is the one that does not include major and minor distributions in the fit (see table 3.2).
- Introducing the identified particle spectra distributions in the fit (which means going from sample A to B) has a large effect on the tuned values of some parameters: QCDLAM, CLPOW, PSPLT(1) and DECWT increase while RMASS(13) and CLMAX decrease.
- The tuned parameter values are independent on the measured distribution of x_E^b (ALEPH or SLD) used in the fit, since the results obtained for samples B and C are compatible.
- Fixing DECWT in sample A has a big effect on some parameters: QCDLAM, CLPOW and PSPLT(1) increase while CLMAX and PSPLT(2) decrease.

The next step is to decide from all the tuned sets which one gives the best prediction for the Monte Carlo, i.e. the closest to the data distributions. The way to proceed is to take each tuning result, run the Monte Carlo with those settings and compare each observable distribution with data. The problem is that there's no tuning result that gives the best prediction for all observable distributions but a choice has to be made and that depends on what is considered more important to be better reproduced.

If one considers that event shapes, jet rates and inclusive single particle distributions are the most important ones to be better predicted by the Monte Carlo, then one should take any set of sample A but number 8. However, some of the identified particle spectra are better predicted if one takes a set of sample B or C, since they include these distributions in the fit, being then some of the other distributions degraded.

For those QCD analysis that make use of event shape and jet rate observables, as determinations of α_s, QCD colour factors or the b quark mass (which is the case we are interested

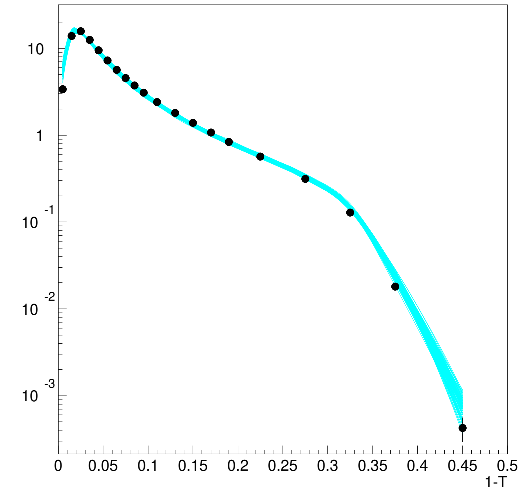

(a) Thrust.

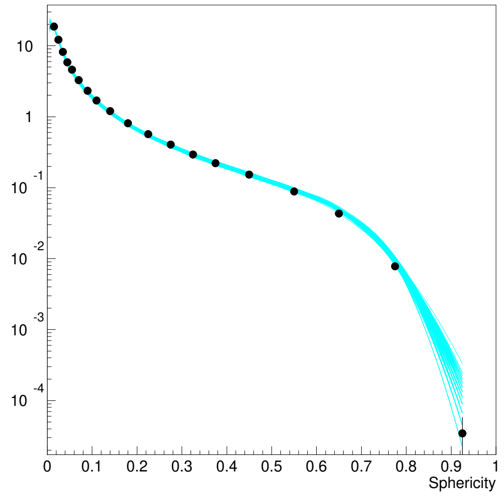

(b) Sphericity.

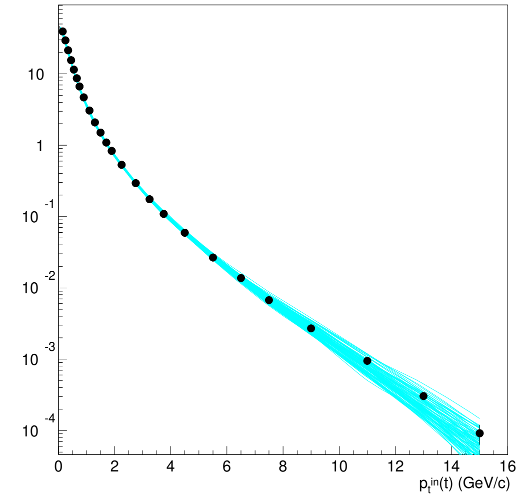

(c) $p_t^{in}(t)$.

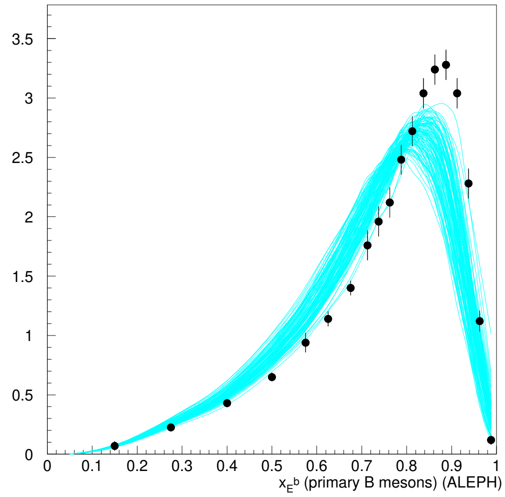

(d) Scaled energy for primary B mesons measured by ALEPH.

Figure 3.1: Some of the distributions used in the fit. The dots correspond to the data and the lines are the 100 Monte Carlo prediction with their own parameter setting within the selected ranges.

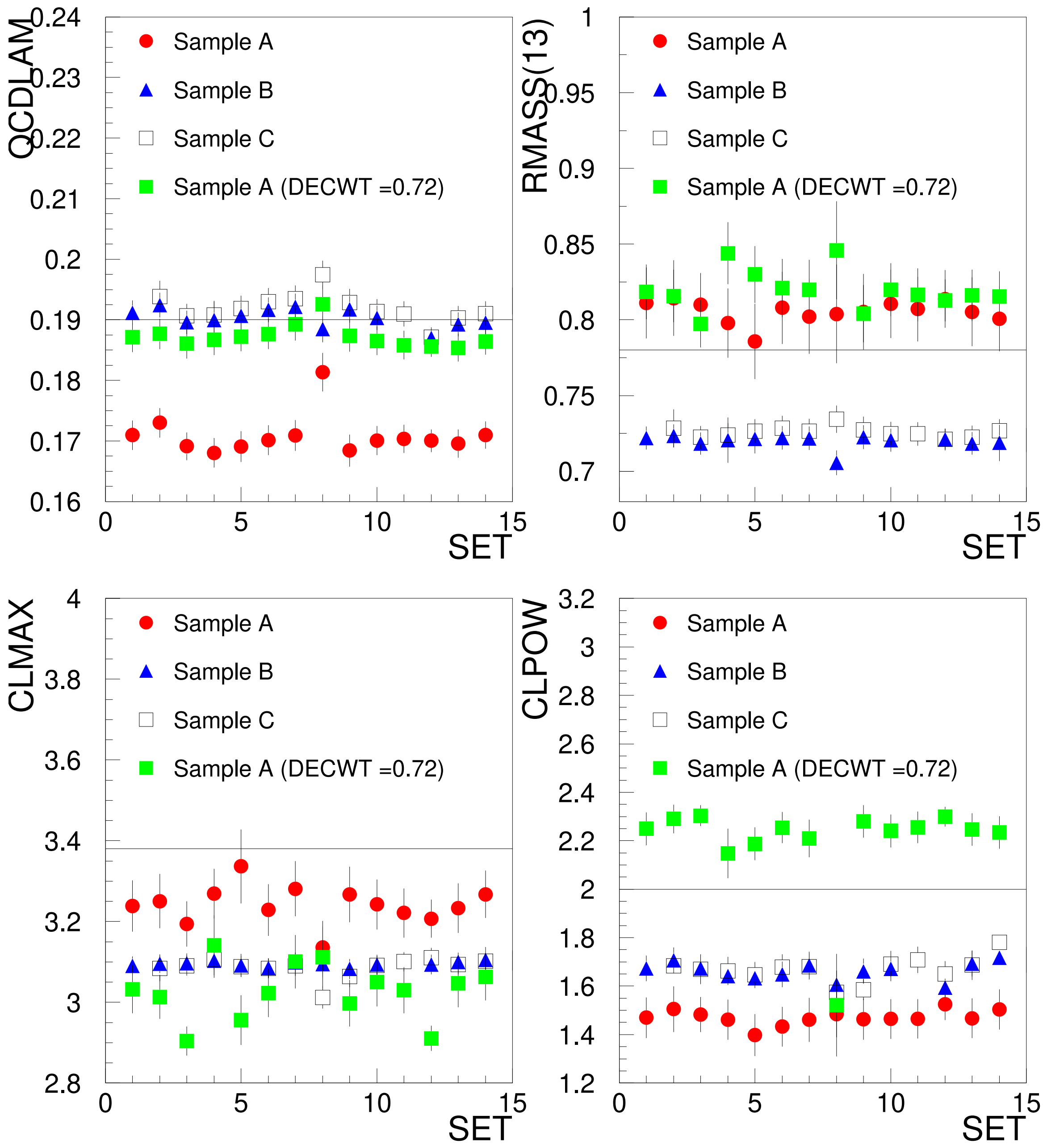

Figure 3.2: Results of the fit to the different sample sets of observables for the parameters QCDLAM, RMASS(13), CLMAX and CLPOW. The straight line shows the result obtained by Aleph.

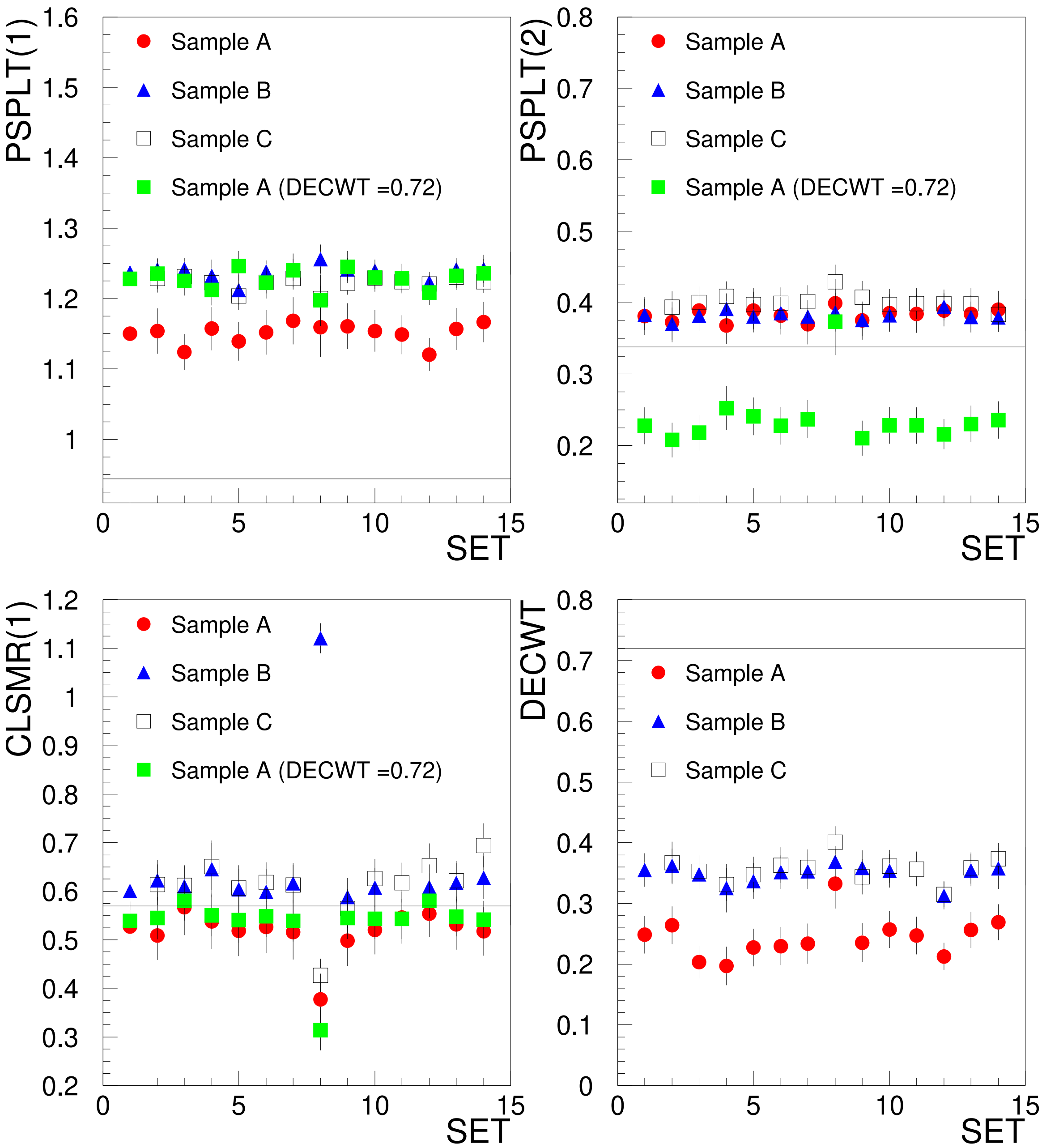

Figure 3.3: Results of the fit to the different sample sets of observables for the parameters PSPLT(1), PSPLT(2), CLSMR(1) and DECWT. The straight line shows the result obtained by ALEPH.

in), it is more interesting to have the best possible description of this kind of observables than the particle spectra. Therefore set number 14 of sample A was taken as the DELPHI tuning for this analysis. The values of the parameters obtained when fitting to sample A_{14} are shown in table 3.3, where the errors are just statistical.

Parameter	DELPHI
QCDLAM	0.171 ± 0.002
RMASS(13)	0.801 ± 0.021
CLMAX	3.267 ± 0.059
CLSMR(1)	0.517 ± 0.050
CLSMR(2)	0 (fixed)
DECWT	0.269 ± 0.030
PSPLT(1)	1.167 ± 0.029
PSPLT(2)	0.391 ± 0.026
CLPOW	1.503 ± 0.083

Table 3.3: The DELPHI tuned parameters obtained by fitting to set 14 of sample A.

3.2.5 Data/MC comparison

In this section the data distributions are compared with the ones obtained for HERWIG 6.1 with the DELPHI tuned parameters of table 3.3. In the same plots, the results obtained with the old version HERWIG 5.8 and with PYTHIA 6.125 are also shown, using for both generators the DELPHI tuning of Ref. [17]. All figures are located in appendix A, where the upper part of the plot shows the distribution of the given observable and the lower one the ratio of Monte Carlo and data, being the shaded band the total experimental error.

Event shape distributions are in general well reproduced. The $1 - T$, S, A, M and m distributions are slightly overestimated at large values, although an improvement with respect to the previous version has been observed for the A distribution.

The three-jet rate looks also fine but the differential four and higher jet rates are still overestimated for this HERWIG 6.1, as it has been so far in all versions [9].

Concerning the inclusive charged particle distributions, the mean charged multiplicity is extremely well reproduced (see table 3.4). The tail of the p_t^{out} has improved with respect to the old version 5.8 while the p_t^{in} has been degraded, the tail is underestimated. The improvement on the p_t^{out} is not only with respect to previous versions of HERWIG but also with respect to other generator predictions as PYTHIA or ARIADNE. In all cases an underestimation is observed for large values of p_t^{out} (> 0.8 GeV/c). The large tail of p_t^{out} is mainly

[9] Note that PYTHIA also reproduces the three-jet rate but, in this case, the higher differential rates are underestimated. It seems that both generators, HERWIG and PYTHIA, cannot describe simultaneously the different multi-jet rates. Up to now, the only generator that seems to represent well all jet rates at the same time is ARIADNE [107]. In [97] it was argued that this could be due the fact that ARIADNE does not make any matching of the parton shower to the first order $q\bar{q}g$ ME calculations since in this model all splitting probabilities are given by the lowest order ME expression.

due to gluon radiation, in Ref. [17] it was argued that this bad behaviour could be caused by the missing large angle emissions in the parton shower approach. If this were the case, a matching of the parton shower to the second order ME calculations should lead to a better description. The x_p distribution has improved, with respect to the 5.8 version, in the region from 0.4 to 0.7 (before it was too high) but it has gotten worse for larger values, being now even lower. The $y(t)$ distribution is now better reproduced (in version 5.8 it was too high at large values).

Regarding the identified particle spectra, the η spectrum is too low, for the K^0 at large $\xi_p = \log(1/x_p)$ there's an overestimation, the ω^0, K^{*0} and $K^{*\pm}$ spectra are better reproduced than with HERWIG 5.8 but the Λ^0 and Ξ^- spectra are too high.

Note that the big improvement of HERWIG 6.1 with respect to 5.8 has to do with the b distributions. As can be seen in figure A.8, the x_E^b distribution has become much harder in the new version, getting closer to the data and to the PYTHIA prediction (not shown in the plot). The mean charged multiplicity for $b\bar{b}$ events is also better reproduced by HERWIG 6.1 (see table 3.4).

As already mentioned, this HERWIG tuning was performed using version 6.1. It has been checked that this tuning is also valid for a more recent version of HERWIG, 6.2 [10].

	HERWIG 6.1	HERWIG 5.8	DATA
$< N_{ch} >$	20.95	20.86	20.95±0.21
$< N_{ch}^b >$	23.11	25.25	23.16±0.45

Table 3.4: Mean charged multiplicity for all events, N_{ch}, and for $b\bar{b}$ events, N_{ch}^b, obtained with two versions of HERWIG, 5.8 and 6.1, both with their corresponding DELPHI tuning.

3.3 Summary

If Monte Carlo QCD generators want to be used to compute reliable hadronization corrections for the different observables used in QCD analysis, it is important to determine first the values of their free parameters that give the best possible description of the observed data at hadron level.

The PYTHIA generator, which uses the string fragmentation model, was altready tuned in Ref. [17]. A tuning of HERWIG, based on the cluster hadronization model, was already available for previous versions of the generator [17] but important improvements were done in HERWIG in order to improve the fragmentation of b quarks. In this chapter a tuning of an improved version of the HERWIG generator was performed using the method developed in Ref. [17].

[10] HERWIG 6.5 is at the moment the last version of HERWIG. The difference between this last version and 6.2 should not affect the description of Z^0 hadronic events. The main new features have to do with parton distribution functions, new gauge boson pair production processes in hadron collisions, spin correlations between the production and decay of top quarks, τ leptons and SUSY particles, polarization effects in SUSY production processes in lepton collisions and new SM and MSSM Higgs processes in lepton collisions (see [108]).

Eight parameters of the generator were fixed by fitting to the event shape observables, jet rates and inclusive charged particle distributions measured by DELPHI [17] and to the b fragmentation function and charged multiplicity for b events measured by ALEPH [105] and OPAL [104] respectively. The results obtained for the tuned parameters are shown in table 3.3.

The prediction given by HERWIG with the tuned parameter settings has been compared with the measured data for different observables and the agreement found is better than for previous versions of the generator for most distributions, specially for those related with b quarks.

Chapter 4

Hadronization correction

This chapter is devoted to the evaluation of the hadronization correction of the $R_3^{b\ell}$ observable used to measure $m_b(M_Z)$, based on the string and cluster hadronization models available in the QCD generators. The prediction given by the generators for $R_3^{b\ell}$ at the different stages, i.e. after the parton shower, after the fragmentation process and after particle decays, is first shown. The hadronization correction is then computed for each generator and jet clustering algorithm, distinguishing the contributions coming from the hadronization itself and from the decay processes. Finally, the different sources of uncertainties affecting the hadronization correction are discussed and evaluated.

4.1 The Monte Carlo prediction for $R_3^{b\ell}$

As explained in Section 1.5.5, the $R_3^{b\ell}$ observable of Eq. (1.66), i.e. the ratio of the normalized three-jet rate for b over ℓ quark events, can be used to determine $m_b(M_Z)$ by comparing the measured quantity with the prediction given by the NLO theoretical calculations. However, these perturbative calculations are applied to partons whereas experimentally the observed objects are hadrons.

In chapter 3 the two hadronization models of Pythia (string) and Herwig (cluster) were described. For both models, their free parameters have been fixed by fitting to the observed data at hadron level using the Delphi tuning method. The Pythia tuning was performed in Ref. [17] and the Herwig generator was tuned in previous chapter. Therefore these generators can be used to bring the $R_3^{b\ell}$ observable from hadron to parton level.

Within the generator, $R_3^{b\ell}$ can be determined at different stages of the event:

1. parton level, after the parton shower,

2. hadron level, immediately after the hadronization process and before unstable particles start to decay,

3. hadron level, after the hadronization process and after unstable particles have decayed.

Figures 4.1 and 4.2 show the predictions given by both generators for $R_3^{b\ell}$ as a function of the y_c for the three different stages mentioned above, for the Durham and Cambridge

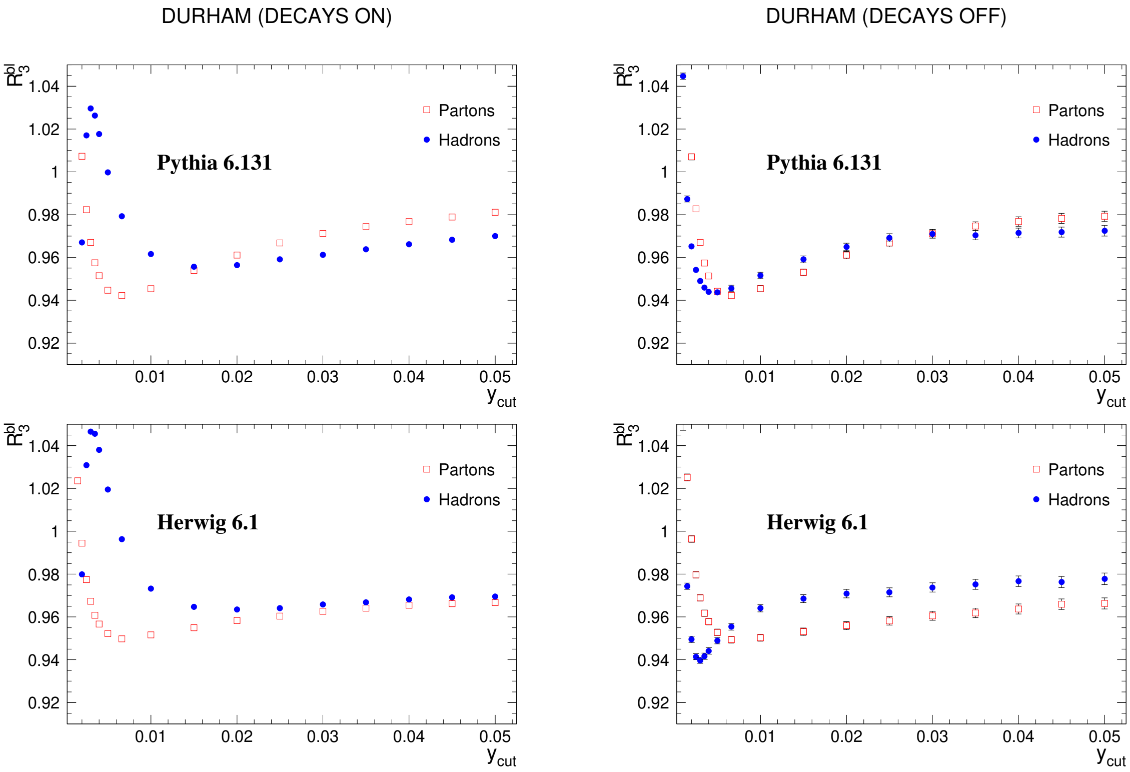

Figure 4.1: $R_3^{b\ell}$ at parton and hadron level as a function of y_c predicted by PYTHIA (top) and HERWIG (bottom) for the DURHAM algorithm. Hadron decays are turned on in the left plots and off in the right ones.

jet algorithms respectively. The plots on the left show the comparison of 1-3 stages and the ones in the right the 1-2.

A common behaviour of both generators is that at hadron level, the decay of particles makes $R_3^{b\ell}$ decrease for large values of y_c ($y_c > 0.01$ for DURHAM and $y_c \geq 0.003$ for CAMBRIDGE) and increase for very small y_c values (except for the case of PYTHIA with CAMBRIDGE). Figure 4.3 shows the ratio of the observable at hadron level after and before particles decay.

For the DURHAM algorithm, the increase at low y_c values of $R_3^{b\ell}$ when particles are allowed to decay is due to the larger increase of R_{3b} with respect to the one produced in $R_{3\ell}$. For larger values of y_c, the decrease of $R_3^{b\ell}$ is caused by the increase of $R_{3\ell}$ (see figure 4.4 left).

For the case of CAMBRIDGE, both flavour jet rates decrease when the decays are turned on, but more for b than for ℓ events (except for some very small values of the y_c), making the $R_3^{b\ell}$ ratio decrease (see figure 4.4 right).

The observed behaviour can be understood by looking at the migrations from events that, at a given y_c, are reconstructed to $n \neq 3$ jets at parton level and become three jets at hadron level. As an example, at small y_c, particle decays make a lot of events that are two jets at parton level to be reconstructed as a three-jet event at hadron level. This is specially the case for b quark events, as can be deduced from figure 4.5, where P_{23} denotes the fraction

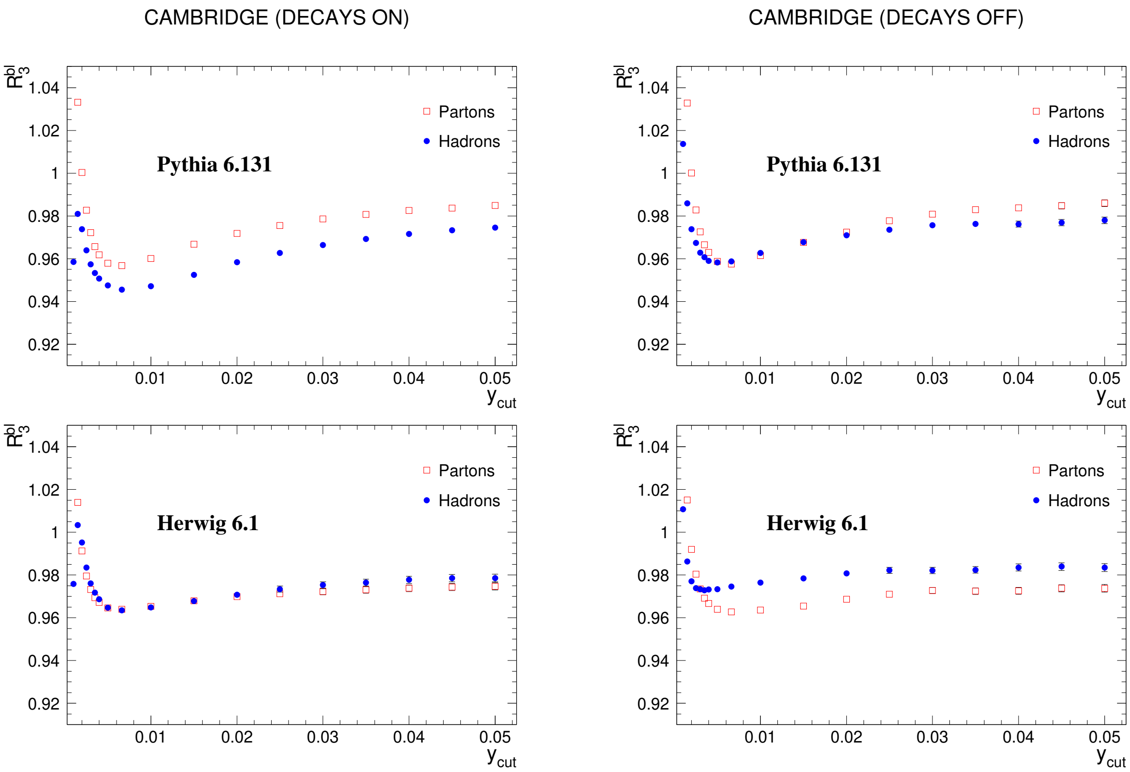

Figure 4.2: $R_3^{b\ell}$ at parton and hadron level as a function of y_c predicted by PYTHIA (top) and HERWIG (bottom) for the CAMBRIDGE algorithm. Hadron decays are turned on in the left plots and off in the right ones.

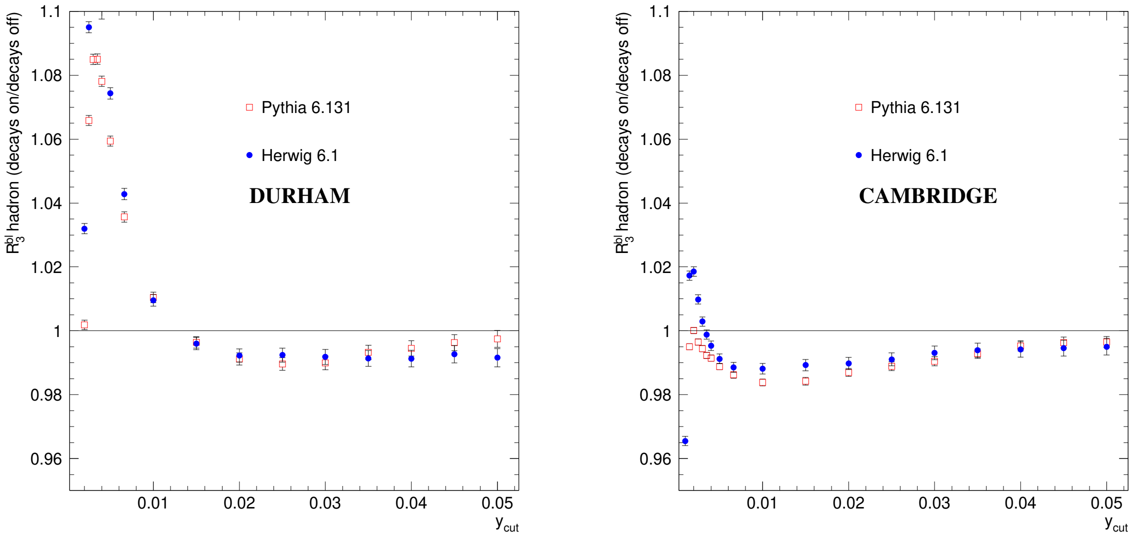

Figure 4.3: Ratio of $R_3^{b\ell}$ at hadron level when particle decays are turned on and off for both generators, for Durham (left) and Cambridge (right) algorithms.

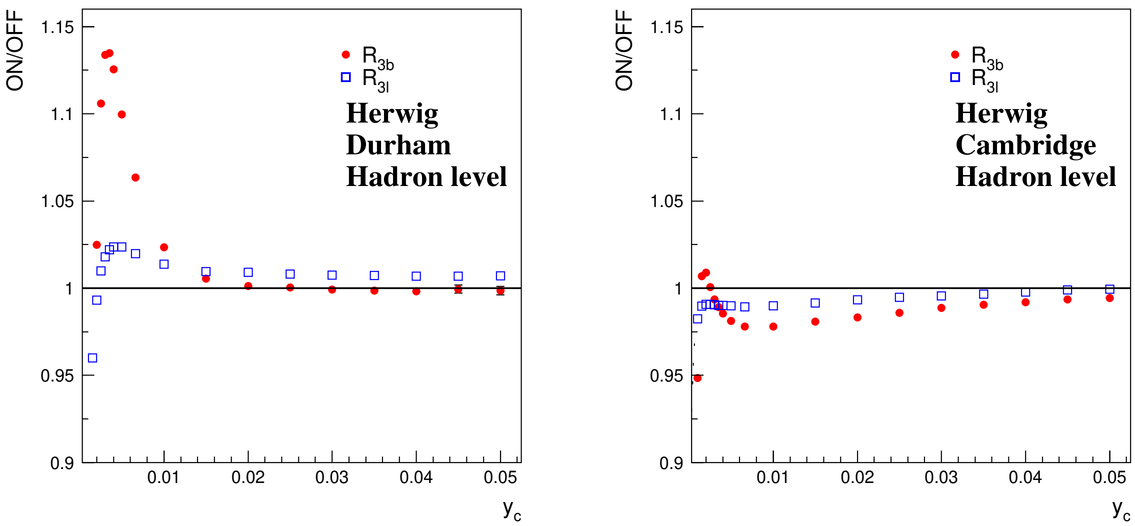

Figure 4.4: Ratio of R_{3q} ($q = b, \ell$) at hadron level when particle decays are turned on and off in Herwig for Durham (left) and Cambridge (right) algorithms.

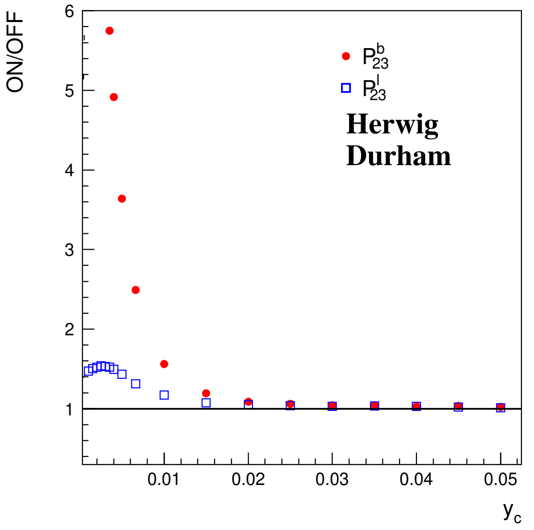

Figure 4.5: P_{23}^q $(q = b, \ell)$ ratio between the case in which particles are allowed to decay and when they are kept as stable for q quark events. Events were generated with HERWIG and DURHAM was used to form jets.

of three-jet events at hadron level that are reconstructed to two jets at parton level.

4.2 Hadronization correction of $R_3^{b\ell}$

The hadronization correction of $R_3^{b\ell}$ is given by,

$$C^{had}(y_c) = \frac{R_3^{b\ell-parton}(y_c)}{R_3^{b\ell-hadron}(y_c)} \tag{4.1}$$

where hadron refers to the last stage in which all particles have decayed. But, in order to separate the contribution of the fragmentation process to the one coming from the decay process, it is interesting to compute the ratio above but where $R_3^{b\ell-hadron}$ now means before hadrons start decaying.

The total hadronization correction can then be written as $C^{had}(y_c) = C^{frag-only}(y_c) \times C^{decays}(y_c)$, being $C^{frag-only}(y_c)$ the hadronization correction obtained when the decays are turned off and $C^{decays}(y_c)$ the correction due to the decay processes. Figures 4.6 and 4.7 show, for DURHAM and CAMBRIDGE respectively, the hadronization correction given for each generator when particle decays are turned on and off. As an example, the numbers at a $y_c = 0.02$ and 0.01 for DURHAM and CAMBRIDGE respectively are written in table 4.1 [1].

[1]The size of the hadronization correction (for not very small y_c values) is small due to the partial cancellation of the hadronization corrections of R_{3b} and $R_{3\ell}$, as will be shown in the next chapter (Section 5.2).

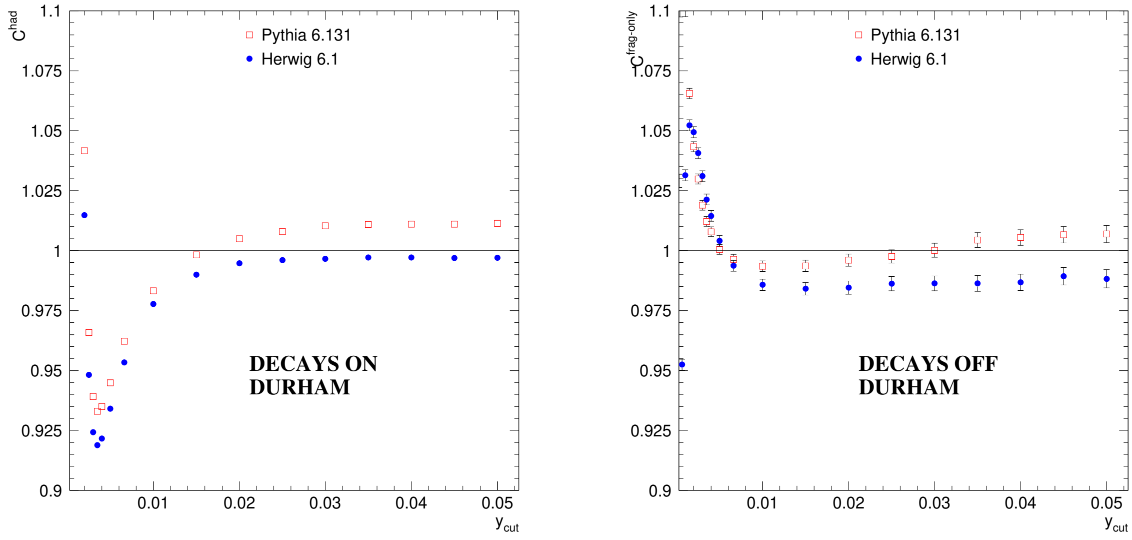

Figure 4.6: Hadronization correction of $R_3^{b\ell}$ as a function of y_c predicted by Pythia and Herwig for the Durham algorithm when the decays are on (left) and off (right).

At these y_c values, $C^{frag-only}(y_c) < 1$, i.e. the hadronization process makes $R_3^{b\ell}$ increase, while $C^{decays} > 1$, i.e. the decays make $R_3^{b\ell}$ decrease. For Pythia, the decay correction is larger than the fragmentation correction while for Herwig the fragmentation correction is larger than for Pythia, being very similar to the decay correction for Cambridge and even larger than that correction for Durham. Notice that the decay corrections predicted for both generators are equal to each other within the statistical uncertainty.

Durham ($y_c = 0.02$)	C^{had}	$C^{frag-only}$	C^{decays}
Pythia	1.005 ± 0.001	0.996 ± 0.003	1.009 ± 0.003
Herwig	0.995 ± 0.001	0.985 ± 0.003	1.010 ± 0.003
Cambridge ($y_c = 0.01$)			
Pythia	1.014 ± 0.001	0.999 ± 0.001	1.015 ± 0.001
Herwig	1.001 ± 0.002	0.987 ± 0.002	1.014 ± 0.003

Table 4.1: Hadronization correction for Durham and Cambridge algorithms at a $y_c = 0.02$ and 0.01 respectively for the case in which the decays are turned on (C^{had}) and off ($C^{frag-only}$) and the correction due to the decays (C^{decays}).

In order to estimate the hadronization correction uncertainty, different contributions have to be taken into account:

- $\sigma^{mod}(y_c)$: It is due to the hadronization model uncertainty (string, cluster or different fragmentation functions within the string model).

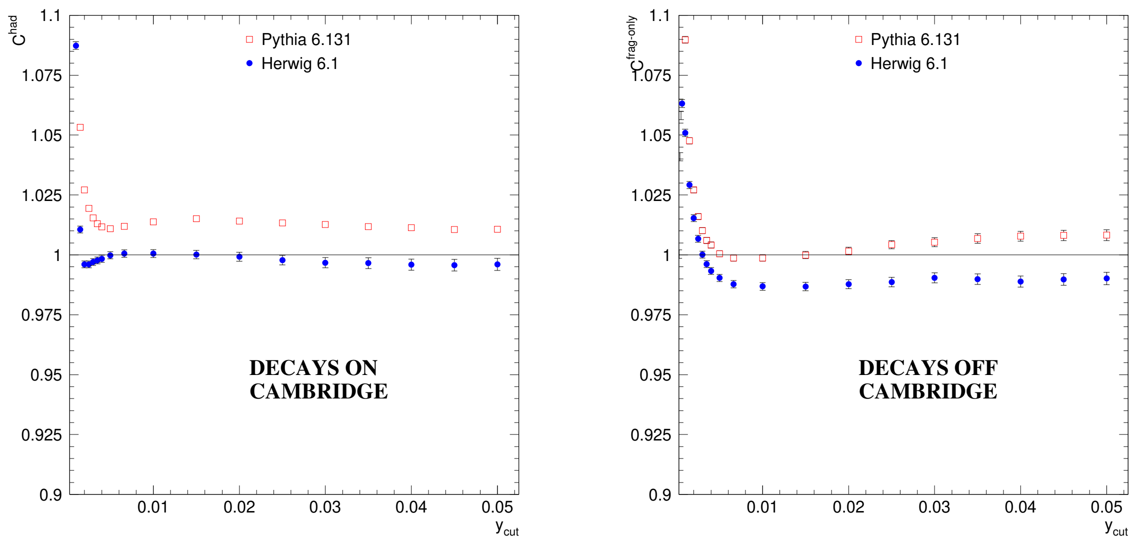

Figure 4.7: $C^{had}(R_3^{b\ell})$ as a function of y_c predicted by Pythia and Herwig for the Cambridge algorithm when the decays are on (left) and off (right).

- $\sigma^{tun}(y_c)$: It is due to the uncertainty on the tuned parameters of the generator that are relevant in the fragmentation process.
- $\sigma^{mass}(y_c)$: Due to the uncertainty on the b mass parameter used in the generator.

The total fragmentation uncertainty can be then written as,

$$\sigma^{had}(y_c) = \sqrt{\sigma^{mod}(y_c)^2 + \sigma^{tun}(y_c)^2 + \sigma^{mass}(y_c)^2} \tag{4.2}$$

In the following sections each contribution will be evaluated.

4.3 Hadronization model uncertainty

Two fragmentation models are available, the string and cluster, implemented in Pythia and Herwig respectively. If the mean between the hadronization corrections predicted for each model is taken to correct the data, the fragmentation model uncertainty can then be estimated as,

$$\sigma^{mod}(y_c) = \frac{1}{2}\left(C^{had}_{Herwig}(y_c) - C^{had}_{Pythia}(y_c)\right) \tag{4.3}$$

As already mentioned, the C^{had} gives the correction to the hadronization process itself plus the decay processes. Therefore, the difference on C^{had} predicted by each generator could not only be due to the difference on their fragmentation models but also on their

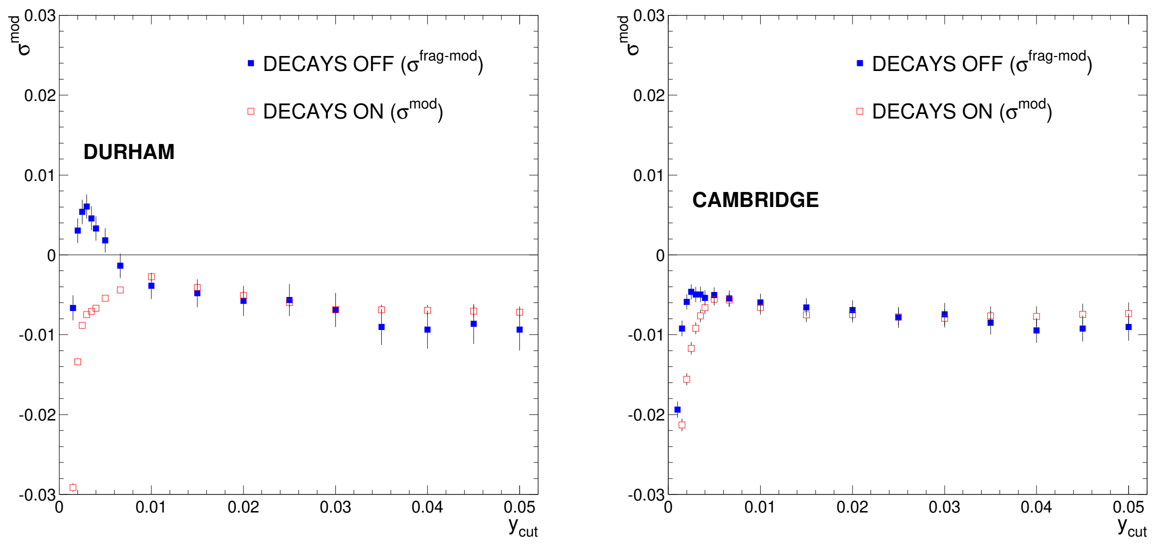

Figure 4.8: Hadronization model uncertainty of $R_3^{b\ell}$ as a function of y_c when the decays are turned on (σ^{mod}), and off ($\sigma^{frag-mod}$).

decay models. σ^{mod} has then two contributions, one from the fragmentation scheme itself, $\sigma^{frag-mod}$, and the other one from the decay model used, $\sigma^{dec-mod}$, so $\sigma^{mod}(y_c) = \sqrt{\sigma^{frag-mod}(y_c)^2 + \sigma^{dec-mod}(y_c)^2}$. For $y_c \geq 0.01$ for DURHAM and $y_c \geq 0.005$ for CAMBRIDGE, the contribution of $\sigma^{dec-mod}$ to the total uncertainty has been observed to be negligible (see figure 4.8).

As an example, the model uncertainty for DURHAM is of ± 0.006 at a $y_c = 0.02$ and for CAMBRIDGE of ± 0.007 at $y_c = 0.01$. Previous determinations of $m_b(M_Z)$ have shown that this is the dominant error on the measurement [7,11,112]. Therefore it is worthwhile to find a method to reduce this uncertainty. A strategy, based on the study of the b fragmentation function of each model, has been found.

The $R_3^{b\ell}$ observable and its fragmentation correction were found to depend on the B-hadron scaled energy, $x_E^b = 2E_{B-\mathrm{hadron}}/E_{CM}$. The x_E^b distribution is shown in figure 4.9 (left) for PYTHIA and HERWIG. For the case of PYTHIA different fragmentation functions can be selected, the plot shows the obtained distributions when Peterson and Bowler are chosen. It is important to note that the DELPHI tuning of PYTHIA was done with the Peterson fragmentation function, so all the results obtained with PYTHIA up to now have been deduced for this function.

Figure 4.10 shows for the PYTHIA generator (with Peterson) the x_E^b distribution and the contribution of the different number of jets reconstructed by DURHAM at a $y_c = 0.02$ (left plot). The plot on the right shows the proportion of n-jet events (for n = 2,3,4) as a function of x_E^b. The conclusion is that high and low values of x_E^b mean a preference for a two-jet like configuration while the intermediate values correspond mostly to three-jet events.

As it was mentioned, the hadronization correction of $R_3^{b\ell}$ depends on x_E^b and the σ^{mod}

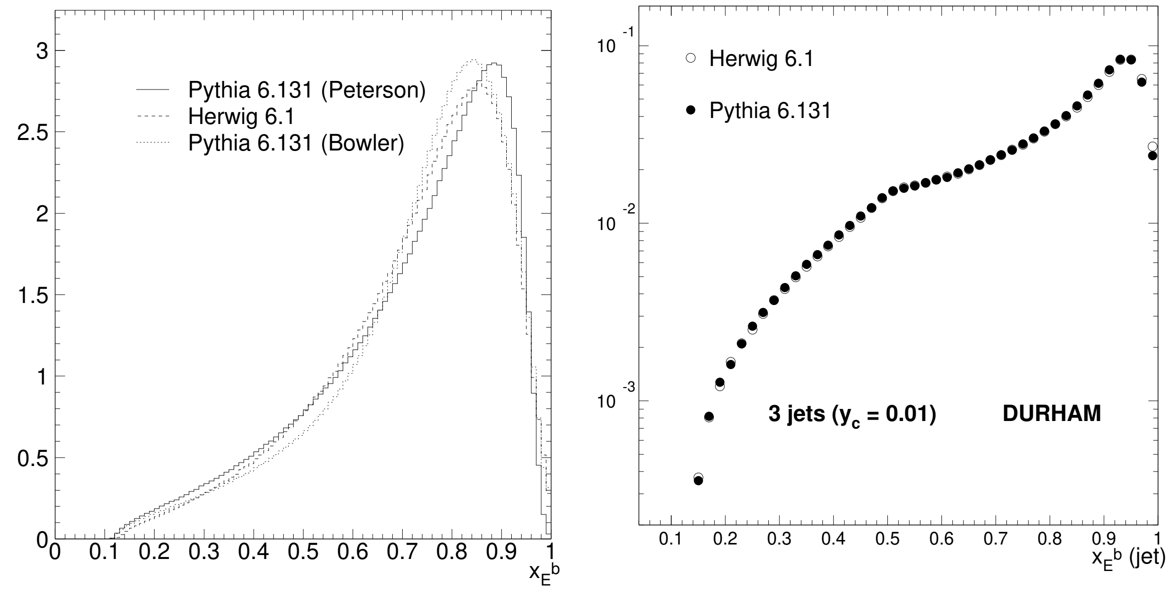

Figure 4.9: (Left) x_E^b distribution for the different Monte Carlo generators, normalized to N_{ent}/N_{bin}, being N_{ent} and N_{bin} the number of entries and bins respectively. (Right) x_E^b(jet) distribution for PYTHIA and HERWIG at a $y_c = 0.01$ for DURHAM, normalized to N_{ent}.

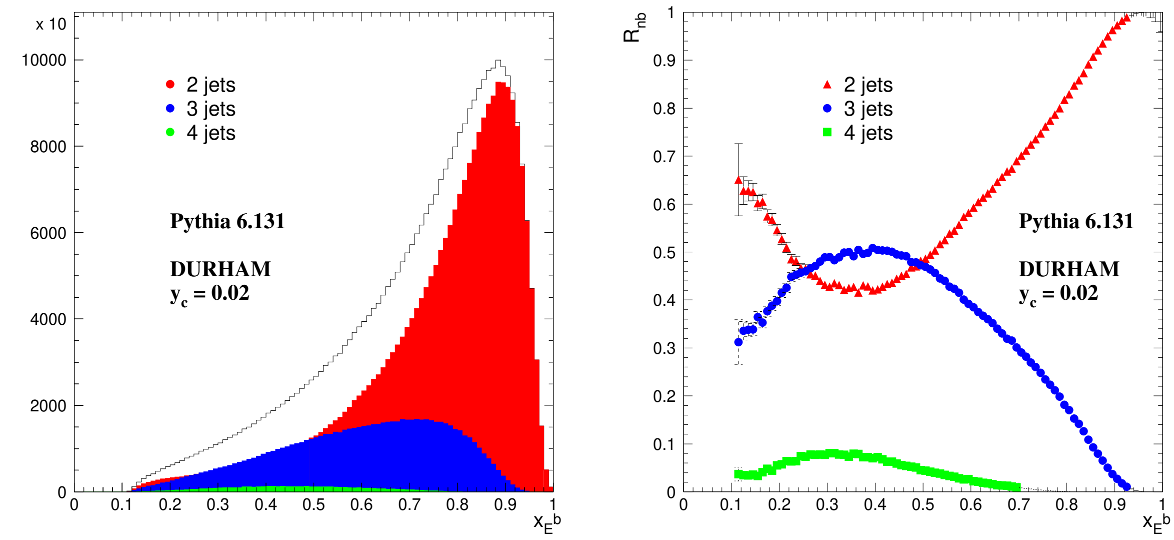

Figure 4.10: (Left) x_E^b distribution predicted by PYTHIA and the contribution of the different number of jets reconstructed by DURHAM at a $y_c = 0.02$. (Right) The n-jet rate for b events, R_{nb}, as a function of x_E^b, predicted also by PYTHIA.

uncertainty was also found to depend on this variable. Therefore, if the measurement of $R_3^{b\ell}$ is restricted to a certain region of x_E^b, the σ^{mod} uncertainty could be reduced.

Since from the experimental point of view, it is easier to measure jet energies than particle energies [2], a new variable is defined instead. For a three-jet event, the b-jet scaled energy, $x_E^b(\text{jet})$, is given by,

$$x_E^b(\text{jet}) = 2\,\frac{E_{b-\text{jet}}}{E_{CM}} \tag{4.4}$$

where $E_{b-\text{jet}}$ is the energy of the jets originated by the primary b quarks in a $Z^0 \to b\bar{b}$ event. So for each b event there are two values of $x_E^b(\text{jet})$. Its distribution can be seen in figure 4.9 (right) for the two generators and its correlation with the B hadron scaled energy, x_E^b, is shown in figure 4.11 for PYTHIA. The two variables can also be defined at parton level, so this figure shows the correlation at both, hadron and parton level [3].

The aim is to find the dependence of the hadronization correction with $x_E^b(\text{jet})$ for each generator and see if a region of $x_E^b(\text{jet})$ in which the two models give a similar correction exists.

The procedure followed is illustrated in figure 4.12. First, the distribution of $x_E^b(\text{jet})$ is divided into 18 intervals. For each of them, we take all b events that have the smallest of the two $x_E^b(\text{jet})$ values within that interval and compute the $R_3^{b\ell}(y_c)$ (at parton and hadron level) and its hadronization correction for that region of $x_E^b(\text{jet})$. This is done for both generators, the results obtained with PYTHIA for some of the intervals of $x_E^b(\text{jet})$ can be seen in figure 4.13.

Fixing now the y_c, figure 4.14 shows the hadronization correction predicted by the two generators and the hadronization model uncertainty as a function of $< x_E^b(\text{jet}) >$ for DURHAM at a $y_c = 0.02$. $< x_E^b(\text{jet}) >$ represents the mean of the $x_E^b(\text{jet})$ distribution obtained for each cut.

Therefore a region of $x_E^b(\text{jet})$ where the two fragmentation models behave similarly was selected, $x_E^b(\text{jet}) \geq 0.55$ [4], and the hadronization model uncertainty was reduced from ± 0.006 to ± 0.001 for a $y_c = 0.02$ with DURHAM and from ± 0.007 to ± 0.002 for CAMBRIDGE at a $y_c = 0.01$ (see figure 4.15). The cut efficiency was of around 70%.

Since the difference between the two fragmentation models has been significantly reduced, different fragmentation functions can be used in the string model of PYHTIA to estimate the

[2]Jet energies can be extracted from the jet directions, as described in Ref. [109]. For massless quarks, if θ_{ij} is the angle formed by jets i and j, the energy of jet k is given by,

$$E_k = \sqrt{s}\,\frac{\sin\theta_{ij}}{\sin\theta_{12} + \sin\theta_{23} + \sin\theta_{13}}$$

In Ref. [109] it was shown that the energy resolution improves if jet energies are obtained from jet directions instead of the total reconstructed energy.

[3]In the generator, at parton level the b jets are easily identified as those containing the primary b quarks. However, at hadron level the information is lost and each jet has to be associated to a jet at parton level. Different methods to make this association were studied in [109] and we have taken here the one that associates each jet at hadron level to the one at parton level that is closest in angle. Those jets associated to the b jets at parton level are then taken as the b jets at hadron level.

[4]This corresponds to exclude the region $< x_E^b(\text{jet}) >$ smaller than 0.7 in the plot of figure 4.14 where the two models give different predictions for the hadronization correction.

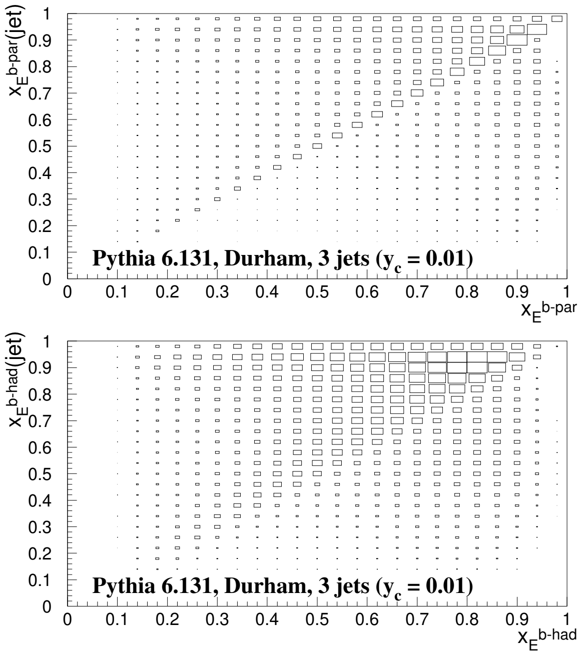

Figure 4.11: Correlation between x_E^b and x_E^b(jet) at parton (top) and hadron (bottom) level for PYTHIA at a $y_c = 0.01$ with DURHAM.

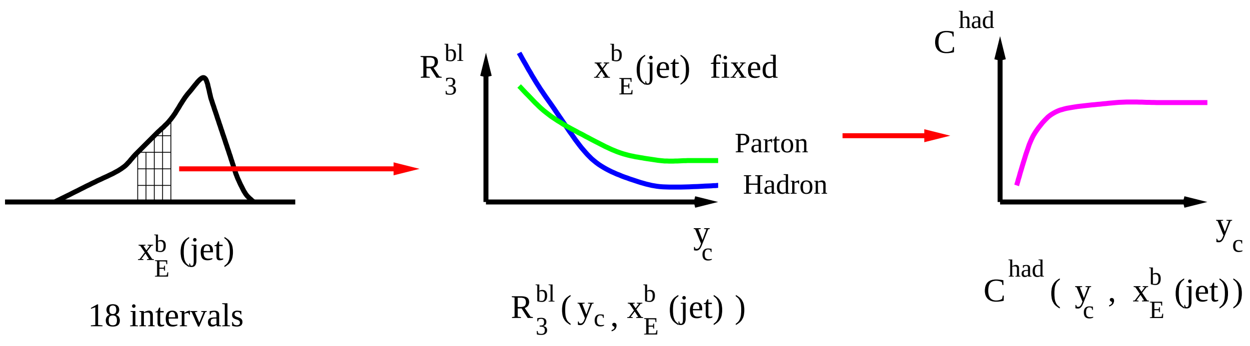

Figure 4.12: Schematic view of the method followed to calculate the hadronization correction as a function of x_E^b(jet).

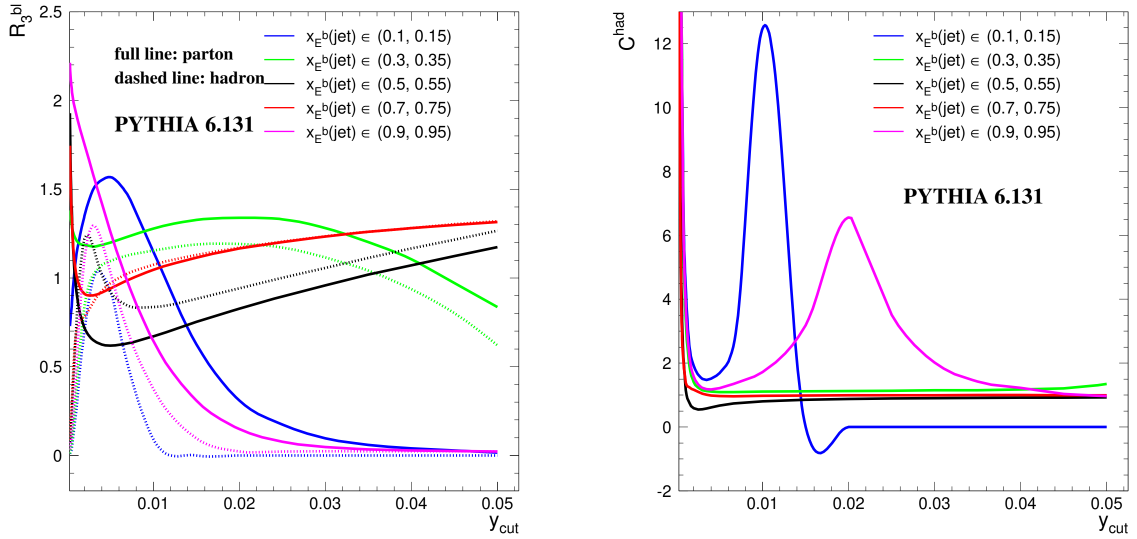

Figure 4.13: $R_3^{b\ell}(y_c)$ at parton (full lines) and hadron (dashed lines) level and $C^{had}(y_c)$ predicted by PYTHIA for the different intervals of x_E^b(jet).

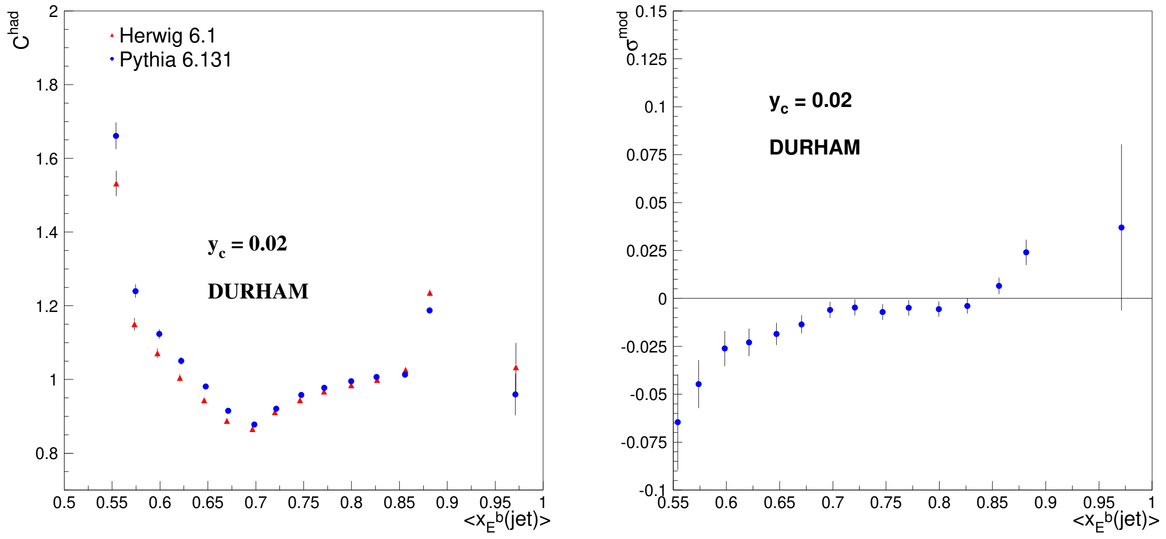

Figure 4.14: (Left) C^{had} predicted by PYTHIA and HERWIG as a function of $< x_E^b(\text{jet}) >$ for events that are reconstructed to three jets at a $y_c = 0.02$ with DURHAM. (Right) Hadronization model uncertainty as a function of $< x_E^b(\text{jet}) >$ for the same events.

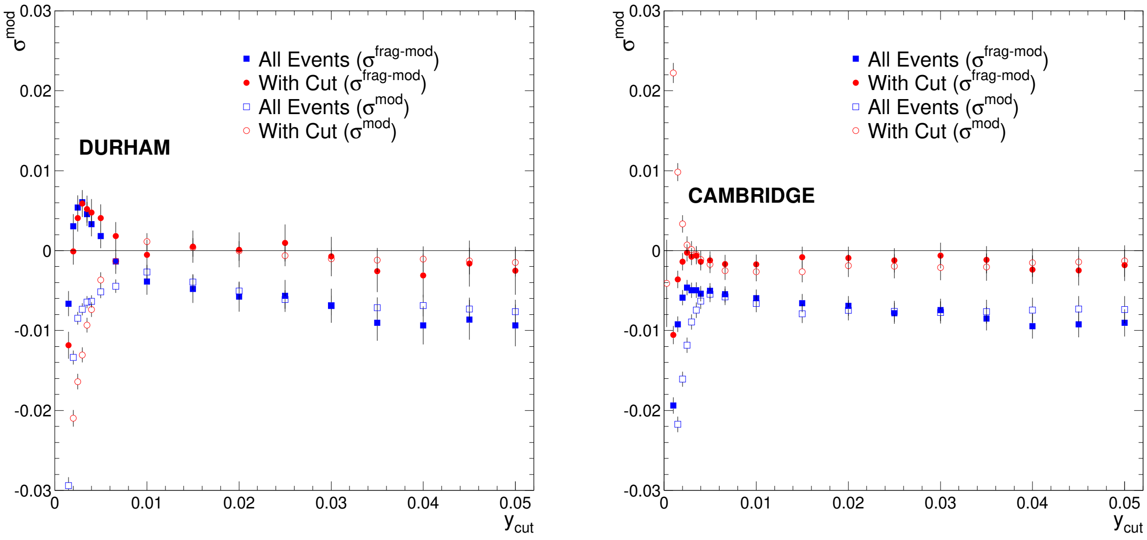

Figure 4.15: Hadronization model uncertainty as a function of y_c for DURHAM and CAMBRIDGE when all events are considered (squares) and when the cut on x_E^b(jet) is applied (circles). The $\sigma^{frag-mod}$ obtained by turning off particle decays is also shown in both cases.

hadronization model uncertainty. The Peterson and Bowler fragmentation functions have been considered for this purpose.

The model uncertainty of the hadronization correction of $R_3^{b\ell}$ is taken now as the standard deviation of the hadronization corrections predicted by the three following models,

- string model with Peterson b fragmentation function,
- string model with Bowler b fragmentation function,
- cluster model.

The result is shown in figure 4.16 (left), which is around ± 0.003 for both DURHAM and CAMBRIDGE at a $y_c = 0.02$ and 0.01 respectively. For comparison, the plot on the right shows the σ^{mod} one gets if no cut on x_E^b(jet) is made.

4.4 Tuning uncertainty

Another source of uncertainty to the $R_3^{b\ell}$ hadronization correction is due to the uncertainties of the tuned parameters that play a role in the fragmentation process. The PYTHIA generator has been used to evaluate this source of uncertainty and these parameters are the following:

- $\Lambda_{\rm QCD}$: Λ parameter used in the running of α_s for the parton shower produced after the Z^0 decay.

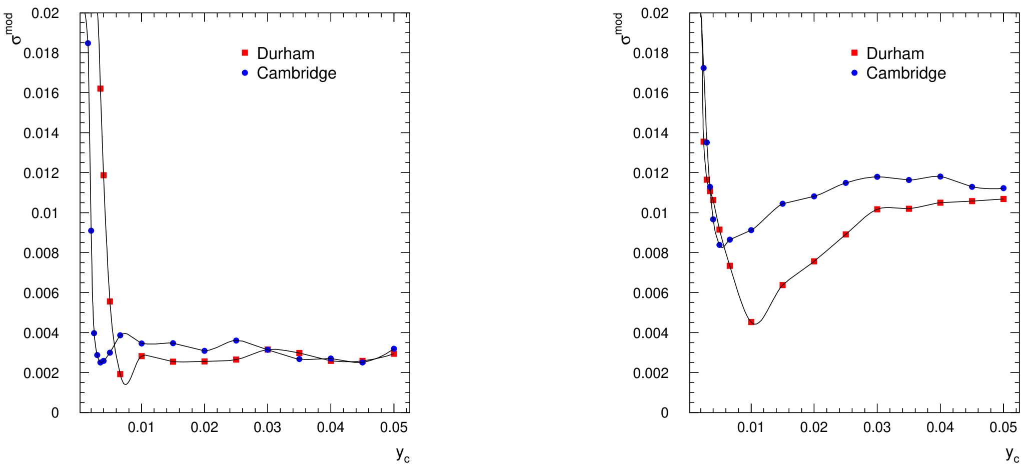

Figure 4.16: Hadronization model uncertainty as a funcion of y_c for DURHAM and CAMBRIDGE when the cut on $x_E^b(\text{jet}) \geq 0.55$ is applied (left) and when no cut is made (right).

- Q_0: Mass scale cut-off below which partons are not allowed to radiate. It gives then the end of the parton shower and the beginning of fragmentation.
- a: The a parameter of the symmetric Lund fragmentation function (see Eq. (1.56)).
- σ_q: It corresponds to the standard deviation of the p_t^2 Gaussian distribution, being p_t the transverse momentum of primary hadrons.
- ϵ_b: It is the free parameter of the Peterson fragmentation function applied to b quarks (see Eq. (1.58)).

The values obtained for these parameters after tuning to the DELPHI data are shown in table 4.2 and their correlation factors in 4.3 [17].

Parameter	PYTHIA name	DELPHI tuning $\pm$ (stat.) $\pm$ (syst.)
Λ_{QCD}	PARJ(81)	$0.297 \pm 0.005^{+0.012}_{-0.007}$
Q_0	PARJ(82)	$1.34 \pm 0.08^{+0.15}_{-0.09}$
a	PARJ(41)	$0.409 \pm 0.020^{+0.009}_{-0.013}$
σ_q	PARJ(21)	$0.401 \pm 0.006^{+0.003}_{-0.013}$
ϵ_b	PARJ(55)	$-0.00284 \pm 0.00006^{+0.00013}_{-0.00009}$

Table 4.2: Tuned parameters of the PYTHIA generator obtained in Ref. [17].

In order to calculate the tuning error of $C^{had}(R_3^{b\ell})$, each of these parameters was variated within $\pm\sigma$. Taking correlations among parameters into account, the tuning uncertainty is

	Λ_{QCD}	Q_0	a	σ_q	ϵ_b
Λ_{QCD}	1.00	0.18	-0.60	-0.69	0
Q_0		1.00	0.01	-0.08	0
a			1.00	0.33	0
σ_q				1.00	0
ϵ_b					1.00

Table 4.3: Correlation coefficients for the PYTHIA coefficients obtained in Ref. [17].

given by,

$$(\sigma^{tun}(y_c))^2 = \sum_{j=1}^{5} \frac{\partial C^{had}(y_c)}{\partial p_j} \left(\sum_{i=1}^{5} \frac{\partial C^{had}(y_c)}{\partial p_i} \rho_{ji} \sigma_j \sigma_i \right) \tag{4.5}$$

where

$$\frac{\partial C^{had}(y_c)}{\partial p_i} \sigma_i = \frac{C^{had}(p_i + \sigma_i, y_c) - C^{had}(p_i - \sigma_i, y_c)}{2} \tag{4.6}$$

The result obtained is shown in figure 4.17 for the DURHAM and CAMBRIDGE jet algorithms. The contribution of the error due to its individual tuned parameter is also shown in the plots as well as the total uncertainty calculated as if all parameters were completely independent of each other (dashed line).

The total tuning error is of 1.5‰ for DURHAM and 1‰ for CAMBRIDGE at a y_c of 0.02 and 0.01 respectively. The highest contribution is coming from the uncertainty on the Q_0 cut-off for DURHAM while for CAMBRIDGE the uncertainty on ϵ_b dominates. The effect of the variation of Λ_{QCD} and σ_q on the hadronization correction are negligible for both algorithms.

4.5 b mass parameter uncertainty

The study presented here of the dependence of the $R_3^{b\ell}$ hadronization correction with the value given to the b mass parameter in the generator has been done with the PYTHIA generator.

All results shown below have been obtained for both algorithms, DURHAM and CAMBRIDGE. For simplicity most results will be shown for the DURHAM algorithm only.

4.5.1 b masses in PYTHIA

The PYTHIA generator uses three sets of b masses to describe the parton shower and hadronization of b quarks:

- The kinematical mass [5], M_b, entering in the parton shower and in the LO matrix element expressions used to correct the probability of gluon emission of the first branch-

[5] This mass, although called here kinematical, can be considered as an effective mass.

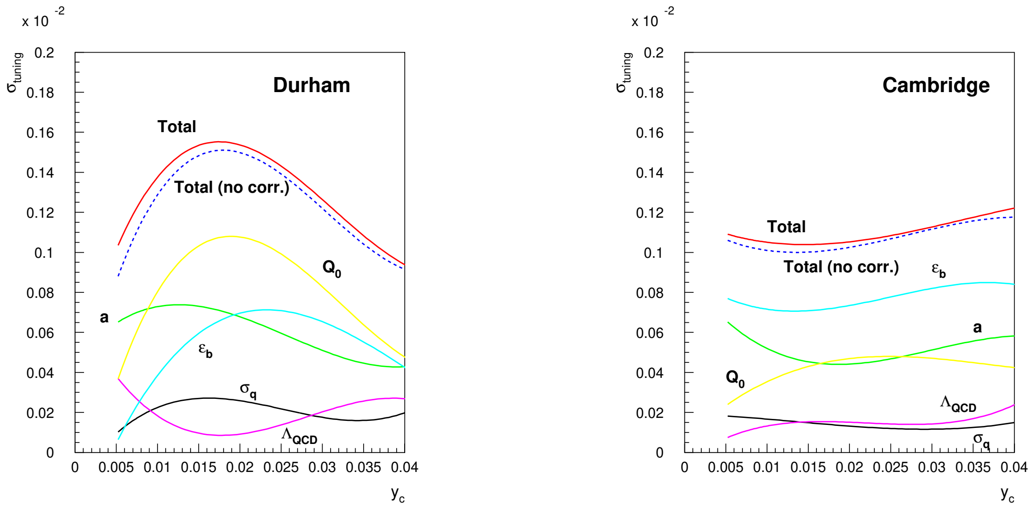

Figure 4.17: Tuning error of the hadronization correction of $R_3^{b\ell}$ for DURHAM (left) and CAMBRIDGE (right) jet clustering algorithms. The contribution of each individual parameter error as well as the uncertainty obtained as if they were completely independent are also shown.

ing of the parton shower, as described in Section 3.1.1 (default value: PMAS(5,1) = 5 GeV/c^2).

- The constituent mass, M_b^{const}, used to derive not yet found B hadron masses and entering also in the string hadronization process (default value: PARF(105) = 5 GeV/c^2).

- The set of already known B hadron masses.

It is essential to stress that, although not completely arbitrary, these three kinds of masses are not connected to each other in the generator and are set independently. An exception is the connection made between the constituent mass and B hadron masses in cases of B hadrons not yet found experimentally. The expression used to derive these masses in PYTHIA is the hadron mass formula [15,110],

$$m_B = m_0 + \sum_i M_i^{const} + k(M_d^{const})^2 \sum_{i<j} \frac{< \sigma_i \cdot \sigma_j >}{M_i^{const} M_j^{const}} \qquad (4.7)$$

where we have a constant term, a sum over constituent masses and a spin-spin interaction term for each quark pair in the hadron. The constants m_0 and k are fitted from known masses, treating mesons and baryons separately, and M_d^{const} is the constituent d quark mass. For mesons with orbital angular momentum $L = 1$ the spin-spin coupling is assumed to be vanishing. This formula is based on a constituent quark model and though remarkably successful [111] it is not derived from the QCD Lagrangian. Hence the constituent b quark masses extracted from this expression do not have a well defined relationship to the quark mass appearing in the QCD Lagrangian.

4.5.2 Sensitivity to variations of the M_b parameter in PYTHIA

It has been observed in various studies [7, 11, 12] that when the kinematical mass parameter M_b is varied, the $R_3^{b\ell}$ observable changes accordingly at parton level, but remains almost constant at hadron level. Therefore, the hadronization correction automatically shifts by as much as $R_3^{b\ell}$ does at parton level (see figure 4.18). This situation has led to lot of discussion among experimentalists and theorists.

Discussion in the context of the b quark mass measurement at LEP

The consequence of this behaviour of the generator for the $m_b(M_Z)$ measurement is that the result obtained can become arbitrary, since it depends strongly on the choice made for the input parameter M_b. However such a dependence of the hadronization correction with M_b cannot be considered physical. Different methods have been used in different studies to show this:

- Turn *on* and *off* mass effects in the generator (MSTJ(47) = 3 or 1). This means that the massive or massless ME calculations are used in the matching of the first branching of the parton shower [7, 11].
- Consider the variations of the M_b input parameter only in the LO ME expression used for the just mentioned matching [12], and not in the parton shower process.
- The mass parameter can also be understood in the QCD Lagrangian as a coupling constant at the quark-gluon vertex. Hence, one can modify α_s^b rather than M_b in order to change the amount of gluon radiation off b quarks. This is equivalent to varying Λ_{QCD} in PYTHIA only for $b\bar{b}$ events [6].

In all three cases the hadronization correction remains constant, i.e. the effects observed at parton level are also present at hadron level. However these checks don't explain why PYTHIA behaves in this way when M_b is modified. Moreover, they don't help to specify which value of M_b should be used in the generator.

Interpretation of the observed behaviour

It is important to understand why when M_b is changed in PYTHIA the effect observed at parton level does not propagate to hadron level. This lack of sensitivity was shown in figure 4.18 for the $R_3^{b\ell}$ observable. A similar insensitivity is observed for the b quark scaled energy distribution (see figure 4.19). The situation described above is understood if one takes into account the following features of the generator:

- M_b and M_b^{const} are not connected,
- known B hadron masses are hardcoded [7],

[6] It is for this reason that the measurement of $R_3^{b\ell}$ can be interpreted both as a determination of the b quark mass at the Z^0 boson mass scale or as a test of the flavour independence of α_s.

[7] For those not yet found experimentally the mass formula in Eq. (4.7) is used.

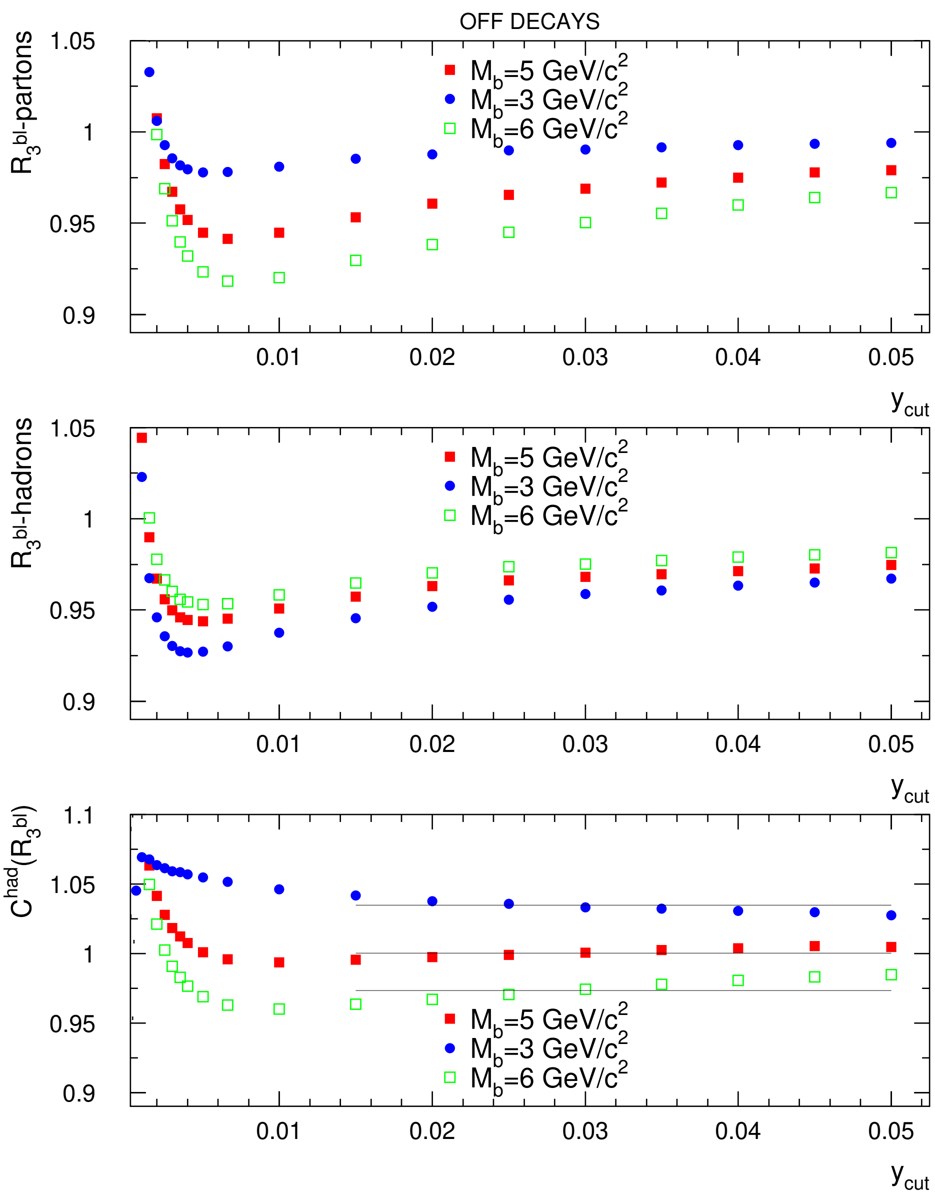

Figure 4.18: $R_3^{b\ell}$ at parton and hadron level and its hadronization correction as a function of y_c for three different values of the kinematical mass of Pythia. Durham is used to reconstruct jets.

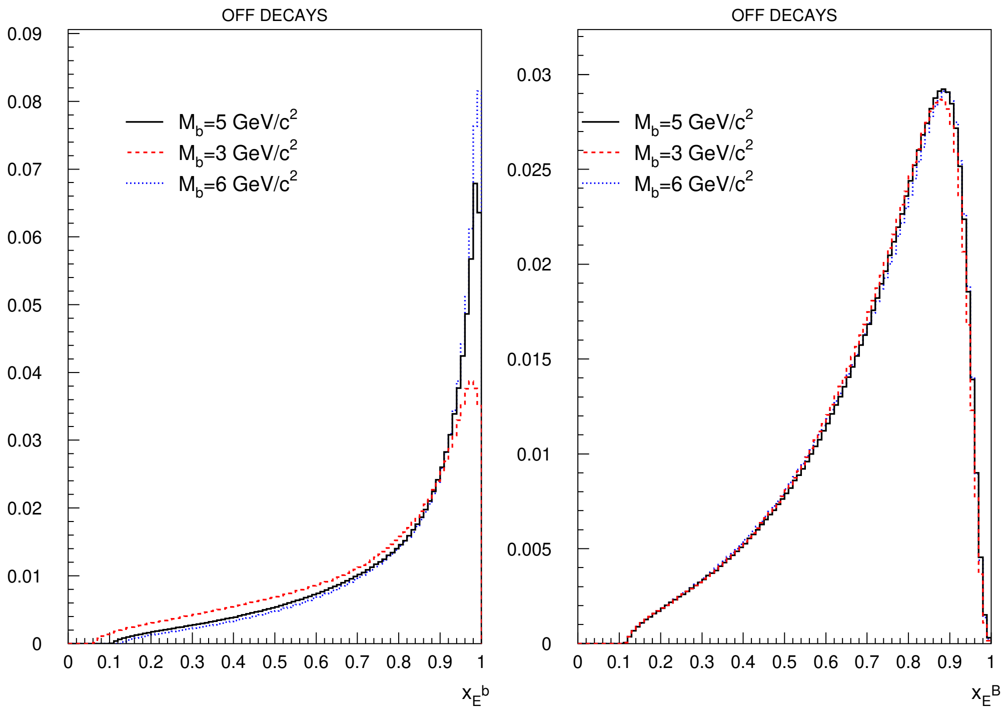

Figure 4.19: b quark scaled energy distribution (left) and B hadron scaled energy distribution (right) for $M_b = 3$, 5 and 6 in PYTHIA.

- the Peterson fragmentation function depends on the ϵ_b parameter, which is fixed to the tuned value.

When M_b is changed in PYTHIA the constituent mass remains constant and so do hadron masses and energies. Therefore, if M_b changes, decreased or increased, the number of jets at parton level increases or decreases but, as hadron masses remain constant, the particles/jets/energy needed to form B hadrons are the same, so these particles/jets/energy are recombined to form the same number of jets at hadron level. This situation however is unphysical in the sense that if M_b changes B hadron masses should also change accordingly.

Modified PYTHIA setup for technical investigations

It was found that when all b mass parameters used in the generator (see Section 4.5.1) are physically connected the above described behaviour disappears. To prove this, the following modifications of the PYTHIA generator have been made in order to connect the three kinds of masses:

- Connect the two b quark masses (kinematical and constituent) by the simplest assumption of $M_b = M_b^{const}$,

- make all B hadron masses (including already known ones) depend on M_b^{const} through the mass formula of Eq. (4.7),

- make the Peterson fragmentation function depend on M_b^{const} through $\epsilon_b \propto 1/(M_b^{const})^2$.

Figures 4.20 and 4.21 show that now, when M_b is changed, the effects produced at parton level are also observed - almost identically - at hadron level. In such setup of the generator, the hadronization corrections to be applied to the $R_3^{b\ell}$ observable would remain basically constant [8].

From this exercise we conclude that a coherent picture within the generator is obtained when the mass parameter values are connected. The next step is to find the value to be used for the b quark mass M_b in the standard generator (where the mass parameters are not connected) and the uncertainty associated to it.

4.5.3 Identifying the kinematical mass M_b in PYTHIA with the pole mass in NLO ME calculations

The NLO analytical calculations [9,14] used to interpret the $R_3^{b\ell}$ measurements in terms of a b quark mass at the scale of M_Z are not expressed in terms of the mass parameters described in Section 4.5.1 for PYTHIA. They use instead either running or pole mass definitions which are directly derived from the QCD Lagrangian. The first step is to find out how precisely M_b, the kinematical b quark mass parameter used in the perturbative part of the PYTHIA treatment, can be identified, in a quantitative sense (for the $R_3^{b\ell}$ observable), with one of these two definitions: the pole mass [9].

To check this identification we should use the theoretically most precise ME calculations [9,14] to compute $R_3^{b\ell}$ and compare with the PYTHIA prediction. If consistency is found, then the values of the mass parameter used in PYTHIA and of that used in the ME calculation should be very close (i.e. within the theoretical uncertainty of the ME calculation used). The NLO ME calculations [9, 14] are available for $R_3^{b\ell}$ using both the running and pole mass definitions. Either definition can be used as long as the corresponding theoretical uncertainties are estimated and propagated to the result. Here we choose to use the running mass definition.

We then fit the prediction from PYTHIA (using its default value $M_b = 5$ GeV/c^2) to the NLO prediction to extract a value for the running mass $m_b(M_Z)$, following the procedure described in Section 1.5.5, i.e. by taking the average of the results obtained by the two possible ways to get to $m_b(M_Z)$. The uncertainty on the extracted $m_b(M_Z)$ will have then contributions coming from the statistics of the generated sample and the theoretical uncertainty of the NLO calculations (scale and mass ambiguity) described also in 1.5.5.

Then we have two equivalent possibilities to do the comparison:

1. The value of $m_b(M_Z)$ obtained can be re-expressed in terms of a pole mass using perturbative QCD, and compared directly to $M_b = 5$ GeV/c^2 used in PYTHIA.

[8]Particle decays have been turned off for this exercise since, for small values of M_b, the computed B hadron masses are too low and problems appear in the decay processes. It has been checked that the same behaviour is observed when particles are allowed to decay for variations of M_b above 4 GeV/c^2.

[9]The pole mass is chosen here because it seems a priori more closely related to the kinematical mass parameter in PYTHIA than the running mass.

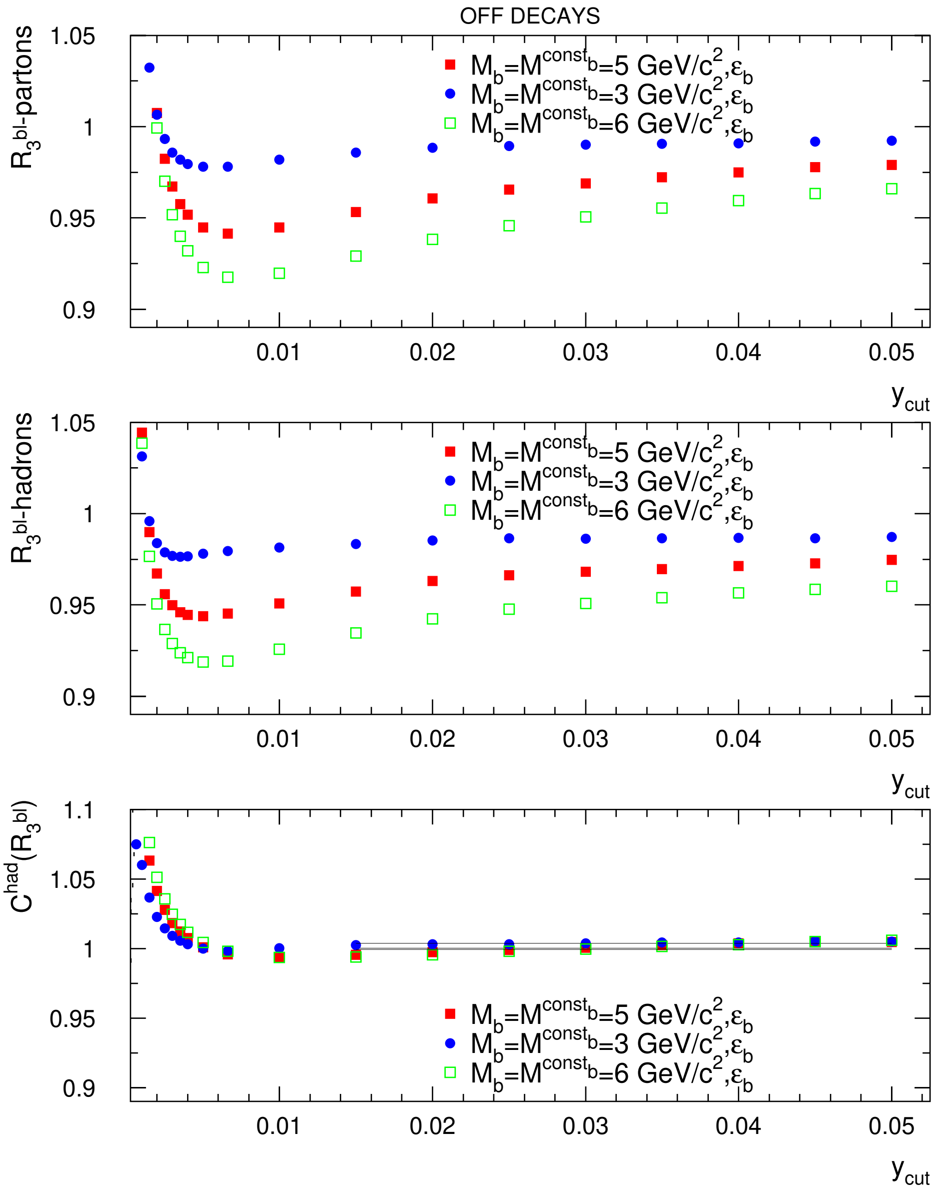

Figure 4.20: $R_3^{b\ell}$ at parton and hadron level and its hadronization correction as a function of y_c for three different values of the of M_b when $M_b = M_b^{const}$, B hadron masses are constructed from M_b^{const} and $\epsilon_b \propto 1/(M_b^{const})^2$.

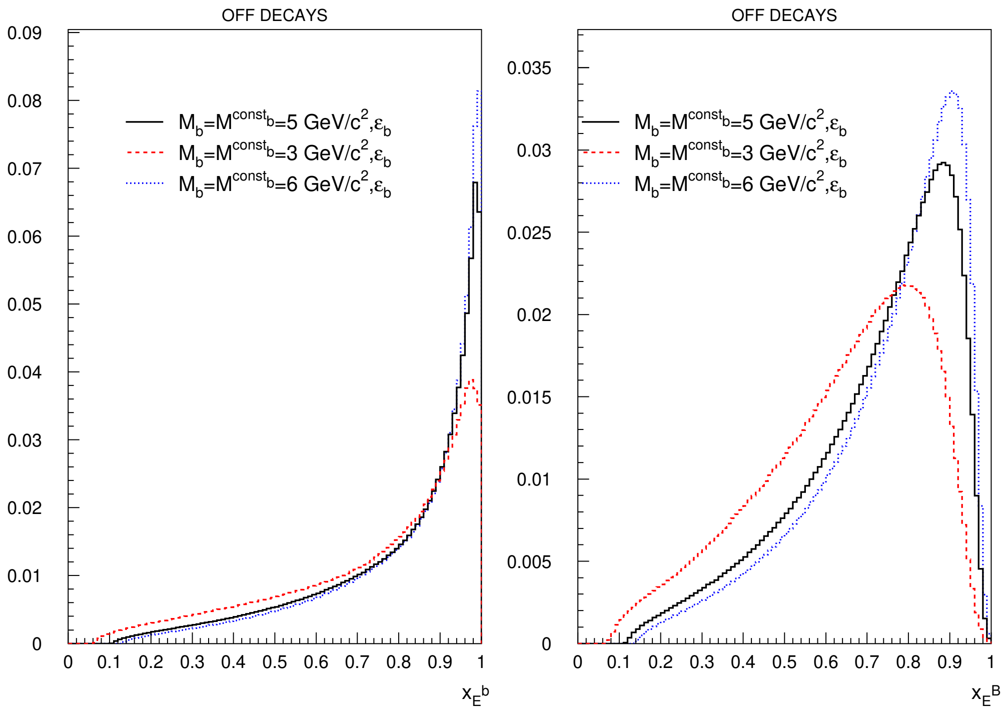

Figure 4.21: b quark scaled energy distribution (left) and B hadron scaled energy distribution (right) for $M_b = 3$, 5 and 6 in PYTHIA.

2. Or else the reverse: the value $M_b = 5$ GeV$/c^2$ used in PYTHIA, assumed to be the pole mass, can be re-expressed in terms of a running mass using perturbative QCD. One obtains $m_b(M_Z) = 3.08$ GeV$/c^2$ [10]. Then this value can be compared directly to the value extracted by fitting the NLO ME calculations to the prediction from PYTHIA.

The results from this comparison (following the second prescription) are shown in table 4.4 for different values of y_c, using DURHAM and CAMBRIDGE jet clustering algorithms. The difference between the PYTHIA and NLO predictions is well within the estimated theoretical errors [11]. This mass difference could in principle be added up as an additional source of uncertainty or else consider that it is already included in the theoretical error estimated in the analysis. We believe the latter option is the correct one, otherwise we would double count the theoretical uncertainty.

We conclude from this comparison that the kinematical mass parameter M_b in PYTHIA can be identified with the pole mass used in fixed order NLO calculations within the precision of the NLO calculations expressed in terms of the running mass. This argument is however presumably not general and can only be applied to the $R_3^{b\ell}$ observable.

[10] In order to go from the pole mass to the running mass at the M_b scale the 2-loop expression was used and to evolve the running mass from M_b to M_Z the 3-loop RGE was used. The value of $\alpha_s(M_Z) = 0.1183 \pm 0.0027$ obtained in Ref. [113] was taken.

[11] The contribution of the statistical uncertainty of the predicted $R_3^{b\ell}$ to the total error on the extracted $m_b(M_Z)$ is negligible.

y_c (DURHAM)	$R_3^{b\ell}$	$m_b(M_Z)$ (GeV/c^2)	$\Delta_{m_b(M_Z)}$ (GeV/c^2)
0.015	0.9539 ± 0.0004	3.28 ± 0.27	0.20 ± 0.27
0.02	0.9611 ± 0.0005	3.13 ± 0.29	0.05 ± 0.29
0.025	0.9667 ± 0.0005	3.00 ± 0.29	-0.08 ± 0.29
0.03	0.9711 ± 0.0006	2.89 ± 0.29	-0.19 ± 0.29
y_c (CAMBRIDGE)	$R_3^{b\ell}$	$m_b(M_Z)$ (GeV/c^2)	$\Delta_{m_b(M_Z)}$ (GeV/c^2)
0.005	0.9578 ± 0.0004	3.00 ± 0.13	-0.08 ± 0.13
0.007	0.9567 ± 0.0004	3.10 ± 0.04	0.02 ± 0.04
0.01	0.9601 ± 0.0004	3.12 ± 0.09	0.04 ± 0.09
0.015	0.9667 ± 0.0005	3.01 ± 0.16	-0.07 ± 0.16

Table 4.4: Extracted values of $m_b(M_Z)$ obtained for DURHAM and CAMBRIDGE at different values of y_c taking the $R_3^{b\ell}$ predicted by PYTHIA as input. The differences between the values obtained and the mass set in PYTHIA, which corresponds to $m_b(M_Z) = 3.08$ GeV/c^2, are also written.

4.5.4 Determining the value of the kinematical mass M_b in PYTHIA

As was shown in the previous section the kinematical mass M_b in PYTHIA can be identified with the pole mass used in NLO calculations of $R_3^{b\ell}$. Hence one could use directly the pole mass value determined from the low energy data.

However, one potential drawback is that the b physics involved when considering mass effects in inclusive [12] observables such as $R_3^{b\ell}$ is not exactly the same as that relevant to the exclusive analyses of specific B hadrons which are used to extract values of the pole mass near the production threshold. In particular the detailed mixture of bound hadrons and the fraction of excited states are different, and moreover not entirely known experimentally.

For this reason we have investigated an alternative method to determine the kinematical mass M_b in PYTHIA, based on the LEP data itself. As was shown in Section 4.5.2, the only way to see effects at hadron level which can be compared to data upon varying M_b is to use the modified setup of the generator described in Section 4.5.2, where a connection was established between M_b and the constituent mass M_b^{const}, and where the latter was used to compute all B hadron masses. This modified setup could be used to tune M_b based on the data and the result would be meaningful as long as the connection assumed could be justified. As a first approximation we have used $M_b = M_b^{const}$, although in principle a more complicated relation could also be considered.

As already mentioned, the constituent mass is not well defined in QCD. However, it does predict (phenomenologically) masses for all B hadrons. On the contrary, in Heavy Quark Effective Theory (HQET) mass parameters are well defined but, at present, it can describe only a subset of the B hadron masses. Having all this in mind, our proposed strategy is the following:

1. establish the relation between the pole mass M_b used in HQET - which we can identify with the kinematical mass parameter M_b in PYTHIA - and the constituent mass M_b^{const},

[12] By inclusive here we mean that all B hadrons are used to calculate the observable.

such that both predict the same B hadron masses for the subset where this comparison can be done,

2. extract the value of M_b^{const} which best describes our data using observables which are independent from (or at least only weakly correlated with) $R_3^{b\ell}$,

3. consider the uncertainties inherent to the use of HQET and those derived from the fit as the error on the determined M_b parameter.

In order to quantify the uncertainty from considering the pole mass as the constituent mass in the mass formula to determine all B hadron masses, we use HQET to relate the masses of the $B = \bar{b}q$ ($q = u, d, s$) mesons, m_B, with the b quark pole mass, M_b:

$$m_B = M_b + \overline{\Lambda} + \mathcal{O}(1/M_b) \tag{4.8}$$

where $\overline{\Lambda}$ is the binding energy at LO in the $1/M_b$ expansion (see Section 1.5.2). The CLEO Collaboration has measured this binding energy [114] [13]:

$$\overline{\Lambda} = 350 \pm 122 \text{ MeV}/c^2 \tag{4.9}$$

If the measured mass of $B^{\pm}$ and B^0 mesons, $m_B = 5.279$ GeV/c^2, is used to derive the constituent and pole masses needed to describe the measured data through the mass formula of Eq. (4.7) and through the HQET relation of Eq. (4.8), the values found are:

$$\begin{aligned} M_b^{const} &= 4.99 \text{ GeV}/c^2 \\ M_b &= 4.93 \pm 0.12 \text{ GeV}/c^2 \end{aligned} \tag{4.10}$$

The difference between the two masses is 60±122 MeV/c^2, so 0.12 GeV/c^2 is the error made when the assumption of $M_b = M_b^{const}$ is applied and the mass formula is used to derive B hadron masses instead of HQET.

Next we need to find an observable sensitive to the variation of M_b in the modified setup of the generator so that by fitting to the measured data the M_b parameter of PYTHIA can be determined. As shown in figures 4.20 and 4.21 the $R_3^{b\ell}$ and the x_E^b observables are examples of such observables. For this tuning, we use instead the y_{32} distribution of b over ℓ events normalized to the total number of b and ℓ events, $R^{b\ell}(y_{32})$, where y_{32} is the y_c transition value in which a three-jet event becomes a two-jet one:

$$R^{b\ell}(y_{32}) = \frac{N^b(y_{32})/N^b}{N^\ell(y_{32})/N^\ell} \tag{4.11}$$

The two jet clustering algorithms, DURHAM and CAMBRIDGE, were used to form jets.

The $R^{b\ell}(y_{32})$ distribution has been measured at hadron level for both jet algorithms by correcting for detector effects bin by bin (12 bins were taken between 0 and 0.06).

[13] The latest determinations of $\overline{\Lambda}$ performed by CLEO and DELPHI, not yet published, lead to compatible results: $\overline{\Lambda} = 0.39 \pm 0.03$ (stat) ± 0.06 (syst) ± 0.12 (theo) GeV/c^2 [115] and $\overline{\Lambda} = 0.40 \pm 0.10$ (fit) ± 0.02 (syst) GeV/c^2 [116].

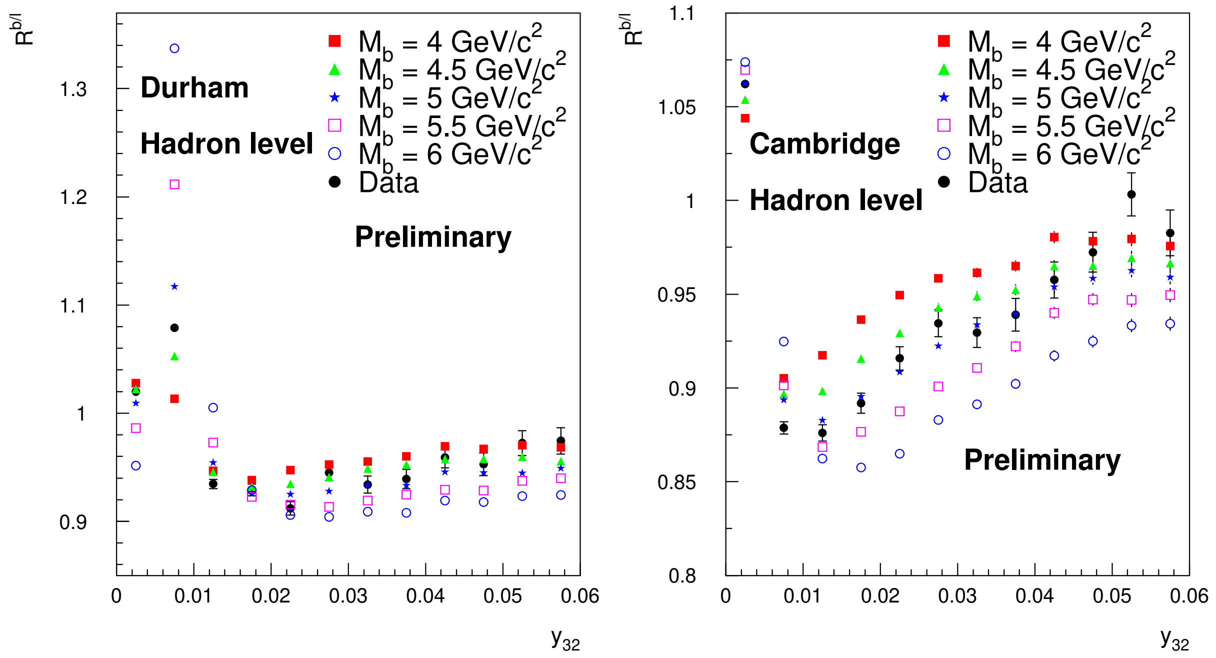

Figure 4.22: The $R^{b\ell}(y_{32})$ observable measured at hadron level and the PYTHIA prediction for different values of the b mass (M_b = 4, 4.5, 5, 5.5 and 6 GeV/c^2) when DURHAM (left) and CAMBRIDGE (right) are used for jet reconstruction.

From the measured $R^{b\ell-det}(y_{32})$ distribution at detector level, the hadron level distribution, $R^{b\ell-hadron}(y_{32})$, was extracted by,

$$R^{b\ell-hadron}(y_{32}) = R^{b\ell-det}(y_{32})C^{det}(y_{32}), \qquad C^{det}(y_{32}) = \frac{R_{MC}^{b\ell-hadron}(y_{32})}{R_{MC}^{b\ell-det}(y_{32})} \tag{4.12}$$

The DELPHI simulation program, DELSIM, described in Section 2.3, was used to obtain the detector correction for each y_{32} bin, $C^{det}(y_{32})$.

The measured distributions for DURHAM and CAMBRIDGE can be seen in figure 4.22, where only statistical errors have been considered. The PYTHIA prediction for this observable at hadron level [14] is also shown for different values of the b mass (M_b = 4, 4.5, 5, 5.5 and 6 GeV/c^2).

For each jet algorithm, a polynomial interpolation was performed to obtain the value of M_b in PYTHIA that reproduces the data for each y_{32} bin, in the region $y_{32} \geq 0.02$ for DURHAM and $y_{32} \geq 0.01$ for CAMBRIDGE [15]. Figure 4.23 shows the M_b values obtained for DURHAM and CAMBRIDGE for each y_{32} bin together with the average result (when relevant) [16].

[14] Here hadron level means including the decays of all particles since the Monte Carlo is compared with the measured data.

[15] The low y_{32} region is dominated by four jets and furthermore, since the distribution varies very rapidly, the result obtained for M_b is more sensitive to the binning. For this reason it was decided not to use this region, although the sensitivity to M_b is larger on some of these bins.

[16] The correlation coefficient ρ was determined for each y_{32} bin by generating with PYTHIA 95 samples

The weighted mean of all bin results was found to be, $M_b = 4.72 \pm 0.12$ GeV/c^2 for DURHAM and $M_b = 4.93 \pm 0.07$ GeV/c^2 for CAMBRIDGE.

Taking into account the uncertainty associated with the identification of the pole mass with the constituent mass in PYTHIA, the b mass parameter of PYTHIA is determined to be,

$$M_b = 4.93 \pm 0.07 \text{ (stat)} \pm 0.12 \text{ (theo) GeV}/c^2 \tag{4.13}$$

which corresponds to the result obtained with CAMBRIDGE, due to its higher precision.

4.5.5 Possibilities to set the kinematical mass M_b in PYTHIA

From all that has been discussed above, there are different possibilities to set the M_b parameter in the standard version of PYTHIA (in which B hadron masses are hardcoded and disconnected from M_b) to assure a reliable hadronization correction for the $R_3^{b\ell}$ observable. We consider them to be:

- As shown in Section 4.5.3, the M_b parameter can be identified with the pole mass within the uncertainty of the NLO matrix element calculations. Therefore, one possibility would be to take the value of M_b from measurements of the pole mass performed at threshold. We could then take the result obtained in [74]:

$$M_b = 4.98 \pm 0.13 \text{ GeV}/c^2 \tag{4.14}$$

  which, compared with other determinations, has a rather conservative error associated.

- Another possibility would be to take directly the pole mass extracted from our fit to the measured $R^{b\ell}(y_{32})$ at hadron level:

$$M_b = 4.93 \pm 0.14 \text{ GeV}/c^2 \tag{4.15}$$

- The last possibility is based on the fact that the mass extracted from our fit, i.e. 4.93 GeV/c^2, is 60 MeV smaller than the constituent mass reproducing the B meson masses through the mass formula (see Eq. 4.11), although both are compatible within errors. It could be justified to consider the range between these two masses as an uncertainty, since in each case the PYTHIA generator describes some aspect of the data better. Therefore, the mean between these masses could be used:

$$M_b = 4.96 \pm 0.14 \text{ GeV}/c^2 \tag{4.16}$$

The three possibilities listed above are compatible within the quoted errors. Among the three results, the one obtained by an independent determination of the pole mass has been chosen, i.e. $M_b = 4.98 \pm 0.13$ GeV/c^2, since it has the smallest correlation with our measurement of $R_3^{b\ell}$.

The total b mass parameter ambiguity of PYTHIA of 0.13 GeV/c^2 is propagated to the hadronization correction of $R_3^{b\ell}$. Figure 4.24 shows this uncertainty as a function of y_c for the two jet finder algorithms. As an example, the mass uncertainty is around 3.5‰ at a y_c = 0.02 and 0.01 for DURHAM and CAMBRIDGE respectively.

of 250,000 b and ℓ events and calculating for each of them the $R^{b\ell}(y_{32})$ observable at hadron level for the DURHAM and CAMBRIDGE algorithms. The values obtained for the ρ coefficients varied between 0.2 and 0.5 depending on the y_{32} bin considered.

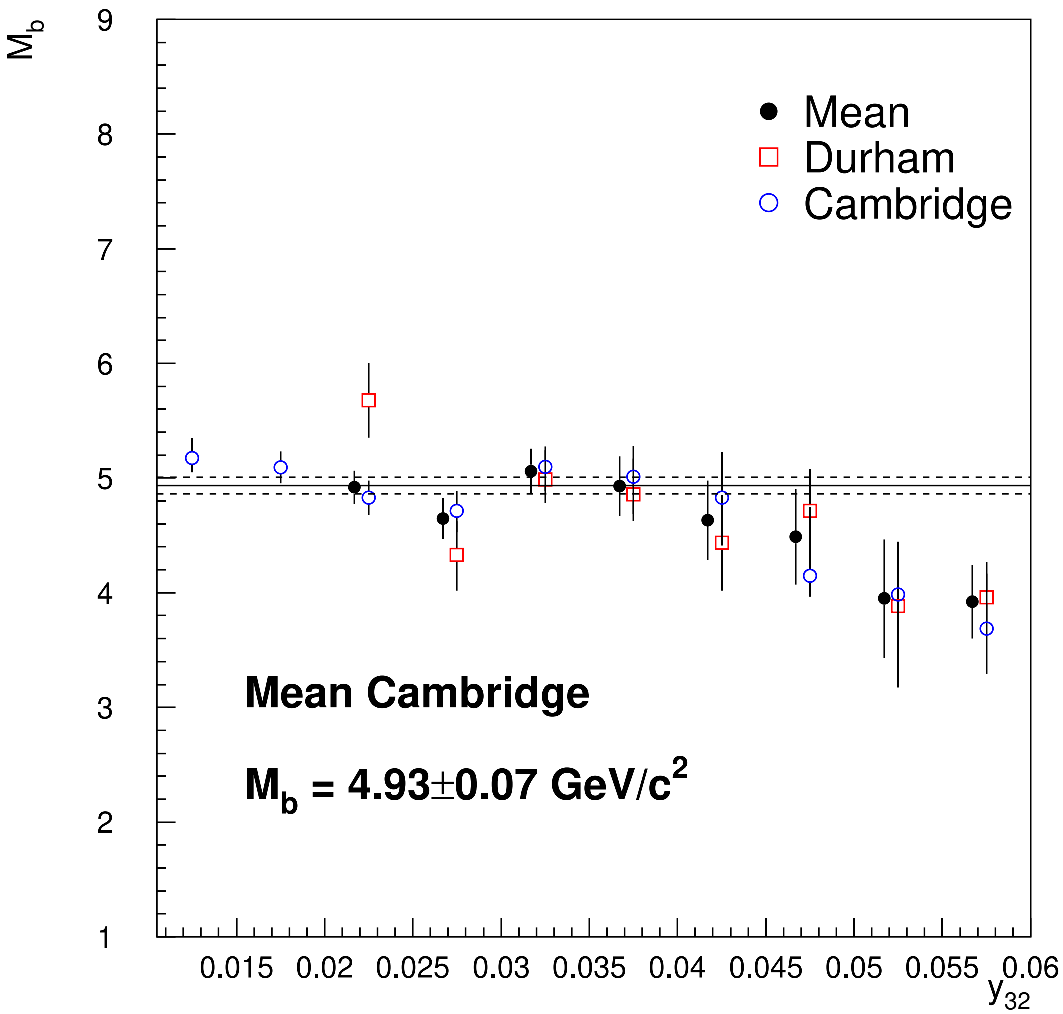

Figure 4.23: The fitted M_b values obtained for the Durham and Cambridge jet clustering algorithms for each bin y_{32}. The average of the two algorithms is also shown for those bins in which a mass has been extracted for both algorithms (for clarity reasons, this mean is shifted). The horizontal full line represents the mean of all bins for Cambridge and the dashed ones correspond to its statistical error.

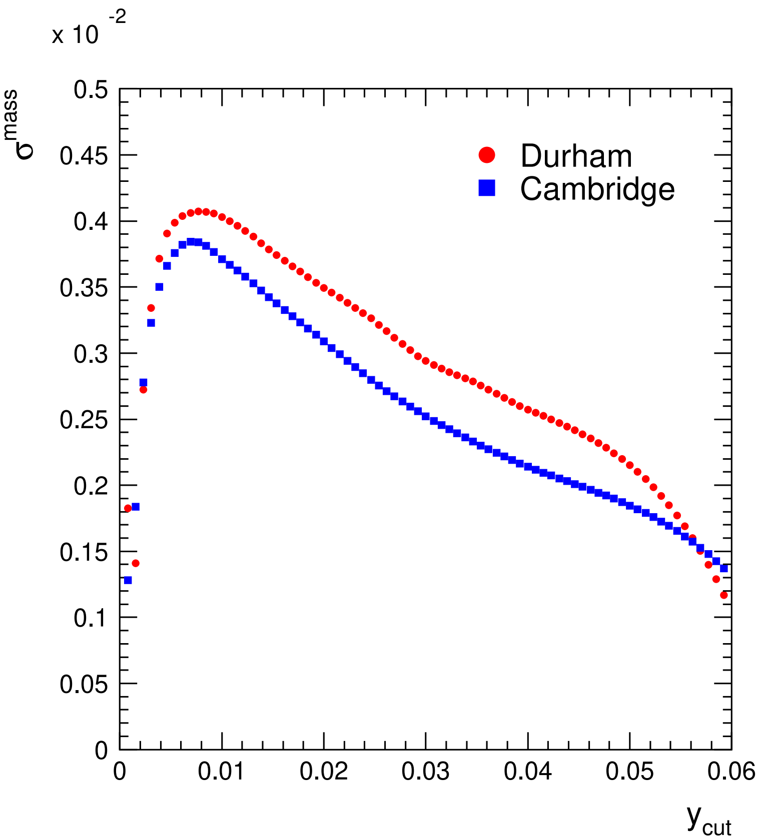

Figure 4.24: Mass uncertainty of the hadronization correction of $R_3^{b\ell}$ for Durham and Cambridge jet clustering algorithms.

4.6 Summary

During this chapter the hadronization correction of the $R_3^{b\ell}$ has been computed by using the QCD generators Pythia and Herwig with the Delphi tuned parameters. This correction is essential in order to compare the measured observable at hadron level with the theoretical predictions performed at parton level and extract a value for the b quark mass.

The prediction given by both generators for our observable at the different stages of the process, i.e. after the parton shower, after the hadronization process and after particle decays, has been calculated for the different y_c values. At the y_c values of interest for this analysis, which are around $y_c = 0.02$ for Durham and $y_c = 0.01$ for Cambridge, it was found that the fragmentation process makes $R_3^{b\ell}$ increase while the decays make it decrease. For Pythia the effect produced by particle decays on $R_3^{b\ell}$ is larger than that produced by fragmentation and therefore the total hadronization correction to be applied to the measured observable is larger than unity. For Herwig the effect produced by the hadronization process is larger than with Pythia, being similar to that produced by particle decays for the case of Cambridge (and therefore the total correction ~ 1) and even larger for Durham (and thus the total correction < 1).

Different sources of uncertainties affecting the hadronization correction have also been studied:

- Model: Half of the difference between the hadronization correction given by the two generators was computed and found to be ± 0.006 for Durham at $y_c = 0.02$ and ± 0.007 for Cambridge at $y_c = 0.01$, which represented the dominant contribution to the total error on $R_3^{b\ell}$. Therefore, a method to reduce this source of uncertainty was developed based on the study of the b fragmentation function. For b events, a cut on the b jet scaled energy, $x_E^b(\text{jet}) \geq 0.55$, was applied to be in a region of phase space in which the hadronization corrections given by both generators were similar.

  The hadronization model uncertainty was evaluated in this restricted region of phase space as the standard deviation of the hadronization correction predicted by Herwig and that given by Pythia with two different fragmentation functions, Peterson and Bowler. The result was about ± 0.003 for Durham and Cambridge at a $y_c = 0.02$ and 0.01 respectively.

  The contribution of the difference on the decay models of both generators was also studied and it was found to be negligible for the region of interest y_c values.

- Tuning: The Pythia tuned parameters relevant in the fragmentation process were varied within their uncertainty and the impact on the hadronization correction was evaluated taking into account correlations among them. The total tuning uncertainty is of 1.5‰ for Durham and 1‰ for Cambridge at a y_c of 0.02 and 0.01 respectively.

- b mass parameter: A detailed study on the way the so-called kinematical b quark mass of Pythia was entering in the parton shower and in the hadronization process of the generator was done. The unphysical dependence of the hadronization correction with this parameter was understood as a consequence of the disconnection between hadron masses and quark masses in the generator. If this connection is forced the dependence disappears.

A comparison of the parton shower prediction for $R_3^{b\ell}$ with that given by the NLO calculations of [9, 14] allowed to identify the kinematical b quark mass of PYTHIA with the pole mass definition. This parameter was then set to $M_b = 4.98 \pm 0.13$ GeV/c^2 [74] in the generator and it translated into an ambiguity of around 3.5‰ in the hadronization correction, at a $y_c = 0.02$ and 0.01 for DURHAM and CAMBRIDGE respectively.

As a cross check, the kinematical b mass parameter was obtained by making use of the modified version of the generator in which all b masses are connected. The value of M_b reproducing the measured $R^{b\ell}(y_{32})$ observable at hadron level was found to be $M_b = 4.93 \pm 0.14$ GeV/c^2, which is compatible with independent measurements of the pole mass.

The total hadronization correction uncertainty is of about 5‰ at $y_c = 0.02$ and 0.01 for DURHAM and CAMBRIDGE respectively and the dominant contribution comes from the ambiguity on the b mass parameter of the generator.

Chapter 5

Data analysis

Data collected by the DELPHI detector from 1994 until 2000 at the Z^0 peak was analysed in order to measure the $R_3^{b\ell}$ observable. The first step was to select the sample of Z^0 hadronic decays, i.e. $Z^0 \to q\overline{q}$ events. From those events, the b and ℓ quark initiated events were separated using the DELPHI tagging method.

For the case of the b tagged sample, as explained in Section 4.3, the hadronization process is better controled if a cut on the b quark jet energies is done. Therefore, a method to distinguish the b quark jets from the gluon jet was used based on the tagging of the quark flavour.

The jet clustering algorithms DURHAM and CAMBRIDGE were applied to obtain the $R_3^{b\ell}$ observable at detector level (or reconstruction level). Data was corrected for detector and tagging effects and the hadronization process to bring the observable to parton level, where the NLO theoretical calculations were performed.

Through this chapter, the whole analysis procedure will be described in detail, leading at the end to the $R_3^{b\ell}$ observable at parton level.

5.1 Selection of the data sample

5.1.1 Z^0 hadronic events

The selection of Z^0 hadronic events was done in three steps:

1. Particle selection: Charged and neutral particles reconstructed, respectively, in the tracking devices and in the calorimeters were selected in order to ensure a reliable determination of their momenta and energies.

2. Event selection: based on global event properties, $Z^0 \to q\overline{q}$ events were selected.

3. Kinematic selection: Further kinematical cuts were applied for each event once it was reconstructed to three jets by the given jet clustering algorithm.

Particle selection

For the charged particle selection the same requirements of [5,109,112] were imposed. These are (see table 5.1):

- minimum track momentum, p, of 0.1 GeV/c,
- track polar angle between 25° and 155°,
- measured track length greater than 50 cm,
- track impact parameter with respect to the interaction point, d, smaller than 5 cm in the $R\phi$ plane and smaller than 10 cm in z.

The above cuts force the particles to be within the detector acceptance and to be originated close to the interaction point, they also ensure a good momentum resolution. All charged particles were assumed to be pions in order to measure its energy.

Neutral particles were selected by demanding a minimum energy for the cascade produced by the neutral particle in the calorimeters. The cut is different for each subdetector, HPC, FEMC and HAC. Table 5.1 shows the different cuts applied, which are identical to those used in Ref. [112].

The processes $\gamma \to e^+e^-$ and $\pi^0 \to \gamma\gamma$ were also taken into account. For the case of photon conversions, if the sum of the electron and positron momentum was greater than 600 MeV/c, then they were considered as a single neutral cluster. Neutral cascades produced by two very closed photons were considered as a single π^0 if the energy of the cascade was greater than 6 GeV.

Event selection

A sample of hadronic Z^0 decays was then selected by imposing some global event conditions [109,112],

- at least 5 charged particles,
- the total energy of the charged particles greater than 15 GeV,
- charge conservation, $|\sum_i q_i| \leq 6$,
- no charged particle with momentum greater than 40 GeV/c, so a single particle does not determine completely the thrust axis [1] nor the jet direction,
- the polar angle of the thrust axis, θ_{thrust}, between 45° and 135°, so the event is well contained within the detector volume.

[1]The thrust axis is defined in Appendix A and it gives an estimation of the direction with the highest energy flow in the event.

Charged Particle Selection	$p \geq 0.1$ GeV/c $25° \leq \theta \leq 155°$ L$\geq$ 50 cm $d \leq 5$ cm in $R\phi$ plane $d \leq 10$ cm in z direction	
Neutral Cluster Selection	$E \geq 0.5$ GeV, $40° \leq \theta \leq 140°$ $E \geq 0.5$ GeV, $8°(144°) \leq \theta \leq 36°(172°)$ $E \geq 1$ GeV, $10° \leq \theta \leq 170°$	HPC FEMC HAC
Event Selection	$N_{ch} \geq 5$ $E_{ch} \geq 15$ GeV $\lvert\sum_i q_i\rvert \leq 6,\ i = 1, ..., N_{ch}$ No charged particle with $p \geq 40$ GeV/c $45° \leq \theta_{thrust} \leq 135°$	

Table 5.1: Particle and hadronic event selection; p is the particle momentum, θ the particle (and θ_{thrust} the *thrust*) polar angle with respect to the beam axis, L the measured track length, d the closest distance to the interaction point, q_i the particle charge, E the cluster energy, N_{ch} the number of charged particles, and E_{ch} the total charged particle energy in the event.

The efficiency of hadronic events was evaluated using the DELSIM simulated data (see Section 2.3) and it was found to be around 63%. Table 5.2 shows the efficiency of each cut by itself and the cumulative efficiency after each cut applied to select the hadronic sample. The main background was coming from $Z^0 \to \tau^+\tau^-$ [2], which contributes to around 0.1% of the selected hadronic events, and $e^+e^- \to e^+e^-q\overline{q}$ [3], which is just $\sim 0.01\%$ [112].

Figure 5.1 shows the comparison between the real and simulated data for the distributions of some of the variables used to select the hadronic sample for the selected events.

Phase	Cut	$\epsilon_{cut}(\%)$	$\epsilon_{cum}(\%)$
Hadronic Selection	N_{ch}	97.89	97.89
	E_{ch}	91.92	91.84
	$\lvert\sum_i q_i\rvert$	99.69	91.54
	p_i^{max}	98.69	90.25
	θ_{thrust}	64.05	62.68

Table 5.2: Efficiencies of the global event cuts applied to select the hadronic sample.

[2]The $Z^0 \to \tau^+\tau^-$ events are typically two jet like events containing particles with large momentum. The requirement of at least 5 charged particles suppresses this kind of events and, in general, all leptonic events.

[3]The so-called two photon events, $e^+e^- \to e^+e^-q\overline{q}$, are characterized by a hadronic system with low energy, which furthermore is concentrated on the low angle region. Therefore, the cuts on the charged energy and on θ_{thrust} give the main suppression of this kind of events.

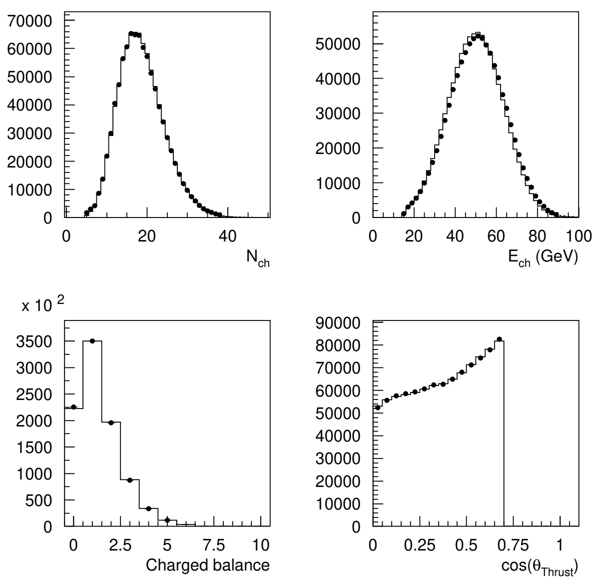

Figure 5.1: Data/MC agreement for the distributions of N_{ch}, E_{ch}, $|\sum_i q_i|$ and $\cos\theta_{thrust}$ for the events collected in 1994 passing the hadronic selection of table 5.2.

Kinematic selection

In order to reduce particle losses and wrong energy-momentum assignment to jets in the selected hadronic events, further kinematical cuts were applied. Each event was reconstructed to three jets by the jet clustering algorithm (Durham or Cambridge) [4], using all charged and neutral selected particles, and the cuts of table 5.3 were applied to each of them,

- minimum visible energy for each jet of 1 GeV,
- at least 1 charged particle per jet,
- each jet had to be well contained within the detector volume, i.e. $25° \leq \theta_j \leq 155°$,
- the sum of the angles between jets projected in the event plane greater than 359°.

The efficiency of each of these cuts is shown in table 5.4 for the Cambridge algorithm, together with the cumulative efficiency after each cut. For those events passing the above cuts, the comparison between the real and simulated data for the jet charged multiplicity, $\cos\theta_j$, jet energies and angles between jets distributions is shown in figures 5.3 for the case of Durham.

[4]For the case of Cambridge, when it was not possible to reconstruct the event to three jets, Durham was used instead.

Kinematic Selection	$N_j^{ch} \geq 1$ per jet $E_j \geq 1$ GeV, $j = 1,2,3$ $25^\circ \leq \theta_j \leq 155^\circ$, $j = 1,2,3$ Planarity cut: $\sum_{ij} \phi_{ij} \geq 359^\circ$, $i < j$, $i,j = 1,2,3$

Table 5.3: Event selection based on the kinematic properties of the events when clustered in three jets by the jet algorithm. N_j^{ch} is the jet charged multiplicity, E_j the jet energy, θ_j the jet polar angle and ϕ_{ij} the angular separation between the pair of jets ij.

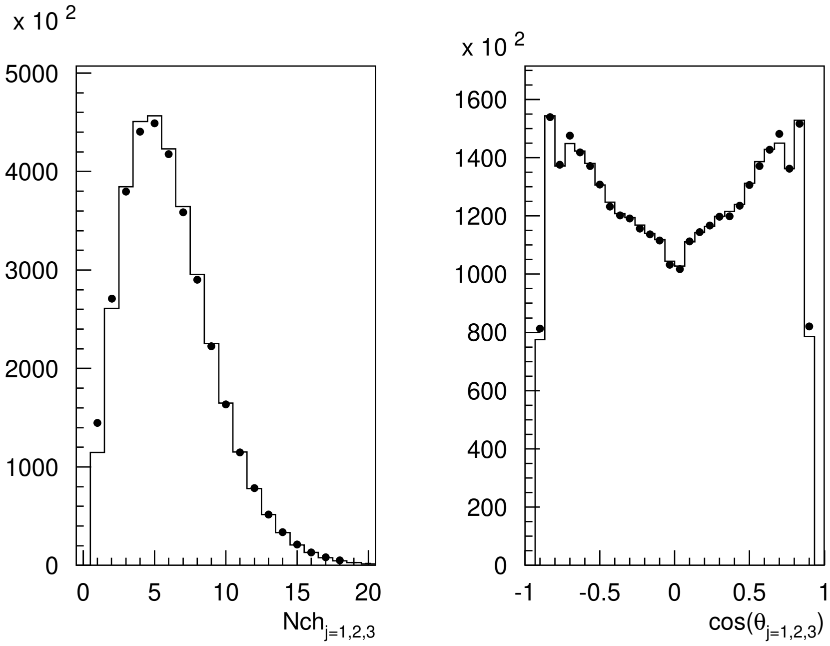

Figure 5.2: Data/MC agreement for the distributions of N_j^{ch} and $\cos\theta_j$ for jets reconstructed with DURHAM for those events passing the cuts of table 5.3.

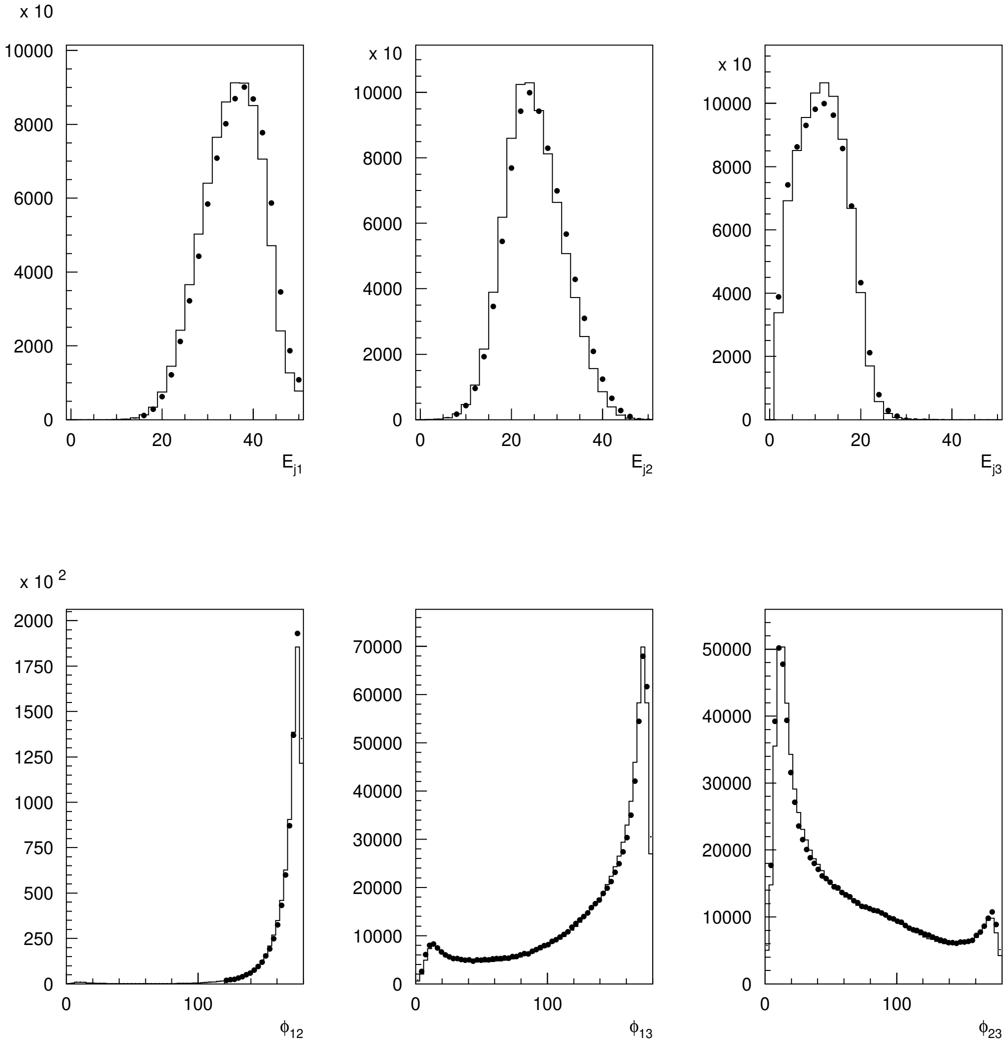

Figure 5.3: Data/MC agreement for the distributions of the jet energies and angles between jets for those events passing the cuts of table 5.3 when DURHAM is used for jet clustering. Jets are ordered in decreasing order of reconstructed energy.

Phase	Cut	Cambridge	
		$\epsilon_{cut}(\%)$	$\epsilon_{cum}(\%)$
kinematic selection	E_j	98.18	62.22
	N_j^{ch}	92.32	59.61
	$\sum_{ij}\phi_{ij}$	90.87	56.37
	θ_j	85.90	55.14

Table 5.4: Efficiencies for the kinematical cuts applied to the events forced to three jets by CAMBRIDGE. The cumulative efficiencies are also shown.

Year	Durham	Cambridge
1994	817,421	772,251
1995	397,785	375,658
1997	26,617	25,200
1998	41,359	39,009
1999	68,778	64,847
2000	52,794	49,931
Total	1,404,754	1,326,896

Table 5.5: Number of hadronic Z^0 decays selected for the data collected at the different years.

After applying all the cuts mentioned above to the data collected from 1994 to 2000 by DELPHI, a sample of 1.4×10^6 (1.3×10^6) hadronic Z^0 decays was selected for the DURHAM (CAMBRIDGE) algorithm. Most of the events correspond to the data collected during the years 1994 and 1995 of the LEP1 period, the calibrations runs produced during the LEP2 stage contribute with 13.5% of the events. Table 5.5 shows the number of selected events for each year.

5.1.2 Flavour tagging

Once the sample of Z^0 hadronic decays was selected, a method to distinguish between the b quark and $\ell \equiv uds$ quark events had to be used. The flavour of the event is considered as that of the quarks coupled to the Z^0, which is the same definition used in the theoretical calculations of the $R_3^{b\ell}$ observable described in Section 1.5.5.

DELPHI has developed two different algorithms for b tagging, the impact parameter and the combined. The tagging of ℓ quark events is accomplished by anti-b tagging. The tagging methods are based on the properties of B hadrons that make them different to other particles. For example, B hadrons have a long lifetime, large mass, high decay multiplicity and leptonic branching rate, where the leptons produced have a tail at large transverse momentum. A brief description of the two methods will be done below, much more detailed descriptions can be found in Ref. [117] and Ref. [118] for the first and second technique respectively and in Ref. [119] for both of them.

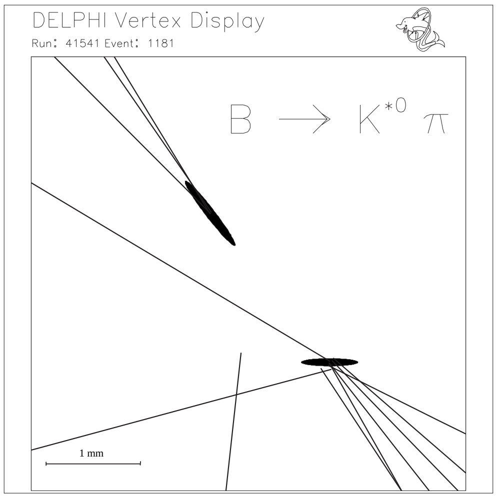

Figure 5.4: Reconstruction of the $B \to K^{*0}\pi$ decay vertex with the DELPHI silicon vertex detector.

- **Impact Parameter (IP)**:

  This technique makes use of the most important property for the selection of B hadrons, their long lifetime, which is around 1.6 ps. This means that a 35 GeV hadron will fly about 3 mm before it decays. Therefore the decay tracks are displaced from the interaction point a distance which can be observed with the DELPHI silicon vertex detector described in 2.2.1 (see figure 5.4).

  A single quantity is then measured for each track, its impact parameter, d. This is defined, in a 3-dimensional space, as the minimal distance between the interaction point (primary vertex) and the track trajectory. Since the DELPHI detector measures the track trajectory in $R\phi$ and Rz planes independently, it is more convenient to separate the 3-dimensional information into the $R\phi$ and Rz components, $d_{R\phi}$ and d_{Rz}. The parameter $d_{R\phi}$ is defined as the minimal distance between the primary vertex and the track trajectory projected on the plane perpendicular to the beam direction. The point of the closest approach (P_C) of the track in the $R\phi$ plane is used to define d_{Rz} as the difference between the z-coordinates of the primary vertex and of the point P_C (see figure 5.5).

  In order to calculate the impact parameter of each track it is necessary to find first the parameters defining the track trajectory, by making a fit, and the position of the primary vertex, which is obtained by fitting a set of selected tracks of the event to a common vertex.

  The so-called track significance is defined as $S = d/\sigma$, where σ is the error on the impact parameter determination. The sign of the track impact parameter (and consequently of its significance) is defined as positive if the vector joining the primary vertex and the point of closest approach of the track lies in the same direction as the jet to which the track belongs, i.e. the angle formed by this vector and the vector defining the jet

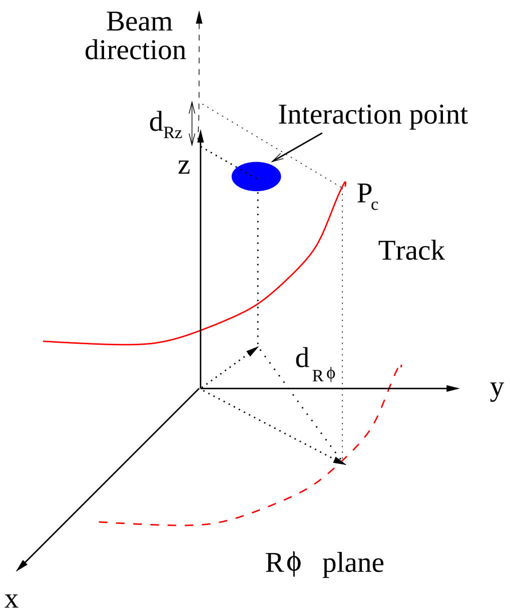

Figure 5.5: Schematic view of the projection of a track in the plane perpendicular to the beam direction and the definition of the impact parameters.

is smaller than $\pi/2$ [5]. Therefore, tracks from B hadron decays have predominantly positive impact parameters while tracks coming from the primary vertex are equally likely to be positive or negative since their non-zero values come from the inaccurate reconstruction of their trajectories (see figure 5.6 and 5.7).

The distribution of negative track significance, $f(S)$, mainly given by tracks coming from the primary vertex, can be used to build the track probability, $P(S^0)$, i.e. the probability for a track from the interaction point to have a significance with absolute value S^0 or greater. Assuming that for positive significance $P(S^0)$ is the same,

$$P(S^0) = \int_{S^0}^{\infty} f(S)dS \tag{5.1}$$

Therefore, tracks coming from the primary vertex should have a flat distribution of $P(S^0)$ while tracks coming from long-lived particles would peak at low values of $P(S^0)$. The transformation of significance to track probability is called the calibration of the detector resolution. This calibration can be done independently for the real and simulated data.

The lifetime probability for any group of N tracks is defined as,

$$P_N = \Pi \sum_{j=0}^{N_{R\phi}+N_{Rz}-1} \frac{(-\log \Pi)^j}{j!}; \quad \Pi = \prod_{i=1}^{N_{R\phi}} P(S^i_{R\phi}) \prod_{i=1}^{N_{Rz}} P(S^i_{Rz}) \tag{5.2}$$

[5]When a secondary vertex (SV) is found the jet direction is defined as the direction from the primary to the secondary vertex.

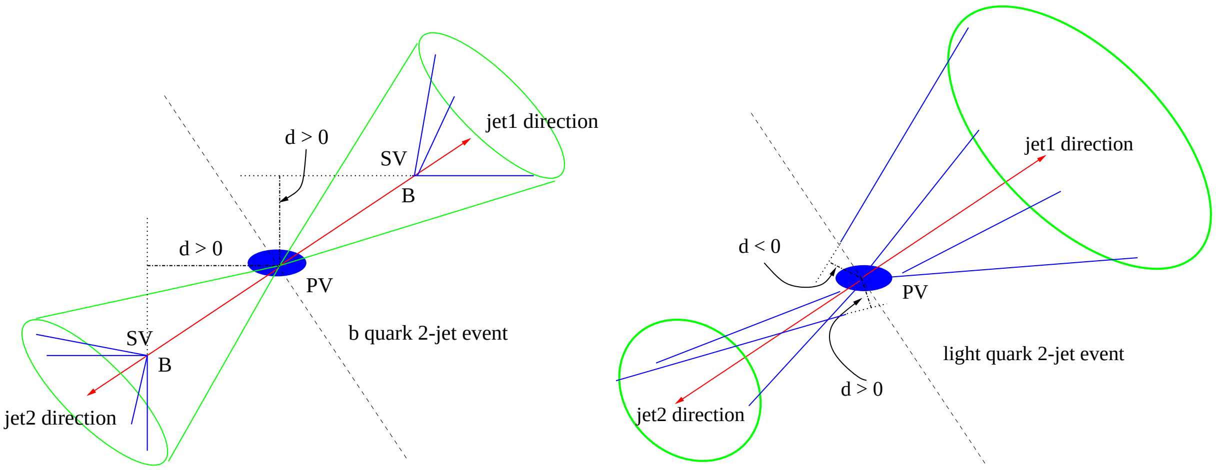

Figure 5.6: Schematic view of the tracks reconstructed in a two-jet b quark event and in a ℓ quark event. In the first case, the tracks coming from the decay of the formed B hadrons are drawn and these all have positive impact parameters. In the other case, tracks are coming from the interaction point and they can have positive or negative impact parameters.

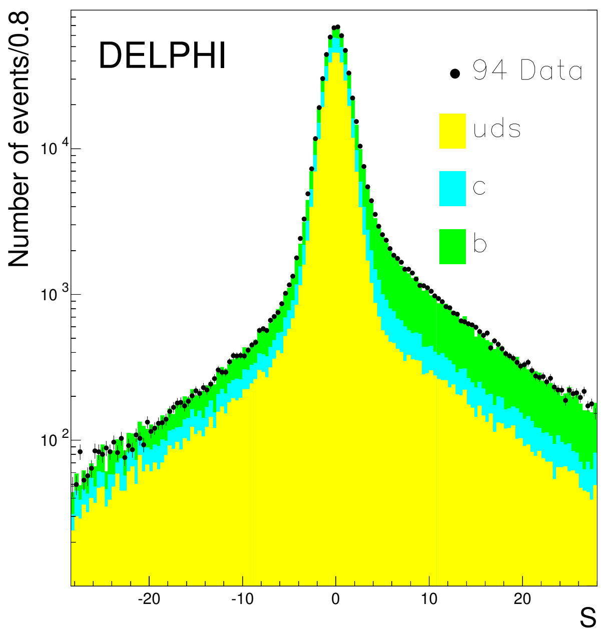

Figure 5.7: Track significance distribution for all hadronic events for real and simulated data from Ref. [120]. For the simulated data the composition of uds, c and b quarks is shown.

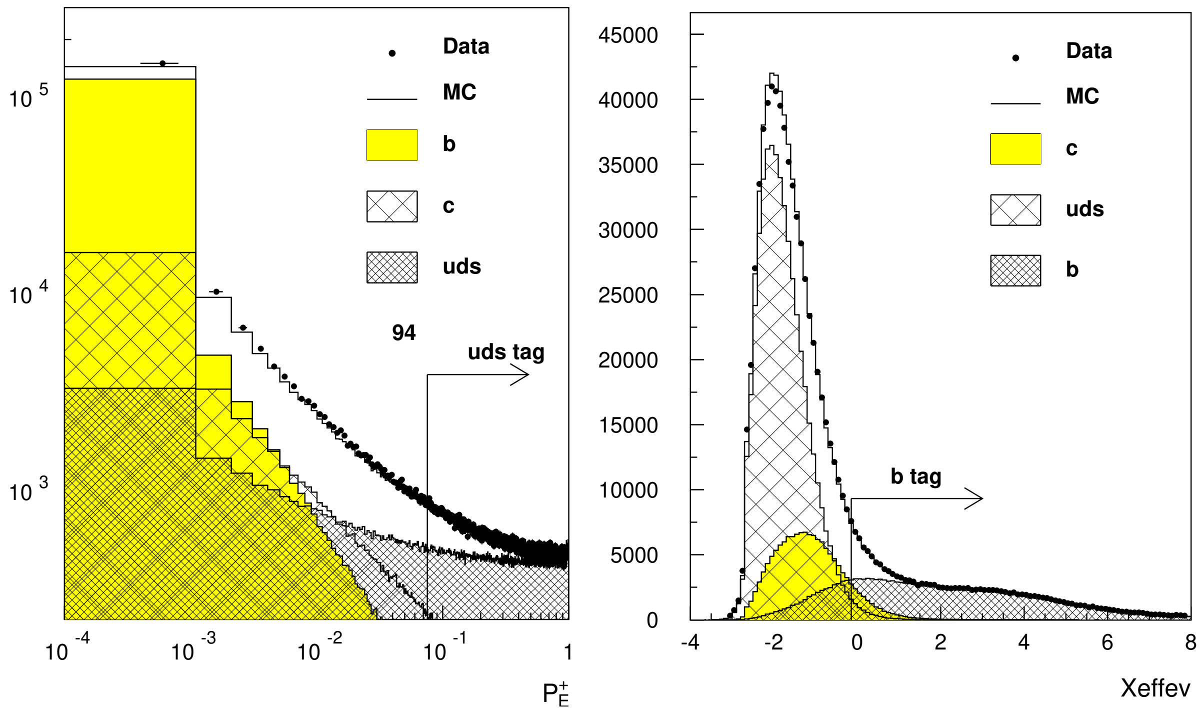

Figure 5.8: Event distribution of P_E^+ (left) X_{effev} (right) when DURHAM is used to form jets. The real (points) and simulated (histogram) data are compared. The specific contribution of each quark flavour is displayed as derived from the DELPHI simulated data. The cuts used to tag the b and ℓ quark sample are also indicated.

where $P(S^i_{R\phi})$ and $P(S^i_{Rz})$ are the track probabilities and $N_{R\phi}$ and N_{Rz} are the number of $R\phi$ and Rz impact parameters used in the tagging. It gives the probability for a group of N tracks all to be from the primary vertex [121].

The lifetime probability can be defined for any group of tracks as those corresponding to a jet, a hemisphere or the whole event. It has a flat distribution for any group of N uncorrelated tracks coming from the primary vertex and it is shifted to lower values when there are tracks coming from secondary decays.

In order to reduce by half the background, only tracks with positive impact parameters are used for b tagging. The lifetime probability for N tracks with positive impact parameters is called P_N^+. For all tracks of the event it is denoted by P_E^+. Figure 5.8 shows the distribution of P_E^+ obtained for the selected sample of Z^0 hadronic decays in the year 1994. The contribution of each quark flavour is also indicated and it can be seen that b events present a peak at low values of P_E^+ while light quark events present a much flatter distribution.

- **Combined (COMB)**:

  The combined technique is based on a combination of a set of different variables into a unique tagging variable. The likelihood ratio method of variable combination is used to define the combined tagging variable [118, 122],

$$y = \frac{f^B(x_1, ..., x_n)}{f^S(x_1, ..., x_n)} \tag{5.3}$$

where $f^B(x_1, ..., x_n)$ and $f^S(x_1, ..., x_n)$ are the probability density functions of the n discriminating variables $x_1, ..., x_n$ for the background (c and ℓ events) and signal (b events) respectively. If the n variables were completely independent the selection of all events with $y < y_0$ would give the optimal tagging of the signal, i.e. the best background suppression for a given signal efficiency. The value y_0 can be varied to select the desired purity or efficiency.

For the case of independent variables,

$$y = \prod_{i=1}^{n} y_i, \qquad y_i = \frac{f_i^B(x_i)}{f_i^S(x_i)} \tag{5.4}$$

being $f_i^B(x_i)$ and $f_i^S(x_i)$, respectively, the probability density functions of the x_i variable for background and signal.

All discriminating variables are computed for each jet of the event. Ideally, all particles coming from the fragmentation of a b quark and from the decay of the formed B hadron are combined in the same jet. All jets in the event are classified into 3 categories:

1. jets with one or more reconstructed secondary vertex,
2. jets without a secondary vertex but with at least two tracks with a track significance probability smaller than 0.05,
3. jets with no secondary vertex and with less than 2 tracks with a track significance probability smaller than 0.05.

The tagging variable is defined separately for each jet category α and the background is split into two independent contributions (c and ℓ events),

$$y_\alpha = \frac{n_\alpha^c}{n_\alpha^b} \prod y_{i,\alpha}^c + \frac{n_\alpha^\ell}{n_\alpha^b} \prod y_{i,\alpha}^\ell = \frac{n_\alpha^c}{n_\alpha^b} \prod \frac{f_{i,\alpha}^c(x_i)}{f_{i,\alpha}^b(x_i)} + \frac{n_\alpha^\ell}{n_\alpha^b} \prod \frac{f_{i,\alpha}^\ell(x_i)}{f_{i,\alpha}^b(x_i)} \tag{5.5}$$

being $f_{i,\alpha}^q(x_i)$ $(q = \ell, c, b)$ the probability density functions of x_i in jet category α generated by q quarks and n_α^q its normalized rate, so that $\sum_\alpha n_\alpha^q = R_q$, i.e. the normalized q quark rate.

Different discriminative variables x_i are used in DELPHI to build the combined jet tagging variable, those are:

- P_j^+: The jet lifetime probability of the tracks with positive impact parameters contained in the jet.
- M_s: The mass of particles included in the secondary vertex. When the jet is generated by a c quark this mass is limited by the mass of the D meson, which is about 1.8 GeV/c^2, while for b jets is extended up to 5 GeV/c^2.

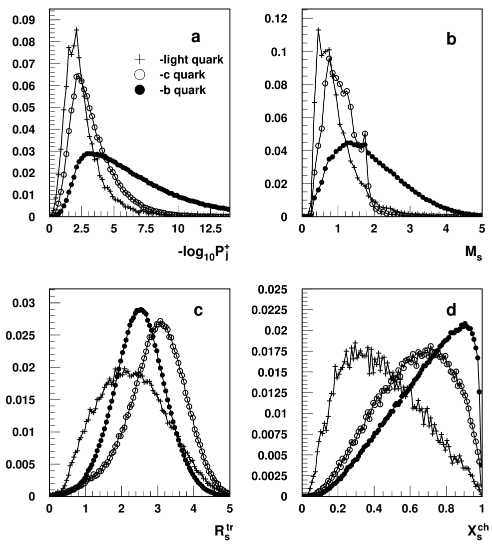

Figure 5.9: Distributions of some of the discriminative variables for b and c and ℓ quark events used in the combined method of b tagging.

- X_s^{ch}: Fraction of the charged jet energy of particles included in the secondary vertex. This distribution is determined by the fragmentation function of the quark which is harder for b quarks.
- P_s^t: The resultant transverse momentum (with respect to the B hadron flight direction) of all charged particles of the secondary vertex. b quark jets have higher values of P_s^t due to the higher mass of the B hadron.
- R_s^{tr}: The rapidity of each track included in the secondary vertex with respect to the jet direction. The rapidities of particles from B decays are lower than those from D decays.
- P_l^t: The transverse momentum of an identified energetic lepton with respect to the direction of the jet to which it belongs (the lepton momentum is subtracted from the total jet momentum). It is independent of the track impact parameter and it can be defined for any jet category containing a muon or an electron. Jets originated by a b quark contain more high transverse momentum leptons.

Figure 5.9 shows the distribution of some of the variables defined above for events of different flavour (ℓ, c and b).

Not all these variables can be defined for all jet categories, since some of them require the existence of a secondary vertex. The set of discriminating variables used for each jet category is then,

- First category: All the above variables can be used.
- Second category: P_j^+, the effective mass of all tracks with track significance probability smaller than 0.05, their rapidities and P_l^t.

– Third category: P_j^+, rapidities of all tracks with positive impact parameters and P_l^t.

The jet tagging variable is defined as $X_{jet} = -\log_{10} y_\alpha$, with y_α given by Eq. 5.5. The event tagging variable, X_{effev}, is calculated as the sum of the largest two X_{jet} values for the individual jets in the event. Figure 5.8 shows the distribution of X_{effev} obtained for the sample of Z^0 hadronic events selected in the year 1994. The contribution of each quark flavour is also shown and, as can be seen, b quarks tend to have greater values of X_{effev}.

The impact parameter and the combined techniques are then the two techniques available in DELPHI to build the b and ℓ quark samples needed to measure $R_3^{b\ell}$. We will discuss now the applicability and optimization of these techniques for this analysis.

As mentioned above, both tagging methods depend on the jet reconstruction algorithm used [6], so the same algorithm used for $R_3^{b\ell}$ (either DURHAM or CAMBRIDGE) was also used in the tagging procedure.

The agreement between simulated and real data for the distribution of the event tagging variables, P_E^+ and X_{effev}, is good in both cases (see figure 5.8). The b sample can be tagged by requiring $P_E^+ < P_b^+$ ($X_{effev} > X_{effev-b}$) when the impact parameter (combined) method is used, being P_b^+ and $X_{effev-b}$ the threshold values used. In order to tag the ℓ sample, anti-b tagging is used, so the requirement now is $P_E^+ > P_l^+$ ($X_{effev} < X_{effev-l}$) for the impact parameter (combined) method, where P_l^+ and $X_{effev-l}$ denote the threshold values used. From now on, B and L will refer, respectively, to the b and ℓ tagged samples while b and ℓ will refer to the real b and ℓ quark events. Therefore, for a given cut, the cut efficiency, purity and contaminations of the Q tagged sample ($Q = B$ or L) are computed with the generated data as follows,

$$\epsilon_Q = \frac{N_Q^{had}}{N^{had}} \qquad P_q = C_Q^q = \frac{N_Q^{had-q}}{N_Q^{had}} \qquad C_Q^{q'} = \frac{N_Q^{had-q'}}{N_Q^{had}} \tag{5.6}$$

being N^{had} the number of Z^0 hadronic events and $q' = \ell, c$ when $Q = B$ and $q' = b, c$ when $Q = L$. So, N_Q^{had} denotes the number of hadronic events that are tagged as Q and $N_Q^{had-q'}$ the number of real q' quark events that are tagged as Q. Figure 5.10 shows the cut efficiency, purity and contaminations for each tagged sample as a function of the cut applied for the two tagging methods. The DURHAM algorithm has been used to form jets in this case.

In order to see the performance of the tagging method, the selection efficiency-purity curve of each tagged sample was calculated for each technique. The selection efficiency is defined as the fraction of b (ℓ) quark events that, after being selected as hadronic events, are tagged as b (ℓ).

$$E^q \equiv E_Q^q = \frac{N_Q^{had-q}}{N^q} \tag{5.7}$$

[6]For the whole event tagging, the dependence of the tagging with the jet algorithm in the impact parameter method comes only from the definition of the sign of the impact parameter while for the combined technique the dependence is even higher, since the event combined tagging variable is built from the jet combined variables.

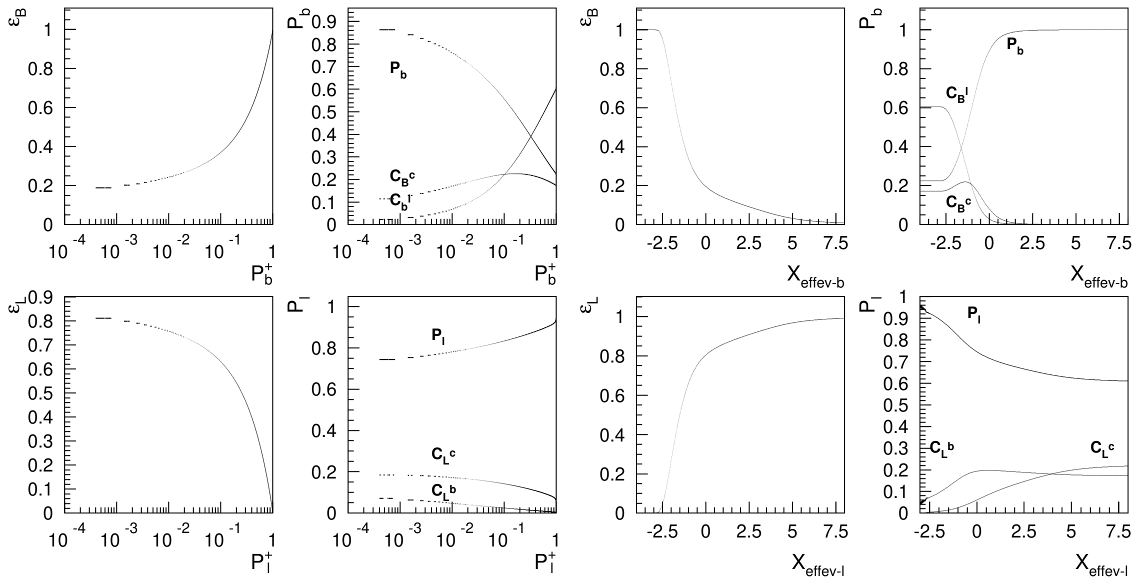

(a) Impact parameter method. **(b)** Combined method.

Figure 5.10: Cut efficiencies, purities and contaminations of the b and ℓ tagged samples as a function of the cut on the tagging variable. The DURHAM clustering algorithm was used for jet reconstruction.

where N^q is the number of q quark (b or ℓ) generated events. Figure 5.11 shows, for the case of DURHAM, the selection efficiency-purity curves of each tagged sample obtained with the simulated sample for the two tagging methods. We find that the combined tagging yields a better performance (i.e. a higher purity is reached for the same selection efficiency) than the impact parameter method for the case of b tagging while for ℓ tagging, although the curves are very similar, it is the other way around.

The tagging working points were chosen based on the stability of the final result. The cuts to tag b and ℓ events were variated and the impact on R_{3b} and $R_{3\ell}$ at parton level was evaluated. Figure 5.12 shows, for the CAMBRIDGE algorithm, the obtained R_{3b} ($R_{3\ell}$) as a function of the purity of the b sample, P_b, (ℓ sample, P_ℓ) for the two tagging methods [7].

For b tagging, the stability with P_b is similar for both techniques. The most stable region was found to be [70%, 80%] for the impact parameter and [81%, 91%] for the combined. For ℓ tagging, the stability with P_ℓ is much better for the impact parameter method but a stable region could also be found for both techniques, being [77%, 87%] for the impact parameter and [70%, 80%] for the combined [8].

As a cross check, the point of optimum tagging performance, i.e. that of closest approach to (1,1) in the selection efficiency-purity plane, was calculated for each case and it was found

[7] In order to bring the measured R_{3q} at parton level the DELSIM DELPHI simulation, which uses JETSET 7.3 to generate the events, was used to correct for both detector and hadronization effects.

[8] The same stability regions were found for the two jet clustering algorithms, DURHAM and CAMBRIDGE.

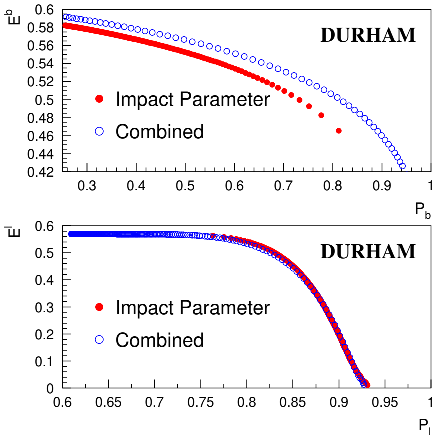

Figure 5.11: Selection efficiency-purity curves of the b (top) and ℓ (bottom) tagged samples for the two tagging methods, impact parameter and combined. The DURHAM clustering algorithm was used for jet reconstruction.

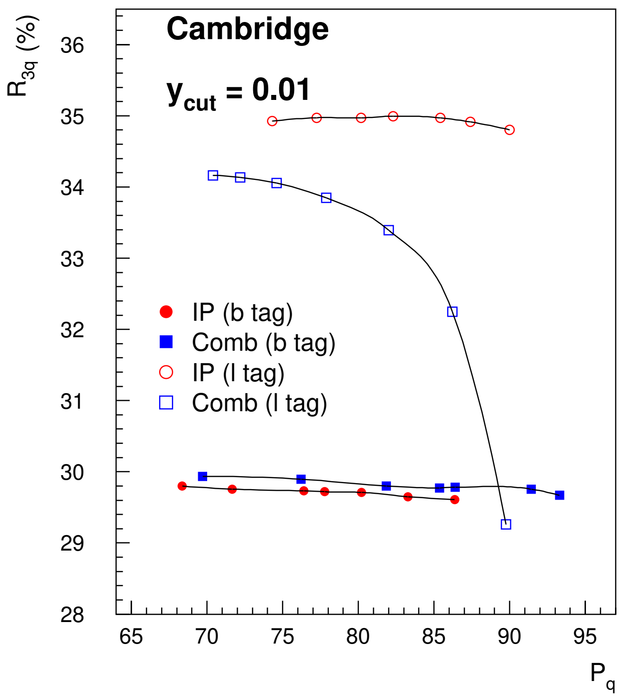

Figure 5.12: R_{3q} at parton level as a function of the purity of the q tagged sample, P_q, for $q = b, \ell$, when CAMBRIDGE is used to form jets.

Durham	$P_b(\%)$	$E^b(\%)$	$P_\ell(\%)$	$E^\ell(\%)$
Impact Parameter	78	48	78	56
Combined	82	50	77	56
Cambridge				
Impact Parameter	78	46	78	53
Combined	82	48	77	53

Table 5.6: Points of closest approach to (1,1) in the selection efficiency-purity plane of the b and ℓ tagged samples for the two tagging methods and for the two jet clustering algorithms.

to be within the above intervals (as can be seen from table 5.6). But the working point for each tagging method was chosen as the center of the stability range, the corresponding purities and selection efficiencies are shown in table 5.7. If these working points were used to measure $R_3^{b\ell}$ the results obtained with both techniques were found to be compatible at the 2‰ level.

Method	P_b (%)	P_ℓ (%)	E_b (%)	E_ℓ (%)
Impact Parameter	76	82	49	51
Combined	86	75	47	57

Table 5.7: Working points found to select the b and ℓ quark initiated samples for the impact parameter and the combined techniques.

Nonetheless, regarding the stability of the final result (see figure 5.12), the combined technique was used to select b events by requiring $X_{effev} > -0.15$ ($P_b = 86\%$) while the impact parameter method was used for ℓ tagging by $P_E^+ > 0.07$ ($P_\ell = 82\%$). For b tagging both techniques were observed to be equally stable and the combined method was chosen because higher purities could be reached with the same efficiency.

5.1.3 Jet identification

In order to perform the cut on the b quark energies, described in Section 4.3, an identification of the gluon and b quark jets is required for the b tagged events. The two tagging techniques can also provide a discriminative variable per jet and therefore both are available for jet identification.

The procedure applied is the following: Each b tagged event is forced to three jets by the given jet clustering algorithm. For all possible jet pairs the tagging variable is calculated, i.e. P_{ij}^+ for the impact parameter and X_{eff-ij} for the combined, where ij denotes the pair of jets i and j. The pair of jets originated from the b quarks is identified as the one with minimum P_{ij}^+ for the impact parameter and the one with maximum X_{eff-ij} for the combined. Purities around 75% and 78% are obtained for the impact parameter and the combined techniques

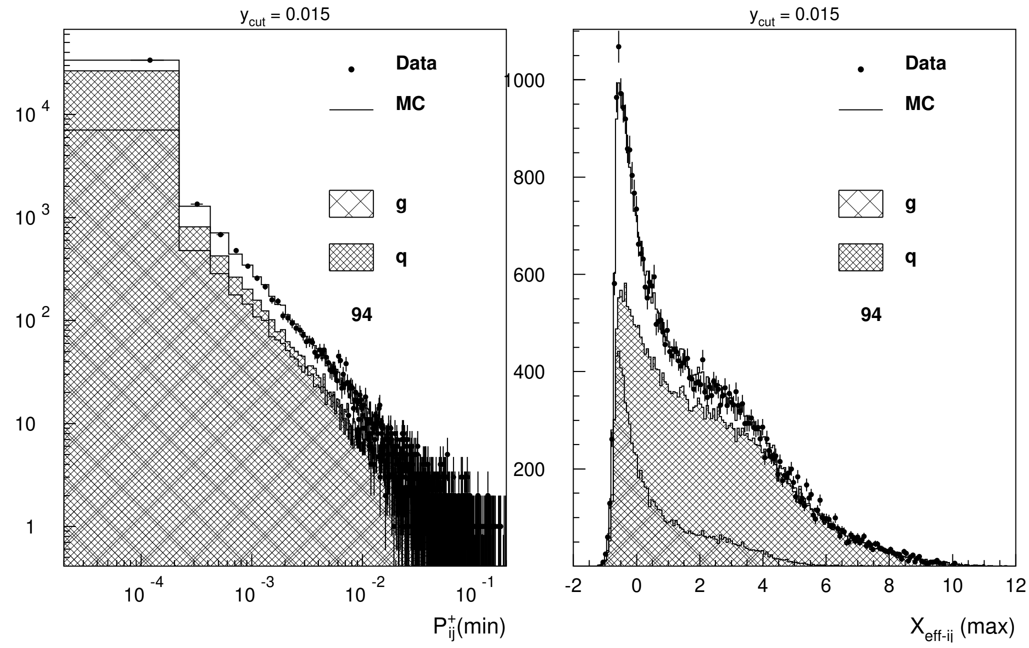

Figure 5.13: Distribution of the minimum P^+_{ij} (left) and of the maximum X_{eff-ij} (right) of the three jet pairs for b tagged three-jet events at a $y_c = 0.015$ for CAMBRIDGE. The contributions of gluon and quark jets are also shown.

respectively [9].

Figure 5.13 shows, for b tagged three-jet events at a $y_c = 0.015$ for CAMBRIDGE, the data/MC agreement for the distributions of the minimum P^+_{ij} and the maximum X_{eff-ij}, together with the contamination of the gluon jets and the contribution of the quark jets. The purity of the jet identification can be then increased by making some cuts on these distributions, i.e. by requiring P^+_{ij}(min) (X_{eff-ij}(max)) to be smaller (greater) than a given threshold. Figure 5.14 shows the variation of the purity and the efficiency of the jet identification with this threshold.

The R_{3b} at parton level was calculated as a function of the jet identification purity, P_{jet-id}, as can be seen in figure 5.15, for both tagging techniques. The result is that the R_{3b} is more stable for a wider P_{jet-id} range for the combined than for the impact parameter method. Furthermore, with the combined technique higher purities can be obtained. Therefore, the combined tagging was used to identify the pair of jets more likely to come from b quarks by requiring $X_{eff-ij}(\text{max}) > -0.5$. This led to work with 81% purity with a cut efficiency of 90%.

Once the b quark jets were identified their energy was computed from the jets directions [109], as described in Section 4.3. Figure 5.16 shows the x^b_E(jet) distribution for real and DELSIM simulated data. The cut $x^b_E(\text{jet}) \geq 0.55$ was then applied for both b jets. The purity

[9]The purity of the jet identification was evaluated using the data simulated by DELSIM. In order to know if the jet comes from a quark or a gluon an association between the jets at hadron and parton level is needed. The same criteria of Section 4.3, proposed in [109], was used, i.e. each jet at hadron level was associated to the one at parton level that is closest in angle.

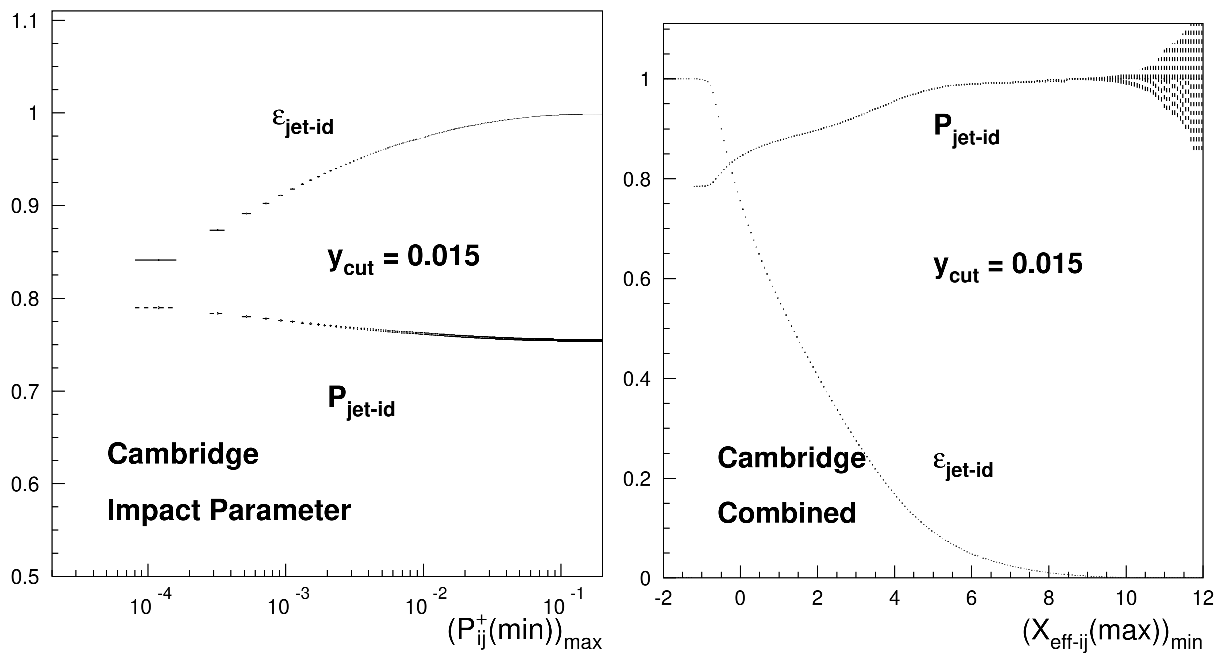

Figure 5.14: Variation of the efficiency and purity of the jet identification with the cut applied on $P^+_{ij}(\text{min})$ (left) and $X_{eff-ij}(\text{max})$ (right).

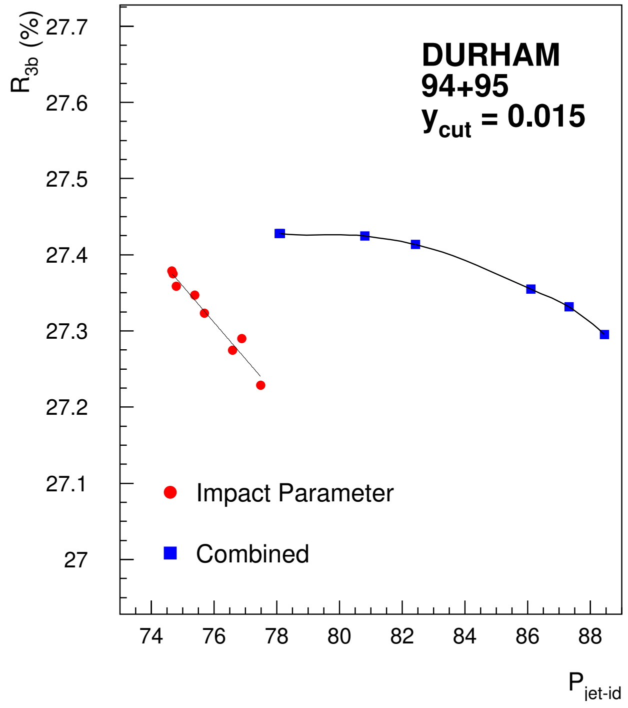

Figure 5.15: R_{3b} as a function of the jet identification purity at a $y_c = 0.015$ for the DURHAM algorithm.

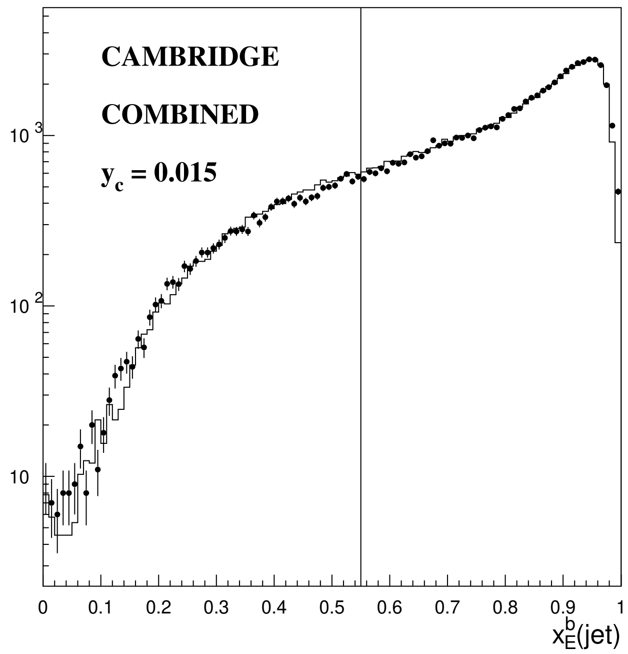

Figure 5.16: x_E^b(jet) distribution for real and DELSIM simulated data for three-jet b tagged events at a $y_c = 0.015$ for CAMBRIDGE.

and contamination of the b and ℓ tagged samples obtained after the cut is made are shown in table 5.8. The number of hadronic b and ℓ tagged events are listed in table 5.9 for each year and for the two jet algorithms.

Method	Type q	$\ell \to q$ (%)	$c \to q$ (%)	$b \to q$ (%)
Impact Parameter	ℓ	82	15	3
Combined	b	2	7	91

Table 5.8: Flavour composition of the samples tagged as ℓ or b quark events.

5.2 Correction procedure

Once the b and ℓ quark hadronic events were selected from the collected data, the jet clustering algorithm was applied to get the $R_3^{b\ell}$ observable at detector level, $R_3^{b\ell-det}$. A correction procedure was then needed to bring the observable to parton level where a comparison with the theoretical calculations can be performed. The observable was corrected by detector, acceptance and tagging effects and the hadronization process using the following expression

Year	Durham b tagged	Durham ℓ tagged	Cambridge b tagged	Cambridge ℓ tagged
1994	100,354	529,062	104,442	499,928
1995	48,265	258,089	49,955	243,842
1997	3,168	17,524	3,349	16,568
1998	4,927	27,207	5,167	25,636
1999	8,414	44,417	8,632	41,934
2000	6,273	35,418	6,573	33,496
Total	171,401	911,717	178,118	861,404

Table 5.9: Number of b and ℓ tagged events for each analysed year for the DURHAM and CAMBRIDGE jet clustering algorithms.

(which was derived in [7, 112]),

$$R_3^{b\ell-part}(y_c) = \frac{\left[c_B^\ell g_{3B}^\ell(y_c) + c_B^c g_{3B}^c(y_c)\right] - \left[P_\ell g_{3L}^\ell(y_c) + c_L^c g_{3L}^c(y_c)\right] R_3^{b\ell-det}(y_c)}{c_L^b g_{3L}^b(y_c) R_3^{b\ell-det}(y_c) - P_b g_{3B}^b(y_c)} \tag{5.8}$$

where $g_{3Q}^i(y_c) = d_{3Q}^i(y_c) \cdot h_{3i}(y_c)$, being $d(y_c)$ the detector correction factors and $h(y_c)$ the hadronization ones,

$$d_{3Q}^i(y_c) = \frac{R_{3Q-MC}^{i-det}}{R_{3-MC}^{i-had}} \qquad h_{3i} = \frac{R_{3-MC}^{i-had}}{R_{3-MC}^{i-part}} \tag{5.9}$$

where $Q = B, L$ denotes, respectively, the b and ℓ tagged sample and $i = b, c, \ell$ refer to the real i-quark sample. Therefore, R_{3Q-MC}^{i-det} is the Monte Carlo three-jet rate at detector level of events that are tagged as Q and are of flavour i, R_{3-MC}^{i-had} is the three-jet rate at hadron level of the sample of i-quark events and R_{3-MC}^{i-part} the same rate but evaluated at parton level. The remaining factors of Eq. (5.8) correspond to the purities and contaminations of the two tagged samples listed in table 5.8.

The detector correction factors $d_{3Q}^i(y_c)$ were calculated using the DELSIM simulated events and applying to them the same reconstruction chain applied to real data. Figure 5.17 shows these factors as a function of the y_c for the DURHAM jet clustering algorithm. The h_{3i} hadronization factors were taken from an independent generation performed with PYTHIA 6.131 tuned to DELPHI data [10]. Figure 5.18 shows as a function of the y_c these factors for the two jet finder algorithms.

Table 5.10 shows the values for the detector and hadronization correction factors obtained for DURHAM and CAMBRIDGE at a $y_c = 0.02$ and 0.01 respectively. The largest detector factors are d_{3B}^ℓ and d_{3L}^b but these numbers are multiplied in the correction expression by c_B^ℓ and c_L^b respectively, which are small numbers, so the total detector correction remains small.

[10] The PYTHIA generator setup used to get the hadronization correction was the following: all unstable particle were allowed to decay, the Peterson fragmentation function was used to fragment b quarks, mass effects were turned on and the kinematical and constituent b mass parameters were set to 5 GeV/c^2 (default values for that version of the generator).

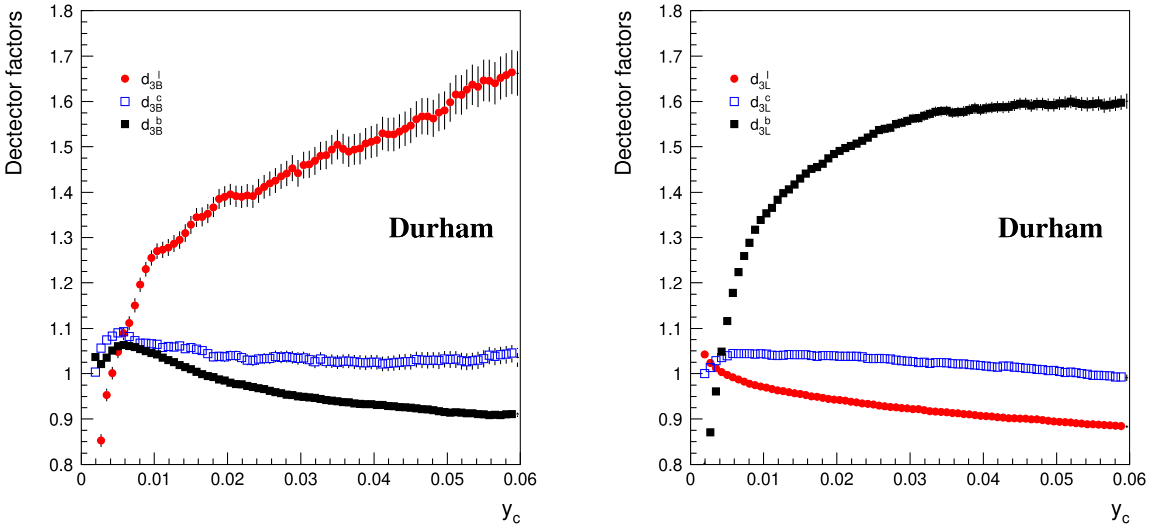

Figure 5.17: Detector correction factors used to correct the measured $R_3^{b\ell}$ from detector to hadron level.

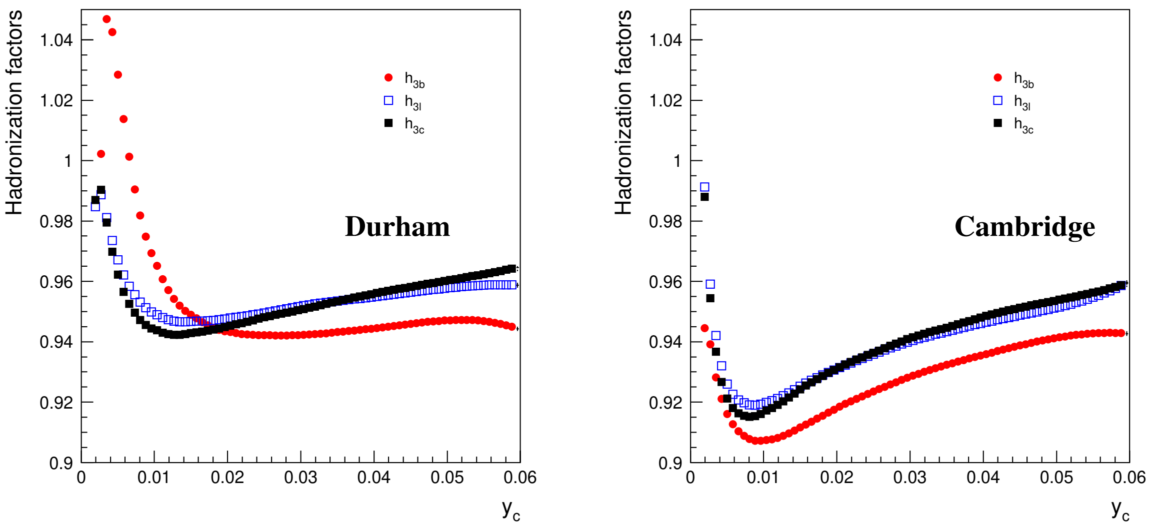

Figure 5.18: Hadronization correction factors used to correct the $R_3^{b\ell}$ from hadron to parton level.

Factor	Durham($y_c = 0.02$)	Cambridge($y_c = 0.01$)
d_{3B}^{ℓ}	1.395	1.259
d_{3B}^{c}	1.040	1.024
d_{3B}^{b}	0.980	1.022
d_{3L}^{ℓ}	0.942	1.026
d_{3L}^{c}	1.038	1.101
d_{3L}^{b}	1.491	1.442
h_{3b}	0.943	0.907
$h_{3\ell}$	0.948	0.920
h_{3c}	0.945	0.917

Table 5.10: Detector and hadronization factors used to correct the $R_3^{b\ell}$ observable to parton level for Durham and Cambridge algorithms at a $y_c = 0.02$ and 0.01 respectively.

The total detector and hadronization corrections are mainly coming from the ratios d_{3L}^{ℓ}/d_{3B}^{b} and $h_{3\ell}/h_{3b}$ respectively. Note that the corrections for each individual flavour (b and ℓ) are large, of a few percent. However, due to the definition of our observable, which is a ratio of b over ℓ events, there is a partial cancellation among the corrections for b and ℓ events and the total corrections are smaller.

In fact, the total size of the detector and hadronization corrections for $R_3^{b\ell}$ are shown in figure 5.19. The detector correction is of about 2% for both algorithms while the fragmentation correction is about 5‰ for Durham and 1% for Cambridge at a $y_c = 0.02$ and $y_c = 0.01$ respectively.

Further corrections need to be applied to the $R_3^{b\ell}$ obtained by Eq. (5.8) in order to have the correct heavy quark gluon splitting rates in the simulated sample and a more reliable hadronization process. These additional corrections will be described in detail in the following sections.

5.2.1 Gluon splitting rate correction

Heavy quark pairs ($Q\overline{Q}$) in Z^0 decays can either be produced directly via $Z^0 \to Q\overline{Q}$ or indirectly, when a gluon is radiated by a quark and then splits into a pair of heavy quarks, $Z^0 \to q\overline{q}g$ with $g \to Q\overline{Q}$, which is also called secondary heavy quark production. The gluon splitting rate to a pair of heavy quarks is defined as the fraction of hadronic Z^0 decays with a gluon coupled to a $Q\overline{Q}$ pair,

$$g_{Q\overline{Q}} = \frac{N(Z^0 \to q\overline{q}g, g \to Q\overline{Q})}{N(Z^0 \to \text{hadrons})} \tag{5.10}$$

where the heavy quark can either be a b or c quark.

In the present analysis, the flavour of the event was defined as that of the quarks directly coupled to the Z^0 boson and not from those quarks coming from secondary emissions due to the gluon splitting process. However, the heavy quarks coming from $g \to Q\overline{Q}$ clearly affect the event tagging. Therefore, it is essential to have the correct gluon splitting rates, $g_{b\bar{b}}$ and

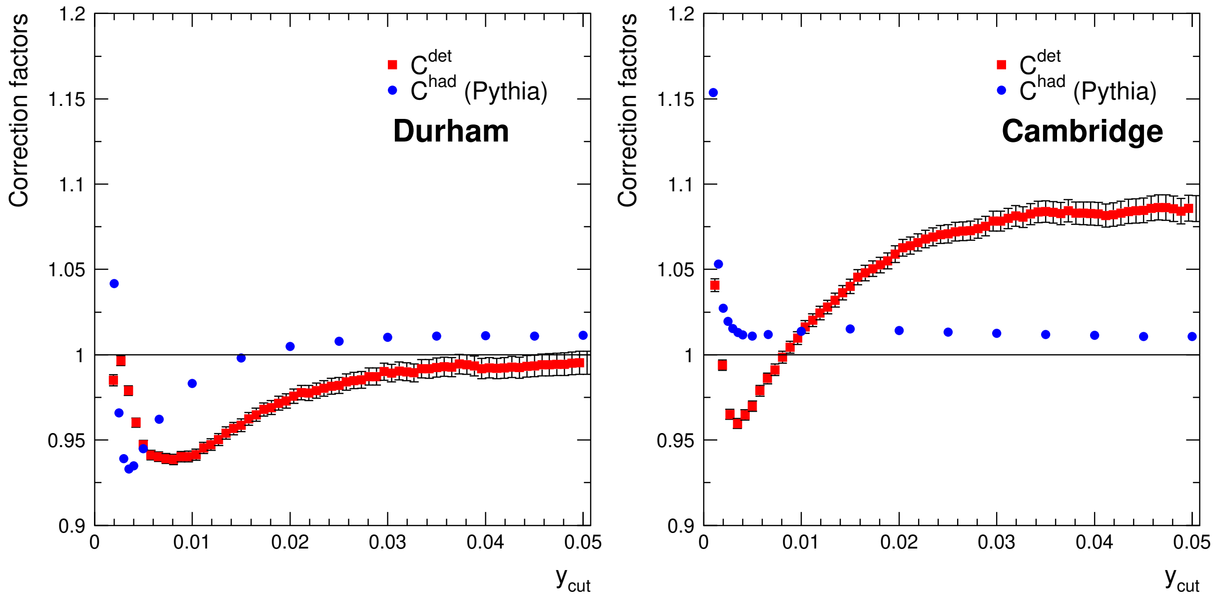

Figure 5.19: Detector and hadronization corrections applied to the measured $R_3^{b\ell}$ for DURHAM and CAMBRIDGE.

$g_{c\bar{c}}$, in the simulated data used to correct the measured observable for detector and tagging effects, i.e. in the data generated by DELSIM.

The gluon splitting rate is an infrared safe quantity, since the quark mass provides a natural cut-off, which can be computed in the framework of perturbative QCD. In fact it has been computed at leading order (i.e. $\mathcal{O}(\alpha_s^2)$) and including resummation of leading and next-to-leading logarithms to all orders in α_s, matched with leading order [123–125]. The results obtained in Ref. [125] give $g_{b\bar{b}} = 0.175\%$ and $g_{c\bar{c}} = 2.007\%$. These processes are then highly suppressed with respect to primary heavy flavour Z^0 decays, specially the $g_{b\bar{b}}$ rate which is about ten times smaller. The calculations depend on α_s and on the quark mass and the associated uncertainty is quite big.

These rates have also been measured experimentally at LEP and SLC. The results are given in tables 5.11 and 5.12 for $g_{b\bar{b}}$ and $g_{c\bar{c}}$ respectively. These analyses try to extract the $Z^0 \to q\bar{q}g \to q\bar{q}Q\overline{Q}$ from all Z^0 hadronic decays. The main background comes then from $Z^0 \to Q\overline{Q}g \to Q\overline{Q}q\bar{q}$ events but the kinematics of these Q jets are typically different, they tend to be back to back and have energies comparable with the beam energy. In contrast, those Q jets coming from $g \to Q\overline{Q}$ tend to be collinear and low energetic.

Different methods have been used to measure $g_{c\bar{c}}$, as fitting to the energy of the D^* in events in which a D^* is reconstructed (since the energy spectrum of the D^* is different for primary and secondary c quarks), looking at the mass difference between hemispheres (a large difference is expected in gluon splitting events) and searching for leptons in three-jet events in the least energetic jet (since $g \to c\bar{c} \to l\nu X$, the pair of c quarks are close enough in angle to be within the same jet and the gluon jet is usually the least energetic).

The measurements of $g_{b\bar{b}}$ are even more challenging since the rate is much smaller. Two different approaches have been used. One of them consists on a generic search of $g \to b\bar{b}$

Experiment	$g_{c\bar{c}} \times 10^{-2}$
ALEPH (2000) [131]	3.23 ± 0.48 (stat) ± 0.53 (syst)
L3 (2000) [132]	2.45 ± 0.29 (stat) ± 0.53 (syst)
OPAL (2000) [133]	3.20 ± 0.21 (stat) ± 0.38 (syst)

Table 5.11: Experimental results for the gluon splitting to $c\bar{c}$ rate, $g_{c\bar{c}}$.

events among all the Z^0 hadronic decays, without specifying the event flavour. These analysis select four-jet events and try to find the two jets coming from the splitted quarks based on tagging techniques and topological cuts. The other possibility is to search for the final state $Z^0 \to b\bar{b}b\bar{b}$, which can only come through gluon splitting to $b\bar{b}$. These events are selected based on tagging methods applied to each jet. Once the rate of this type of events with four b quarks is measured, the $g_{b\bar{b}}$ can be extracted using theoretical calculations including interference and mass effects between the four massive quarks (see [128]).

Experiment	$g_{b\bar{b}} \times 10^{-3}$
DELPHI (1997) [126]	2.1 ± 1.1 (stat) ± 0.9 (syst)
ALEPH (1998) [127]	2.77 ± 0.42 (stat) ± 0.57 (syst)
DELPHI (1999) [128]	3.3 ± 1.0 (stat) ± 0.8 (syst)
SLD (2001) [129]	2.44 ± 0.59 (stat) ± 0.34 (syst)
OPAL (2001) [130]	3.07 ± 0.53 (stat) ± 0.97 (syst)

Table 5.12: Experimental results for the gluon splitting to $b\bar{b}$ rate, $g_{b\bar{b}}$.

In Ref. [134] an average value was calculated for the experimentally measured heavy quark splitting rates, $g_{c\bar{c}}$ and $g_{b\bar{b}}$, and the result was,

$$\begin{aligned} g_{c\bar{c}} &= 0.0296 \pm 0.0038 \\ g_{b\bar{b}} &= 0.00254 \pm 0.00051 \end{aligned} \tag{5.11}$$

The gluon splitting rates on the simulated data of DELSIM (which contains $\sim 4.6 \cdot 10^6$ events) were found to be,

$$\begin{aligned} g_{c\bar{c}}^{Delsim} &= 0.0155 \\ g_{b\bar{b}}^{Delsim} &= 0.00155 \end{aligned} \tag{5.12}$$

which are a factor 1.91 and 1.64 lower than the measured rates of $c\bar{c}$ and $b\bar{b}$ respectively. A reweighting of the DELSIM simulation was then done by these factors in order to have the measured rates.

Technically, the $R_3^{b\ell}$ was obtained at hadron and detector level for the reweighted simulated sample and a correction factor was applied to the $R_3^{b\ell-part}$ of Eq. (5.8) for each y_c

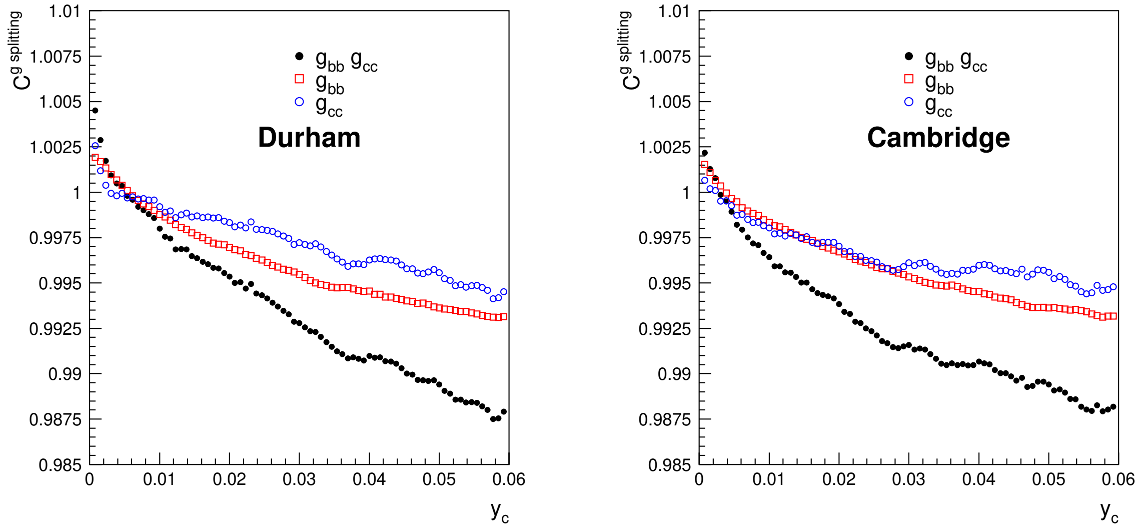

Figure 5.20: Gluon splitting correction factors due to the reweighting of the $g_{c\bar{c}}$ and $g_{b\bar{b}}$ rates as a function of y_c for DURHAM (left) and CAMBRIDGE (right) algorithms.

value [11],

$$C^{g\ splitting}(y_c) = \frac{R^{b\ell-det}_{3-MC}}{R^{b\ell-det}_{3-MC}(\text{reweighted})} \frac{R^{b\ell-had}_{3-MC}(\text{reweighted})}{R^{b\ell-had}_{3-MC}} \tag{5.13}$$

This correction is shown as a function of y_c in figure 5.20 for both jet clustering algorithms, together with the contribution of each individual gluon splitting rate reweighting. As can be seen, for not very small y_c values, the gluon splitting correction is smaller than 1, which means that the increase of the gluon splitting rates in the simulation causes the decrease of the measured $R_3^{b\ell}$ at parton level. As an example, the correction factor is of $5\permil$ at a $y_c = 0.02$ with DURHAM and $4\permil$ at a $y_c = 0.01$ for CAMBRIDGE.

In order to understand the direction of the correction it is important to note that the events in which a gluon splitting has taken place are preferably three-jet events for not very small y_c values. This is shown in figure 5.21 where the three-jet rate of the b and ℓ quark samples for those events containing a gluon splitting to $b\bar{b}$ and $c\bar{c}$ are shown, i.e. $R_{3q}^{g_{b\bar{b}}}(y_c)$ and $R_{3q}^{g_{c\bar{c}}}(y_c)$ $(q = b, \ell)$, with jets reconstructed with DURHAM. These rates were obtained with DELSIM and the results at detector and hadron level are shown in the plot. As can be seen, about 60% of the $g \to b\bar{b}$ $(g \to c\bar{c})$ events are three jets at $y_c = 0.02$ $(y_c = 0.01)$.

[11] The hadronization correction of $R_3^{b\ell}$ was found to be independent of the gluon splitting rates for not very small values of y_c, i.e. for the range of y_c of interest for this measurement. This was expected to be like that because no tagging enters in the definition of the flavour of the event nor at parton neither at hadron level. Therefore, the fraction of gluon splitting events in the three-jet sample is about the same at parton and hadron level for not very small values of y_c and in the total samples of b and ℓ quark events this fraction is obviously exactly the same at both levels.

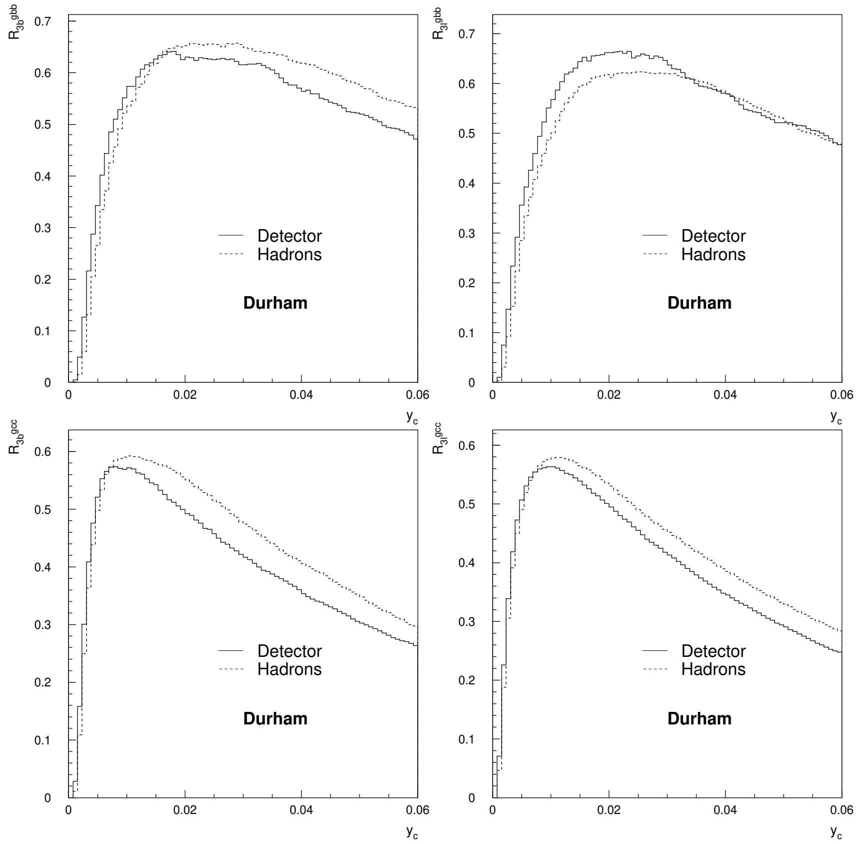

Figure 5.21: DELSIM simulated three-jet rate of events containing a gluon splitting process to $b\bar{b}$ and $c\bar{c}$ for b and ℓ quark events, i.e. $R_{3q}^{g_{b\bar{b}}}(y_c)$ and $R_{3q}^{g_{c\bar{c}}}(y_c)$ $(q = b, \ell)$. The rates are shown at detector and hadron level and DURHAM was used to form jets.

For very small values of y_c, this kind of events become four-jet events and the three-jet rate drops, but this region is not interesting for our analysis.

Having this in mind, it is clear that if the gluon splitting rates increase in the simulated sample the total R_{3q} $(q = b, \ell)$ will also increase. This is shown in figures 5.22 and 5.23 for the increased of $g_{b\bar{b}}$ and $g_{c\bar{c}}$ respectively and in figure 5.24 for the increased of the two rates. The plots show the ratio of R_{3q} obtained with the DELSIM gluon splitting rates over the one with the reweighted sample with higher splitting rates, R_{3q}/R_{3q-W}.

When $g_{b\bar{b}}$ increases (see figure 5.22), R_{3b} increases more at detector level than at hadron level while for $R_{3\ell}$ is the other way around. This makes sense because events with a gluon splitting to $b\bar{b}$ tend to be tagged as b. Therefore, when the fraction of those events increases, the effect on the b tagged sample is expected to be higher than the one on the real b quark sample. For the same reason, since ℓ quark events with a gluon splitting to $b\bar{b}$ tend to be tagged as b, the effects due to the gluon splitting rate are expected to be larger at hadron level for real ℓ quark events than at detector level for ℓ-tagged events.

When $g_{c\bar{c}}$ increases (see figure 5.23), R_{3b} increases as much at detector level as at hadron

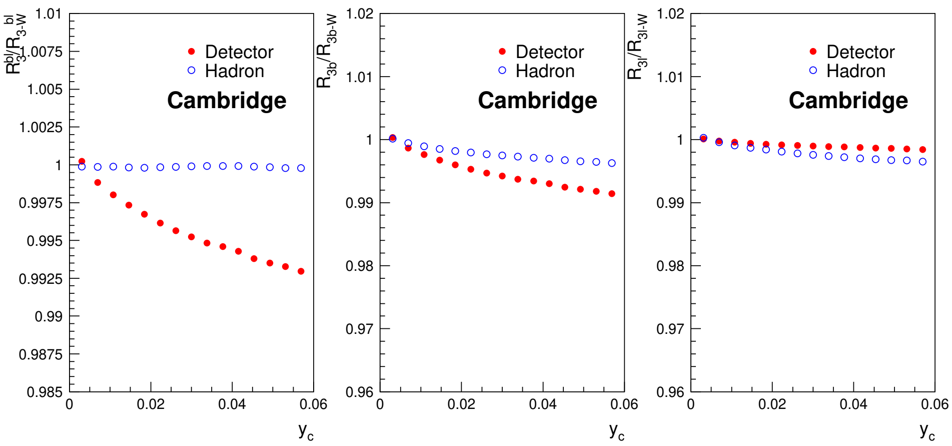

Figure 5.22: Ratio of DELSIM predicted $R_3^{b\ell}$, R_{3b} and $R_{3\ell}$ at detector and hadron level when no reweighting is done for the gluon splitting rates over the same rates when a reweighting is done for $g_{b\bar{b}}$. The CAMBRIDGE algorithm is used to form jets.

level while $R_{3\ell}$ increases more at hadron level. This is due to the fact that, for b quarks events, c quarks coming from a gluon splitting do not affect the flavour tagging while for ℓ quark events they do and the event is more likely tagged as c.

In any case, the effects observed at hadron level are the same for the b and ℓ quark samples, since the gluon splitting rate depends only slightly on the event flavour, and therefore $R_3^{b\ell}$ at hadron level is independent on the gluon splitting rate (see figures 5.22 and 5.23). However, at detector level the impact is higher for the b tagged sample than for the ℓ sample and therefore $R_3^{b\ell}$ increases when the gluon splitting rates are increased.

Figure 5.24 shows the effects when both gluon splitting rates are increased to the measured values. The conclusion is that $R_3^{b\ell}$ at detector level increases when the simulated data is reweighted while at hadron level it remains almost constant. This is why the gluon splitting correction factor is smaller than 1 for the region of y_c that we are interested in.

5.2.2 Hadronization corrections

The hadronization correction factors used in the expression of Eq. (5.8) were computed with the PYTHIA generator using the same options than in the DELPHI tuning. This means that the string model was used for the hadronization process, the Peterson fragmentation function to fragment b quarks and a b mass of 5 GeV/c^2 was used in the perturbative phase. Two additional correction factors have been then applied to the $R_3^{b\ell-part}$ of Eq. (5.8) in order correct for a more reliable hadronization process. These are:

- **Hadronization model correction**:

  As described in Section 4.3, different hadronization models and b fragmentation functions exist and are implemented in Monte Carlo generators. For this analysis, a mean

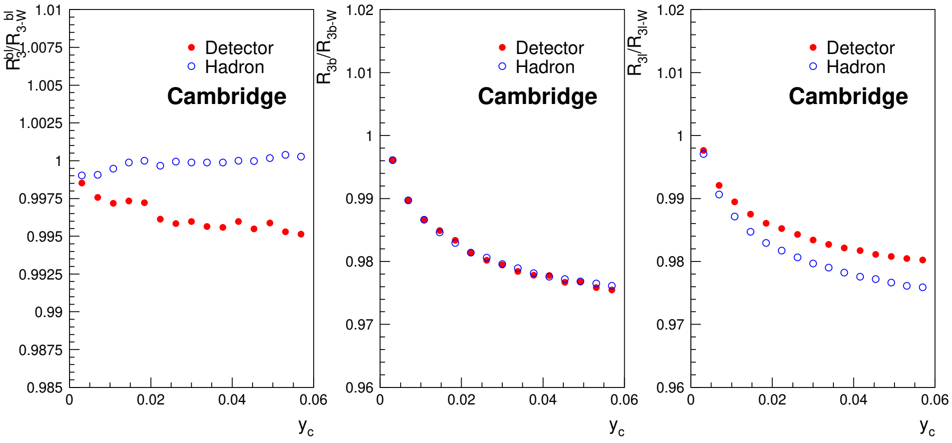

Figure 5.23: Ratio of DELSIM predicted $R_3^{b\ell}$, R_{3b} and $R_{3\ell}$ at detector and hadron level when no reweighting is done for the gluon splitting rates over the same rates when a reweighting is done for $g_{c\bar{c}}$. The CAMBRIDGE algorithm is used to form jets.

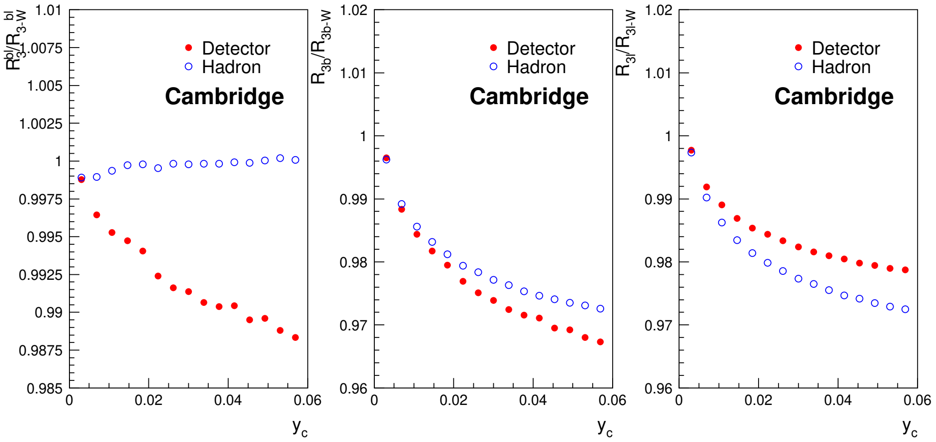

Figure 5.24: Ratio of DELSIM predicted $R_3^{b\ell}$, R_{3b} and $R_{3\ell}$ at detector and hadron level when no reweighting is done for the gluon splitting rates over the same rates when a reweighting is done for $g_{c\bar{c}}$ and $g_{b\bar{b}}$. The CAMBRIDGE algorithm is used to form jets.

of the following hadronization corrections of $R_3^{b\ell}$ was considered to be the most appropriate,

- $C_{Pythia}^{had-Peterson}$, obtained with the string model of PYTHIA and the Peterson b fragmentation function,
- $C_{Pythia}^{had-Bowler}$, obtained with the string model of PYTHIA and the Bowler b fragmentation function,
- C_{Herwig}^{had}, obtained with the cluster model of HERWIG.

The model correction factor is then,

$$C^{mod}(y_c) = \frac{1}{3}\left(1 + \frac{C_{Herwig}^{had}(y_c) + C_{Pythia}^{had-Bowler}(y_c)}{C_{Pythia}^{had-Peterson}(y_c)}\right) \tag{5.14}$$

and it has the effect of decreasing the measured $R_3^{b\ell}$ in 1‰ for DURHAM at $y_c = 0.02$ and in 3‰ for CAMBRIDGE at $y_c = 0.01$.

- **b mass parameter correction**:

  In Section 4.5.1 the b mass parameter of PYTHIA was determined to be $M_b = 4.98 \pm 0.13$ GeV/c^2. Therefore, a correction to go from a mass $M_b = 5$ GeV/c^2 to 4.98 GeV/c^2 was applied, having the effect of increasing the $R_3^{b\ell}$ in about 1‰.

Figure 5.25 shows the size of the different additional corrections applied to the $R_3^{b\ell}$ corrected by Eq. (5.8) for each y_c for the two jet clustering algorithms, i.e. the correction due to the gluon splitting rate and the two just described hadronization corrections (the fragmentation model, C^{mod}, and the generator b mass correction, C^{mass}). The values obtained for $y_c = 0.02$ for DURHAM and $y_c = 0.01$ for CAMBRIDGE are shown in table 5.13. The total correction due to these effects is also shown in the plot and the table.

Correction	Durham ($y_c = 0.02$)	Cambridge ($y_c = 0.01$)
$C^{g\ splitting}$	0.995	0.996
C^{mod}	0.999	0.997
C^{mass}	1.001	1.001
C^{tot}	0.995	0.994

Table 5.13: The different correction factors applied to the $R_3^{b\ell}$ corrected by Eq. (5.8), i.e. the gluon splitting rate correction, the fragmentation model correction, the b mass correction and the total correction due to these effects, for DURHAM at $y_c = 0.02$ and CAMBRIDGE at $y_c = 0.01$.

Figure 5.26 shows for the two jet clustering algorithms the measured $R_3^{b\ell}$ observable at detector level and the one obtained once it is corrected for all the corrections described, i.e. the detector and hadronization factors of Eq. (5.8) and the additional corrections described in Sections 5.2.1 and 5.2.2. The total correction is also shown in the plots, which is about 2% for both DURHAM and CAMBRIDGE at $y_c = 0.02$ and $y_c = 0.01$ respectively, though they go in opposite directions.

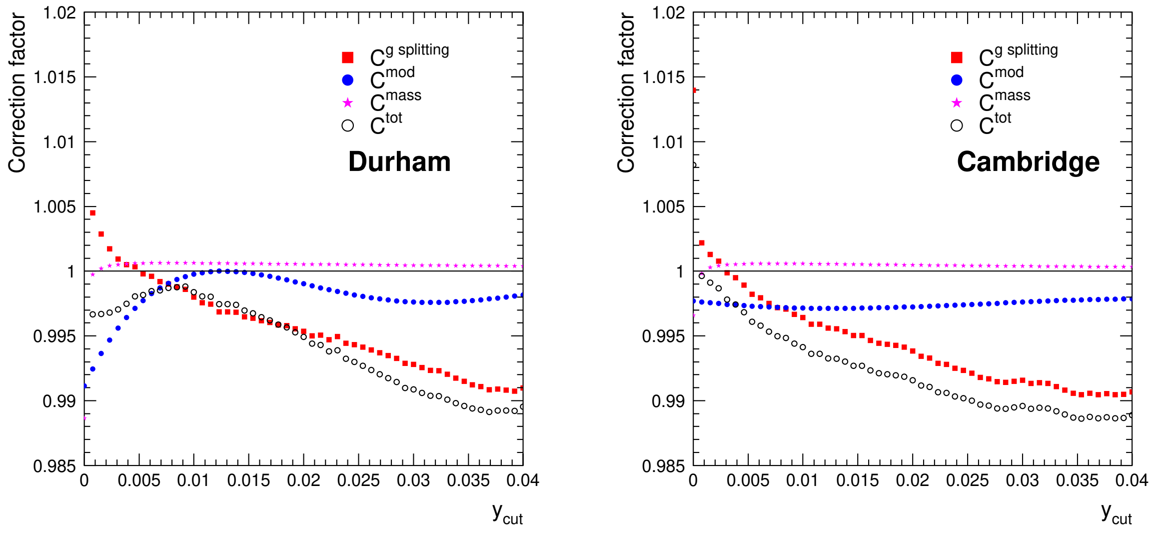

Figure 5.25: The different correction factors applied to the $R_3^{b\ell}$ corrected by Eq. (5.8), i.e. the gluon splitting rate correction ($C^{g\ splitting}$), the fragmentation model correction (C^{mod}), the b mass correction (C^{mass}) and the total correction due to these effects (C^{tot}), for DURHAM (left) and CAMBRIDGE (right).

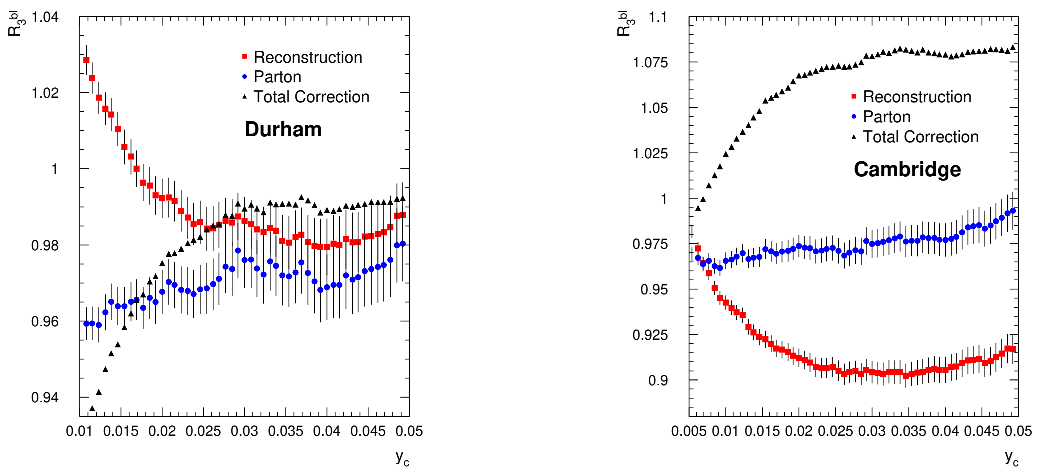

Figure 5.26: The measured $R_3^{b\ell}$ at detector level and parton level after all corrections, for the DURHAM (left) and CAMBRIDGE (right) algorithms. The total correction is also shown. The errors are only statistical.

5.3 Experimental uncertainties

Apart from the statistical uncertainties due to the limited size of the real and simulated data, different sources of systematic uncertainties were considered. They can be divided into two groups: those affecting the hadronization correction and the ones affecting the detector correction.

- **Hadronization**:

  The uncertainties on the hadronization correction were already described in detail in Section 4.2. Its impact on $R_3^{b\ell}$ will be seen here. The different contributions to the error on the fragmentation correction were,

  - Tuning: Uncertainty on the tuned parameters of PYTHIA that are relevant in the fragmentation process. This contribution was evaluated by varying these parameters (Λ_{QCD}, Q_0, σ_q, ϵ_b, a) within $\pm\sigma$ from their central tuned values and taking into account that they are not completely independent. The impact on the measured $R_3^{b\ell}$ at parton level is of about 2‰ (1‰) at $y_c = 0.02$ ($y_c = 0.01$) for DURHAM (CAMBRIDGE).
  - Hadronization model: It was calculated as the standard deviation of the three hadronization corrections used ($C_{Pythia}^{had-Peterson}$, $C_{Pythia}^{had-Bowler}$ and C_{Herwig}^{had}). This results in an uncertainty of about 2‰ for DURHAM at $y_c = 0.02$ and 3‰ for CAMBRIDGE at $y_c = 0.01$.
  - b mass parameter ambiguity in the generator: The uncertainty on the b mass parameter used in the generator, $M_b = 4.98 \pm 0.13$ GeV$/c^2$, was propagated to the effect on the hadronization correction. This translates into an uncertainty of about 3.5‰ for both, DURHAM and CAMBRIDGE, at $y_c = 0.02$ and 0.01 respectively.

- **Detector**:

  The uncertainties of the detector correction, which includes detector and acceptance effects and the tagging procedure, are due to imperfections on physics and detector modeling in the simulation. We have considered the following sources of uncertainties:

  - Gluon splitting: The gluon splitting rates of Eq. (5.12) were varied conservatively within twice their uncertainty and the effect on the measured observable was taken as the gluon splitting error. For example, for DURHAM is about 3‰ at y_c = 0.02 and about 2‰ for CAMBRIDGE at $y_c = 0.01$. These uncertainties are not negligible, specially for DURHAM.

    An attempt to reduce the dependence of the measured $R_3^{b\ell}$ with the gluon splitting rate was done by trying to discriminate between events in which a gluon has split into a pair of heavy quarks and those in which no gluon splitting processes have occurred. Since events with a gluon splitting into heavy quarks are more likely tagged as b than as ℓ, this attempt was only done for b tagged events.

As shown in table 5.14, the sample of b tagged events with a gluon splitting are mostly b quark events, specially for the $g \to c\bar{c}$ sample. For the $g \to b\bar{b}$ sample the contribution of ℓ quark events is also important.

b tagged sample event flavour	$g \to b\bar{b}(\%)$	$g \to c\bar{c}(\%)$
ℓ	42	10
c	15	11
b	44	79

Table 5.14: Flavour composition of the sample of b tagged events in which a gluon splitting to $b\bar{b}$ (second column) and $c\bar{c}$ (third column) has occurred. The DURHAM algorithm was used.

In order to extract the gluon splitting events, topological and tagging arguments can be used. Since the pair of quarks emerging from a gluon splitting are mostly collinear, in a three-jet event these quarks are usually contained in the same jet. Furthermore, this gluon jet will tend to be more energetic than those jets coming from a gluon that has not split into heavy quarks. At the same time, if a tagging method is applied on the gluon jet, a difference will be observed on the tagging variable when that jet contains a pair of heavy quarks.

Figure 5.27 compares, for three-jet events at $y_c = 0.02$ for DURHAM, some normalized distributions for events without a gluon splitting (full line) with events with a gluon splitting to $b\bar{b}$ (dashed line) and to $c\bar{c}$ (dotted line) for the sample of simulated b tagged events. As just mentioned, the gluon jet for gluon splitting events is observed to be more energetic and the combined tagging variable of that jet is larger, indicating the presence of tracks displaced from the interaction point.

However, for the real data, the identification of the gluon jet among the three jets is not trivial. If the three jets are ordered in decreasing energy and having in mind that the least energetic jet (jet 3) is the most likely to be the gluon jet, some of the distributions that could be used are,

* X_{jet1}: The tagging combined variable of the most energetic jet, which is a jet coming from a quark in most cases. It allows to get rid of events $Z^0 \to \ell\bar{\ell}g \to \ell\bar{\ell}Q\overline{Q}$ since for these kind of events X_{jet1} peaks at low values.
* X_{jet3}: The tagging combined variable of the least energetic jet, which is the most likely to be the gluon jet. For events of any flavour containing a gluon splitting this variable extends to larger values since the gluon jet contains heavy quarks.
* x_{E-jet3}: Scaled energy, with respect to the beam energy, of the least energetic jet. It peaks at higher values for events with a gluon splitting.
* $M_{inv}(12)$: Invariant mass of the pair of jets with the highest energy. It peaks at lower values for events containing a gluon splitting since the gluon jet in this case is more energetic.

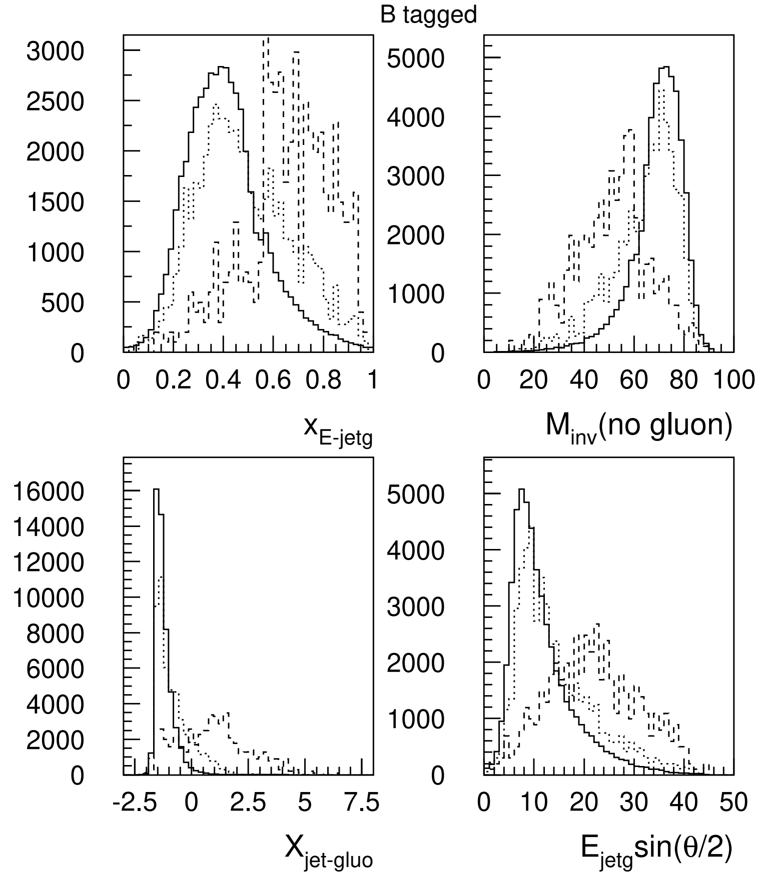

Figure 5.27: Distribution of the scaled energy of the gluon jet, x_{E-jetg}, invariant mass of the two quark jets, M_{inv}(no gluon), tagging combined variable of the gluon jet, $X_{jet-gluo}$, and $E_{jetg}\sin(\theta/2)$ where E_{jetg} is the gluon jet energy and θ the angle formed with its closest jet. All events are three-jet events at $y_c = 0.02$ for DURHAM. The full line corresponds to events without a gluon splitting, the dashed line are events with a gluon splitting to $b\bar{b}$ and the dotted line represents those with a gluon splitting to $c\bar{c}$.

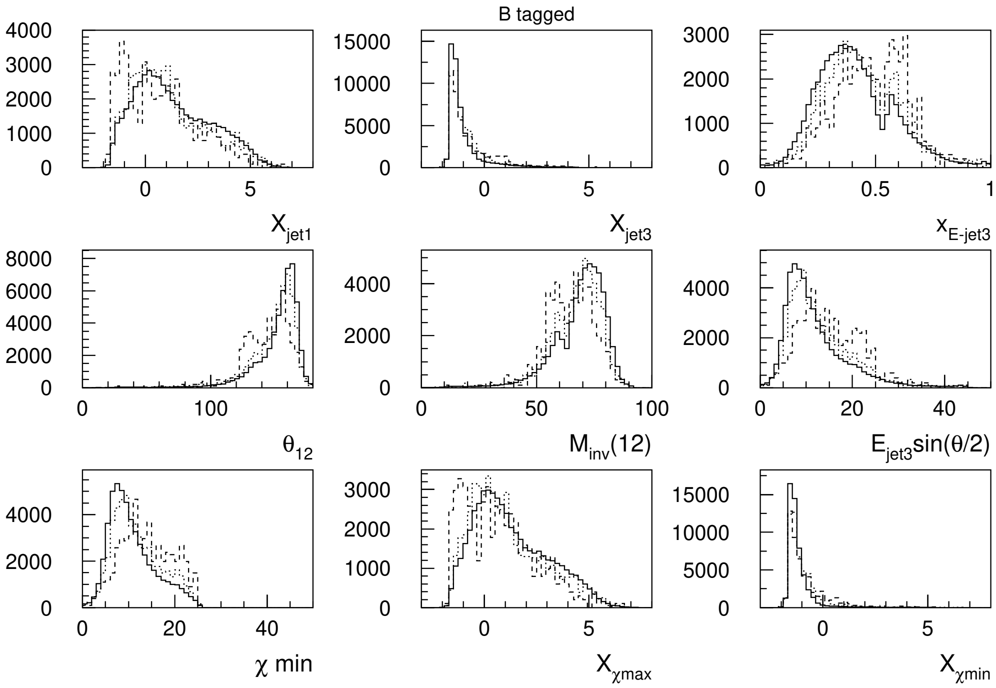

Figure 5.28: Distribution of X_{jet1}, X_{jet3}, x_{E-jet3}, θ_{12}, $M_{inv}(12)$, χ_3, χ_{min}, $X_{\chi_{min}}$ and $X_{\chi_{max}}$. All events are three-jet events at $y_c = 0.02$ for DURHAM. The full line corresponds to events without a gluon splitting, the dashed line are events with a gluon splitting to $b\bar{b}$ and the dotted line represents those with a gluon splitting to $c\bar{c}$.

* θ_{12}: Angle between the two most energetic jets. For events with a gluon splitting it peaks at lower values.
* $\chi_3 = E_{jet3}\sin(\theta/2)$, where θ is the angle between jet 3 and its closest jet. This variable extends to larger values for events with a gluon splitting.
* χ_{min}: Minimum of χ_1, χ_2 and χ_3, where $\chi_n = E_{jetn}\sin(\theta/2)$. As χ_3, it tends to larger values for gluon splitting events.
* $X_{\chi_{min}}$: Tagging combined variable for the jet with minimum χ, it behaves similarly to X_{jet3} but the discriminative power is a bit higher.
* $X_{\chi_{max}}$: Tagging combined variable for the jet with maximum χ, it behaves similarly to X_{jet1} but with a higher discriminative power.

Figure 5.28 shows, for the b tagged sample, the above distributions for three-jet events at $y_c = 0.02$ with DURHAM for events with no gluon splitting (full line), with a gluon splitting to $b\bar{b}$ (dashed line) and to $c\bar{c}$ (dotted line). All distributions are normalized to the number of events without a gluon splitting.

For all listed variables, the signal to background, where signal means those events without a gluon splitting and background means events with a gluon splitting to $Q\overline{Q}$ ($Q = b$ or c), was calculated as a function of the cut applied in the discriminative variable. Figure 5.29 shows the ratio signal to background, S/B, as a function of the cut on χ_{min} for $Q = b$ and c. The cut efficiency, defined

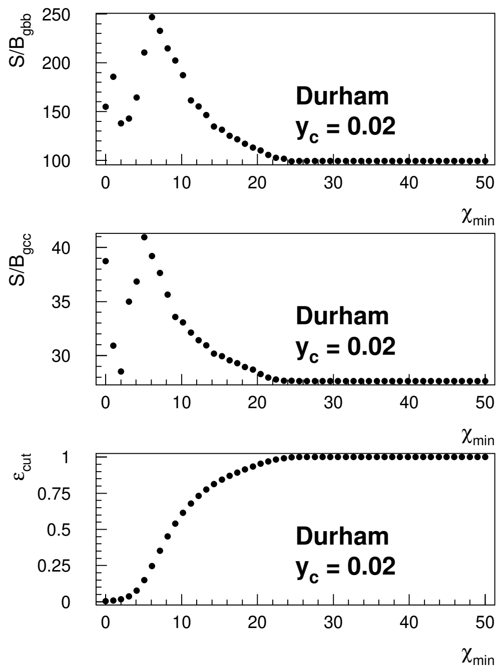

Figure 5.29: Signal to background and cut efficiency as a function of the cut on χ_{min} for the case in which the background are events with a gluon splitting to $b\bar{b}$ and when they are events containing a gluon splitting to $c\bar{c}$, for DURHAM at $y_c = 0.02$.

as the fraction of signal events that remain for each cut, is also shown. Table 5.15 shows the values obtained of signal to background for a cut efficiency of 90% for different discriminative variables. χ_{min} and $X_{\chi_{min}}$ are the variables with the highest discriminative power.

Variable	$S/B_{gbb}(90\%)$	$S/B_{gcc}(90\%)$
χ_{min}	122	29
χ_3	119	29
X_{jet1}	121	28
X_{jet3}	117	29
$X_{\chi_{max}}$	121	28
$X_{\chi_{min}}$	122	33

Table 5.15: Signal to background for a cut efficiency of 90% for the case in which the background are events with a $g \to b\bar{b}$ and when they are events containing $g \to c\bar{c}$, for DURHAM at $y_c = 0.02$.

As an example, figure 5.30 shows the error due to the measured gluon splitting rate uncertainty, divided by the measured $R_3^{b\ell}$ before its gluon splitting correction, as a function of y_c for different cuts on $X_{\chi_{min}}$ compared to the case in which no cut is made. For DURHAM, at $y_c = 0.02$, the gluon splitting uncertainty is reduced from 3‰ to about 2‰ when the cut $X_{\chi_{min}} < -0.5$ is made, where about 5%

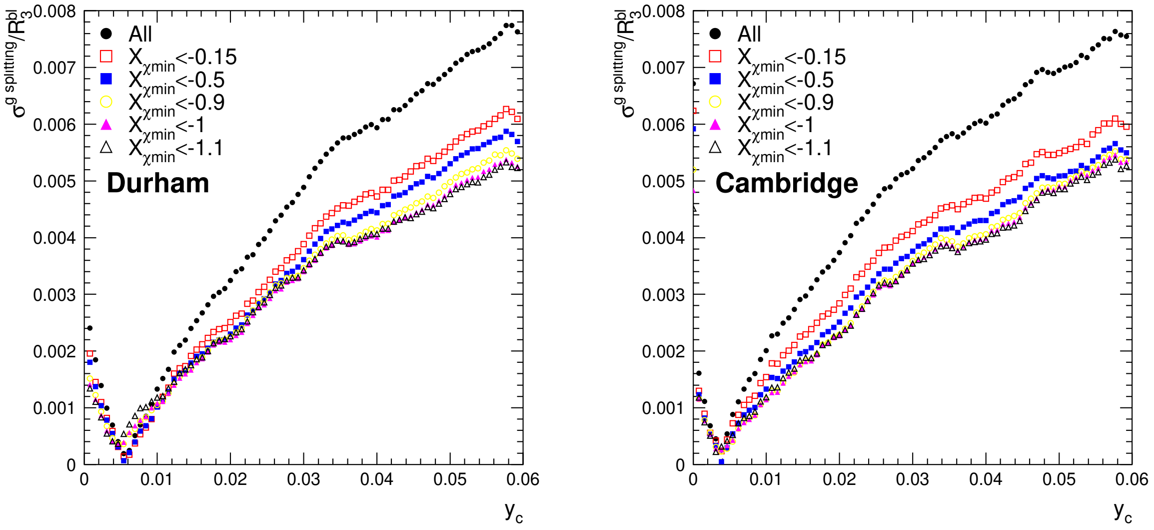

Figure 5.30: Gluon splitting uncertainty divided by the measured $R_3^{b\ell}$ (without the gluon splitting correction) as a function of y_c for DURHAM (left) and CAMBRIDGE (right) for different cuts on $X_{\chi_{min}}$ compared to the case in which no cut is made.

of non gluon splitting events are lost. For CAMBRIDGE, at $y_c = 0.01$, the error is reduced from 2‰ to about 1‰ for the same cut, where now about 3% of the signal events are lost.

The conclusion of this study is that the dependence of the measured $R_3^{b\ell}$ with the gluon splitting rate could be reduced substantially by making some cuts on several discriminative distributions for b tagged events, reducing then the fraction of events containing gluon splittings. Considering the increased produced on the statistical uncertainty when these kind of cuts are made, the decision was to stay with the whole b tagged sample without making any cut. This kind of cuts would be though very interesting for a future combination of all LEP data and that is the reason why it has been presented here.

– Tagging: It was evaluated by varying the purities and contamination factors of the correction formula Eq. (5.8) within their uncertainty.

The errors on P_b and P_ℓ were obtained from the known relative error of the b tagging and mistagging efficiencies. The tagging efficiencies, ϵ_Q^q $(q = b, \ell)$, are defined as the number of q-quark hadronic events that are tagged as q. The mistagging efficiencies are the fraction of hadronic non q-quark events that are tagged as q. In general,

$$\epsilon_Q^{q'} = \frac{N_Q^{had-q'}}{N^{had-q'}} \tag{5.15}$$

where $Q = B, L$ denote the tagged sample and q' the real event flavour.

The relative uncertainties for the b tagging and mistagging efficiencies are taken from [135], $\Delta\epsilon_B^b/\epsilon_B^b = 3\%$ and $\Delta\epsilon_B^\ell/\epsilon_B^\ell = \Delta\epsilon_B^c/\epsilon_B^c = 8\%$. Since ℓ tagging is just anti-b tagging, i.e. that $\epsilon_L^q = 1 - \epsilon_B^q$ and therefore $\Delta\epsilon_L^q = \Delta\epsilon_B^q$ $(q = b, c, \ell)$ for the same cut value, the relative uncertainties for the ℓ tagging and mistagging efficiencies can be obtained as,

$$\frac{\Delta\epsilon_L^q}{\epsilon_L^q} = \frac{\Delta\epsilon_B^q}{\epsilon_B^q}\left(\frac{N^{had-q} - N_L^{had-q}}{N_L^{had-q}}\right) \tag{5.16}$$

At the working point used to tag ℓ quark events, the values obtained are then $\Delta\epsilon_L^b/\epsilon_L^b = 32\%$, $\Delta\epsilon_L^\ell/\epsilon_L^\ell = 1\%$ and $\Delta\epsilon_L^c/\epsilon_L^c = 6\%$.

The purities of the tagged samples can be expressed in terms of the tagging and mistagging efficiencies as,

$$P_b = \frac{N_B^{had-b}}{\sum_{q=b,c,\ell} N_B^{had-q}} = \frac{\epsilon_B^b N^{had-b}}{\sum_{q=b,c,\ell}\epsilon_B^q N^{had-q}} \tag{5.17}$$

$$P_\ell = \frac{N_L^{had-b}}{\sum_{q=b,c,\ell} N_L^{had-q}} = \frac{\epsilon_L^b N^{had-b}}{\sum_{q=b,c,\ell}\epsilon_L^q N^{had-q}}$$

The efficiencies were then varied within their uncertainties and the maximum variation observed in each purity was taken as its uncertainty. The result was P_b = 91.2 ± 1.0 % and P_ℓ = 82.3 ± 1.6 %.

For each variation of the purities in the correction formula of Eq. (5.8) the contamination factors were varied accordingly having in mind that $\sum_{q'=b,c,\ell} c_Q^{q'} = 1$ (where $c_Q^q \equiv P_q$) and keeping the factors c_B^ℓ/c_B^c and c_L^b/c_L^c constant.

The purities and contaminations of the b and ℓ tagged samples were varied separately. Figure 5.31 shows the effect on $R_3^{b\ell}$ at parton level corrected by Eq. (5.8) when P_b and P_ℓ are increased and decreased within 1σ. The effects due to the P_b and P_ℓ variation were added in quadrature to give the error due to the tagging procedure. This is of about 3‰ for DURHAM at $y_c = 0.02$ and about 2‰ for CAMBRIDGE at $y_c = 0.01$.

– Jet identification: It was evaluated by varying the cut applied to distinguish the b quark jets from the gluon jet in a b tagged event (described in Section 4.3) within cut efficiencies of 80% (which corresponds to the cut $X_{eff-ij}(\max) > -0.18$) to 100%. Half of the difference observed in the measured $R_3^{b\ell}$ at parton level is taken as the error due to the jet identification. For example, this uncertainty is about 2‰ for DURHAM and CAMBRIDGE at $y_c = 0.02$ and 0.01 respectively.

The breakdown of all considered statistical and systematic uncertainties of $R_3^{b\ell}$ at parton level is shown in figure 5.32 as a function of y_c for both algorithms. For both algorithms, at y_c values around 0.02 and 0.01 for DURHAM and CAMBRIDGE respectively, the error due to the limited statistics of the data and simulated samples dominates.

Regarding systematic errors, for DURHAM the uncertainties due to the b mass parameter and the tagging procedure dominate (3.4‰), although the one due to the gluon splitting

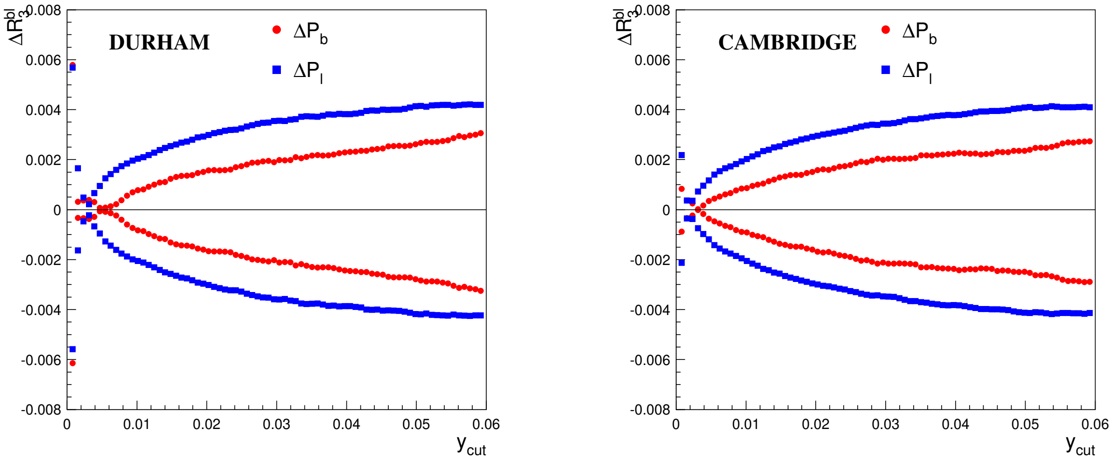

Figure 5.31: Variation of $R_3^{b\ell}$ corrected by Eq. (5.8) as a function of y_c produced when P_b and P_ℓ are increased and decreased by 1 σ, for DURHAM (left) and CAMBRIDGE (right) jet algorithms.

rates ($\sim$3‰) is very close. Smaller contributions come from the hadronization model, jet identification and the tuning of the generator, which are at the level of 2‰.

For the case of CAMBRIDGE, at y_c around 0.01, the dominant systematic error comes from the b mass parameter uncertainty of the generator ($\sim$3.5‰), which increases for smaller y_c values. It follows the fragmentation model uncertainty ($\sim$3‰) and the tagging, jet identification and gluon splitting rates uncertainties, which are around 2‰. The smallest contribution comes from the tuning parameters, which is only $\sim$1‰.

If all statistical and systematic uncertainties are added in quadrature, as shown in figure 5.33, the measurement of $R_3^{b\ell}$ at parton level is dominated by systematics for both jet clustering algorithms at the just mentioned y_c region.

5.4 The measured $R_3^{b\ell}$ at parton level

After all the corrections described in Section 5.2, the $R_3^{b\ell}$ obtained at parton level is shown in figure 5.34 as a function of y_c. The LO and NLO theoretical curves in terms of the pole and the running mass are also shown in the plot, for $M_b = 5$ GeV/c^2 and $m_b(M_Z) = 3$ GeV/c^2.

The final result was obtained by averaging the results of each separate year since, as figure 5.35 shows for a given y_c, all of them give compatible results. In fact the χ^2/ν obtained when the mean value is computed is of 0.7 and 1.2 for DURHAM and CAMBRIDGE for the y_c values of the figure.

The jet resolution parameters of $y_c = 0.02$ and $y_c = 0.0085$ were chosen to give the final result for DURHAM and CAMBRIDGE respectively, so to keep the correction, the total uncertainty and the four-jet rate small. As shown in figure 5.19, the hadronization correction is constant for large values of y_c and it starts to decrease (increase) at $y_c = 0.015$ ($y_c = 0.005$) for DURHAM (CAMBRIDGE). In order not to be close to that region and to have the smallest uncertainty on $R_3^{b\ell}$ (see figure 5.33) these y_c values were selected. The measured $R_3^{b\ell}$ for these

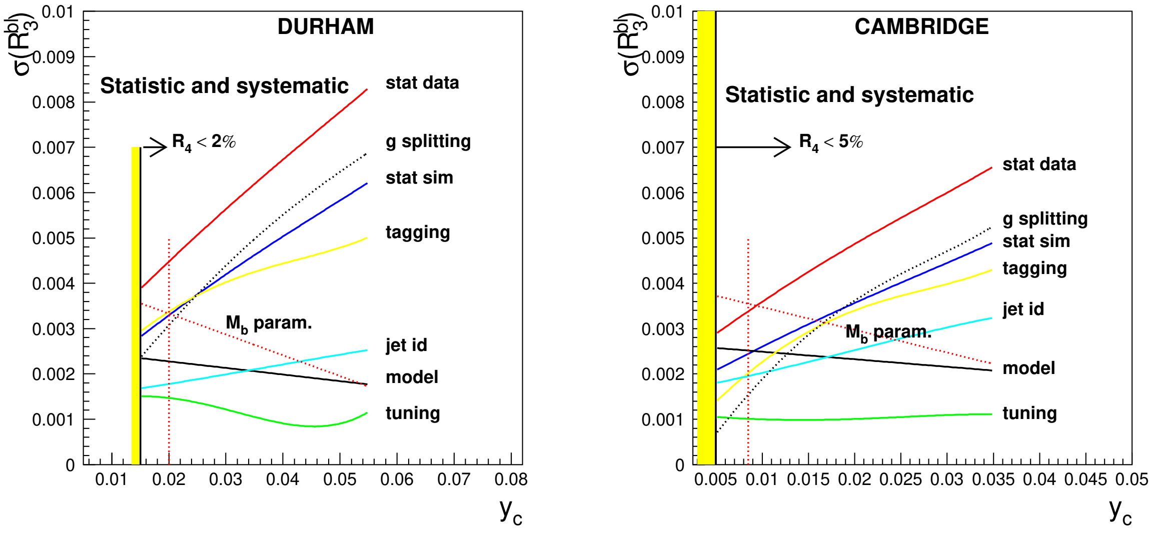

Figure 5.32: Individual statistical and systematic errors of $R_3^{b\ell}$ at parton level as a function of y_c for Durham (left) and Cambridge (right).

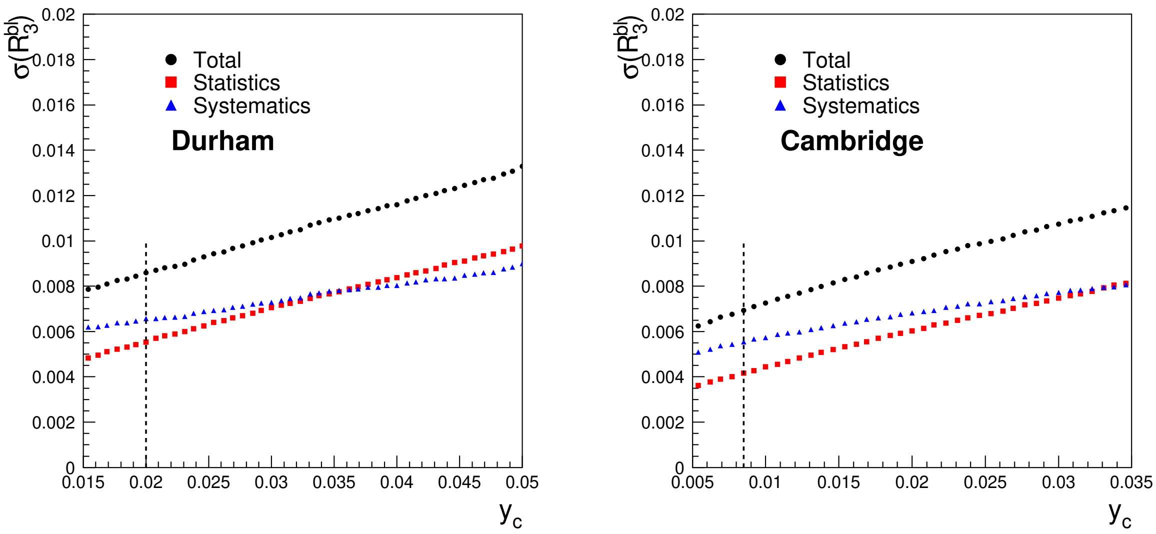

Figure 5.33: Total, statistical and systematic errors of $R_3^{b\ell}$ at parton level as a function of y_c for Durham (left) and Cambridge (right). The vertical lines show the y_c working points selected.

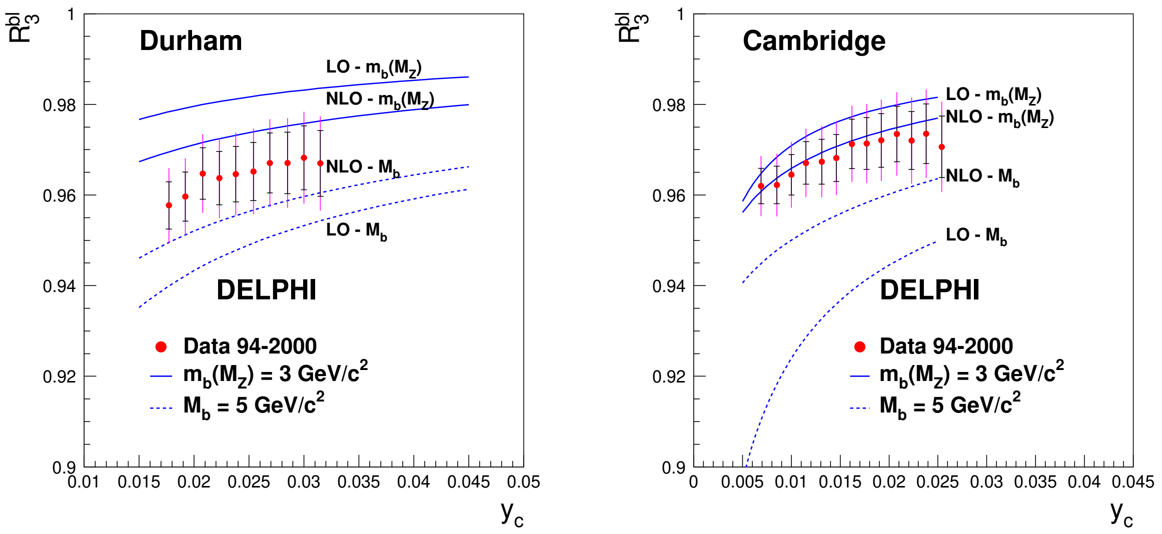

Figure 5.34: $R_3^{b\ell}$ as a function of y_c obtained at parton level compared with the LO and NLO theoretical predictions calculated in terms of a pole mass of $M_b = 5$ GeV/c^2 and in terms of a running mass of $m_b(M_Z) = 3$ GeV/c^2.

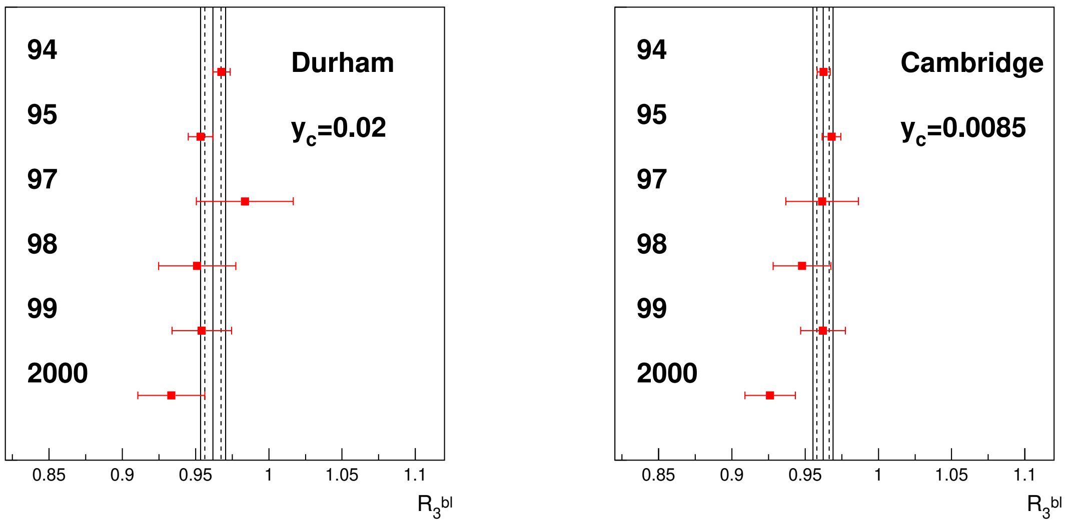

Figure 5.35: $R_3^{b\ell}$ at parton level obtained for each analysed year for a fixed y_c for DURHAM (left) and CAMBRIDGE (right). The error bars represent the statistical error. The vertical lines show the average value with its statistical and total error.

y_c values and its different experimental uncertainties are shown in table 5.16.

Data 1994-2000	$R_3^{b\ell-Durham}(y_c = 0.02)$	$R_3^{b\ell-Cambridge}(y_c = 0.0085)$
Value	0.9619	0.9622
Statistical data	±0.0045	±0.0034
Statistical simulation	±0.0033	±0.0024
Fragmentation Tuning	±0.0015	±0.0010
Fragmentation Model	±0.0022	±0.0025
b mass parameter	±0.0034	±0.0036
Gluon Splitting	±0.0031	±0.0015
Tagging	$^{+0.0034}_{-0.0035}$	±0.0021
Jet identification	±0.0018	±0.0020

Table 5.16: Values of $R_3^{b\ell}$ with DURHAM and CAMBRIDGE algorithms and break-down of their associated errors (statistical and systematic) for $y_c = 0.02$ and y_c=0.0085 respectively.

5.5 The measured $R_3^{b\ell}$ at hadron level

$R_3^{b\ell}$ was also measured at hadron level by following the same correction procedure described in 5.2 but without correcting for the hadronization process. The purpose of this measurement was twofold: First, to compare with the prediction given by the PYTHIA and HERWIG generators in order to study how well b mass effects are modeled. Second, a value at hadron level could be useful to have in order to correct for more precise future fragmentation models.

Figure 5.36 shows, as a function of the y_c, the measured $R_3^{b\ell}$ at hadron level together with the curves predicted for the two generators. For the case of PYTHIA, the curves are shown for the Peterson and Bowler b fragmentation functions. For large values of y_c, both Monte Carlo describe well the data while, for small values, HERWIG gives a better prediction than PYTHIA, which tends to overestimate the mass effect.

At hadron level, systematic errors are only due to detector and physics modeling effects. These uncertainties, together with the statistical ones, are shown in figure 5.37 as a function of y_c.

5.6 Summary

During this chapter the analysis procedure used to measure the $R_3^{b\ell}$ observable with the data collected by the DELPHI detector from 1994 until 2000 at the Z^0 peak has been described. Two jet clustering algorithms were used, DURHAM and CAMBRIDGE, for which NLO calculations taking mass effects into account are available [9, 14].

First of all, a sample of 1.4×10^6 (1.3×10^6) hadronic Z^0 decays was selected for the DURHAM (CAMBRIDGE) algorithm. In order to distinguish the b quark initiated events

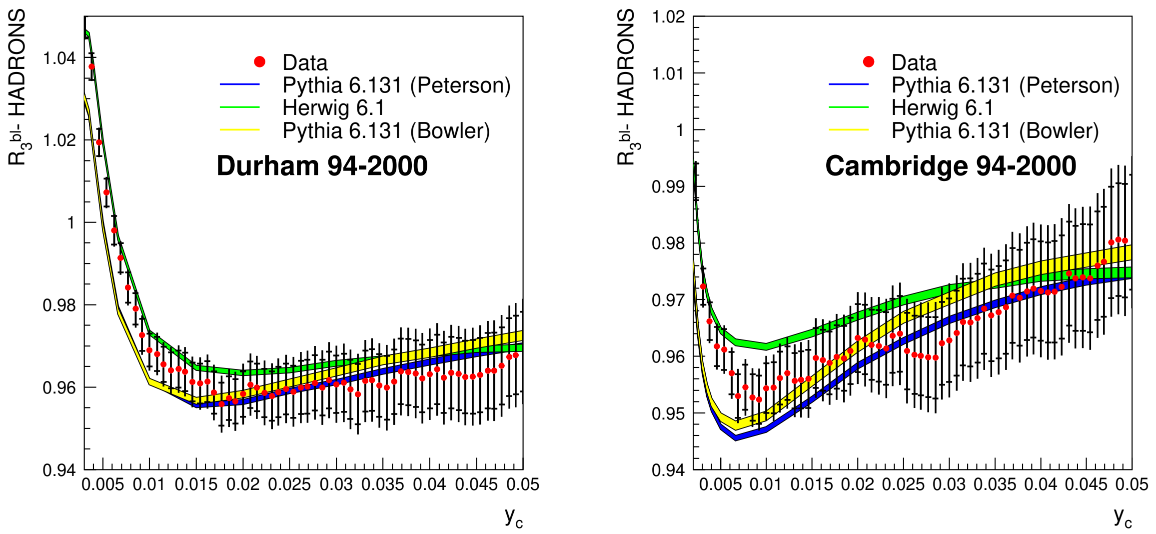

Figure 5.36: $R_3^{b\ell}$ at hadron level as a function of y_c compared with the PYTHIA 6.131 (with Peterson and Bowler fragmentation b functions) and HERWIG 6.1 predictions.

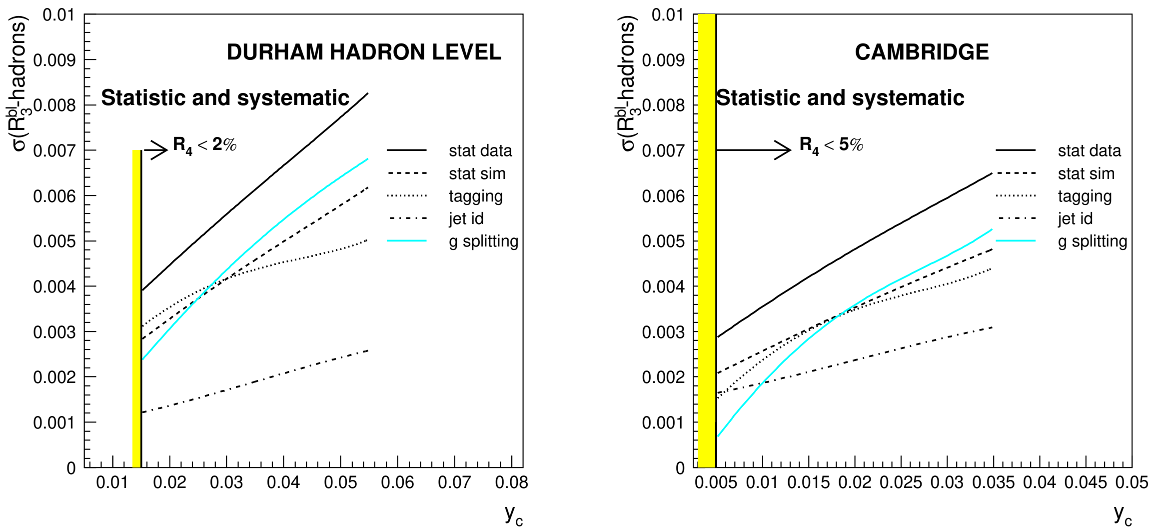

Figure 5.37: Statistical and systematic uncertainties of $R_3^{b\ell}$ at hadron level as a function of y_c for DURHAM (left) and CAMBRIDGE (right).

from those originated by ℓ quarks, the two b tagging methods developed in DELPHI were studied: the impact parameter and the combined technique. The former discriminates the flavour of the event by calculating the probability of having all particles compatible with being generated in the event interaction point by measuring the charged particle impact parameters. For the second technique, an optimal combination of a set of discriminating variables defined for each reconstructed jet was performed leading to a single discriminative variable per event. The tagging of ℓ quark events was achieved by anti-b tagging.

Regarding the stability of the final result, the combined technique was used to select b events and the impact parameter method for tagging ℓ quarks. For the b tagged sample, the combined technique was found to be more optimal for the identification of gluon and quark jets, also based on stability arguments. The energy of the b jets was then measured and the cut $x_E^b(\text{jet}) \geq 0.55$ applied. The selected b and ℓ samples contained about 170,000 and 900,000 events respectively, with purities of 91% and 82% each.

The two jet clustering algorithms were applied to the b and ℓ samples in order to get the $R_3^{b\ell}$ observable at detector level. The result obtained was then corrected for detector effects (including the tagging method) and the hadronization process in order to bring the observable to parton level. The detector correction was given by the DELSIM simulated data, which was reweighted in order to have the measured heavy quark gluon splitting rates. The hadronization correction was taken as the mean of that given by the cluster model of HERWIG 6.1 and the string model of PYTHIA 6.131 with the Peterson and Bowler b fragmentation functions. The b mass parameter of the generator was taken as the pole mass measured in Ref. [74].

The detector correction made $R_3^{b\ell}$ decrease (increase) in about 3% (1%) for the DURHAM (CAMBRIDGE) algorithm at $y_c = 0.02$ ($y_c = 0.01$). The effect produced by the hadronization process correction at the same y_c values was to increase the observable in about 5‰ (1%) for DURHAM (CAMBRIDGE). The total correction applied to $R_3^{b\ell}$ to bring it from detector to parton level was a decrease (increase) of about 2% for DURHAM (CAMBRIDGE).

Different systematic uncertainties affecting the detector and hadronization corrections were considered. Detector correction uncertainties are due to imperfections on physics and detector modeling as: uncertainties on the measured gluon splitting rates, those affecting the tagging procedure (such as detector resolution and B physics modeling) and those affecting the b quark jets identification and their measured energy.

The different sources of uncertainties affecting the hadronization correction (model, tuning and b mass parameter) were already discussed in previous chapter. In this chapter, the impact on the measured $R_3^{b\ell}$ at parton level was computed.

The total statistical uncertainty due to the limited size of the real and simulated data was found to be greater than any of the individual systematic uncertainties. At the y_c values chosen to measure $R_3^{b\ell}$, 0.02 for DURHAM and 0.0085 for CAMBRIDGE, we have that: For DURHAM the uncertainties due to the b mass parameter and the tagging procedure dominate (3.4‰), although the one due to the gluon splitting rates (∼3‰) is very close. Smaller contributions come from the hadronization model, jet identification and the tuning of the generator, which are at the level of 2‰. For the case of CAMBRIDGE, the dominant systematic error comes from the b mass parameter uncertainty of the generator (∼3.5‰), which increases for smaller y_c values. It follows the fragmentation model uncertainty (∼3‰)

and the tagging, jet identification and gluon splitting rates uncertainties, which are around 2‰. The smallest contribution comes from the tuning parameters, which is only ∼1‰.

The $R_3^{b\ell}$ observable was also measured at hadron level and the result was compared with the predictions given by the PYTHIA and HERWIG generators. For large values of y_c, both describe well the data while, for small values, HERWIG gives a better prediction than PYTHIA, which tends to overestimate the mass effect.

Chapter 6

Results and discussion

The measurement of the $R_3^{b\ell}$ observable at parton level obtained in previous chapter, when compared with the NLO massive calculations of [9,14], can be used to: Extract the b quark mass assuming α_s universality or take as an input the b quark mass measured at threshold and extract the ratio of α_s for b and ℓ quark events.

In this chapter the results obtained with the two alternatives will be shown, although more emphasis will be put on the measurement of the b quark mass. For this case, both quark mass definitions, the running mass at the M_Z scale and the pole mass, will be derived from the measured observable. The different sources of theoretical uncertainties will be also discussed.

These results will be compared with other measurements performed at the Z^0 peak at LEP and SLC.

6.1 Determination of the b quark mass

As described in Section 1.5.5, NLO massive calculations can be used to determine the b quark mass from the measured $R_3^{b\ell}$ for each jet clustering algorithm. The theoretical calculations can only be used in a given range of y_c, which for DURHAM is $y_c \in [0.01, 0.1]$ [9] and for CAMBRIDGE $y_c \in [0.005, 0.025]$ [14].

For the case of the running mass extraction, $m_b(M_Z)$, two different methods are available. The former is based on the used of Eq. (1.67), i.e. the parameterization of $R_3^{b\ell}$ in terms of the pole mass, and the second one is based on the used of the $R_3^{b\ell}$ expression in terms of the running mass, i.e. making use of Eq. (1.68).

For both methods, the result depends on the value taken for the arbitrary scale μ. Figure 6.1 shows, for the measured values of $R_3^{b\ell}$ for DURHAM and CAMBRIDGE at $y_c = 0.02$ and $y_c = 0.0085$ respectively, the extracted $m_b(M_Z)$ for different values of μ within the range $[M_Z/10, 2M_Z]$. As can be seen, both methods give different values for $m_b(M_Z)$ at the same scale μ. The average of the results obtained at $\mu = M_Z$ with the two methods is taken as the measured $m_b(M_Z)$.

As also mentioned in Section 1.5.5, the error due to uncomputed higher order terms in the perturbative series, i.e. the theoretical uncertainty, was estimated by considering the following sources:

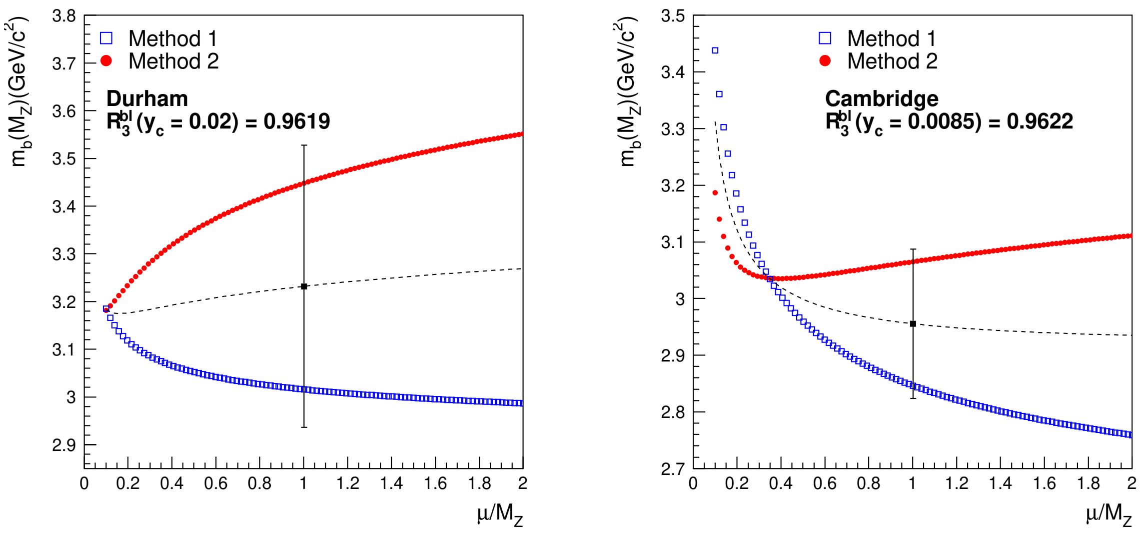

Figure 6.1: The extracted $m_b(M_Z)$ from the measured $R_3^{b\ell}$ as a function of the scale μ used, for Durham (left) and Cambridge (right). The result obtained for each method is shown, as well as the average of the two (dashed line). The result given at $\mu = M_Z$ is also displayed, where the error is just the theoretical one.

- μ dependence: The μ scale was varied in the second method from $M_Z/2$ to $2M_Z$ and half of the difference of the result obtained on $m_b(M_Z)$ was taken as the μ scale error.
- Mass ambiguity: Half of the difference between the $m_b(M_Z)$ obtained for each method at $\mu = M_Z$ was taken as the error due to the mass ambiguity.
- α_s uncertainty: $\alpha_s(M_Z) = 0.1183 \pm 0.0027$ [113] was varied within its uncertainty and the effect on $m_b(M_Z)$ was taken as the error due to the uncertainty on α_s.

Figure 6.2 shows the total theoretical uncertainty on $m_b(M_Z)$, together with its three different contributions considered, as a function of y_c for both algorithms, obtained from the measured $R_3^{b\ell}(y_c)$. For both jet algorithms, the dominant contribution to the total error comes by far from the mass ambiguity and the error due to the α_s uncertainty is negligible.

Another important aspect to stress is that Cambridge gives a smaller theoretical uncertainty than Durham, specially for small y_c values.

In order to compare the size of the theoretical error with the experimental uncertainties, figure 6.3 shows the theoretical error on $m_b(M_Z)$ together with the statistical and systematic experimental errors as a function of y_c for both jet clustering algorithms. As can be seen, at the y_c value in which we measure (vertical lines in the plots), the error coming from the uncertainty on the NLO calculations has the smallest contribution to the total error for Cambridge while for Durham it is as big as the statistical uncertainty.

As already mentioned in Section 5.4, the jet resolution parameters of $y_c = 0.02$ and 0.0085 for Durham and Cambridge respectively were chosen to give the final results of $m_b(M_Z)$.

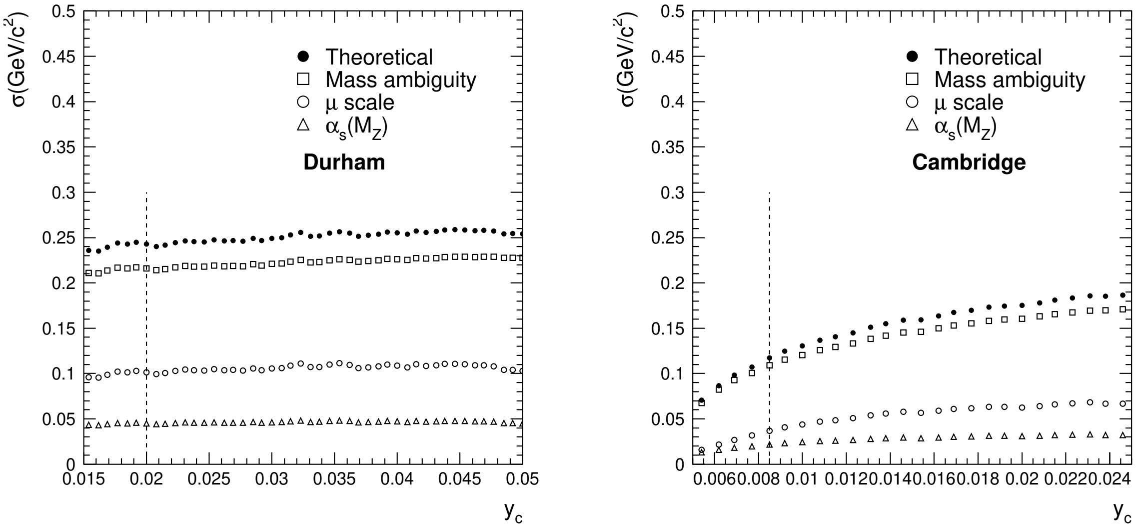

Figure 6.2: Theoretical uncertainty of $m_b(M_Z)$ and its different contributions (mass ambiguity, μ dependence and α_s uncertainty) as a function of y_c obtained from the measured values of $R_3^{b\ell}$ for DURHAM (left) and CAMBRIDGE (right). The vertical line represents the y_c value chosen to give the final $m_b(M_Z)$.

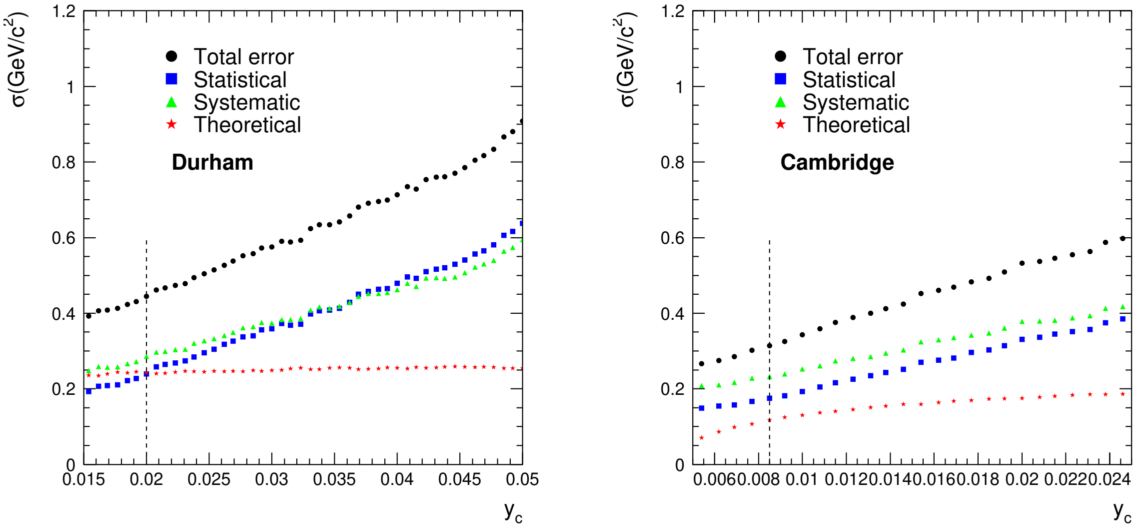

Figure 6.3: Total, statistical, systematic and theoretical uncertainty of $m_b(M_Z)$ as a function of y_c obtained from the measured values of $R_3^{b\ell}$ for DURHAM (left) and CAMBRIDGE (right). The vertical line represents the y_c value chosen to give the final $m_b(M_Z)$.

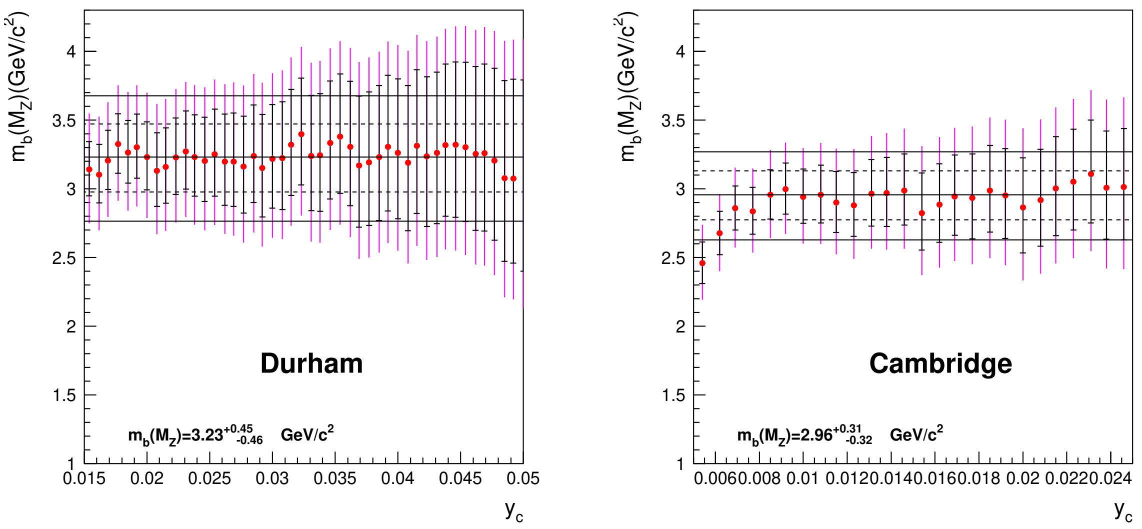

Figure 6.4: $m_b(M_z)$ extracted from the measured $R_3^{b\ell}(y_c)$ as a function of y_c for DURHAM (left) and CAMBRIDGE (right). The central horizontal lines show the $m_b(M_z)$ obtained at $y_c = 0.02$ and 0.0085 for DURHAM and CAMBRIDGE respectively. The dashed and full external lines represent, respectively, its statistical and total error band.

These are,

$$m_b(M_Z) = 3.23^{+0.24}_{-0.25}\ \text{(stat)}^{+0.19}_{-0.20}\ \text{(had)}^{+0.22}_{-0.23}\ \text{(exp)} \pm 0.24\ \text{(theo) GeV/c}^2 \tag{6.1}$$

when DURHAM is used to reconstruct jets and,

$$m_b(M_Z) = 2.96^{+0.17}_{-0.18}\ \text{(stat)} \pm 0.19\ \text{(had)} \pm 0.14\ \text{(exp)} \pm 0.12\ \text{(theo) GeV/c}^2 \tag{6.2}$$

when CAMBRIDGE is the algorithm used. The systematic uncertainties have been divided into the ones due to hadronization (had) and those due to the detector and physics modeling (exp). The contribution of each individual source of uncertainty is shown in table 6.1.

Both results are compatible with each other within their statistical error. The result obtained with CAMBRIDGE is much more precise than the one obtained with DURHAM, mainly due to the reduction of the theoretical uncertainty, reaching a total error of $^{+310}_{-320}$ MeV/c^2 instead of $^{+450}_{-460}$ MeV/c^2.

It was checked that any other value of y_c would have led to a compatible result. This is shown in figure 6.4 where the extracted $m_b(M_Z)$ for each measured $R_3^{b\ell}(y_c)$ is shown for different y_c values within the theoretically appropriate range.

A combination of the results obtained with both jet algorithms can be made provided the correlation between the two observables is known. The correlation factor between the DURHAM and CAMBRIDGE $R_3^{b\ell}$ observable at parton level was calculated for different values of y_c. For this purpose, 95 samples of 250,000 b and ℓ quark events were generated and the two jet clustering algorithms were applied to each of them.

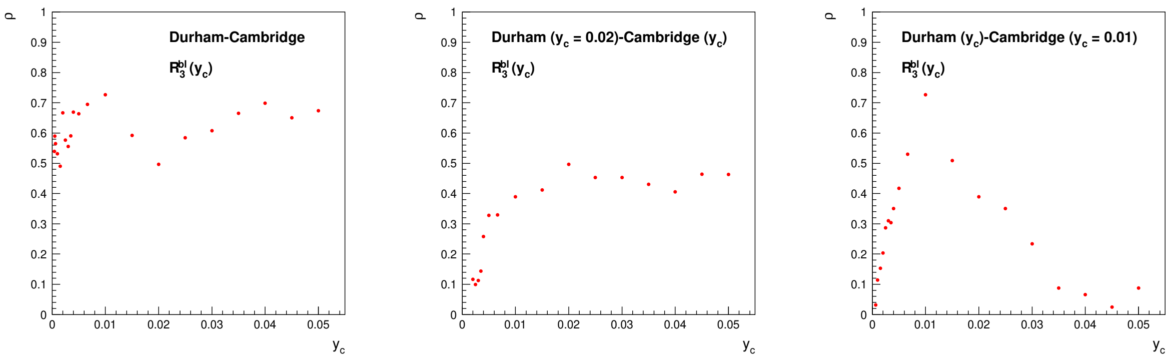

Figure 6.5: Correlation factors (ρ) for $R_3^{b\ell}$ at parton level between DURHAM and CAMBRIDGE for different combination of y_c. (Left) The ρ is calculated for the same y_c for both algorithms. (Middle) It shows the ρ for $R_3^{b\ell}$ with DURHAM at $y_c = 0.02$ as a function of the CAMBRIDGE y_c. (Right) It represents the ρ for $R_3^{b\ell}$ with CAMBRIDGE at $y_c = 0.01$ as a function of the DURHAM y_c.

Figure 6.5 shows the correlation factor obtained for $R_3^{b\ell}$ between the two algorithms for different y_c values. The first plot of the figure shows the correlation factors when both algorithms reconstruct jets at the same y_c value. The middle plot shows the correlation between DURHAM at $y_c = 0.02$ and different values of y_c for CAMBRIDGE and in the last plot CAMBRIDGE is fixed at $y_c = 0.01$.

If the measurements performed at $y_c = 0.02$ with DURHAM and $y_c = 0.0085$ with CAMBRIDGE are combined with a correlation factor of 0.4 for the statistical errors, assuming that the systematic errors are completely correlated and that theoretical uncertainties are uncorrelated, the result obtained is:

$$m_b(M_Z) = 2.99 \pm 0.17 \text{ (stat)}^{+0.24}_{-0.25} \text{ (syst)} \pm 0.11 \text{ (theo) GeV/c}^2 \tag{6.3}$$

with a $\chi^2/\nu = 0.6$. With respect to the result obtained just with CAMBRIDGE, the theoretical and statistical uncertainties are reduced but the systematic error increases so that the total error remains the same, i.e. $^{+310}_{-320}$ MeV/c^2.

Apart from the running mass, the b quark pole mass, M_b, can also be extracted from the measured $R_3^{b\ell}$ using the NLO expression of $R_3^{b\ell}$ in terms of the b pole mass, i.e. Eq. (1.67). The M_b obtained does also depend on the μ scale used, coming from the dependence in $\alpha_s(\mu)$. This dependence is shown in figure 6.6 for the measured $R_3^{b\ell}$ with both algorithms.

The theoretical uncertainty in this case was considered as the contribution of just the μ scale dependence and the α_s uncertainty, but no error was given due to the mass ambiguity. The μ scale was varied within a larger range, from $M_Z/10$ to $2M_Z$. Again, the α_s uncertainty contribution to the total theoretical error was found to be negligible.

The measured b quark pole mass at $\mu = M_Z$ was found to be,

$$M_b = 4.48^{+0.30}_{-0.32} \text{ (stat)}^{+0.36}_{-0.39} \text{ (syst)} \pm 0.13 \text{ (theo) GeV/c}^2 \tag{6.4}$$

when DURHAM is used to reconstruct jets at $y_c = 0.02$ and,

$$M_b = 4.26^{+0.22}_{-0.23} \text{ (stat)}^{+0.30}_{-0.31} \text{ (syst)} \pm 0.44 \text{ (theo) GeV/c}^2 \tag{6.5}$$

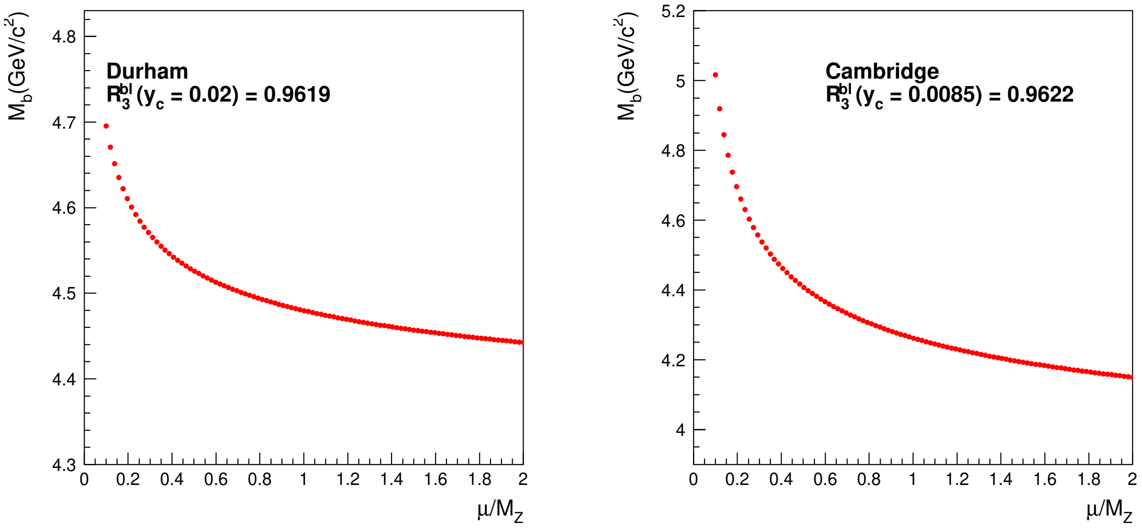

Figure 6.6: M_b as a function of the scale μ obtained from the measured $R_3^{b\ell}$ with DURHAM (left) and CAMBRIDGE (right).

when CAMBRIDGE is used instead at $y_c = 0.0085$.

These values are low compared with the results obtained when the b pole mass is measured at low energy, as for example the one of Ref. [74] (4.98 ± 0.13 GeV/c^2), although they are compatible within errors. For the case of DURHAM it is less than 1σ away and for CAMBRIDGE it is 1.2σ lower. It is important to remember that the theoretical uncertainty is underestimated since no mass ambiguity has been considered for the pole mass measurement, as it was considered for $m_b(M_Z)$. If instead of $\mu = M_Z$, a lower μ scale had been chosen, the M_b obtained would be higher and therefore closer to what it is measured at threshold (see figure 6.6).

Tables 6.2 and 6.3 show the values obtained for $m_b(M_Z)$ and M_b from the NLO calculations compared with the b quark mass obtained from the LO theoretical predictions. At LO, as mentioned in Section 1.5.5, no distinction between the pole and the running mass can be made and therefore a single value is obtained.

For CAMBRIDGE, the b quark mass obtained at LO is closer to the running mass extracted from the NLO calculations than to the pole mass. This means that at LO the data is better described if the mass is set to the running mass at M_Z than to the pole mass. For DURHAM instead the mass obtained at LO is closer to the pole mass measured at NLO than to the running mass, so the argument would be opposite.

6.2 Test of α_s flavour independence

The measurement of $R_3^{b\ell}$ can alternatively be used to test α_s flavour independence if the b quark mass is taken from the low energy measurements. The expression used is [7]:

$$\alpha_s^b/\alpha_s^\ell = R_3^{b\ell}(y_c) - H(m_b(M_Z), y_c) + \mathcal{O}(\alpha_s) \tag{6.6}$$

where $H(m_b(M_Z), y_c)$ is the mass correction term of Eq. (1.68).

Evolving the averaged b quark mass, $m_b(m_b) = 4.24 \pm 0.11$ GeV$/c^2$, from low energy measurements [75] to the M_Z scale using the 3-loop RGE, for $\alpha_s(M_Z) = 0.1183 \pm 0.0027$, one gets $m_b(M_Z) = 2.91 \pm 0.10$ GeV$/c^2$. If this value is taken as an input to compute $H(m_b(M_Z), y_c)$ the ratio α_s^b/α_s^ℓ measured is,

$$\alpha_s^b/\alpha_s^\ell = 0.989^{+0.006}_{-0.005}\ (\text{stat}) \pm 0.007\ (\text{syst}) \pm 0.005\ (\text{theo}) \tag{6.7}$$

for Durham at $y_c = 0.02$, and

$$\alpha_s^b/\alpha_s^\ell = 0.996 \pm 0.004\ (\text{stat}) \pm 0.006\ (\text{syst}) \pm 0.003\ (\text{theo}) \tag{6.8}$$

for Cambridge at $y_c = 0.0085$.

The statistical and systematic uncertainties are due to the experimental uncertainties of $R_3^{b\ell}$. The theoretical uncertainty reflects the uncertainty on the mass correction term $H(m_b(M_Z), y_c)$. This error comes from the uncertainty on the input $m_b(M_Z)$ used and on the uncalculated higher order terms.

The 0.10 GeV$/c^2$ uncertainty on $m_b(M_Z)$ was added in quadrature to the errors due to the μ scale dependence and mass ambiguity obtained in the previous section. $m_b(M_Z)$ was then varied within this error (± 0.26 for Durham and ± 0.15 for Cambridge) and the effect on α_s^b/α_s^ℓ was taken as the theoretical uncertainty. The error due to the α_s uncertainty was added in quadrature to the theoretical error but it was found to be negligible.

For both algorithms, α_s universality was verified with a precision of around 1%.

6.3 Comparison with other measurements at the M_Z scale

Mass effects at the M_Z energy scale have also been measured at other LEP and SLC experiments (Aleph, Opal and Sld) using jet rates or event shape observables. A comparison with different NLO calculations has been made to either measure the b quark mass or the α_s^b/α_s^ℓ ratio. In this section we will review these measurements and compare them with the Delphi results presented in this analysis.

- **SLD**:

  In order to measure $m_b(M_Z)$ the observable used by Brandenburg et al., with the data collected by the Sld experiment at SLC, was the $R_3^{b\ell}(y_c)$ ratio used by Delphi but with the difference than here $R_3^q(y_c)$ is the fraction of events classified as containing three or more jets instead of just three jets.

Six infrared and safe jet finding algorithms were used: E, E0, P, P0 [136], DURHAM and GENEVA [137] and NLO predictions in terms of $m_b(M_Z)$ were considered for all of them [79].

In order to measure $R_3^{b\ell}$, 77,896 hadronic Z^0 events were selected from the 150,000 recorded during 1993 and 1995 at SLD. A flavour tagging algorithm, based on the mass and momentum of the reconstructed secondary vertices, was then applied to select the b and ℓ quark samples, with purities of 90% and 91% respectively. Each of the six jet clustering algorithms was then applied to the selected samples. A Monte Carlo simulation of the detector, with events generated by JETSET 7.4 and previously tuned to the data, was used to correct for detector effects, the flavour tagging bias and the hadronization process. This means that the hadronization model used to correct the data was the string model with a b quark mass parameter of 5 GeV/c^2.

For each algorithm an optimal y_c value was selected so as to minimize the combined statistical and experimental systematic error. The results of $m_b(M_Z)$ for the six algorithms go from 2.3 to 4.1 GeV/c^2, with an r.m.s deviation of 0.7 GeV/c^2 [10].

The large spread of values was higher than expected, given the strong correlations between measurements using different jet clustering algorithms. This suggested that there was some additional source of uncertainty for each algorithm (~2% on $R_3^{b\ell}$, ~0.5 GeV/c^2 on the extracted $m_b(M_Z)$) that could be provided by the uncalculated higher order perturbative QCD contributions.

The best estimate of $m_b(M_Z)$ was obtained taking into account statistical correlations between the six results as well as correlations in the systematic uncertainties:

$$m_b(M_Z) = 2.56 \pm 0.27 \text{ (stat)}^{+0.28}_{-0.38} \text{ (syst)}^{+0.49}_{-1.48} \text{ (theo) GeV}/c^2 \qquad (6.9)$$

where the theoretical error corresponds to the sum in quadrature of the hadronization uncertainty ($^{+0.25}_{-1.42}$ GeV/c^2) and the propagation of the uncorrelated additional error of ± 0.02 considered for each $R_3^{b\ell}$ (± 0.42 GeV/c^2).

The SLD collaboration, besides $R_3^{b\ell}$, also measured the ratio $R_3^{c\ell}$ in order to test flavour independence of α_s for b, c and ℓ quarks. A mass of $m_b(M_Z) = 3.0 \pm 0.5$ GeV/c^2 was taken as input in the NLO calculations and the results were [138]:

$$\begin{aligned} \alpha_s^b/\alpha_s^\ell &= 1.004 \pm 0.018 \text{ (stat)}^{+0.026}_{-0.031} \text{ (syst)}^{+0.018}_{-0.029} \text{ (theo)} \\ \alpha_s^c/\alpha_s^\ell &= 1.036 \pm 0.043 \text{ (stat)}^{+0.041}_{-0.045} \text{ (syst)}^{+0.020}_{-0.018} \text{ (theo)} \end{aligned} \qquad (6.10)$$

corresponding to the average of the six algorithms, considering 100% correlation among them. The hadronization uncertainty and the r.m.s of the results obtained with the different algorithms are included in the theoretical error.

These $m_b(M_Z)$ and α_s^b/α_s^ℓ results are compatible with the obtained in our DELPHI analysis. The number of hadronic Z^0 decays used by SLD is about 6% of that used by DELPHI, an so the statistical uncertainty is larger, even though the information of six observables is used. The hadronization uncertainty is much larger too, specially due to the used of the Geneva, E, E0, P and P0 jet algorithms. The theoretical uncertainty is also greater since, in order to have a compatible result with the six algorithms, an additional source of uncertainty had to be introduced.

- **ALEPH**:

  The ALEPH experiment at LEP has taken as observables sensitive to b mass effects the three-jet rate defined with the DURHAM algorithm at a $y_c = 0.02$ and the first and second moments of some event shape variables: thrust T, the C parameter, the three to two jets transition value y_{32} and the total and wide jet broadening B_T and B_W [1].

  The ratios from b tagged events to an inclusive sample were measured for the above observables and from those ratios the b to ℓ quark ratios at parton level were derived.

  A sample of 2.3 million of Z^0 hadronic events were selected from the data recorded from 1991 to 1995. A b tagging method, based on the long B hadron lifetime, was applied to select b events with a purity of 83.1%.

  A simulation of the detector is used to correct for detector effects and the tagging procedure. The hadronization correction used was obtained with the string model of JETSET 7.4 setting the kinematical b mass to 4.75 GeV/c^2.

  The requirement that the NLO contribution to the perturbative prediction be clearly smaller than the LO terms and that the size of the hadronization corrections does not exceed the measured mass effect, leaves only the three-jet rate and the first moment of y_{32} as observables. For these two observables, the b to ℓ ratios were compared with the massive NLO calculations of Ref. [9] (for $R_3^{b\ell}$) and [80] (for y_{32}).

  Since the smallest total uncertainty was obtained with y_{32}, the ALEPH results for $m_b(M_Z)$ or α_s^b/α_s^ℓ are given for this observable. Assuming α_s universality, the extracted $m_b(M_Z)$ is [11],

  $$m_b(M_Z) = 3.27 \pm 0.22\ \text{(stat)} \pm 0.22\ \text{(exp)} \pm 0.38\ \text{(had)} \pm 0.16\ \text{(theo)}\ \text{GeV}/c^2 \quad (6.11)$$

  where the average between the two methods described in Section 1.5.5 is taken. The pole mass is found to be,

  $$M_b = 4.73 \pm 0.29\ \text{(stat)} \pm 0.29\ \text{(exp)} \pm 0.49\ \text{(had)} \pm 0.18\ \text{(theo)}\ \text{GeV}/c^2 \quad (6.12)$$

  being (exp) the uncertainties due to the detector and physics modeling and (had) the ones due to the hadronization process.

  The result obtained from $R_3^{b\ell}(y_c = 0.02)$ with DURHAM is also given in [11], $m_b(M_Z) = 2.76 \pm 0.28$ (stat) ± 0.28 (exp) ± 0.62 (had) and $M_b = 3.65$ GeV/c^2.

  If the measured first moment of y_{32} was used to test α_s universality, taking as input the b quark mass of $m_b(m_b) = 4.2 \pm 0.1$ GeV/c^2, the result found was:

  $$\alpha_s^b/\alpha_s^\ell = 0.997 \pm 0.004\ \text{(stat)} \pm 0.004\ \text{(exp)} \pm 0.007\ \text{(had)} \pm 0.003\ \text{(theo)} \quad (6.13)$$

  which is a confirmation of flavour independence at a precision level of 1%.

[1] For a definition of the event shape variables see Appendix A.

These results are compatible with the DELPHI determinations presented in this thesis. The error due to the hadronization uncertainty, which is the dominant source in the ALEPH measurement, has been significantly reduced in the present DELPHI analysis, due to the cut described in Section 4.3.

- **OPAL**:

The OPAL experiment at LEP tested α_s universality by measuring some event shape observables (T, M_H, B_W, y_{32} and C) for ℓ, c and b tagged samples and performing a 3 parameter fit to $O(\alpha_s^2)$ massive calculations to get simultaneously α_s^ℓ, α_s^c/α_s^ℓ and α_s^b/α_s^ℓ [4]:

$$\begin{aligned} \alpha_s^c/\alpha_s^\ell &= 0.997 \pm 0.038 \text{ (stat)} \pm 0.030 \text{ (syst)} \pm 0.012 \text{ (theo)} \\ \alpha_s^b/\alpha_s^\ell &= 0.993 \pm 0.008 \text{ (stat)} \pm 0.006 \text{ (syst)} \pm 0.011 \text{ (theo)} \end{aligned} \tag{6.14}$$

The massive NLO calculations used are the ones of Ref. [80] which are performed in the pole mass scheme. The values used for c and b quark masses were 1.35 GeV/c^2 and 5.0 GeV/c^2 respectively.

Recently, OPAL has also measured the running b quark mass at the M_Z scale, assuming α_s flavour independence. The observable used was the three-jet rate double ratio, $B_3(y_c) = R_{3b}/R_{3udsc}$, which differs from the one used by DELPHI and ALEPH, $R_3^{b\ell}$, in different aspects. First, by the event flavour definition, in this case an event having b quarks in the final state, either coming from primary or secondary production via gluon splitting, are considered as b quark events. Another difference is that the c quark events also enter in the denominator, R_{3udsc}, which represents in this case the three-jet rate for $udsc$ quark events normalized to the hadronic born cross section.

Data collected by the OPAL detector at the Z^0 peak during 1994 was analysed to measure $B_3(y_c)$ for eight different jet finder algorithms, JADE, E, E0, P, P0, DURHAM, GENEVA and CAMBRIDGE, and compare it with the NLO massive calculations of Ref. [79] for all algorithms but CAMBRIDGE.

Events originated by b quarks were selected by identifying the displaced decay vertices of B hadrons [139]. A complete simulation of the detector with events generated by JETSET 7.4 with $M_b = 5$ GeV/c^2, tuned to OPAL data, was used to correct for detector effects and the hadronization process.

For each jet algorithm, $m_b(M_Z)$ was extracted. By minimizing the χ^2 of the correlated determinations a single result for the b quark mass $m_b(M_Z)$ was found to be [12],

$$m_b(M_Z) = 2.67 \pm 0.03 \text{ (stat)}^{+0.29}_{-0.37} \text{ (syst)} \pm 0.19 \text{ (theo) GeV/c}^2 \tag{6.15}$$

with a χ^2/ν of 100/6 if only statistical uncertainties are considered.

This result is also compatible with the one obtained in this analysis. By combining the results obtained by the seven jet clustering algorithms, the statistical uncertainty quoted by OPAL is a factor 6 smaller than the one given in the present analysis. The result is dominated by systematics.

6.3.1 Towards a combined result

Table 6.4 summarizes the results obtained on $m_b(M_Z)$ for each experiment and the result obtained in this analysis. All results are compatible with each other even though different observables, theoretical calculations, analysis methods and data were used in each case.

Concerning the size of the total uncertainty, the present analysis has led to the most precise determination of the b quark mass at M_Z performed so far, i.e. $2.96\ ^{+0.31}_{-0.32}$ GeV/c^2. It is important to emphasize that the dominant error on this measurement comes from the uncertainty on the b quark mass parameter used in the PYTHIA Monte Carlo, $^{+0.15}_{-0.16}$ GeV/c^2. This uncertainty was not taken into account in any of the previous measurements so, since it is not a negligible effect, it should be added to all of them when comparing.

In the following, some differences among the performed measurements are listed. We will refer by the DELPHI analysis the one presented here.

- Statistics: The size of the data sample decreases as we go from ALEPH, to DELPHI, to OPAL and to SLD analysis. But, since SLD and OPAL combine the results obtained with six and seven, respectively, different jet clustering algorithms, the statistical error is reduced. In particular, it stands out the OPAL result, where the statistical error reached is of ± 0.03 GeV/c^2.

- Hadronization: All experiments but DELPHI use the hadronization model implemented in JETSET to correct for the hadronization process, after tuning the Monte Carlo to their data. DELPHI has also considered the prediction given by the HERWIG cluster model. In any case, except for OPAL, the HERWIG model was used to estimate the hadronization model uncertainty. This uncertainty appears to be one of the dominant errors in all measurements. However, in the DELPHI analysis it is not anymore since it was reduced by making the measurement in a restricted region of the phase space.

  As shown in Section 4.5, the hadronization correction (at least for the $R_3^{b\ell}$ observable) depends strongly on the kinematical b mass parameter set in the Monte Carlo. It was proved in Section 4.5.3 that this mass could be identified with the pole mass used in the NLO calculations of $R_3^{b\ell}$ and therefore it was set to 4.98 ± 0.13 GeV/c^2.

  SLD and OPAL use a value of 5 GeV/c^2 and ALEPH of 4.75 GeV/c^2, which are also compatible with pole mass determinations [2]. But, as already mentioned, no error was assigned due to this mass parameter uncertainty.

- Detector: The detector correction obviously depends on the detector, b tagging method (including the tagging working point) and the detector simulation used. This is therefore specific for each experiment. Thus, the corrections and the associated uncertainties can be completely different even for the same observable.

  However, apart from the simulation of the detector, the different Monte Carlo generators used may simulate differently some physic processes, as the gluon splitting rate. In Section 5.2.1, it was shown that the gluon splitting rate of the simulated sample

[2] In fact ALEPH set this b mass parameter to the determined pole mass at the time the measurement was done. SLD and OPAL used the default value of JETSET.

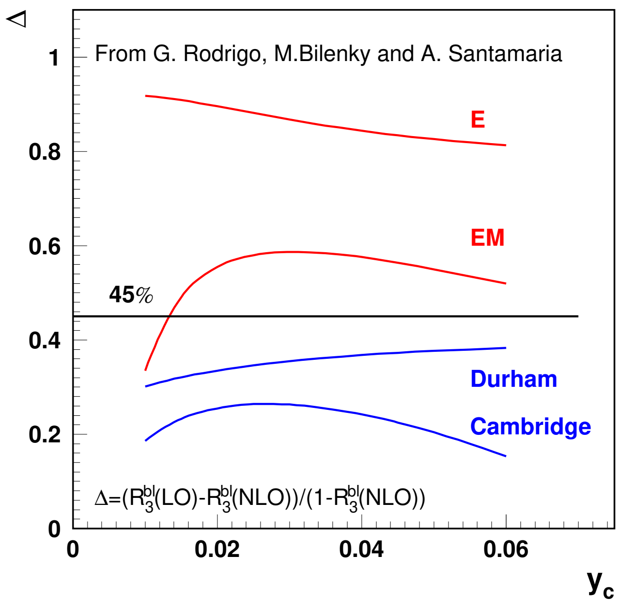

Figure 6.7: Size of the NLO correction with respect to the mass effect for $R_3^{b\ell}$ with different jet clustering algorithms.

affected the measured value for the case of the $R_3^{b\ell}$ observable. In SLD, ALEPH and DELPHI the Monte Carlo simulation was reweighted in order to have the measured rates [3]. This reweighting was not done in OPAL but, since the observable used differs on the event flavour definition, it may be that this observable is less sensitive to the gluon splitting rate of the simulated sample.

- Theoretical calculations: All different analysis compare the measured observable at parton level with NLO massive calculations. However, these computations are not identical and can therefore have different uncertainties. SLD and OPAL use the the calculations of Ref. [79] in terms of the running mass and ALEPH and DELPHI the ones of Refs. [80] and [9] respectively, where calculations in terms of both, the pole and the running mass, were used.

  It is also important to note that not all observables are as good from the theoretical point of view, i.e. from the convergence of the series. As an example, figure 6.7 shows for the $R_3^{b\ell}$ observable the size of the NLO corrections with respect to the mass effect for different jet clustering algorithms. As can be seen, they are as high as 90% for the E algorithm while for CAMBRIDGE they are only about 20%. This could be considered as an indication that the contribution from higher order terms is higher for the E algorithm than for CAMBRIDGE.

It would be interesting to combine all this measurements and end up with a single and more precise value of $m_b(M_Z)$. However, not too much gain is expected on the systematics

[3]The measured values of the gluon splitting rate and their errors are not the same in all cases since this measurement has been getting more precise. But all of them are compatible within errors.

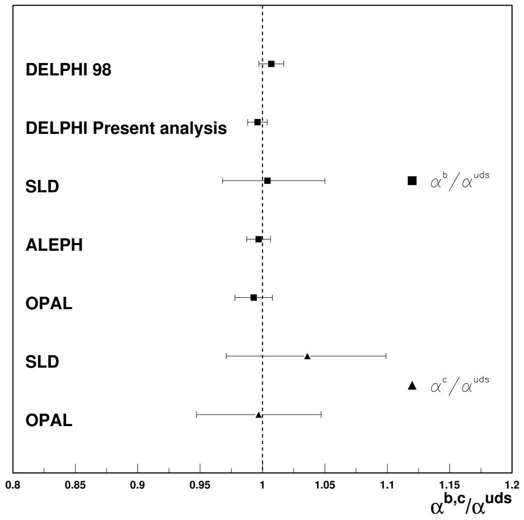

Figure 6.8: α_s^b/α_s^ℓ and α_s^c/α_s^ℓ measured by the different LEP and SLC experiments.

since most errors are completely correlated although the statistical error would be reduced. A lot of work would be needed in order to agree on the way corrections should be done and therefore to redo or rescale some of the results obtained. The correlation between the different systematic errors would also need to be studied.

As a summary of the measurements performed by the different experiments on the ratios α_s^b/α_s^ℓ and α_s^c/α_s^ℓ, figure 6.8 shows the different values obtained. All of them verify flavour independence of the strong coupling constant.

DURHAM (94-2000)	$R_3^{b\ell}(y_c = 0.02)$	$m_b(M_Z)$ GeV/c^2
Value	0.9619	3.23
Statistical	± 0.0045	${}^{+0.20}_{-0.21}$
Simulation	± 0.0033	${}^{+0.14}_{-0.15}$
Total statistical	± 0.0056	${}^{+0.24}_{-0.25}$
Fragmentation Tuning	± 0.0015	± 0.07
Fragmentation Model	± 0.0022	± 0.10
Mass parameter	± 0.0034	± 0.15
Total hadronization	± 0.0042	${}^{+0.19}_{-0.20}$
Gluon Splitting	± 0.0031	± 0.14
Tagging	${}^{+0.0034}_{-0.0035}$	${}^{+0.15}_{-0.16}$
Jet identification	± 0.0018	± 0.08
Total experimental	${}^{+0.0049}_{-0.0050}$	${}^{+0.22}_{-0.23}$
Mass Ambiguity	–	± 0.22
μ-scale $(0.5 \leq \mu/M_Z \leq 2)$	–	± 0.10
$\alpha_s(M_Z)$	–	± 0.05
Total theoretical		± 0.24
CAMBRIDGE (94-2000)	$R_3^{b\ell}(y_c = 0.0085)$	$m_b(M_Z)$ GeV/c^2
Value	0.9622	2.96
Statistical	± 0.0034	${}^{+0.14}_{-0.15}$
Simulation	± 0.0024	± 0.10
Total statistical	± 0.0042	${}^{+0.17}_{-0.18}$
Fragmentation Tuning	± 0.0010	± 0.04
Fragmentation Model	± 0.0025	± 0.11
Mass parameter	± 0.0036	${}^{+0.15}_{-0.16}$
Total hadronization	± 0.0045	± 0.19
Gluon Splitting	± 0.0015	± 0.06
Tagging	± 0.0021	± 0.09
Jet identification	± 0.0020	± 0.09
Total experimental	± 0.0033	± 0.14
Mass Ambiguity	–	± 0.11
μ-scale $(0.5 \leq \mu/M_Z \leq 2)$	–	± 0.04
$\alpha_s(M_Z)$	–	± 0.02
Total theoretical		± 0.12

Table 6.1: Values of $R_3^{b\ell}$ and $m_b(M_Z)$ obtained with DURHAM and CAMBRIDGE algorithms and break-down of their associated errors (statistical and systematic) for $y_c = 0.02$ and y_c=0.0085 respectively. The total errors may not be equal to the quadratic sum of the individual errors due to rounding effects.

DURHAM	$m_b(M_Z)$ (GeV/c^2)	M_b (GeV/c^2)
NLO	3.23	4.48
LO	4.10	

Table 6.2: Results of $m_b(M_Z)$ and M_b obtained directly from the NLO calculations and the mass extracted from the LO calculations for the DURHAM algorithm.

CAMBRIDGE	$m_b(M_Z)$ (GeV/c^2)	M_b (GeV/c^2)
NLO	2.96	4.26
LO	3.29	

Table 6.3: Results of $m_b(M_Z)$ and M_b obtained directly from the NLO calculations and the mass extracted from the LO calculations for the CAMBRIDGE algorithm.

Experiment	$m_b(M_Z)$ (GeV/c^2)	(stat)	(exp)	(had)	(theo)	(total)
SLD	2.56	±0.27	$^{+0.28}_{-0.38}$	$^{+0.25}_{-1.42}$	±0.42	$^{+0.63}_{-1.55}$
ALEPH	3.27	±0.22	±0.22	±0.38	±0.16	±0.52
OPAL	2.67	±0.03	$^{+0.29}_{-0.37}$		±0.19	$^{+0.35}_{-0.42}$
DELPHI 98	2.67	±0.25	-	±0.34	±0.27	±0.5
Present analysis	2.96	$^{+0.17}_{-0.18}$	±0.14	$\pm$ 0.19	±0.12	$^{+0.31}_{-0.32}$

Table 6.4: Measured b quark mass at the M_Z scale by the different LEP and SLC experiments. The previous DELPHI measurement is also shown to compare with the present result.

Chapter 7

Resultats i discussió

La mesura de l'observable $R_3^{b\ell}$ a nivell de partons (obtinguda al Capítol ??), en comparar-la amb els càlculs NLO amb efectes de massa de [9,14], es pot emprar per tal de: Extraure la massa del quark b assumint universalitat de α_s, o pendre com a entrada la massa del quark b obtinguda en el llindar de producció i extraure el quocient α_s^b/α_s^ℓ.

En aquest capítol es mostraran els resultats obtinguts amb les dos alternatives, tot i que es posarà més èmfasi en la mesura de la massa del quark b. Per a aquest cas, es derivaran dues definicions de massa del quark, la massa *running* a l'escala M_Z i la massa pol, a partir de l'observable mesurat. Es discutiran també les diferents fonts d'errors teòrics.

Finalment, es comparan els resultats obtinguts per aquest anàlisi amb els obtinguts per altres mesures realitzades en el pic del Z^0 en LEP i SLC.

6.1 Determinació de la massa del quark b

Tal i com es va descriure en la Secció 1.5.5, els càlculs NLO es poden utilitzar per tal de determinar la massa del quark b a partir de la mesura de $R_3^{b\ell}$, per a cada algoritme de reconstrucció de jets. Els càlculs teòrics només són vàlids en un rang de y_c determinat, $y_c \in [0.01, 0.1]$ en el cas de DURHAM [9] i $y_c \in [0.005, 0.025]$ per a CAMBRIDGE [14].

Per al cas de l'extracció de la massa *running*, $m_b(M_Z)$, hi ha dos mètodes disponibles. El primer es basa en l'ús de Eq. (1.67), i.e. la parametrització de $R_3^{b\ell}$ en termes de la massa pol, i el segon es basa en l'ús de l'expressió de $R_3^{b\ell}$ en termes de la massa *running*, i.e. utilitzant Eq. (1.68).

En ambdòs mètodes, el resultat depén del valor que es pren per a l'escala arbitrària μ. La figura 6.1 mostra, per als valors de $R_3^{b\ell}$ mesurats per a DURHAM i CAMBRIDGE a $y_c = 0.02$ i $y_c = 0.0085$ respectivament, la massa $m_b(M_Z)$ obtinguda per a distints valors de μ dins del rang $[M_Z/10, 2M_Z]$. Com es pot vore, ambdòs mètodes donen valors diferents de $m_b(M_Z)$ per a la mateixa escala μ. Prenem la mesura de $m_b(M_Z)$ com la mitja dels resultats obtinguts a l'escala $\mu = M_Z$ amb els dos mètodes.

L'error degut als termes d'ordre superior no calculats en la sèrie pertorbativa, i.e. l'incertesa teòrica, s'ha estimat considerant les següents fonts d'error:

- Dependència amb μ: L'escala μ es va variar en el segon mètode des de $M_Z/2$ fins a

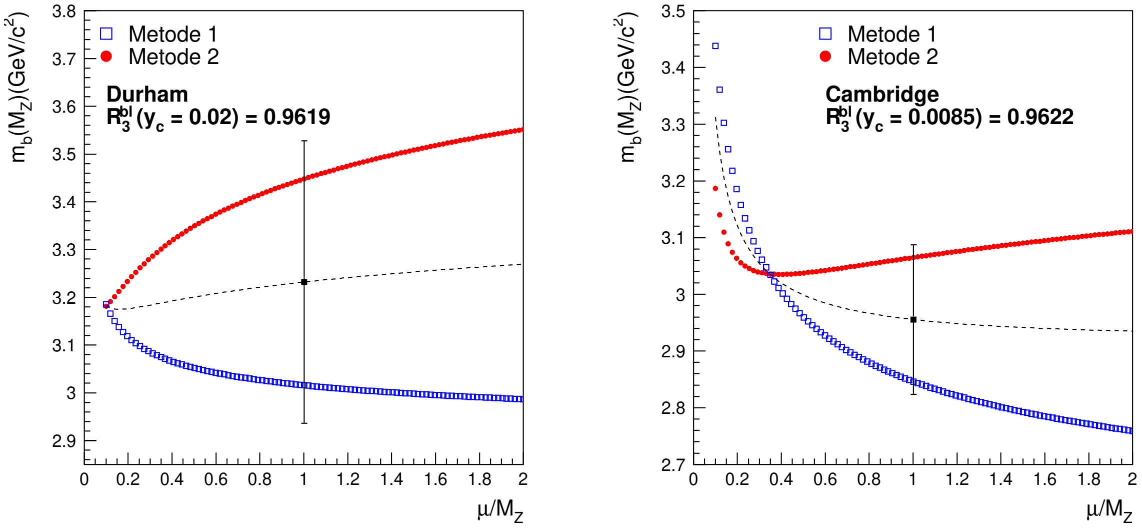

Figure 6.1: La $m_b(M_Z)$ obtinguda a partir de la mesura de $R_3^{b\ell}$ en funció de l'escala μ utilitzada, per a DURHAM (esquerra) i CAMBRIDGE (dreta). Es mostra resultat obtingut per a cada mètode, així com la mitja dels dos mètodes (línia trencada). També es mostra el resultat donat a $\mu = M_Z$ amb el seu error teòric.

$2M_Z$ i la meitat de la diferència del resultat obtingut per a $m_b(M_Z)$ en cada cas es va pendre com a l'error en l'escala μ.

- Ambigüetat en la massa: La meitat de la diferència entre la $m_b(M_Z)$ obtinguda per a cada mètode en $\mu = M_Z$ es va pendre com l'error degut a l'ambigüetat en la massa.
- Incertesa en α_s: Es va variar $\alpha_s(M_Z) = 0.1183 \pm 0.0027$ [113] entre els valors donats pel seu error i es va pendre com a incertesa en α_s l'efecte produït en $m_b(M_Z)$.

La figura 6.2 mostra l'error teòric total de $m_b(M_Z)$, junt amb les tres contribucions considerades, en funció de y_c per als dos algoritmes. En ambdòs algoritmes de jets, la contribució dominant a l'error total ve donada per l'ambigüetat de massa, mentre que la incertesa en α_s és menyspreable.

És important destacar també que CAMBRIDGE dóna un error teòric menor que DURHAM, especialment per a valor de y_c menuts.

Per tal de comparar la grandària de l'error teòric amb el de les incerteses experimentals, la figura 6.3 mostra l'error teòric de $m_b(M_Z)$ junt als errors experimentals (estadístic i sistemàtic) en funció del y_c. Tal i com es pot vore, als valors de y_c en els que mesurem (línies verticals en els gràfics), l'error provinent de la incertesa en els càlculs NLO té la menor contribució a l'error total per a CAMBRIDGE, mentre que per a DURHAM és tan gran com l'error estadístic.

Tal i com es va mencionar en la Secció 5.4, els paràmetres de resolució de jets $y_c = 0.02$ i 0.0085, per a DURHAM i CAMBRIDGE respectivament, es van escollir per tal de donar els

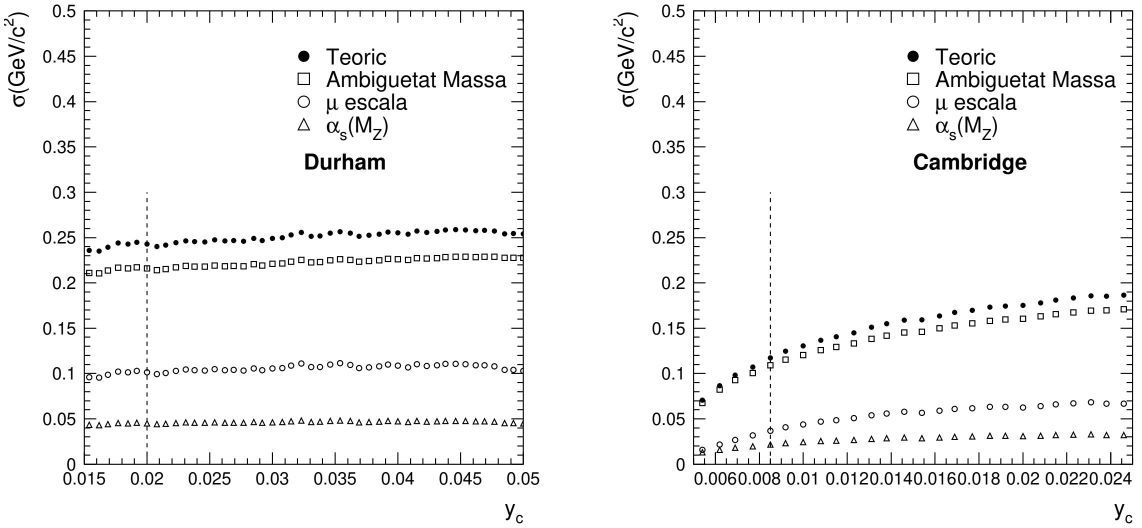

Figure 6.2: Error teòric de $m_b(M_Z)$ i les seues diferents contribucions (amgigüetat de massa, dependència amb μ i incertesa de α_s) en funció de y_c, obtingut a partir dels valors mesurats de $R_3^{b\ell}$ per a Durham (esquerra) i Cambridge (dreta). La línia vertical mostra els valors de y_c escollits per tal de donar el resultat final de $m_b(M_Z)$.

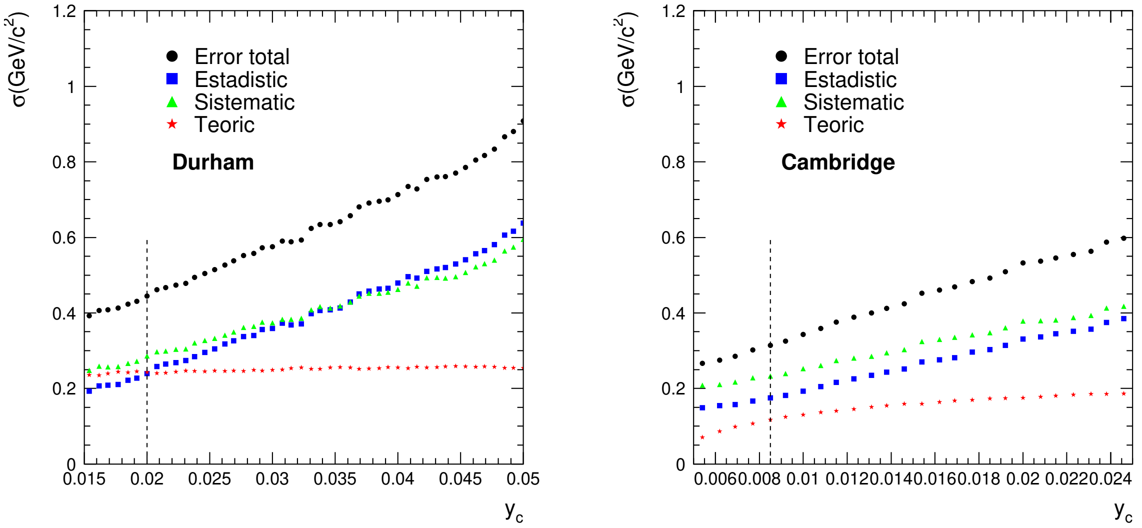

Figure 6.3: Error total, estadístic, sistemàtic i teòric de $m_b(M_Z)$ en funció del y_c, obtingut dels valors mesurats de $R_3^{b\ell}$ per a Durham (esquerra) i Cambridge (dreta). La línia vertical representa el valor de y_c escollit per tal de donar el resultat final de $m_b(M_Z)$.

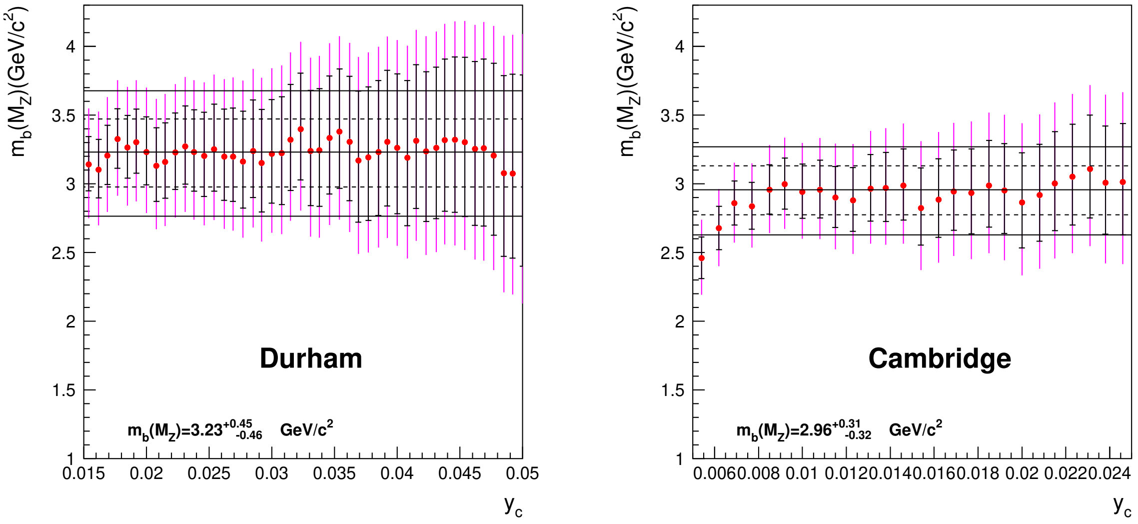

Figure 6.4: Valor de $m_b(M_z)$ obtingut a partir de la mesura de $R_3^{b\ell}(y_c)$ en funció de y_c per a Durham (esquerra) i Cambridge (dreta). Les línies horitzontals mostren els valors de $m_b(M_z)$ obtinguts a $y_c = 0.02$ i 0.0085 per a Durham i Cambridge respectivament. Les línies discontínues i contínues representen, respectivament, el seu error estadístic i total.

resultats finals de $m_b(M_Z)$. Aquests són,

$$m_b(M_Z) = 3.23^{+0.24}_{-0.25}\ (\text{estad})^{+0.19}_{-0.20}\ (\text{had})^{+0.22}_{-0.23}\ (\text{exp}) \pm 0.24\ (\text{teo})\ \text{GeV/c}^2 \tag{6.1}$$

quan Durham s'utilitza per a reconstruir jets i,

$$m_b(M_Z) = 2.96^{+0.17}_{-0.18}\ (\text{estad}) \pm 0.19\ (\text{had}) \pm 0.14\ (\text{exp}) \pm 0.12\ (\text{teo})\ \text{GeV/c}^2 \tag{6.2}$$

quan s'empra Cambridge. Els errors sistemàtics s'han dividit entre aquells deguts a l'hadrodronització (had) i els deguts a la modelització del detector i dels processos físics (exp). La contribució de cada font d'error individual es mostra en la taula 6.1.

Ambdòs resultats són compatibles entre ells dins de l'error estadístic. El resultat obtingut amb Cambridge és molt més precís que l'obtingut amb Durham, degut principalment a la reducció en l'error teòric, assolint un error total de $^{+310}_{-320}$ MeV/c^2 en comptes de $^{+450}_{-460}$ MeV/c^2.

S'ha comprovat que qualsevol altre valor de y_c condueix a resultats compatibles. Açò es mostra en la figura 6.4, on es representa la massa $m_b(M_Z)$ obtinguda a partir de $R_3^{b\ell}(y_c)$ per a diferents valors de y_c dins del rang teòricament apropiat.

Els resultats obtinguts amb ambdòs algoritmes es poden combinar si es coneix la correlació entre els dos observables. El factor de correlació entre l'observable $R_3^{b\ell}$ amb Durham i Cambridge a nivell de partons s'ha calculat per a distints valors de y_c. Amb aquest propòsit es van generar 95 mostres amb 250.000 esdeveniments iniciats per quarks b i ℓ i els dos algoritmes es van aplicar sobre cada mostra.

La figura 6.5 mostra el coeficient de correlació obtingut per a $R_3^{b\ell}$ entre els dos algoritmes per a distints valors de y_c. El primera gràfic de la figura mostra els factors de correlació per

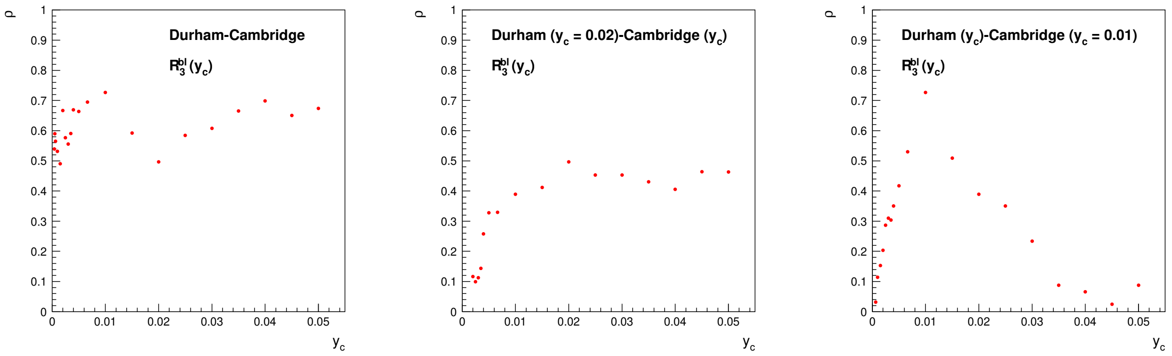

Figure 6.5: Factors de correlació (ρ) de $R_3^{b\ell}$ a nivell de partons entre DURHAM i CAMBRIDGE per a diferents combinacions de y_c. (Esquerra) El factor ρ es calcula per al mateix y_c per a ambdòs algoritmes. (Centre) Mostra el factor ρ de $R_3^{b\ell}$ amb DURHAM a $y_c = 0.02$ en funció del y_c de CAMBRIDGE. (Dreta) ρ de $R_3^{b\ell}$ amb CAMBRIDGE a $y_c = 0.01$ en funció del y_c de DURHAM.

al cas en què els dos algoritmes reconstruixen jets al mateix valor de y_c. El gràfic del mitg mostra la correlació entre DURHAM a $y_c = 0.02$ i diferents valors de y_c per a CAMBRIDGE, i en l'últim gràfic CAMBRIDGE està fix a $y_c = 0.01$.

Si les mesures realitzades a $y_c = 0.02$ amb DURHAM i $y_c = 0.0085$ amb CAMBRIDGE es combinen amb un coeficient de correlació de 0.4 per als errors estadístics, assumint que els errors sistemàtics estan totalment correlacionats i que els teòrics estan descorrelacionats, el resultat és:

$$m_b(M_Z) = 2.99 \pm 0.17 \text{ (estad)}^{+0.24}_{-0.25} \text{ (sist)} \pm 0.11 \text{ (teo) GeV/c}^2 \tag{6.3}$$

amb $\chi^2/\nu = 0.6$. Respecte al resultat obtingut amb CAMBRIDGE, l'error estadístic i el teòric es redueixen però el sistemàtic augmenta, de manera que l'error total es manté idèntic, i.e. $^{+310}_{-320}$ MeV/c^2.

A banda de la massa *running*, també es pot extraure la massa pol del quark b, M_b, a partir de la mesura de $R_3^{b\ell}$ i emprant les expressions NLO de $R_3^{b\ell}$ en termes de la massa pol, i.e. Eq. (1.67). La M_b obtinguda depén també de l'escala μ utilitzada, degut a la dependència en $\alpha_s(\mu)$. Aquesta dependència es mostra en la figura 6.6 per a la $R_3^{b\ell}$ mesurada amb els dos algoritmes.

L'error teòric en aquest cas s'ha considerat només com la contribució de la dependència amb l'escala μ i la incertesa en α_s, però no s'ha tingut en compte l'error provinent de l'ambigüetat en la massa. L'escala μ s'ha variat en un rang major, des de $M_Z/10$ fins a $2M_Z$. De nou, la contribució deguda a la incertesa de α_s és menyspreable en l'error teòric.

La massa pol del quark b mesurada, prenent $\mu = M_Z$, és,

$$M_b = 4.48^{+0.30}_{-0.32} \text{ (estad)}^{+0.36}_{-0.39} \text{ (sist)} \pm 0.13 \text{ (teo) GeV/c}^2 \tag{6.4}$$

quan s'empra DURHAM per tal de reconstruir jets a $y_c = 0.02$ i,

$$M_b = 4.26^{+0.22}_{-0.23} \text{ (estad)}^{+0.30}_{-0.31} \text{ (sist)} \pm 0.44 \text{ (teo) GeV/c}^2 \tag{6.5}$$

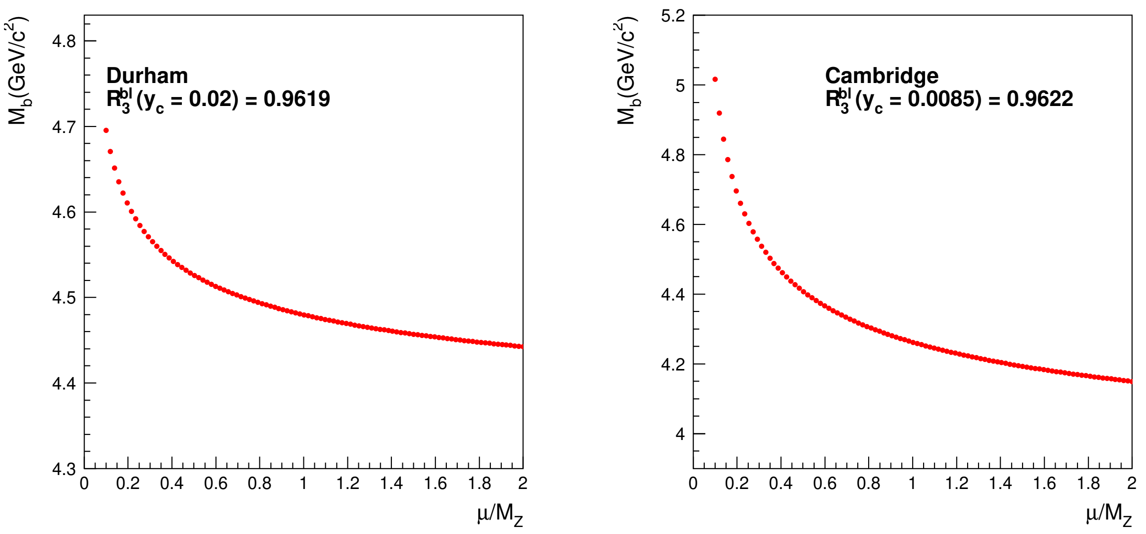

Figure 6.6: M_b en funció de l'escala μ obtinguda de la mesura $R_3^{b\ell}$ amb Durham (esquerra) i Cambridge (dreta).

si és Cambridge l'algoritme emprat a $y_c = 0.0085$.

Aquests valors són baixos en comparació amb els obtinguts quan la massa pol es mesura a baixa energia, com per exemple l'obtinguda en [74] (4.98 ± 0.13 GeV/c^2), tot i que són compatibles dins de l'error. Per al cas de Durham es troba a menys de 1σ i el resultat de Cambridge està 1.2σ per baix. Cal recordar que l'error teòric està subestimat ja que no en la mesura de la massa pol no s'ha considerat l'incertesa deguda a l'ambigüetat de massa, que sí que es va tenir en compte en la mesura de $m_b(M_Z)$.

Si en comptes de $\mu = M_Z$, es pren una escala μ menor, la M_b obtinguda és major, i per tant és més semblat al resultat mesurat en el llindar de producció (vore figura 6.6).

Les taules 6.2 i 6.3 mostren els valors obtinguts per a $m_b(M_Z)$ i M_b a partir dels càlculs NLO en comparació amb la massa del quark b obtinguda a partir de les prediccions teòriques a LO. A LO, tal i com es va mencionar en la Secció 1.5.5, no es pot fer cap distinció entre la massa pol i la *running* i per tant s'obté un únic valor.

Per a Cambridge, la massa obtinguda a LO es troba més a prop de la massa *running* extreta dels càlculs NLO que de la massa pol. Açò significa que a LO les dades estan millor descrites si la massa es pren com la massa *running* a l'escala M_Z que si es pren la massa pol.

En canvi, per a Durham la massa obtinguda a LO està més a prop de la massa pol mesurada a NLO que de la massa *running*, de manera que l'argument és l'oposat.

6.2 Independència de sabor de α_s

Alternativament, la mesura de $R_3^{b\ell}$ es pot emprar per a verificar la independència de sabor de α_s si la massa del quark b es pren de les mesures realitzades a baixa energia. L'expressió utilitzada és [7]:

$$\alpha_s^b/\alpha_s^\ell = R_3^{b\ell}(y_c) - H(m_b(M_Z), y_c) + \mathcal{O}(\alpha_s) \tag{6.6}$$

sent $H(m_b(M_Z), y_c)$ el terme de correcció de massa de Eq. (1.68).

Si la mitja de la massa del quark b, $m_b(m_b) = 4.24 \pm 0.11$ GeV$/c^2$ (obtinguda a partir de les mesures a baixa energia [75]), s'evoluciona fins a l'escala M_Z utilitzant RGE amb 3-loops i $\alpha_s(M_Z) = 0.1183 \pm 0.0027$, s'obté $m_b(M_Z) = 2.91 \pm 0.10$ GeV$/c^2$. Si aquest valor es pren en el càlcul de $H(m_b(M_Z), y_c)$, la mesura del quocient α_s^b/α_s^ℓ és,

$$\alpha_s^b/\alpha_s^\ell = 0.989^{+0.006}_{-0.005} \text{ (estad)} \pm 0.007 \text{ (sist)} \pm 0.005 \text{ (teo)} \tag{6.7}$$

per a DURHAM a $y_c = 0.02$, i

$$\alpha_s^b/\alpha_s^\ell = 0.996 \pm 0.004 \text{ (estad)} \pm 0.006 \text{ (sist)} \pm 0.003 \text{ (teo)} \tag{6.8}$$

per a CAMBRIDGE a $y_c = 0.0085$.

Els errors estadístic i sistemàtic es deuen a les incerteses experimentals de $R_3^{b\ell}$. L'error teòric reflexa l'incertesa en el terme de correcció $H(m_b(M_Z), y_c)$. Aquest error ve de la incertesa en la massa $m_b(M_Z)$ i en els termes d'ordre superior sense calcular.

L'error de 0.10 GeV$/c^2$ en $m_b(M_Z)$ s'ha afegit quadràticament als errors deguts a la dependència amb l'escala μ i a l'ambigüetat en la massa obtinguts en la secció anterior. Així, $m_b(M_Z)$ s'ha variat dins d'aquest error (±0.26 per a DURHAM i ±0.15 per a CAMBRIDGE) i l'efecte produït en α_s^b/α_s^ℓ s'ha pres com a l'error teòric. L'error degut a l'incertesa en α_s s'ha afegit quadràticament a l'error teòric però aquesta contribució és menyspreable.

Per a ambdós algoritmes, la universalitat de α_s s'ha verificat amb una precisió d'al voltant de 1%.

6.3 Comparació amb altres mesures a l'escala M_Z

En altres experiments de LEP i SLC (ALEPH, OPAL i SLD)) s'han mesurat també efectes de massa a l'escala d'energia M_Z utilitzant seccions eficaces de producció de jets o observables de forma. La mesura d'aquests observables s'ha comparat amb distints càlculs NLO per tal de determinar la massa del quark b o el quocient α_s^b/α_s^ℓ. En aquesta secció es descriuran aquestes altres mesures i es compararan amb els resultats de DELPHI obtinguts en aquest anàlisi.

- **SLD**:

  Per tal de mesurar $m_b(M_Z)$ Brandenburg et al. han emprat les dades recollides per l'experiment SLD i el mateix observable utilitzat en DELPHI, $R_3^{b\ell}(y_c)$, amb la diferència de que ací $R_3^q(y_c)$ representa la fracció d'esdeveniments que contenen tres o més jets, en comptes de només tres jets.

  S'han utilitzat sis algoritmes de reconstrucció de jets: E, E0, P, P0 [136], DURHAM i GENEVA [137] i s'han considerat prediccions NLO en termes de $m_b(M_Z)$ per a cadascun d'ells [79].

Per tal de mesurar $R_3^{b\ell}$, s'han seleccionat 77.896 esdeveniments de desintegracions hadròniques del Z^0, a partir dels 150.000 recollits entre 1993 i 1995 en SLD. Per tal de seleccionar els esdeveniments iniciats per quarks b i ℓ s'ha emprat un mètode basat en la massa i moment reconstruïts en els vèrtex secundaris, treballant amb pureses de 90% i 91% respectivament. Cadascun dels sis algoritmes de jets s'ha aplicat sobre les mostres seleccionades. Per tal de corregir per efectes de detector, el mètode d'identificació de sabor i el procés d'hadronització, s'ha utilitzat una simulació de Monte Carlo del detector, amb esdeveniments generats per JETSET 7.4 on els paràmetres s'havien ajustat prèviament a les dades. Per tant, el model d'hadronització emprat per tal de corregir les dades fou el model de cordes amb un paràmetre de massa del quark b de 5 GeV/c^2.

Per a cada algoritme es va seleccionar el valor de y_c òptim, de manera que minimitzara la combinació dels errors estadístic i sistemàtic. Els resultats de $m_b(M_Z)$ obtinguts per als sis algoritmes van de 2.3 a 4.1 GeV/c^2, amb una desviació r.m.s de 0.7 GeV/c^2 [10].

Donada la forta correlació que existeix entre els diferents algoritmes, les diferències entre els resultats obtinguts amb cadascun d'ells foren majors que les esperades. Aquest fet va suggerir que hi havia una altra font d'incertesa ($\sim$2% en $R_3^{b\ell}$, $\sim$0.5 GeV/c^2 en $m_b(M_Z)$) que podria provenir de la contribució d'ordres superiors sense calcular en l'expansió pertorbativa.

La millor estimació de $m_b(M_Z)$ es va obtindre tenint en compte les correlacions estadístiques entre els sis resultats, així com les correlacions en els errors sistemàtics:

$$m_b(M_Z) = 2.56 \pm 0.27 \text{ (estad)}^{+0.28}_{-0.38} \text{ (sist)}^{+0.49}_{-1.48} \text{ (teo) GeV}/c^2 \tag{6.9}$$

on l'error teòric correspon a la suma quadràtica de la incertesa d'hadronització ($^{+0.25}_{-1.42}$ GeV/c^2) i la propagació de l'error addicional de $\pm$0.02 considerat en cada $R_3^{b\ell}$ ($\pm$0.42 GeV/c^2).

La Col·laboració SLD, a banda de $R_3^{b\ell}$, també ha mesurat el quocient $R_3^{c\ell}$ per tal de verificar la independència de sabor de α_s per a quarks b, c i ℓ. Es va pendre com a entrada una massa de $m_b(M_Z) = 3.0 \pm 0.5$ GeV/c^2 en els càlculs NLO i els resultats obtinguts foren [138]:

$$\begin{aligned} \alpha_s^b/\alpha_s^\ell &= 1.004 \pm 0.018 \text{ (estad)}^{+0.026}_{-0.031} \text{ (sist)}^{+0.018}_{-0.029} \text{ (teo)} \\ \alpha_s^c/\alpha_s^\ell &= 1.036 \pm 0.043 \text{ (estad)}^{+0.041}_{-0.045} \text{ (sist)}^{+0.020}_{-0.018} \text{ (teo)} \end{aligned} \tag{6.10}$$

corresponent a la mitja dels sis algoritmes, considerant una correlació de 100% entre ells. L'error d'hadronització i el r.m.s dels resultats obtinguts amb els distints algoritmes estan inclosos en l'error teòric.

Els resultats obtinguts per a $m_b(M_Z)$ i α_s^b/α_s^ℓ són compatibles amb els del nostre anàlisi de DELPHI. El número de desintegracions hadròniques del Z^0 emprat per SLD correspon al 6% de l'utilitzat per DELPHI, i per tant l'error estadístic és major, tot i que s'utilitza la informació de sis observables. L'error d'hadronització també és major, degut principalment a la utilització dels algoritmes de reconstrucció de jets Geneva, E, E0, P i P0. L'error teòric també és major ja que, per tal de tenir un resultat compatible amb els sis algoritmes, es va haver d'introduir una font addicional d'error.

- **ALEPH**:

L'experiment ALEPH de LEP ha pres com a observables sensibles a la massa del quark b la secció eficaç de producció de tres jets definit amb l'algoritme de DURHAM a $y_c = 0.02$ i els moments primer i segon dels observables de forma: T, el paràmetre C, el valor de transició de tres a dos jets, y_{32}, B_T i B_W [1].

S'han mesurat els quocients entre la mostra d'esdeveniments identificats com a b i la mostra inclusiva per a cadascun dels observables i, a partir d'aquests quocients s'han derivat els quocients entre esdeveniments de quark b i ℓ a nivell de partons.

S'ha seleccionat una mostra de 2.3 milions d'esdeveniments hadrònics del Z^0 a partir de les dades recollides des de 1991 fins a 1995. S'ha aplicat un mètode d'identificació de sabor, basat en la vida mitja llarga dels hadrons B, per tal de seleccionar la mostra d'esdeveniments b amb una puresa de 83.1%.

Per tal de corregir per efectes de detector i el procés d'identificació de sabor s'ha emprat una simulació del detector. La correcció d'hadronització utilitzada és la donada pel model de cordes de JETSET 7.4 amb una massa cinemàtica del quark b de 4.75 GeV/c^2.

Després d'imposar que la contribució NLO a la predicció pertorbativa fos menor que els termes LO i que la grandària de la correcció d'hadronització fos menor que l'efecte de massa mesurat, de tots els observables només quedaren R_3 i el primer moment de y_{32}. Per a aquests dos observables, es van comparar els quocients d'esdeveniments b sobre ℓ amb els càlculs NLO de [9] (per a $R_3^{b\ell}$) i de [80] (per a y_{32}).

Com que el menor error total es va obtindre amb y_{32}, els resultats d'ALEPH per a $m_b(M_Z)$ o α_s^b/α_s^ℓ es donen per a aquest observable. Assumint universalitat de α_s, la $m_b(M_Z)$ obtinguda és [11],

$$m_b(M_Z) = 3.27 \pm 0.22 \text{ (estad)} \pm 0.22 \text{ (exp)} \pm 0.38 \text{ (had)} \pm 0.16 \text{ (teo) GeV}/c^2 \quad (6.11)$$

on s'ha pres la mitja entre els dos mètodes descrits en la Secció 1.5.5. La determinació de la massa pol és,

$$M_b = 4.73 \pm 0.29 \text{ (estad)} \pm 0.29 \text{ (exp)} \pm 0.49 \text{ (had)} \pm 0.18 \text{ (teo) GeV}/c^2 \quad (6.12)$$

on (exp) representa les incerteses degudes a la modelització del detector i dels processos físics i (had) aquelles deguedes al procés d'hadronització.

També es donen en [11] els resultats obtinguts a partir de $R_3^{b\ell}(y_c = 0.02)$ amb DURHAM, $m_b(M_Z) = 2.76 \pm 0.28$ (estad) ± 0.28 (exp) ± 0.62 (had) i $M_b = 3.65$ GeV/c^2.

Si la mesura del primer moment de y_{32} s'emprava per a verificar universalitat de α_s, prenent com a entrada $m_b(m_b) = 4.2 \pm 0.1$ GeV/c^2, el resultat trobat fou:

$$\alpha_s^b/\alpha_s^\ell = 0.997 \pm 0.004 \text{ (estad)} \pm 0.004 \text{ (exp)} \pm 0.007 \text{ (had)} \pm 0.003 \text{ (teo)} \quad (6.13)$$

constituint així una confirmació de la independència de sabor amb un nivell de precisió de 1%.

[1] La definició d'aquests observables de forma es pot trobar a l'Appendix A.

Aquests resultats són compatibles amb les determinacions de DELPHI presentades en aquest anàlisi. L'error degut a la incertesa d'hadronització, que és el dominant en la mesura d'ALEPH, s'ha reduït considerablement en aquest anàlisi de DELPHI, gràcies al tall descrit en la Secció 4.3.

- **OPAL**:

L'experiment OPAL de LEP va verificar universalitat de α_s mesurant alguns observables de forma (T, M_H, B_W, y_{32} i C) per a esdeveniments identificats com a ℓ, c i b, i realitzant un ajust de tres paràmetres als càlculs $O(\alpha_s^2)$ amb efectes de massa per tal d'obtenir simultàniament: α_s^ℓ, α_s^c/α_s^ℓ i α_s^b/α_s^ℓ [4]:

$$\begin{aligned} \alpha_s^c/\alpha_s^\ell &= 0.997 \pm 0.038 \text{ (estad)} \pm 0.030 \text{ (sist)} \pm 0.012 \text{ (teo)} \\ \alpha_s^b/\alpha_s^\ell &= 0.993 \pm 0.008 \text{ (estad)} \pm 0.006 \text{ (sist)} \pm 0.011 \text{ (teo)} \end{aligned} \tag{6.14}$$

Els càlculs NLO amb efectes de massa utilitzats són els de [80], realitzats amb la definició de massa pol. Els valors utilitzats per a la massa del quark c i b són de 1.35 GeV/c^2 i 5.0 GeV/c^2 respectivament.

Recentment, OPAL ha mesurat també la massa *running* del quark b a l'escala M_Z, assumint independència de sabor de α_s. Ha emprat l'observable $B_3(y_c) = R_{3b}/R_{3udsc}$, que difereix de l'utilitzat per DELPHI i ALEPH, $R_3^{b\ell}$, en diferents aspectes. En primer lloc, en la definició del sabor de l'esdeveniment. En aquest cas, un esdeveniment amb quarks b en l'estat final, tant si provenen de la producció primària com de la secundària (processos de gluons convertits en parelles de quarks), es consideren esdeveniments b. Una altra diferència és que els esdeveniments de quarks c també entren en el denominador, R_{3udsc}, que representa en aquest cas la secció eficaç de producció de tres jets per a esdeveniments *udsc* normalitzada a la secció eficaç hadrònica de born.

Es van analitzar les dades recollides pel detector OPAL en el pic del Z^0 durant 1994 per tal de mesurar $B_3(y_c)$ amb vuit algoritmes de reconstrucció de jets diferents (JADE, E, E0, P, P0, DURHAM, GENEVA i CAMBRIDGE) i comparar el resultat amb els càlculs NLO amb efectes de massa de [79] per a tots els algoritmes excepte CAMBRIDGE.

Els esdeveniments b es van seleccionar identificant els vèrtex desplaçats dels hadrons B [139]. Es va utilitzar una simulació completa del detector amb esdeveniments generats per JETSET 7.4 amb $M_b = 5$ GeV/c^2, ajustat a les dades d'OPAL, per tal de corregir per efectes de detector i pel procés d'hadronització.

Es va extraure $m_b(M_Z)$ per a cadascun dels algoritmes. Minimitzant el χ^2 de les distintes determinacions, es va obtindre un resultat únic per a la massa del quark b [12],

$$m_b(M_Z) = 2.67 \pm 0.03 \text{ (estad)}^{+0.29}_{-0.37} \text{ (sist)} \pm 0.19 \text{ (teo) GeV/c}^2 \tag{6.15}$$

amb $\chi^2/\nu = 100/6$ si només es consideren els errors estadístics.

Aquest resultat també és compatible amb l'obtingut en aquest anàlisi. Com a conseqüència de combinar els resultats obtinguts amb els set algoritmes, l'error estadístic donat per OPAL és un factor 6 menor que l'obtingut en el nostre anàlisi. El resultat d'OPAL està dominat per la sistemàtica.

6.3.1 En direcció a una mesura combinada

La taula 6.4 resumeix els resultats obtinguts per a $m_b(M_Z)$ en cada experiment i el d'aquest anàlisi. Tots els resultats són compatibles entre ells, tot i que s'han emprat distints observables, càlculs teòrics, mètodes d'anàlisi i dades en cada cas.

Pel que fa a la grandària de l'error total, l'anàlisi presentat ací ha proporcionat la determinació més precisa de $m_b(M_Z)$ que s'ha realitzat fins al moment, i.e. $2.96\,^{+0.31}_{-0.32}$ GeV/c^2. És important emfatitzar que l'error dominant en aquesta mesura ve de la incertesa en el paràmetre de massa del generador PYTHIA, $^{+0.15}_{-0.16}$ GeV/c^2. Aquest error no s'havia tingut en compte en cap de les mesures anteriors i per tant, com que no té un efecte menyspreable, deuria afegir-se en totes elles a l'hora de comparar.

A continuació, comentarem algunes de les diferències entre les mesures realitzades. L'anàlisi presentat en aquesta tesi el designarem com a l'anàlisi de DELPHI.

- Estadística: La grandària de la mostra de dades decreix en passar dels anàlisis d'ALEPH, a DELPHI, a OPAL i a SLD. Però, com que SLD i OPAL combinen els resultats obtinguts amb sis i set, respectivament, algoritmes de jets distints, l'error estadístic es redueix. En particular, destaca el resultat obtés per OPAL, on l'error estadístic assolit és només de ± 0.03 GeV/c^2.

- Hadronització: Excepte DELPHI, tots els experiments utilitzen el model d'hadronització implementat en JETSET per tal de corregir pel procés de fragmentació, una vegada ajustat el generador a les dades. DELPHI també ha considerat la predicció donada pel model de cúmuls de HERWIG. En tots els casos, excepte OPAL, el model de HERWIG s'ha utilitzat per tal d'estimar l'error degut al model d'hadronització. De fet aquesta incertesa constitueix un dels errors dominants en totes les mesures. En canvi, en l'anàlisi de DELPHI ja no ho és perquè, en fer la mesura en una regió restringida de l'espai fàsic, aquest error es va reduir.

  Tal i com es va mostrar en la Secció 4.5, la correcció d'hadronització (almenys per a l'observable $R_3^{b\ell}$) depén del paràmetre de massa cinemàtica del b fixat en el generador de Monte Carlo. En la Secció 4.5.3 es va provar que aquest paràmetre de massa es podia identificar amb la massa pol que s'empra en els càlculs NLO de $R_3^{b\ell}$ i, per tant, es va fixar a 4.98 ± 0.13 GeV/c^2.

  SLD i OPAL utilitzen un valor de 5 GeV/c^2 i ALEPH de 4.75 GeV/c^2, ambdós compatibles amb determinacions de la massa pol [2]. Però, tal i com s'ha mencionat anteriorment, no es va assignar cap error degut a la incertesa d'aquest paràmetre.

- Detector: La correcció de detector depén òbviament del detector, mètode d'identificació de sabor (inclòs el punt de treball) i la simulació del detector emprats. Totes aquestes propietats són específiques de cada experiment. Per tant, les correccions i les incerteses associades poden ser completament distintes, inclús quan es tracta del mateix observable.

[2] De fet ALEPH va fixar el paràmetre de massa del b en el generador a la massa pol determinada en el moment en què es va fer la mesura. SLD i OPAL empraren el valor per defecte de JETSET.

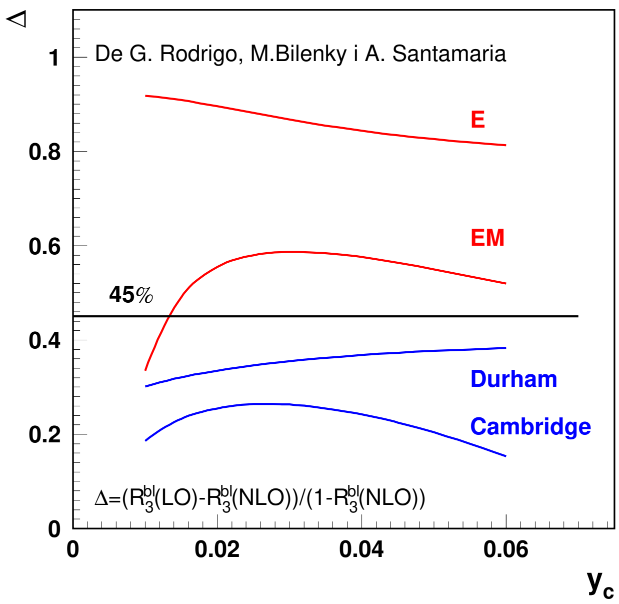

Figure 6.7: Grandària de la correcció NLO respecte a l'efecte de massa per a $R_3^{b\ell}$ amb distints algoritmes de reconstrucció de jets.

En canvi, a banda de la simulació del detector, els diferents generadors de Monte Carlo utilitzats poden simular de manera distinta processos físics, com ara la conversió de gluons en parelles de quarks pesats. En la Secció 5.2.1, es va mostrar que la fracció d'aquestes conversions en la mostra simulada afecten al valor mesurat de l'observable $R_3^{b\ell}$. En SLD, ALEPH i DELPHI la simulació de Monte Carlo es va repesar per tal de tenir les fraccions mesurades [3]. Aquest repesat no es va fer en OPAL però, potser que l'observable emprat en aquest cas siga menys sensible a la fracció d'esdeveniments amb gluons convertits en la mostra simulada.

- Càlculs teòrics: Tots els diferents anàlisis compararen l'observable mesurat a nivell de partons amb els càlculs NLO amb efectes de massa. En canvi, aquests càlculs no són idèntics i per tant poden tenir diferents incerteses. SLD i OPAL empraren els càlculs de [79] en termes de la massa *running* i ALEPH i DELPHI els de [80] i [9] respectivament, on s'utilitzen càlculs en termes de la massa pol i de la *running*.

  També és important resaltar que no tots els observables són igual d'apropiats des del punt de vista teòric, i.e. de la convergència de la sèrie. Com a exemple, la figura 6.7 mostra per a l'observable $R_3^{b\ell}$ la grandària de les correccions NLO respecte a l'efecte de massa per a diferents algoritmes de jets. Com es pot vore, aquestes són d'al vontant de 90% per a l'algoritme E mentre que per a CAMBRIDGE són d'un 20%. Aquest fet podria indicar que la contribució de termes d'ordre superior és major per a l'algoritme E que per al de CAMBRIDGE.

[3]Els valors mesurats per a aquestes fraccions i els seus errors no són els mateixos en tots els casos, ja que aquesta mesura ha anat fent-se més precisa. Tots ells són però compatibles dins dels errors.

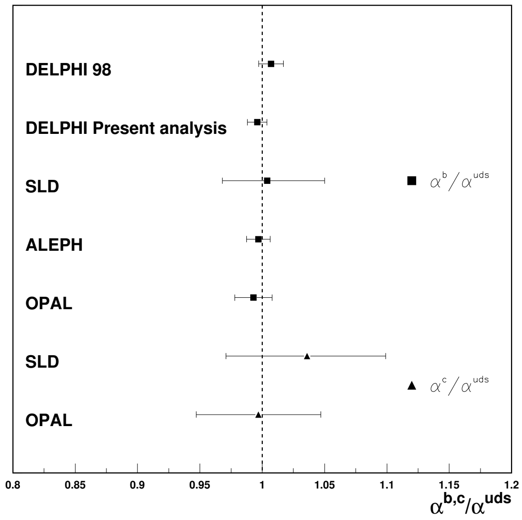

Figure 6.8: Valors de α_s^b/α_s^ℓ i α_s^c/α_s^ℓ mesurats pels diferents experiments de LEP i SLC.

Resultaria interessant combinar totes aquestes mesures per tal d'acabar amb un valor més precís de $m_b(M_Z)$. Però, pel que fa als errors sistemàtics no s'espera un gran guany, tot i que l'error estadístic sí que es reduiria. Caldria molt de treball per tal d'arribar a un acord en com aplicar les correccions i, per tant, repetir o escalar alguns dels resultats obtinguts. La correlació entre els distints errors sistemàtics també s'hauria d'estudiar.

Com a resum de les mesures realitzades pels distints experiments dels quocients α_s^b/α_s^ℓ i α_s^c/α_s^ℓ, la figura 6.8 mostra els distints valors obtinguts. Tots ells verifiquen la independència de sabor de la constant d'acoblament forta.

DURHAM (94-2000)	$R_3^{b\ell}(y_c = 0.02)$	$m_b(M_Z)$ GeV/c^2
Valor	0.9619	3.23
Estadístic data	± 0.0045	$^{+0.20}_{-0.21}$
Estadístic simulació	± 0.0033	$^{+0.14}_{-0.15}$
Total estadístic	± 0.0056	$^{+0.24}_{-0.25}$
Tuning de la fragmentació	± 0.0015	± 0.07
Model de fragmentació	± 0.0022	± 0.10
Paràmetre de massa	± 0.0034	± 0.15
Total hadronització	± 0.0042	$^{+0.19}_{-0.20}$
Gluon splitting	± 0.0031	± 0.14
Identificació de sabor	$^{+0.0034}_{-0.0035}$	$^{+0.15}_{-0.16}$
Identificació de jet	± 0.0018	± 0.08
Total experimental	$^{+0.0049}_{-0.0050}$	$^{+0.22}_{-0.23}$
Ambigüetat massa	–	± 0.22
Escala μ $(0.5 \leq \mu/M_Z \leq 2)$	–	± 0.10
$\alpha_s(M_z)$	–	± 0.05
Total teòric		± 0.24

CAMBRIDGE (94-2000)	$R_3^{b\ell}(y_c = 0.0085)$	$m_b(M_Z)$ GeV/c^2
Valor	0.9622	2.96
Estadístic data	± 0.0034	$^{+0.14}_{-0.15}$
Estadístic simulació	± 0.0024	± 0.10
Total Estadístic	± 0.0042	$^{+0.17}_{-0.18}$
Tuning de la fragmentació	± 0.0010	± 0.04
Model de fragmentació	± 0.0025	± 0.11
Paràmetre de massa	± 0.0036	$^{+0.15}_{-0.16}$
Total hadronització	± 0.0045	± 0.19
Gluon splitting	± 0.0015	± 0.06
Identificació de sabor	± 0.0021	± 0.09
Identificació de jet	± 0.0020	± 0.09
Total experimental	± 0.0033	± 0.14
Ambigüetat massa	–	± 0.11
Escala μ $(0.5 \leq \mu/M_Z \leq 2)$	–	± 0.04
$\alpha_s(M_z)$	–	± 0.02
Total teòric		± 0.12

Table 6.1: Valors de $R_3^{b\ell}$ i $m_b(M_Z)$ obtinguts amb els algoritmes de DURHAM i CAMBRIDGE i els seus errors associats (estadístics i sistemàtics) per a $y_c = 0.02$ i y_c=0.0085 respectivament. Potser que l'error total no siga igual a la suma quadràtica dels errors individuals degut a un efecte de redondeig.

DURHAM	$m_b(M_Z)$ (GeV/c^2)	M_b (GeV/c^2)
NLO	3.23	4.48
LO	4.10	

Table 6.2: Resultats de $m_b(M_Z)$ i M_b obtinguts directament dels càlculs NLO i la massa obtinguda a partir dels càlculs a LO, per a l'algoritme de DURHAM.

CAMBRIDGE	$m_b(M_Z)$ (GeV/c^2)	M_b (GeV/c^2)
NLO	2.96	4.26
LO	3.29	

Table 6.3: Resultats de $m_b(M_Z)$ i M_b obtinguts directament dels càlculs NLO i la massa obtinguda a partir dels càlculs a LO, per a l'algoritme de CAMBRIDGE.

Experiment	$m_b(M_Z)$ (GeV/c^2)	(estad)	(exp)	(had)	(teo)	(total)
SLD	2.56	± 0.27	${}^{+0.28}_{-0.38}$	${}^{+0.25}_{-1.42}$	± 0.42	${}^{+0.63}_{-1.55}$
ALEPH	3.27	± 0.22	± 0.22	± 0.38	± 0.16	± 0.52
OPAL	2.67	± 0.03	${}^{+0.29}_{-0.37}$		± 0.19	${}^{+0.35}_{-0.42}$
DELPHI 98	2.67	± 0.25	-	± 0.34	± 0.27	± 0.5
Anàlisi presentat	2.96	${}^{+0.17}_{-0.18}$	± 0.14	$\pm$ 0.19	± 0.12	${}^{+0.31}_{-0.32}$

Table 6.4: Mesures de la massa del quark b a l'escala M_Z per els distints experiments de LEP i SLC. També es mostra la mesura anterior de DELPHI per tal de comparar amb el resultat presentat.

Conclusions

A new determination of the b quark mass at the M_Z scale has been performed with the DELPHI detector at LEP. The normalized three-jet rate of b quarks with respect to ℓ quarks, $R_3^{b\ell}$, was measured using the data collected at the Z^0 peak from 1994 until 2000. The DURHAM and CAMBRIDGE jet clustering algorithms were used for jet reconstruction. A comparison of the measured $R_3^{b\ell}$ with the NLO massive calculations of [9, 14] allowed to either determine the b quark mass assuming α_s universality or, alternatively, extract the ratio α_s^b/α_s^ℓ taking the b quark mass from low energy determinations as input.

Previous measurements were done in [7, 112] by making use of the same observable. The main improvements of this new analysis are the following:

- The statistics has been increased by using the calibration runs performed at the Z^0 peak from 1997 to 2000.

- In order to correct for the hadronization process more recent versions of the generators, HERWIG 6.1 and PYTHIA 6.131, have been used. The modeling of mass effects in these generators has been substantially improved to better reproduce the measured data.

- A tuning of HERWIG 6.1 to DELPHI data has been done.

- The measurement was performed in a restricted region of phase space in order to have a better control of the fragmentation process. In this region, the two hadronization models used, string and cluster, give similar predictions. Two b fragmentation functions, Peterson and Bowler, were considered in the string model of PYTHIA to give the hadronization correction. The cut on the phase space reduces the hadronization model uncertainty from ± 0.35 GeV/c^2 (± 0.36 GeV/c^2) to ± 0.10 GeV/c^2 (± 0.11 GeV/c^2) for DURHAM (CAMBRIDGE).

- The dependence of the hadronization correction on the b mass parameter set in the PYTHIA Monte Carlo has been understood and quantified. An identification of this effective mass parameter with the pole mass was first done by comparing the parton shower with the NLO massive calculations. A method to constrain this mass by fitting to the measured data was developed and the result obtained was compatible with the pole mass. The error introduced by this mass parameter ambiguity had not been taken into account in the past and it represents the dominant error in this analysis ($^{+0.15}_{-0.16}$ GeV/c^2).

- Based on stability arguments, the tagging method and the working points to select the b and ℓ tagged samples were chosen. The same arguments were also followed when identifying the gluon jet in a b tagged event.

- The effect of the $b\bar{b}$ and $c\bar{c}$ gluon splitting rates of the Monte Carlo on the detector correction has been taken into account. The shift and the error induced on the measured $m_b(M_Z)$ is of $+0.23$ GeV/c^2 and ±0.14 GeV/c^2 respectively for the case of DURHAM and of $+0.09$ GeV/c^2 and ±0.06 GeV/c^2 for CAMBRIDGE.

The final results are given with the CAMBRIDGE algorithm, since the precision reached is higher than with DURHAM. The measured observable at parton level is,

$$R_3^{b\ell}(y_c = 0.0085) = 0.962 \pm 0.004\ (\text{stat}) \pm 0.005\ (\text{had}) \pm 0.003\ (\text{exp}) \tag{6.16}$$

Assuming α_s flavour independence, the running mass extracted by comparing the measured $R_3^{b\ell}$ with the theoretical calculations is,

$$m_b(M_Z) = 2.96^{+0.17}_{-0.18}\ (\text{stat}) \pm 0.19\ (\text{had}) \pm 0.14\ (\text{exp}) \pm 0.12\ (\text{theo})\ \text{GeV/c}^2 \tag{6.17}$$

which has a total error of $^{+310}_{-320}$ MeV/c^2, representing a substantial improvement with respect to the previous DELPHI determination [7] (±500 MeV/c^2).

Figure 6.10 shows the result obtained by this analysis for $m_b(M_Z)$, together with the other LEP and SLC determinations. All measurements are performed at the M_Z energy scale but for displaying reasons they are plotted at different scales. The result obtained when the b quark mass is measured at threshold [75], $M_\Upsilon/2$, is also shown, as well as the 3-loop running predicted by the RGE from this scale up to M_Z.

The result obtained in this analysis is compatible with the other measurements performed at the M_Z energy scale and it has the highest precision. It is also compatible with the measurement performed at low energy taking into account the QCD energy evolution. A net change in the value of the running b quark mass between $\mu_1 = M_\Upsilon/2$ and $\mu_2 = M_Z$ is observed with about 3.5 standard deviations, $m_b(M_\Upsilon/2) - m_b(M_Z) = 1.20^{+0.34}_{-0.36}$ GeV/c^2, verifying the running of the b quark mass with the energy scale predicted by QCD.

Apart from the running mass, the pole mass was also measured,

$$M_b = 4.26^{+0.22}_{-0.23}\ (\text{stat})^{+0.30}_{-0.31}\ (\text{syst}) \pm 0.44\ (\text{theo})\ \text{GeV/c}^2 \tag{6.18}$$

This value is smaller than those obtained at threshold, as for example the one of [74], 4.98 $\pm$ 0.13 GeV/c^2 (in this case it is lower by 1.2σ). The theoretical error of this measurement is underestimated since no uncertainty has been given to the mass ambiguity, as it was done for the running mass.

If instead of assuming α_s universality, $R_3^{b\ell}$ is compared with the NLO calculations for $m_b(M_Z) = 2.91 \pm 0.10$ GeV/c^2, the ratio α_s^b/α_s^ℓ is found to be,

$$\alpha_s^b/\alpha_s^\ell = 0.996 \pm 0.004\ (\text{stat}) \pm 0.006\ (\text{syst}) \pm 0.003\ (\text{theo}) \tag{6.19}$$

which verifies α_s flavour independence with a precision of 8‰.

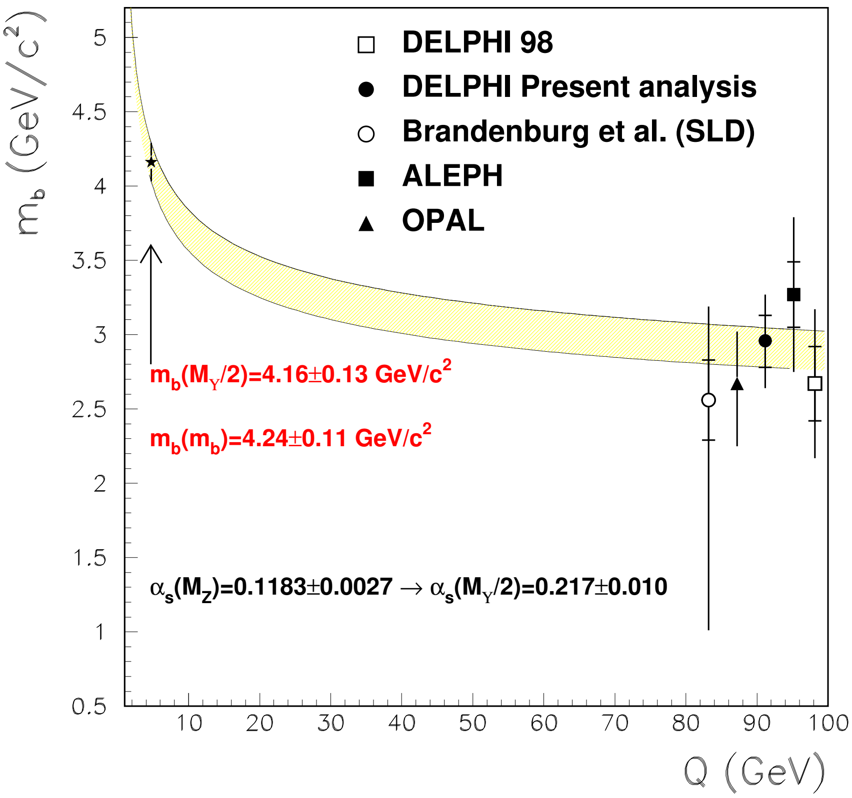

Figure 6.9: The running of $m_b(Q)$. The $m_b(M_Z)$ measured by LEP and SLC are displayed together with their total and statistical errors. The shaded area corresponds to the band associated to $m_b(Q)$ when running the value obtained at $M_\Upsilon/2$ up to the M_Z scale using the QCD renormalization group equations and $\alpha_s(M_Z) = 0.1183 \pm 0.0027$.

Conclusions

Amb el detector DELPHI de LEP s'ha realitzat una determinació nova de la massa del quark b a l'escala M_Z. S'ha mesurat la secció eficaç normalitzada de producció de tres jets en esdeveniments iniciats per quarks b respecte a aquells iniciats per quarks ℓ, $R_3^{b\ell}$, fent ús de les dades recollides en el pic del Z^0 entre 1994 i 2000. Els algoritmes DURHAM i CAMBRIDGE s'han utilitzat per a reconstruir jets. La comparació de la mesura de $R_3^{b\ell}$ amb els càlculs NLO de [9,14] ha permés, per una banda, determinar la massa del quark b, assumint universalitat de α_s i, per altra, extraure el quocient α_s^b/α_s^ℓ prenent la massa del quark b obtinguda a baixa energia com a entrada.

Mesures prèvies a aquesta es van realitzar en [7, 112] fent ús del mateix observable. Les principals millores d'aquest anàlisi respecte als anteriors són les següents:

- L'estadística s'ha augmentat incorporant les dades de calibració realitzades al pic del Z^0 entre 1997 i 2000.
- Per tal de corregir pel procés d'hadronització s'han emprat versions dels generadors més recients, HERWIG 6.1 i PYTHIA 6.131. La modelització d'efectes de massa en aquests generadors s'ha millorat considerablement per tal de reproduir millor les dades experimentals.
- S'han ajustat els paràmetres de HERWIG 6.1 a les dades de DELPHI.
- La mesura es va realitzar en una zona restringida de l'espai de fase per tal de tenir un millor control del procés de fragmentació. En aquesta regió, els dos models d'hadronització emprats, cordes i cúmuls, donen prediccions similars. Les funcions de fragmentació de Peterson i Bowler es van considerar en el model de cordes de PYTHIA per tal de donar la correcció d'hadronització. El tall en l'espai de fase permet reduir l'error degut al model d'hadronització de ± 0.35 GeV/c^2 (± 0.36 GeV/c^2) a ± 0.10 GeV/c^2 (± 0.11 GeV/c^2) per a l'algoritme de DURHAM (CAMBRIDGE).
- La dependència de la correcció d'hadronització amb el paràmetre de massa del quark b utilitzat en el generador de PYTHIA s'ha entés i quantificat. Per a l'observable $R_3^{b\ell}$, aquest paràmetre efectiu s'ha identificat amb la massa pol, mitjançant la comparació de la cascada de partons amb els càlculs NLO que inclouen efectes de massa. S'ha desenvolupat un mètode que permet fitar aquesta massa ajustant a les dades mesurades, donant un resultat compatible amb la massa pol. L'error introduït per l'ambigüetat

d'aquest paràmetre de massa no s'havia tingut en compte en cap mesura anterior i, en aquest anàlisi, representa l'error dominant ($^{+0.15}_{-0.16}$ GeV/c^2).

- Els mètodes d'identificació de sabor i els punts d'operació per tal de seleccionar les mostres d'esdeveniments iniciats per quarks b i ℓ es van escollir basant-se en arguments d'estabilitat. Arguments del mateix tipus es van seguir també per tal de d'identificar el jet de gluó en la mostra d'esdeveniments b.

- S'ha tingut en compte l'efecte produït sobre la correcció de detector per la secció eficaç del procés de gluons convertits en parelles de quarks $b\bar{b}$ i $c\bar{c}$ en la mostra simulada. El desplaçament i l'error induïts en la mesura de $m_b(M_Z)$ és de $+0.23$ GeV/c^2 i ± 0.14 GeV/c^2 respectivament per al cas de DURHAM i de $+0.09$ GeV/c^2 i $\pm$ 0.06GeV/c^2 per a CAMBRIDGE.

Com que la precisió assolida quan s'empra CAMBRIDGE per a reconstruir els jets és major que l'obtinguda amb DURHAM, els nostres resultats finals són els obtinguts amb CAMBRIDGE. L'observable mesurat a nivell de partons és,

$$R_3^{b\ell}(y_c = 0.0085) = 0.962 \pm 0.004\ \text{(estad)} \pm 0.005\ \text{(had)} \pm 0.003\ \text{(exp)} \tag{6.20}$$

Si s'assumeix independència de sabor de α_s, la massa *running* que s'extrau en comparar la mesura de $R_3^{b\ell}$ amb el predit pels càlculs teòrics és,

$$m_b(M_Z) = 2.96^{+0.17}_{-0.18}\ \text{(estad)} \pm 0.19\ \text{(had)} \pm 0.14\ \text{(exp)} \pm 0.12\ \text{(teo)}\ \text{GeV/c}^2 \tag{6.21}$$

que té un error total de $^{+310}_{-320}$ MeV/c^2, representant així una millora considerable respecte a la mesura anterior de DELPHI [7] ($\pm$500 MeV/c^2).

En la figura 6.10 es mostra el resultat obtingut en aquest anàlisi per a $m_b(M_Z)$, junt a la resta de les determinacions realitzades en LEP i SLC. Totes aquestes mesures s'han realitzat a l'escala d'energia M_Z però per claretat estàn representades a escales diferents. Es mostra també el resultat obtingut quan es mesura la massa del quark b en el llindar de producció [75], $M_\Upsilon/2$, així com l'evolució predita per RGE amb 3 loops des d'aquesta escala fins a M_Z.

El nostre resultat és compatible amb la resta de les mesures realitzades a l'escala M_Z, sent però el més precís. Així mateix, està d'acord amb la mesura realitzada a baixa energia tenint en compte l'evolució amb l'energia predita per QCD. S'observa un canvi de 3.5 desviacions estandard en la massa *running* del quark b entre $\mu_1 = M_\Upsilon/2$ i $\mu_2 = M_Z$, $m_b(M_\Upsilon/2) - m_b(M_Z)$ $= 1.20^{+0.34}_{-0.36}$ GeV/c^2, verificant així l'evolució de la massa del quark b amb l'escala d'energia predita per QCD.

A banda de la massa *running*, s'ha mesurat també la massa pol,

$$M_b = 4.26^{+0.22}_{-0.23}\ \text{(estad)}^{+0.30}_{-0.31}\ \text{(sist)} \pm 0.44\ \text{(teo)}\ \text{GeV/c}^2 \tag{6.22}$$

Aquest valor és menor que l'obtingut al llindar de producció, com ara el de [74], 4.98 $\pm$ 0.13 GeV/c^2 (en aquest cas està 1.2σ per baix). L'error teòric d'aquest resultat està infravalorat ja que no s'ha estimat cap incertesa deguda a la definició de massa, que sí que es va tenir en compte en la determinació de la massa *running*.

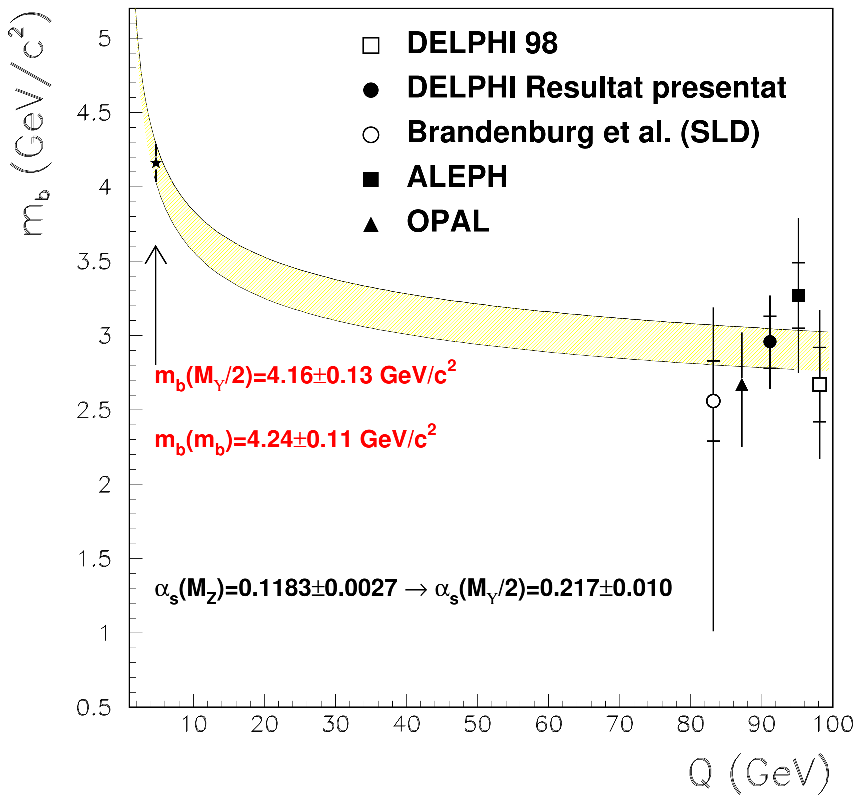

Figure 6.10: Evolució amb l'escala d'energia de $m_b(Q)$. Es mostren els valors de $m_b(M_Z)$ mesurats per LEP i SLC, amb els seus errors totals i estadístics. L'àrea sombrejada correspon a la banda associada a l'evolució de $m_b(Q)$ des del valor obtingut a l'escala $M_\Upsilon/2$ fins a M_Z donada per les equacions del grup de renormalització amb $\alpha_s(M_Z) = 0.1183 \pm 0.0027$.

Si en comptes d'assumir universalitat de α_s, es compara $R_3^{b\ell}$ amb els càlculs NLO per a $m_b(M_Z) = 2.91 \pm 0.10$ GeV/c^2, el quocient α_s^b/α_s^ℓ mesurat és,

$$\alpha_s^b/\alpha_s^\ell = 0.996 \pm 0.004 \text{ (estad)} \pm 0.006 \text{ (sist)} \pm 0.003 \text{ (teo)} \tag{6.23}$$

de manera que la independència de sabor de α_s queda verificada amb una precisió de 8‰.

Appendix A

Tuning aspects

A.1 Definition of variables

A.1.1 Event shape variables

- Thrust T, Major M, Minor m and Oblatness O:

  The thrust of an event is defined as [140]:

$$T = \max_{\vec{n}_T} \frac{\sum_i |\vec{p}_i \cdot \vec{n}_T|}{\sum_i |\vec{p}_i|} \tag{A.1}$$

  where N is the number of selected particles, $\vec{p}_i$ their 3-momentum and $\vec{n}_T$ the unit vector along the axis for which T is maximum. The thrust can then take values in the range $1/2 \leq T \leq 1$ and it tends to 1 for two jet events.

  The Major axis, $\vec{n}_{Major}$, is defined as the direction perpendicular to the thrust axis and the Minor axis as that perpendicular to both of them, i.e. $\vec{n}_{Minor} = \vec{n}_{Major} \times \vec{n}_T$. The Major ($M$) and Minor ($m$) are then defined by Eq. (A.1) but replacing $\vec{n}_T$ by $\vec{n}_{Major}$ or $\vec{n}_{Minor}$ respectively. Therefore, Minor values tend to 0 for planar events.

  The Oblatness is defined as $O = M - m$ [141].

- Sphericity S, Aplanarity A and Planarity P:

  These event shape variables are obtained from the eigenvalues of the momentum tensor,

$$M^{\alpha\beta} = \sum_{i=1}^{N} p_i^{\alpha} p_j^{\beta} \quad (\alpha, \beta = 1, 2, 3) \tag{A.2}$$

  where α and β refer to three components of the momentum and the sum goes though all selected particles.

  Ordering the eigenvalues of the above tensor such that $\lambda_1 \geq \lambda_2 \geq \lambda_3$ and normalizing them such as that $\lambda_1 + \lambda_2 + \lambda_3 = 1$, the sphericity, S, Aplanarity, A, and Planarity, P, are defined as [142]:

$$S = \frac{3}{2}(\lambda_2 + \lambda_3) \tag{A.3}$$

$$A = \frac{3}{2}\lambda_3 \tag{A.4}$$

$$P = \frac{2}{3}(S - 2A) \tag{A.5}$$

The sphericity values are within the range $0 \leq S \leq 1$, approaching 0 for two jet events and 1 for spherical events. The sphericity axis, $\vec{n}_{Sphericity}$, is parallel to the eigenvector corresponding to λ_1. The aplanarity ($0 \leq A \leq 0.5$) measures the flatness of an event, and tends to 0 for planar events.

- C and D Parameters:

  These parameters are defined through the eigenvalues λ_i of the linear momentum tensor [143],

$$\Theta^{i,j} = \frac{1}{\sum_{k=1}^{N} |\vec{p}_k|} \sum_{k=1}^{N} \frac{p_k^i p_k^j}{|\vec{p}_k|} \tag{A.6}$$

  as,

$$C = 3(\lambda_1\lambda_2 + \lambda_2\lambda_3 + \lambda_3\lambda_1) \tag{A.7}$$

$$D = 27\lambda_1\lambda_2\lambda_3 \tag{A.8}$$

  where p_k^i denotes the i-component of $\vec{p}_k$.

- Jet Masses:

  Events can be divided into two hemispheres by a plane perpendicular to the thrust axis. The invariant mass of the particles in each hemisphere, M_a and M_b, can be then calculated to define the heavy jet mass, ρ_H, and the light jet mass, ρ_L, as:

$$\rho_H \equiv \frac{M_H^2}{E_{vis}^2} = \frac{\max(M_a^2, M_b^2)}{E_{vis}^2} \tag{A.9}$$

$$\rho_L \equiv \frac{M_L^2}{E_{vis}^2} = \frac{\min(M_a^2, M_b^2)}{E_{vis}^2} \tag{A.10}$$

  where

$$E_{vis} = \sum_i E_i \tag{A.11}$$

  being E_i the energy of the particle i, calculated assuming the pion mass for charged particles and zero mass for neutral particles.

  Their sum and their difference are denoted by ρ_S and ρ_D respectively.

- Jet Broadening B_{max}, B_{min}, B_{sum}, B_{diff} [144]:

  For each hemisphere, a and b, the transverse momenta of the particles with respect to the thrust axis are summed to define B_a and B_b respectively as,

$$B_{a,b} = \frac{\sum_{i\in a,b} |\vec{p}_i \times \vec{n}_T|}{2\sum_i |\vec{p}_i|} \tag{A.12}$$

  The wide jet broadening, B_{max} (also denoted by B_W), the narrow jet broadening B_{min} (or B_N), the total jet broadening, B_{sum} (or B_T), and B_{diff} are then defined by,

$$B_{max} = \max(B_a, B_b) \tag{A.13}$$

$$B_{min} = \min(B_a, B_b) \tag{A.14}$$

$$B_{sum} = B_{max} + B_{min} \tag{A.15}$$

$$B_{diff} = B_{max} - B_{min} \quad . \tag{A.16}$$

- Differential Jet Rates $D_i(y_c)$:

  For a given jet clustering algorithm, the differential 2-jet rate is defined as,

$$D_2(y_c) = \frac{R_2(y_c + \Delta y_c) - R_2(y_c)}{\Delta y_c} \tag{A.17}$$

  For $(n > 2)$-jet differential rate,

$$D_n(y_c) = \frac{R_n(y_c + \Delta y_c) - R_n(y_c)}{\Delta y_c} + D_{n-1}(y_c) \tag{A.18}$$

  being y_c the jet resolution parameter.

  The differential n-jet rate $D_n(y_c)$ can also be understood as the distribution of $y_{n+1,n}$, i.e. the y_c transition value in which an n event becomes an $n+1$-jet.

- Energy-Energy correlation EEC and Asymmetry $AEEC$:

  The Energy-Energy correlation, EEC, is the histogram of angles χ_{ij} between all pairs of particles weighted by their scaled energies [145],

$$EEC(\cos\chi) = \frac{1}{N}\frac{1}{\Delta\cos\chi}\sum_{events}\sum_{i,j}\frac{E_i}{E_{vis}}\frac{E_j}{E_{vis}}\Theta(\Delta\cos\chi - |\cos\chi - cos\chi_{ij}|) \tag{A.19}$$

  where $\cos\chi$ and $\Delta\cos\chi$ are the low edge and width of a bin and Θ is the step function. For $\cos\chi \geq 0$, the asymmetry, $AEEC$, of the EEC is:

$$AEEC(\cos\chi) = EEC(-\cos\chi) - EEC(\cos\chi) \tag{A.20}$$

A.1.2 Inclusive single particle variables

- Scaled Momentum x_p, ξ_p:

  The scaled momentum of a particle is defined as,

$$x_p = \frac{p}{p_{beam}} \tag{A.21}$$

  being p the absolute momentum of the particle and p_{beam} the beam momentum. And $\xi_p = \log(1/x_p)$.

- Transverse Momenta p_t^{in}, p_t^{out}:

  With respect to the thrust axis, the component of the transverse momentum p_t of a particle in the event plane is $p_t^{in} = \vec{p} \cdot \vec{n}_{Major}$, and the one out of the event plane, $p_t^{out} = \vec{p} \cdot \vec{n}_{Minor}$. For values with respect to the sphericity axis, the axes defined by the eigenvectors of the quadratic momentum tensor are used instead.

  To distinguish the two possibilities, when they are defined with respect to the the thrust axis they are denoted by $p_t^{in}(t)$ and $p_t^{out}(t)$. $p_t^{in}(s)$ and $p_t^{out}(s)$ correspond to the definitions with respect to the sphericity axis.

- Rapidity y:

  The rapidity is given by,

$$y = \frac{1}{2} \log \frac{E - p_{\|}}{E + p_{\|}} \tag{A.22}$$

  where $p_{\|}$ is the particle momentum parallel to $\vec{n}_T$ or $\vec{n}_{Sphericity}$. Each case will be denoted by $y(t)$ and $y(s)$ respectively.

A.2 Comparison of data and Monte Carlo

The following figures show the comparison between the data and the Monte Carlo prediction for different measured event shape variables, inclusive single particle distributions and identified particle spectra. The Monte Carlo predictions correspond to HERWIG 6.1, with the here obtained DELPHI tuned parameters (full line), HERWIG 5.8, with the DELPHI tuning of [17] (dashed line) and PYTHIA 6.125 with the DELPHI tuned parameters obtained in [17] for JETSET 7.3/7.4 (dotted line). The ratio between data and Monte Carlo is also shown for each distribution. The shaded area corresponds to the total experimental error (i.e. the quadratic sum of statistical and systematic errors).

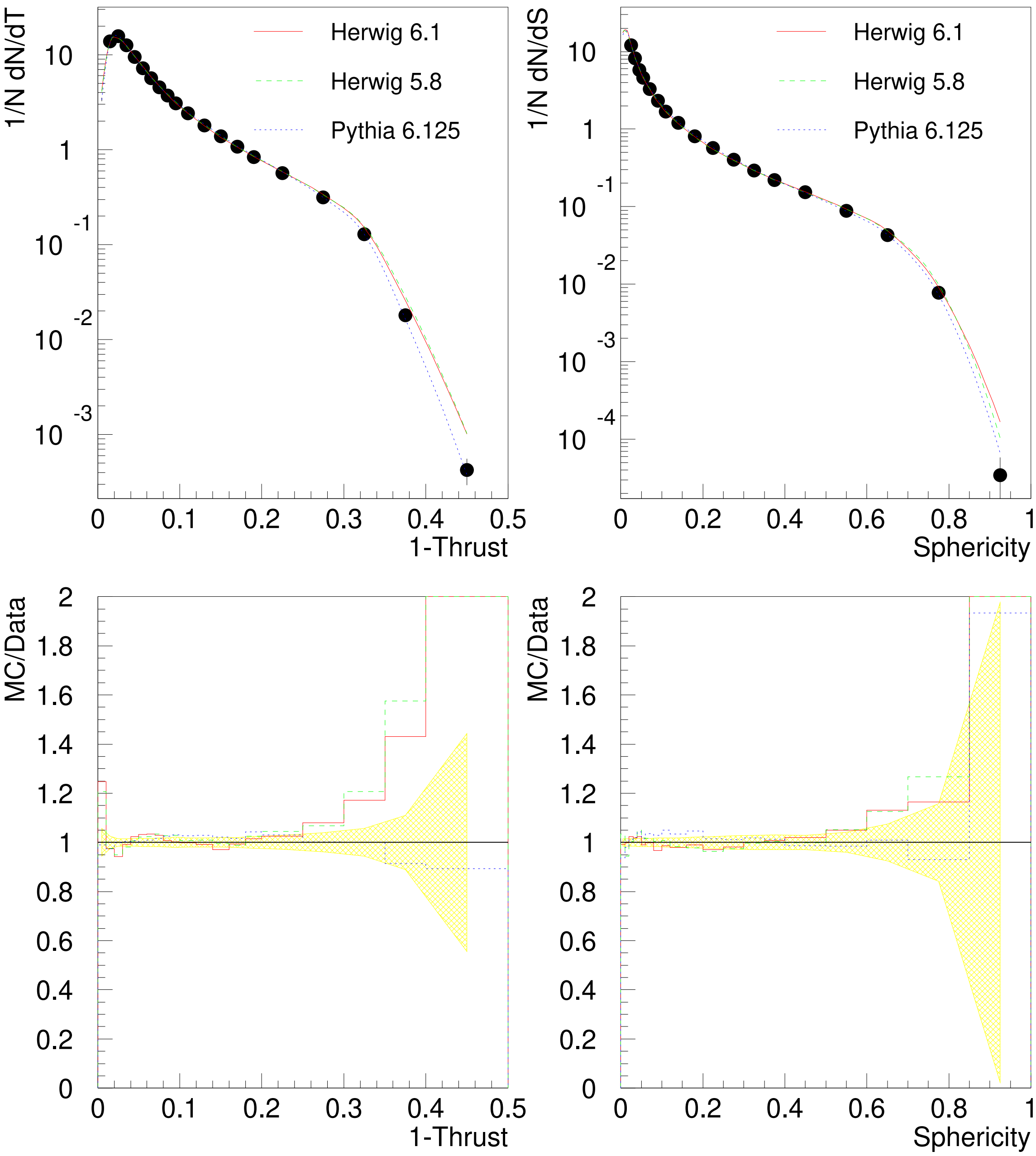

Figure A.1: Data and Monte Carlo comparison for thrust and sphericity.

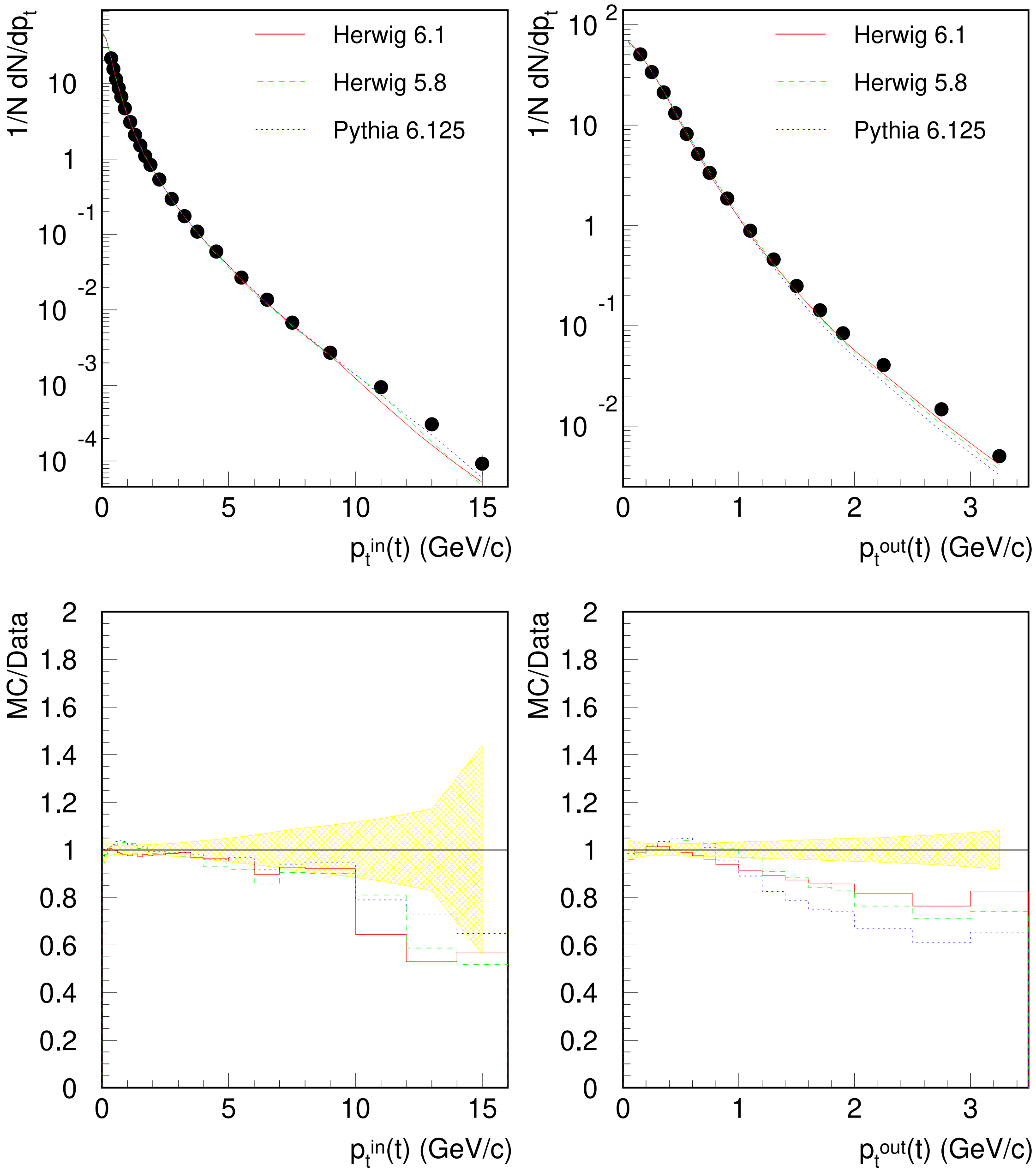

Figure A.2: Data and Monte Carlo comparison for p_t^{in} and p_t^{out} with respect to the thrust axis.

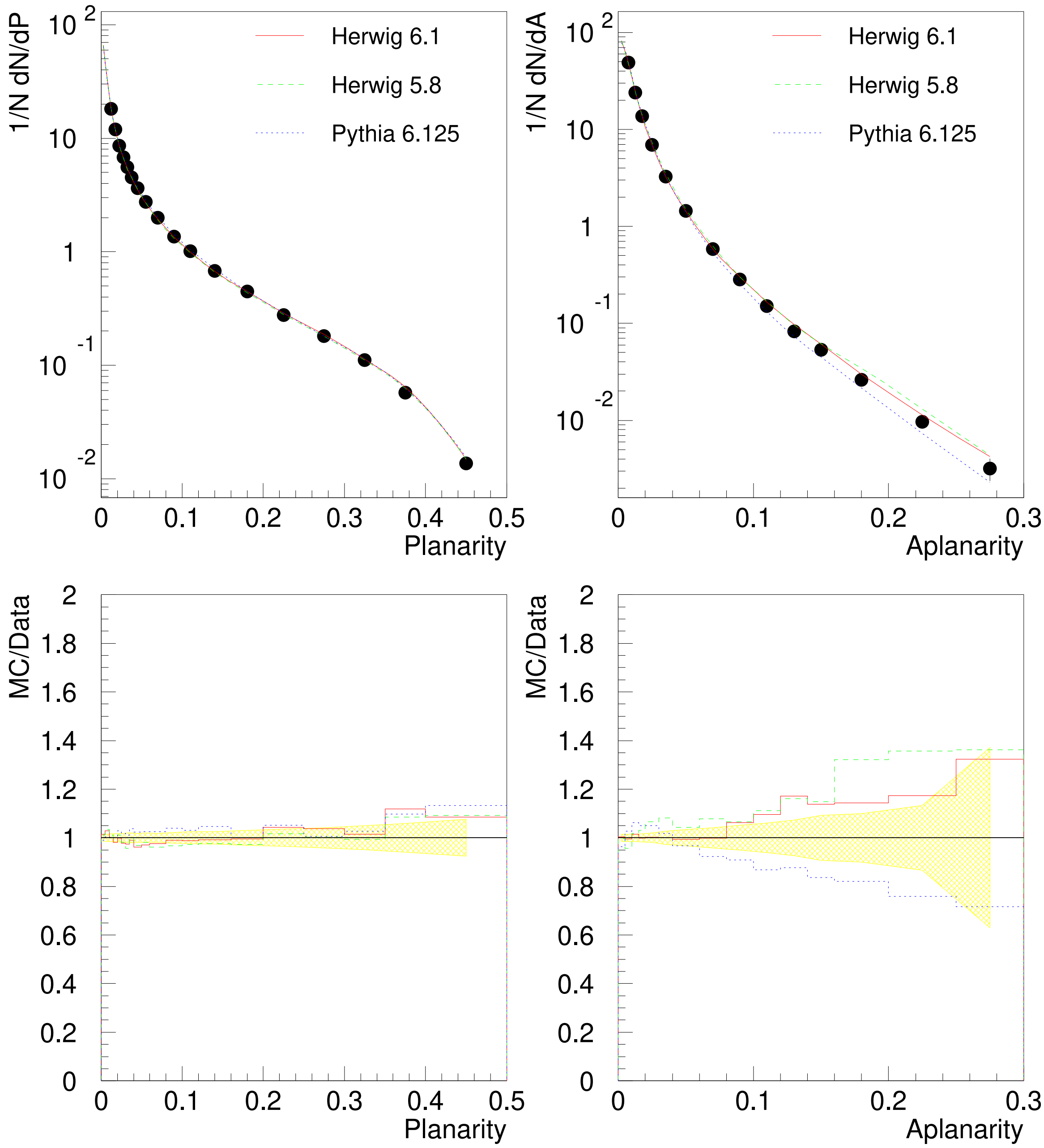

Figure A.3: Data and Monte Carlo comparison for planarity and aplanarity.

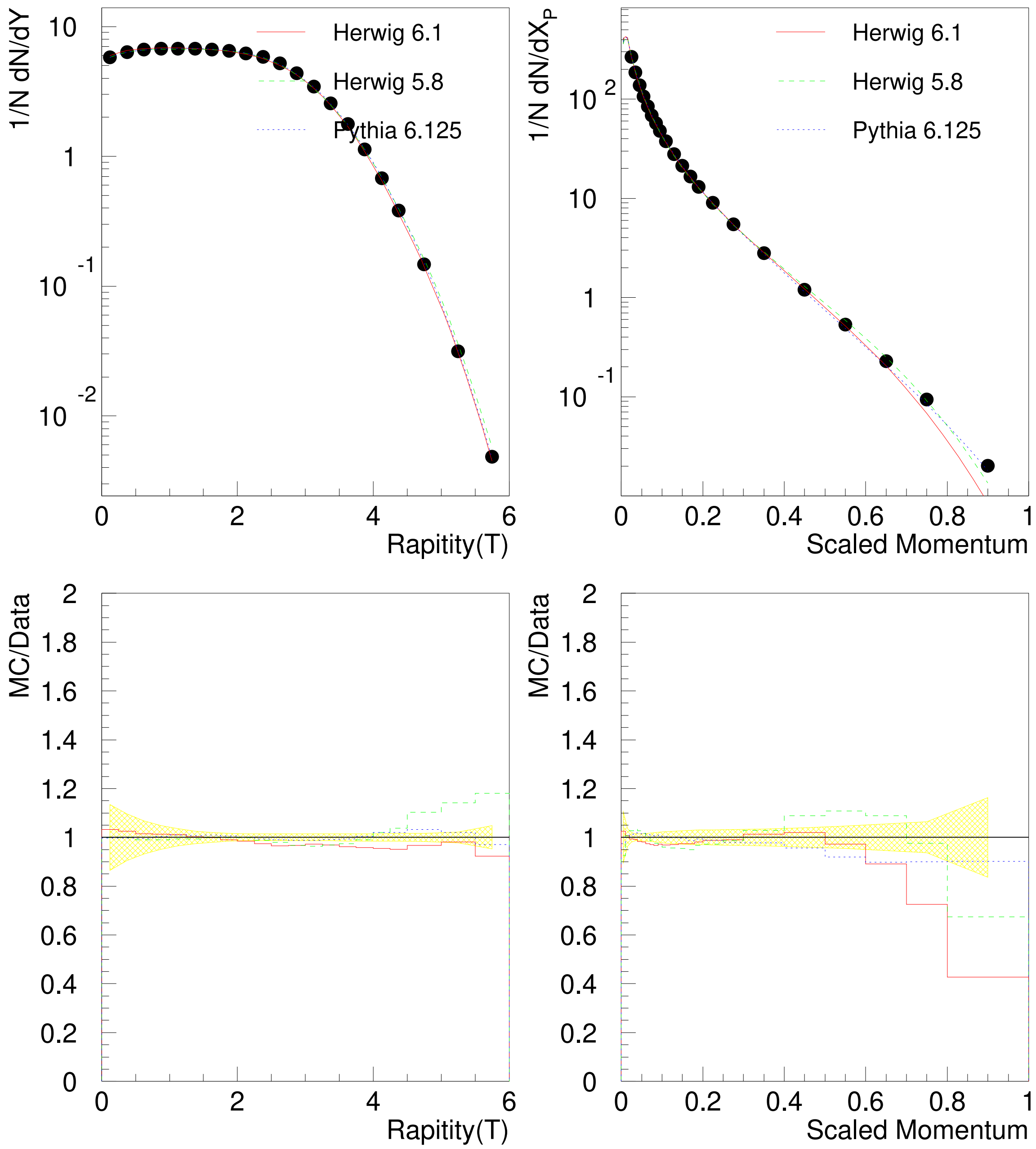

Figure A.4: Data and Monte Carlo comparison for rapidity with respect to the thrust axis and x_p.

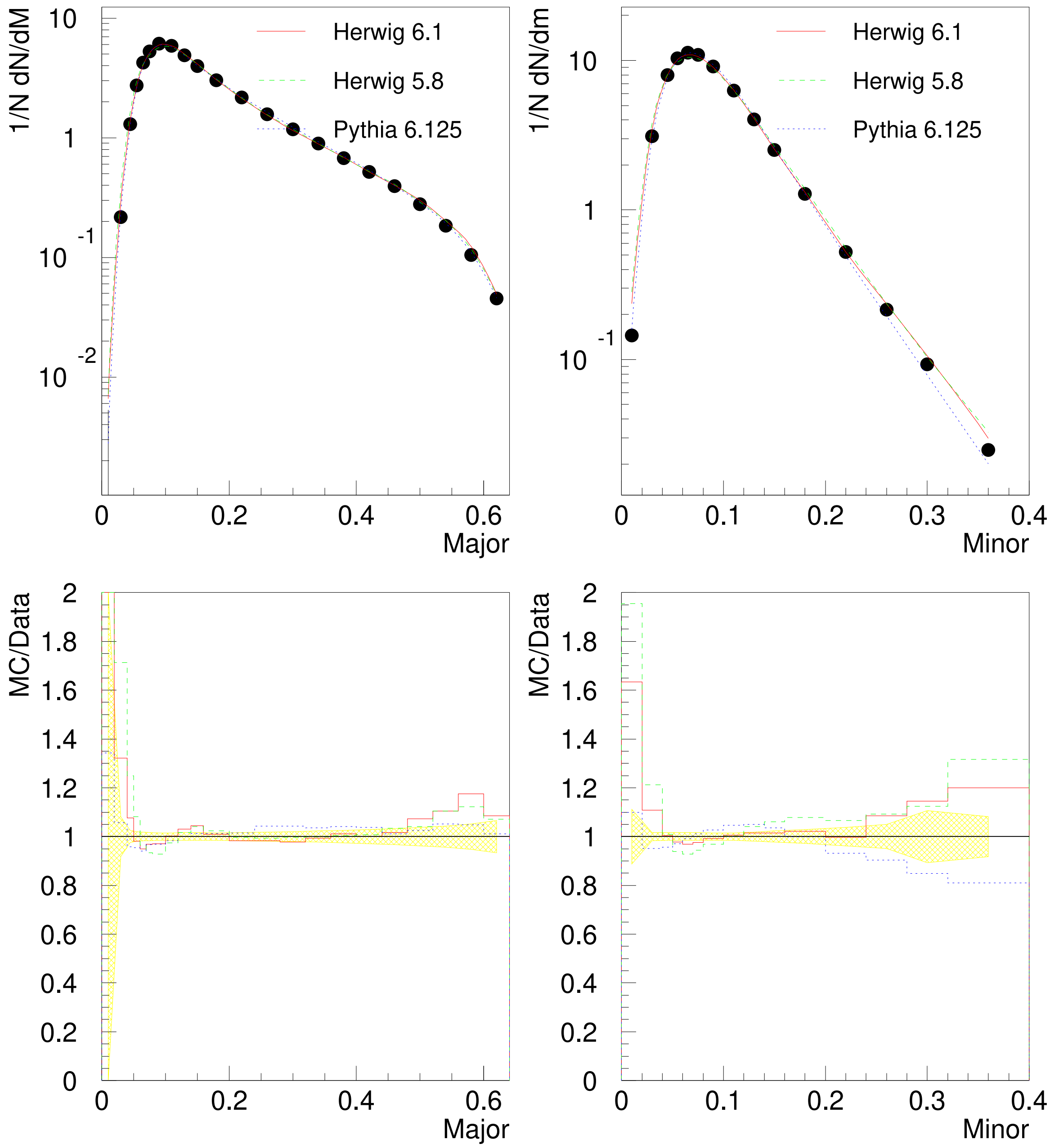

Figure A.5: Data and Monte Carlo comparison for major and minor.

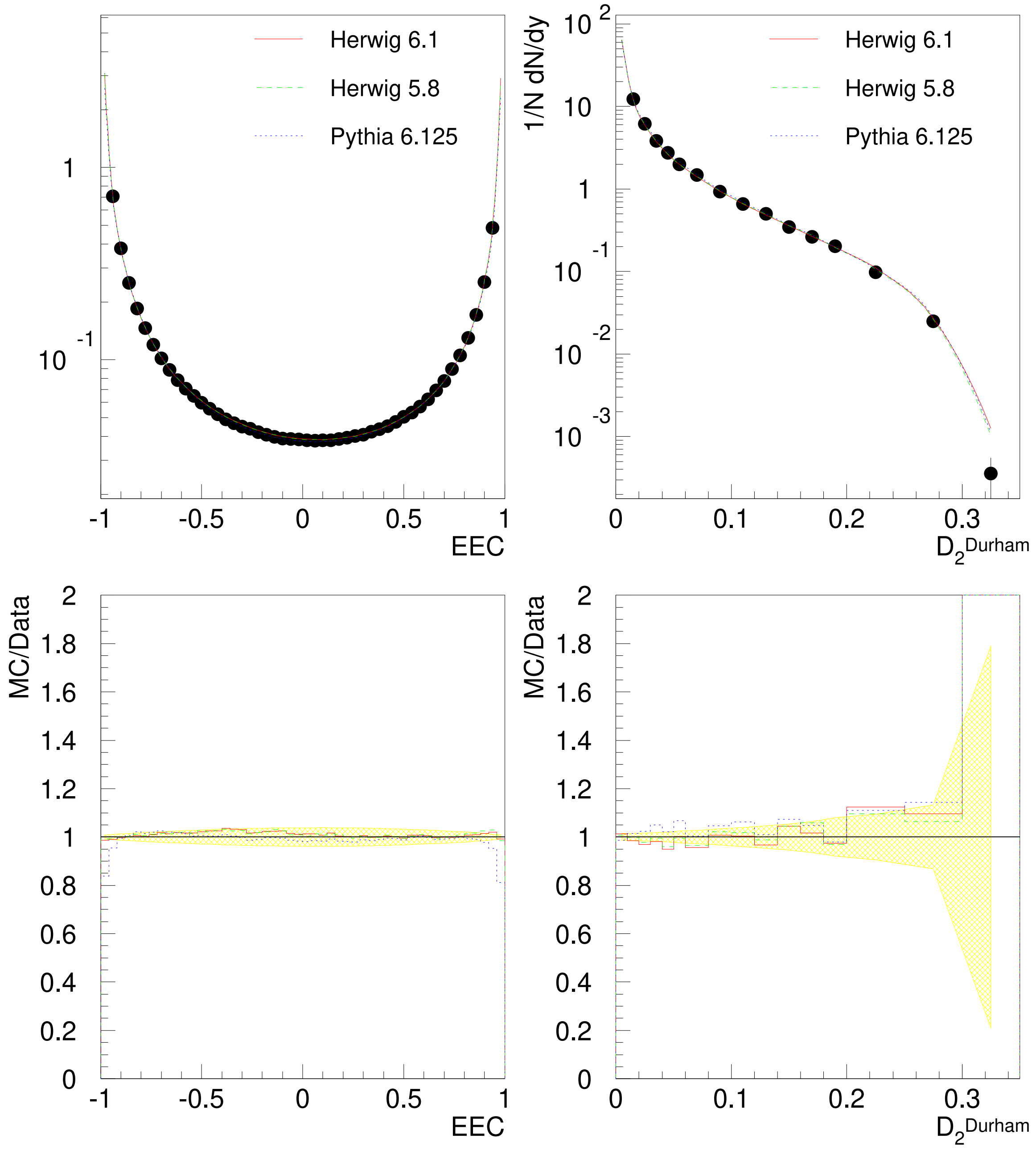

Figure A.6: Data and Monte Carlo comparison for EEC and D_2^{Durham}.

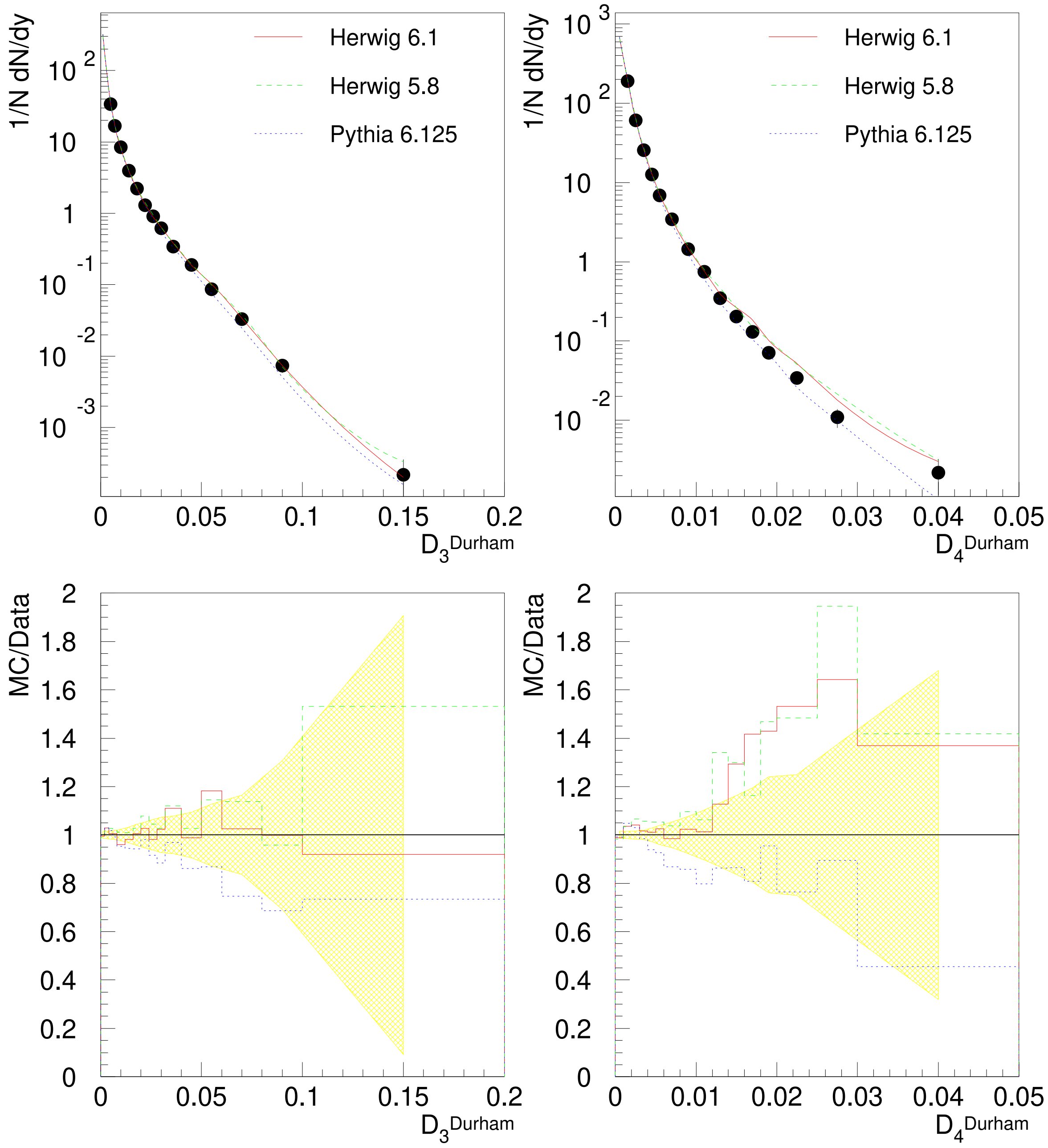

Figure A.7: Data and Monte Carlo comparison for D_3^{Durham} and D_4^{Durham}.

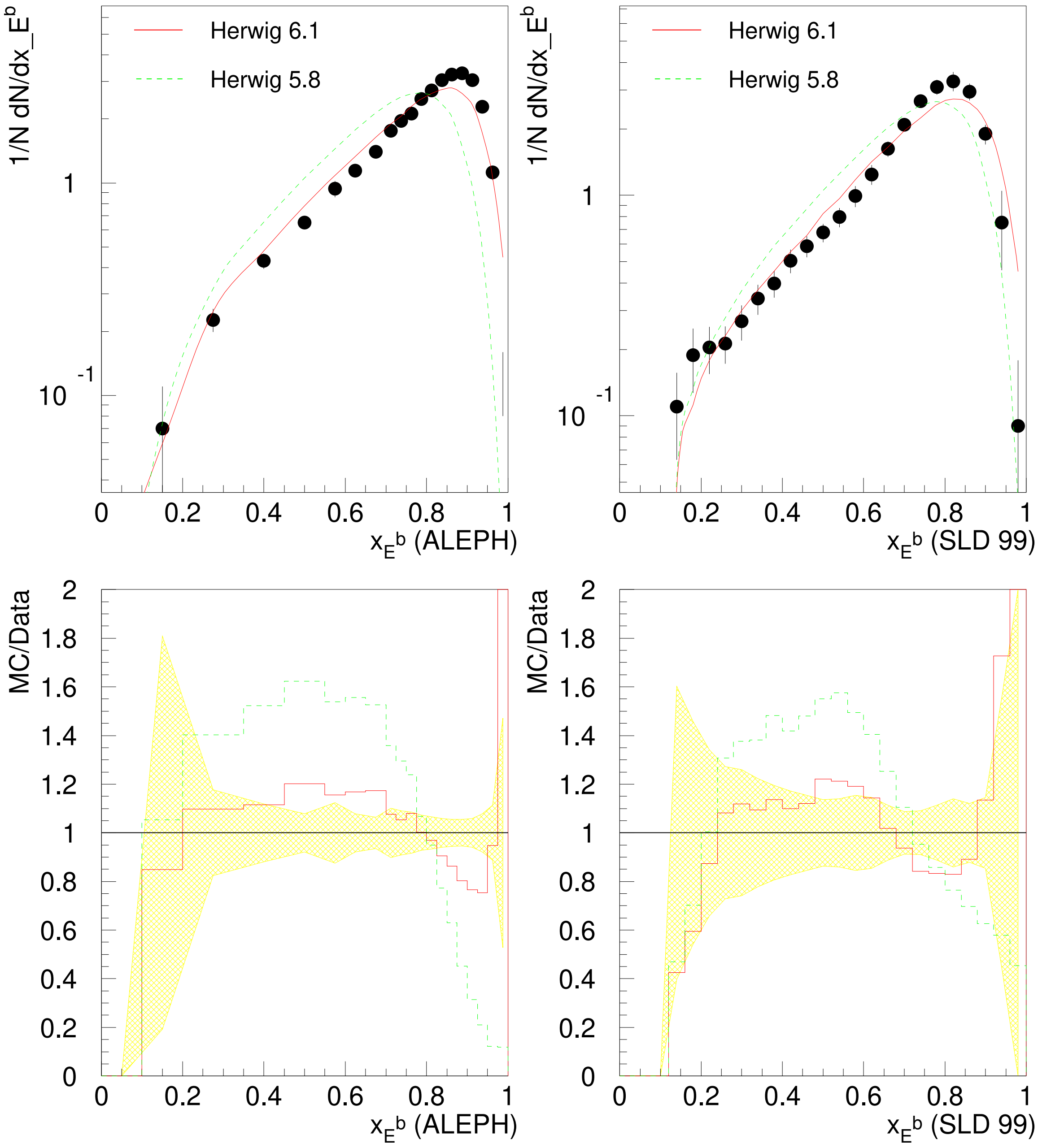

Figure A.8: Data and Monte Carlo comparison for x_E^b measured by ALEPH and SLD.

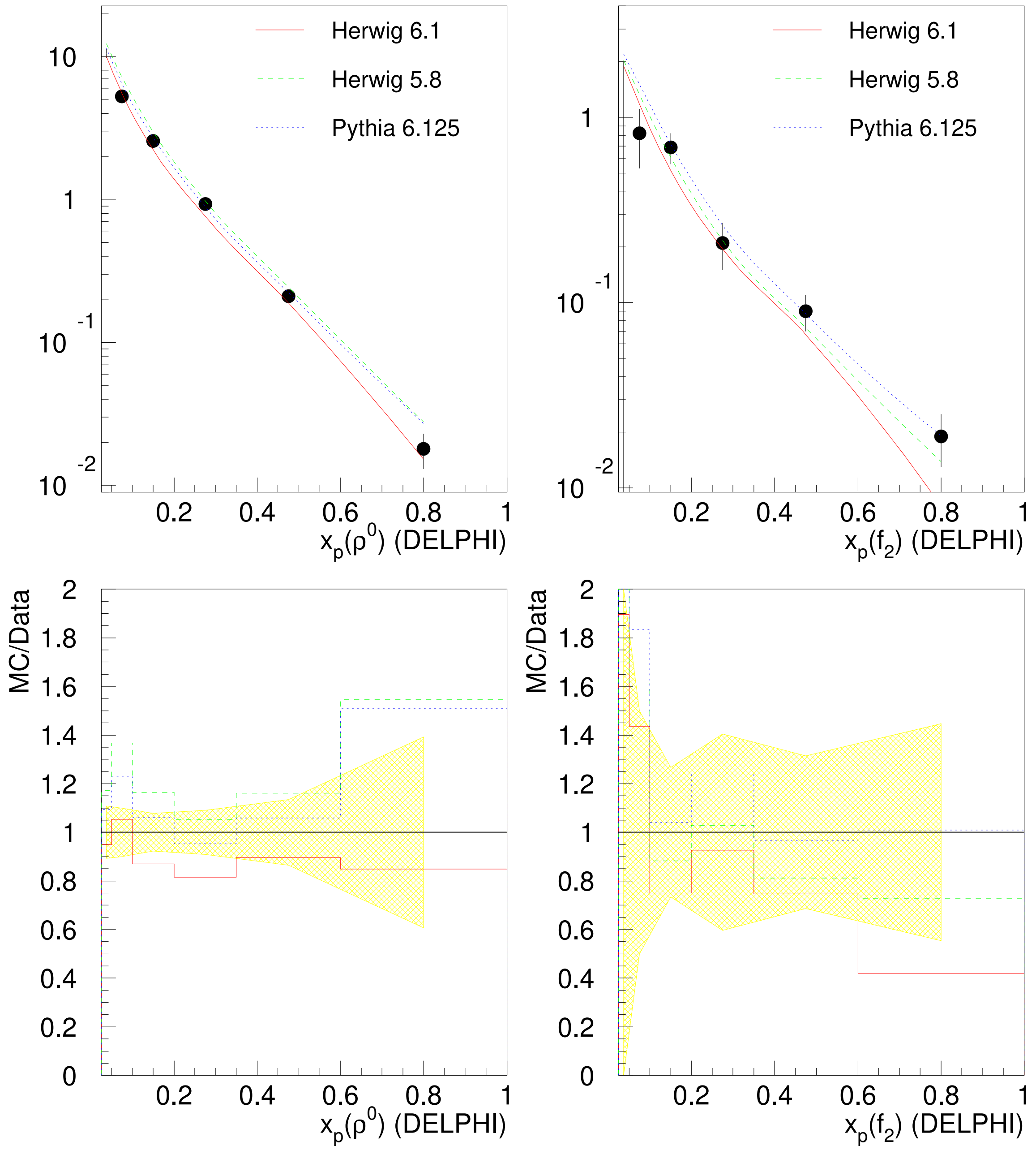

Figure A.9: Data and Monte Carlo comparison for the x_p distribution of ρ^0 and f_2.

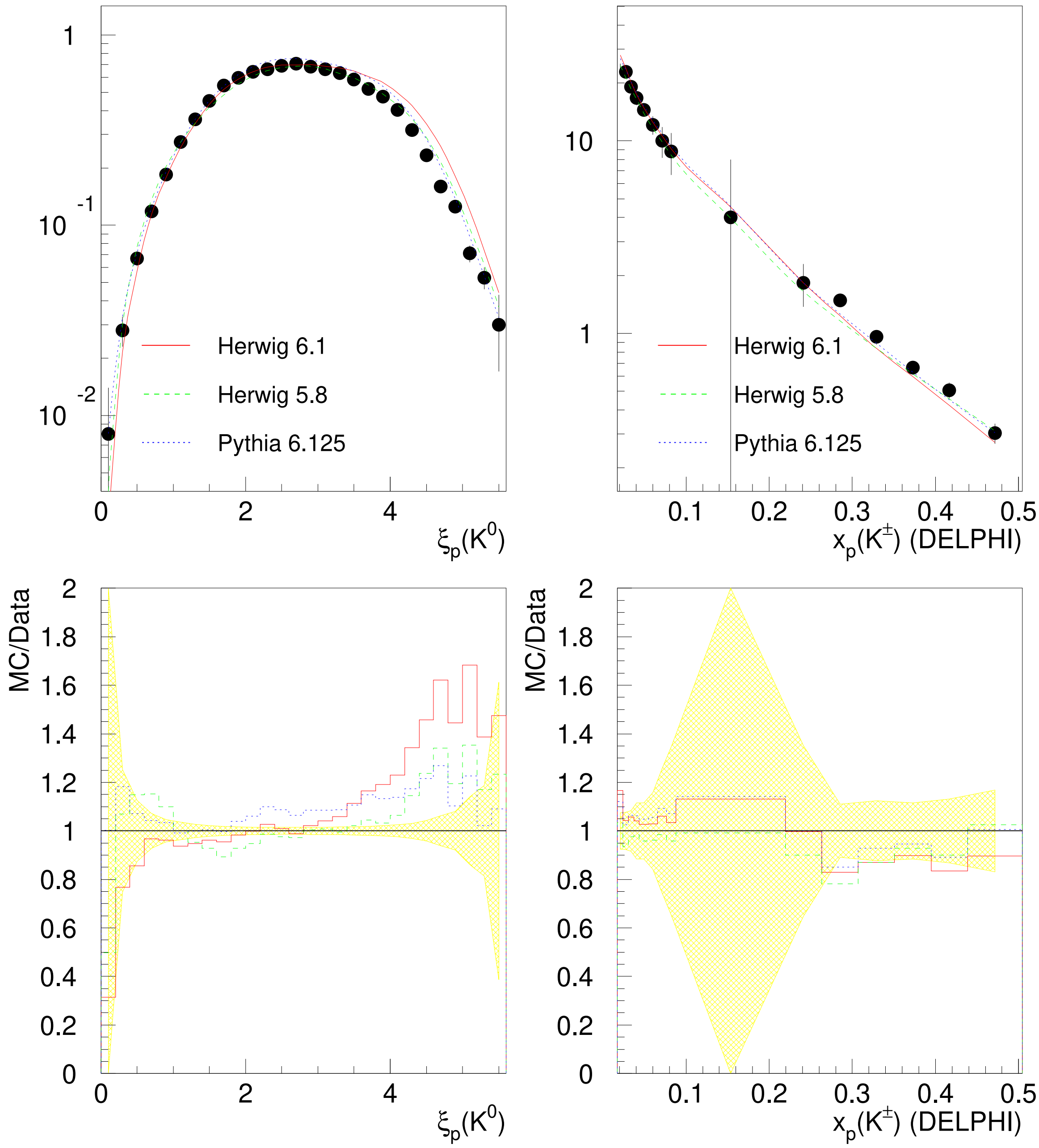

Figure A.10: Data and Monte Carlo comparison for the ξ_p distribution of K^0 and the x_p of $K^{\pm}$.

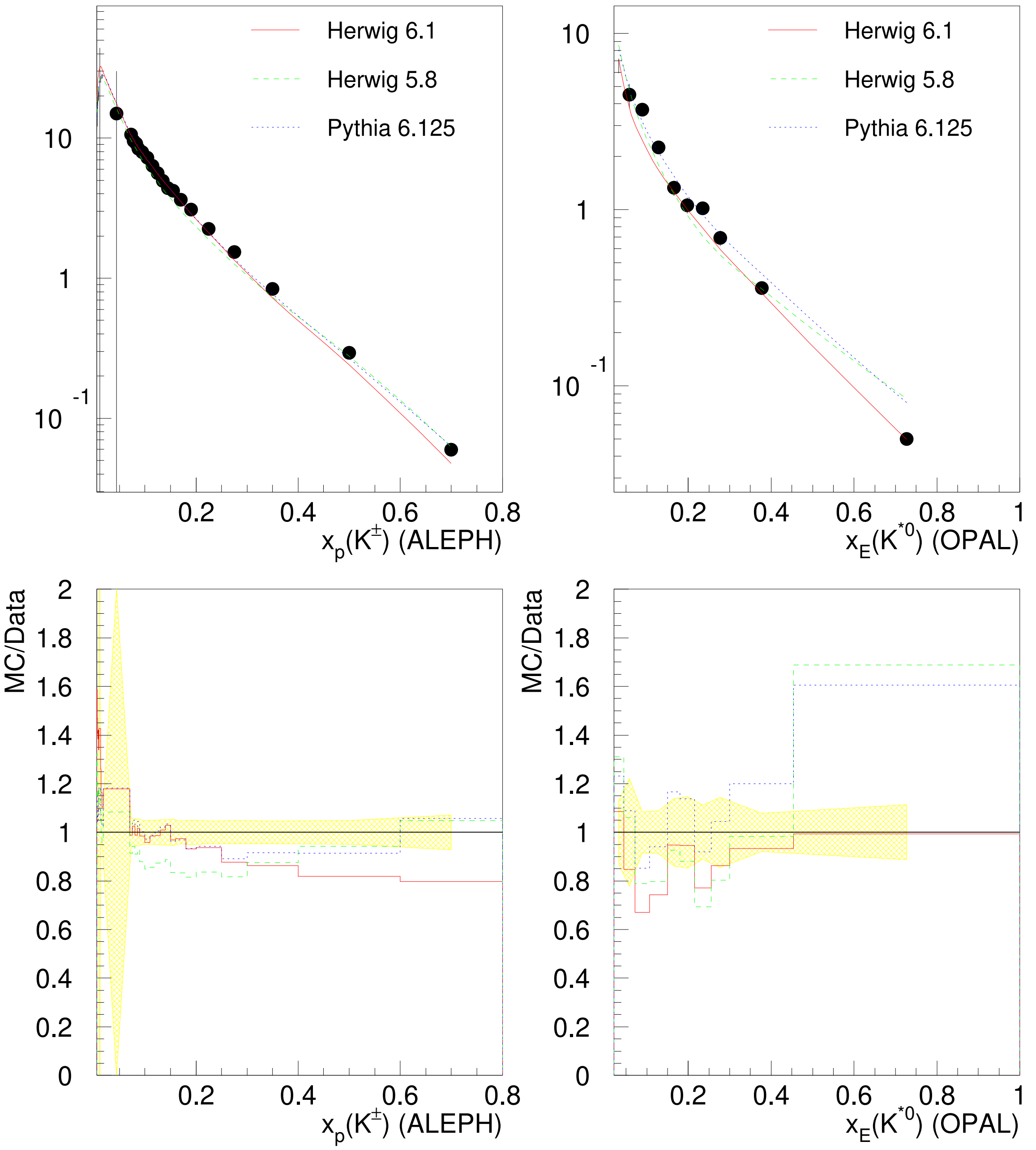

Figure A.11: Data and Monte Carlo comparison for the x_p distribution of $K^{\pm}$ and x_E of K^{*0}.

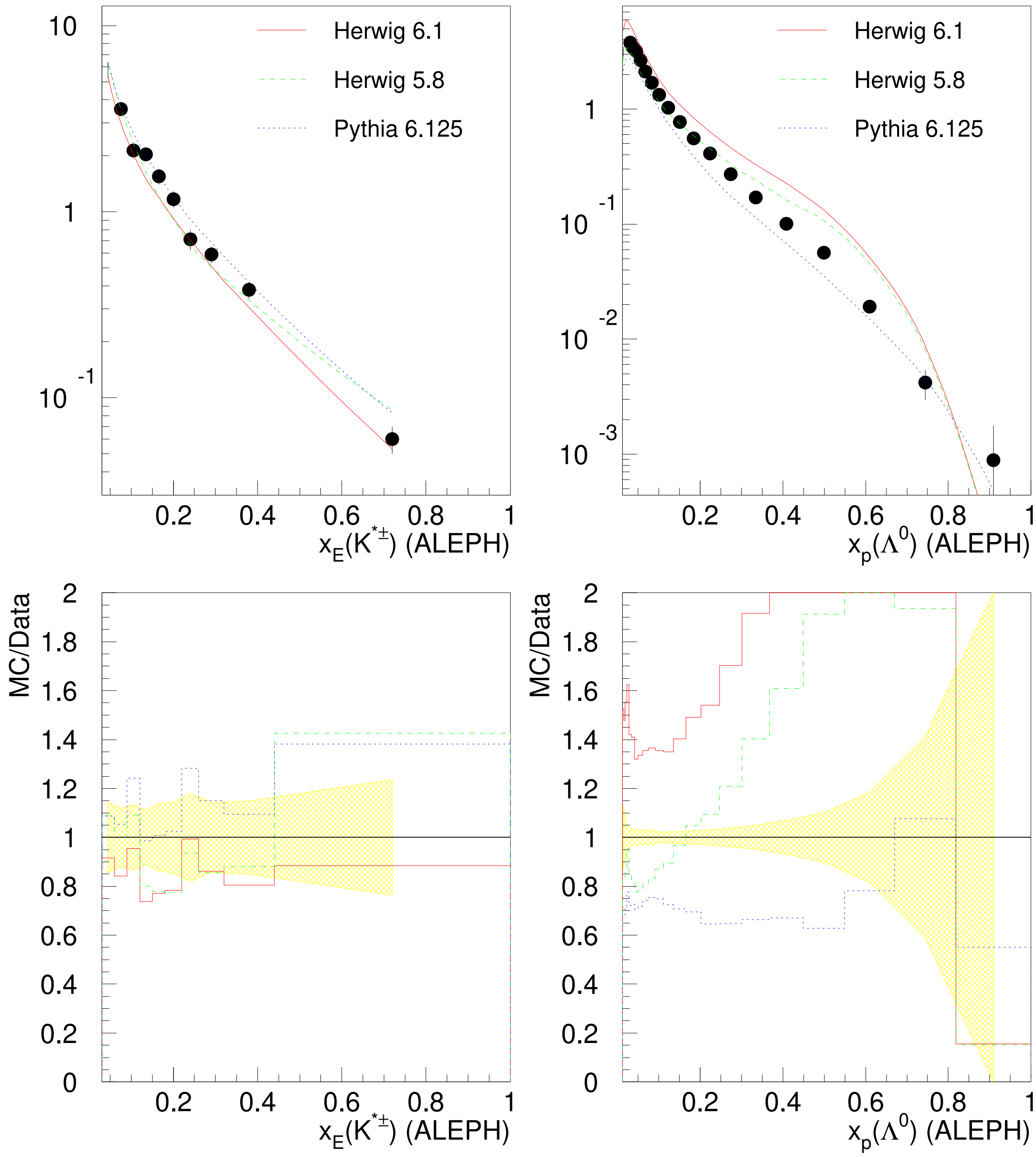

Figure A.12: Data and Monte Carlo comparison for the x_E distribution of $K^{*\pm}$ and the x_p of Λ^0.

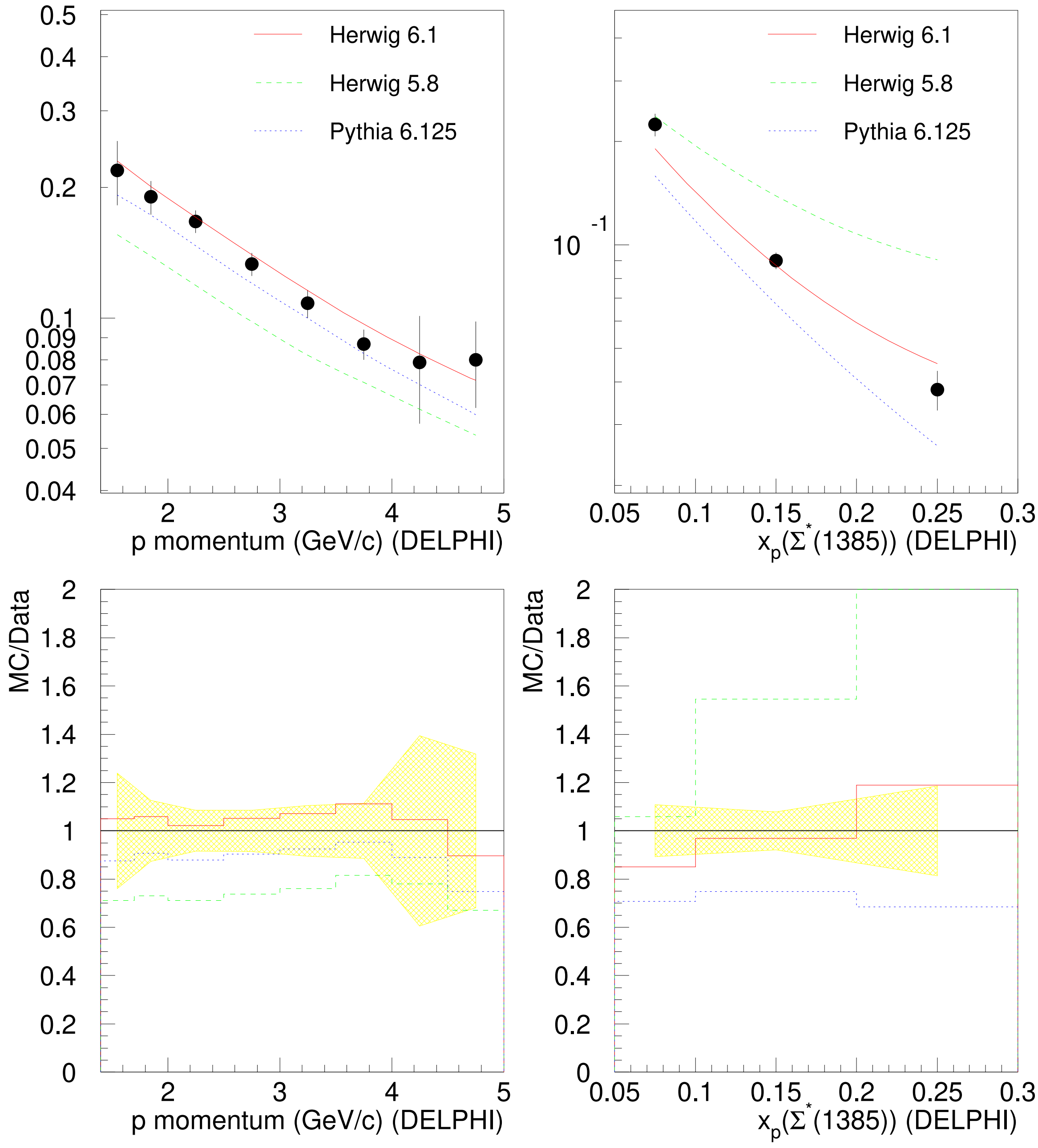

Figure A.13: Data and Monte Carlo comparison for the p momentum and x_p of Σ^* distributions.

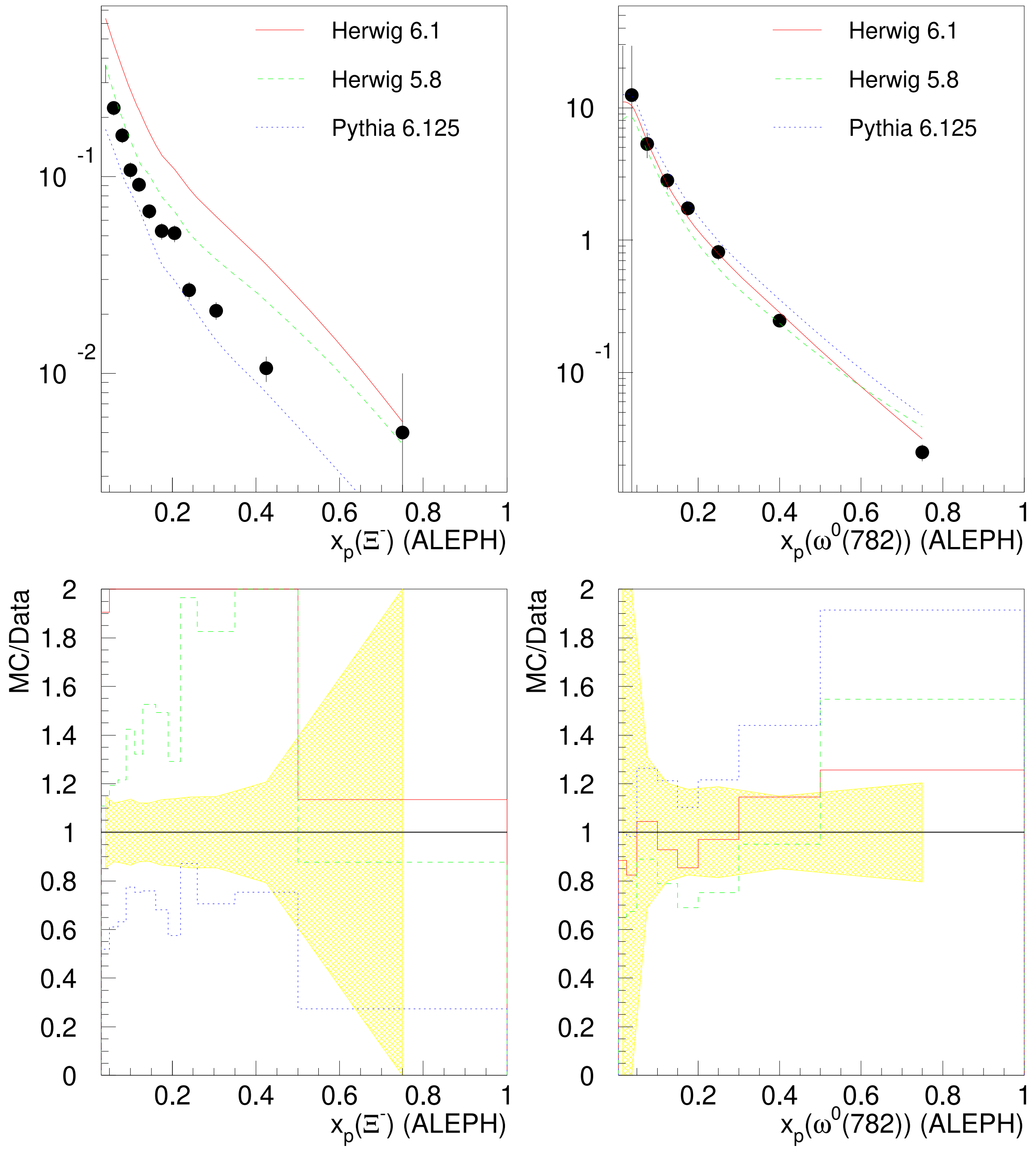

Figure A.14: Data and Monte Carlo comparison for the x_p distributions of Ξ^- and ω^0.

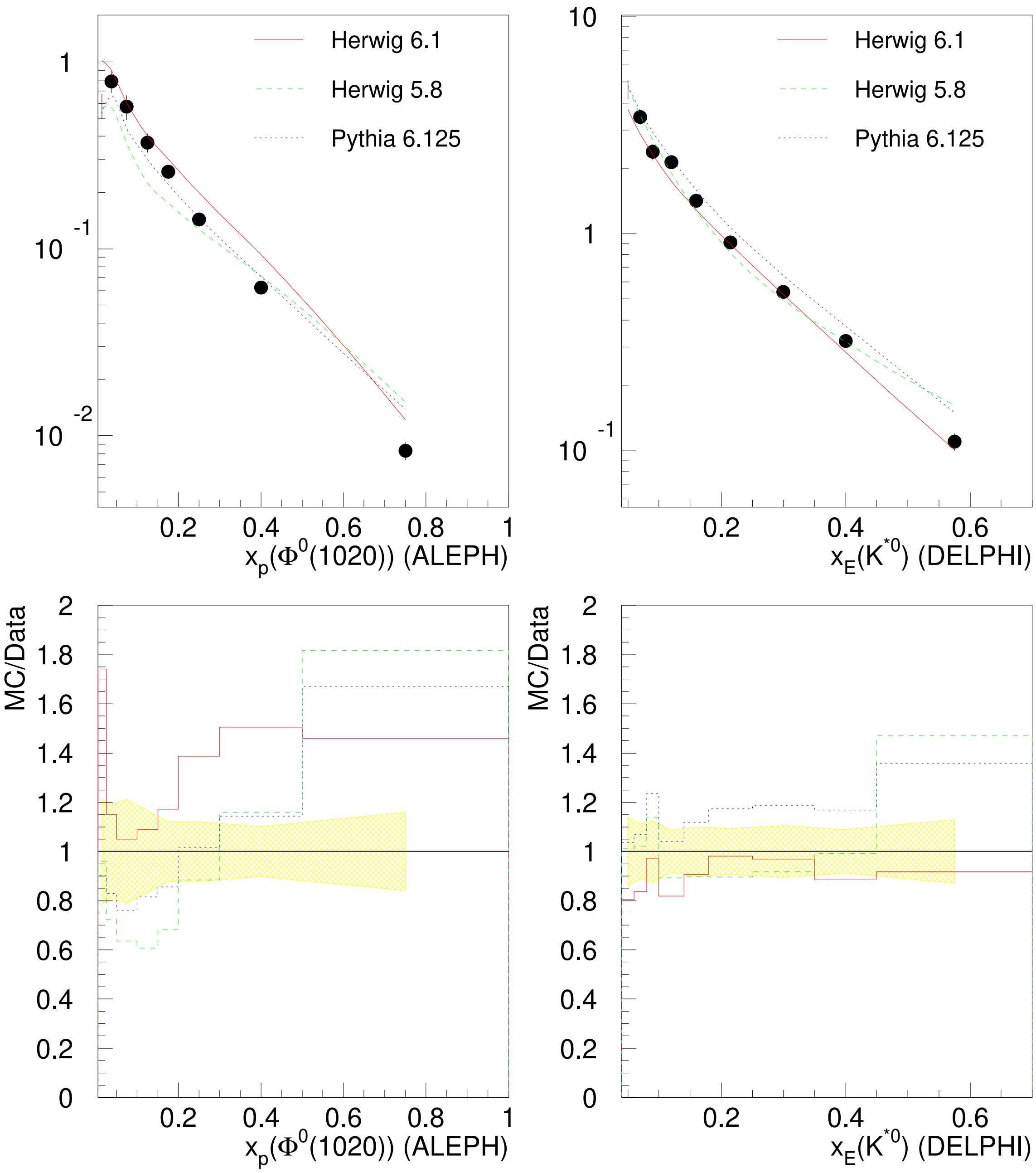

Figure A.15: Data and Monte Carlo comparison for the x_p distribution of ϕ^0 and the x_E of K^{*0}.

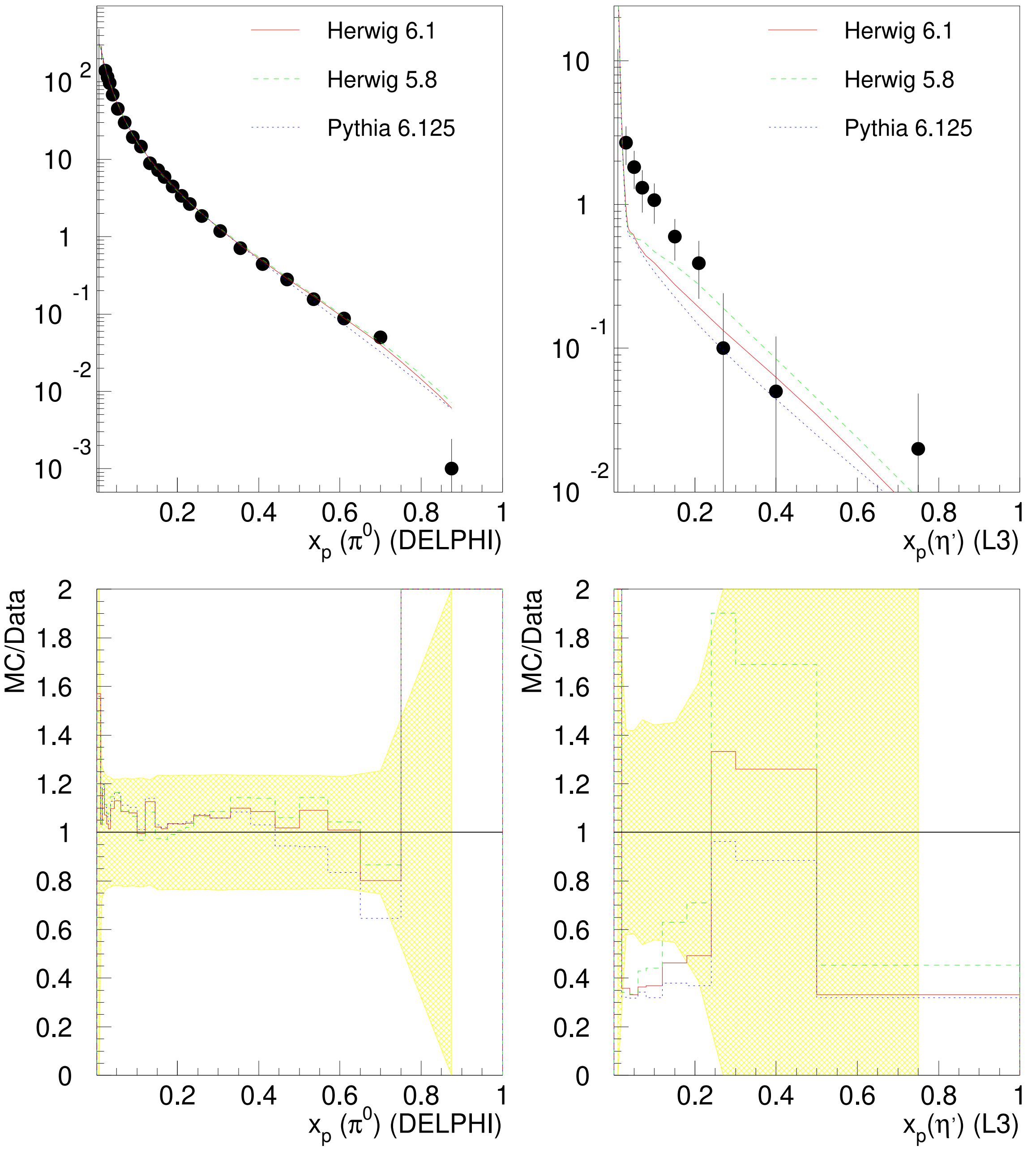

Figure A.16: Data and Monte Carlo comparison for the x_p distribution of π^0 and $\eta\prime$.

Bibliography

[1] D.J. Gross and F. Wilczek, Phys. Rev. Lett. **30** (1973) 1343;
H.D. Politzer, Phys. Rev. Lett. **30** (1973) 1346.

[2] B.R. Webber, Phys. Lett. **B339** (1994) 148;
Yu. Dokshitzer and B.R. Webber, Phys. Lett. **B352** (1995) 451;
P. Nason and M. Seymour, Nucl. Phys. **B454** (1995) 291;
R. Akhoury and V. I. Zakharov, Phys. Lett. **B357** (1995)646; Nucl. Phys. **B465** (1996) 295;
M. Beneke and V. M. Braun, Nucl. Phys. **B454** (1995) 253.

[3] DELPHI Coll., P. Abreu et al., Eur. Phys. J. **C14** (2000) 557.

[4] OPAL Coll., G. Abbiendi et al., Eur. Phys. Jour. **C11** (1999) 643.

[5] J.A. Valls Ferrer, *Derterminación de la constante de acoplamiento fuerte para quarks b, $\alpha_s^b(M_Z)$ con el detector DELPHI de LEP*, PhD thesis, Universitat de València, 1994.

[6] M. Bilenky, G. Rodrigo and A. Santamaria, Nucl. Phys. **B439** (1995) 505.

[7] DELPHI Coll., P.Abreu et al., Phys. Lett. **B418** (1998) 430-442;
S. Martí i García, J. Fuster and S. Cabrera, Nucl. Phys. B (Proc. Suppl.) 64 (1998) 376.

[8] Y.L. Dokshitzer, in *Workshop of Jet Studies at LEP and HERA, Durham, 1990*, J. Phys. **G17** (1991) 1572ff;
S. Catani, Y.L. Dokshitzer, M. Olsson, G. Turnock and B.R. Webber, Phys. Lett. **B269** (1991) 432;
N. Brown, W.J. Stirling, Z. Phys. **C53** (1992) 629.

[9] G.Rodrigo, M.Bilenky, A.Santamaría, Phys. Rev. Lett. **79** (1997) 193.

[10] A. Brandenburg, P.N Burrows, D. Muller, N. Oishi, P Uwer, Phys. Lett. **B468** (1999) 168.

[11] ALEPH Coll., R. Barate et al., Eur. Phys. Jour. **C18** (2000) 1.

[12] OPAL Coll., G. Abbiendi et al., Eur. Phys. J. **C21** (2001) 411.

[13] Y.L. Dokshitzer, G.D. Leder, S.Moretti, B.R. Webber, JHEP **9708** (1997) 001 [hep-ph/9707323].

[14] M. Bilenky, S. Cabrera, J. Fuster, S. Martí, G. Rodrigo, A. Santamaría, Phys. Rev. **D60** (1999) 114006.

[15] T. Sjöstrand. Computer Physics Commun. **82** (1994) 74;
T. Sjöstrand, P. Edén, C. Friberg, L. Lönnblad, G. Miu, S. Mrenna and E. Norrbin, Computer Physics Commun. **135** (2001) 238;
T. Sjöstrand, L. Lönnblad and S. Mrenna, *PYTHIA 6.2 Physics and Manual*, [hep-ph/0108264].

[16] G. Marchesini, B.R. Webber, G. Abbiendi, I.G. Knowles, M.H. Seymour and L. Stanco, Computer Phys. Commun. **67** (1992) 465;
G. Corcella, I.G. Knowles, G. Marchesini, S. Moretti, K. Odagiri, P. Richardson, M.H. Seymour and B.R. Webber, JHEP **0101** (2001) 010 [hep-ph/0011363]; hep-ph/0201201.

[17] P. Abreu et al., Z. Phys. **C73** (1996) 11.

[18] E. Wiechert Abh. Phys.-Ökon. Ges. Königsberg **37** (1897) 1;
J.J. Thomson, Phil. Mag. **44** (1897) 269.

[19] F. Reines and C. Cowan Phys. Rev. **D92** (1953) 830.

[20] C.D. Anderson, Phys. Rev. **D51** (1937) 884.

[21] G. Danby, J.M. Gaillard, K. Goulianos, L.M. Lederman, N. Mistry, M. Schwartz and J. Steinberger, Phys. Rev. Lett. **9** (1962) 36.

[22] J.I. Friedman and H.W. Kendall, Ann. Rev. Nucl. Sci. **22** (1972) 203;
Gargamelle Coll., T. Eichten et al., Phys. Lett. **B46** (1973) 274.

[23] J.J. Aubert et al., Phys. Rev. Lett. **33** (1974) 1404;
J.E. Augustin et al., Phys. Rev. Lett. **33** (1974) 1406.

[24] G. Goldhaber et al., Phys. Rev. Lett. **37** (1976) 255.

[25] M. Perl et al., Phys. Rev. Lett. **35** (1975) 1489;
M. Perl et al., Phys. Lett. **B63** (1976) 466.

[26] S.W. Herb et al., Phys. Rev. Lett. **39** (1977) 252.

[27] CDF Coll., F. Abe et al., Phys. Rev. Lett. **74** (1995) 2626;
D0 Coll., S. Abachi et al., Phys. Rev. Lett. **74** (1995) 2632.

[28] DONUT Coll., K. Kodama et al., Phys. Lett. **B504**, 218-224 (2001).

[29] A. Einstein, Ann. Phys. **17** (1905) 132.

[30] UA1 Coll., G. Arnison et al., Phys. Lett. **B122** (1983) 103;
UA2 Coll., M. Banner et al., Phys. Rev. Lett. **122** (1983) 476.

[31] TASSO Coll., R. Brandelik et al., Phys. Lett. **B86** (1979) 243;
MARK-J Coll., D.P. Barber et al., Phys. Rev. Lett. **43** (1979) 830;
PLUTO Coll., C. Berger et al., Phys. Lett. **B86** (1979) 418.

[32] H. Fritzsch and M. Gell-Mann, Proc. XVI International Conference on High Energy Physics (Fermilab), 1972.

[33] S.L. Glashow, Nucl. Phys. **B20** (1961) 579;
A. Salam, Elementary Particle Theory Svartholm N (ed) (Almqvist and Wiksells, Stockholm) (1968);
S. Weinberg, Phys. Rev. Lett. **19** (1967) 1256.

[34] The LEP working group for Higgs boson searches, *Search for the Standard Model Higgs Boson at LEP*, LHWG Note/2002-01.

[35] The LEP electroweak working group, http://lepewwg.web.cern.ch/LEPEWWG/.

[36] G.D. Rochester and C.C. Butler, Nature **160** (1947) 855;

[37] M. Gell-Mann, California Institue of Technology Synchroton Laboratory Report No. CTSL-20 (1961);
Y. Ne'eman, Nucl. Phys. **26** (1961) 222.

[38] M. Gell-Mann, Phys. Lett. **8** (1964) 214;
G. Zweig, CERN Report No. 8182/TH 401, 1964.

[39] A. Pich, *Aspects of Quantum Chromodynamics*, Lectures given at ICTP Summer School in Particle Physics (1999), hep-ph/0001118.

[40] G. 't Hooft, Nucl. Phys. **B33** (1971) 173.

[41] C.G. Bollini and J.J. Giambiagi, Nuov. Cim. **B12** (1972) 20;
G.'t Hooft and M. Veltman, Nucl. Phys. **B44** (1972) 189;
J. Ashmore, Nuov. Cim. Lett. **4** (1972) 289.

[42] G. 't Hooft, Nucl. Phys. **B61** (1973) 455.

[43] W.A. Bardeen, A.J. Buras, D.W. Duke, T. Muta, Phys. Rev. **D18** (1978) 3998.

[44] T. van Ritbergen, J.A.M. Vermaseren, S.A. Larin, Phys. Lett. **B400** (1997) 379.

[45] K.G. Chetyrkin, B.A. Kniehl, M. Steinhauser, Phys. Rev. Lett. 79 (1997) 2184.

[46] T. Tarrach, Nucl. Phys. **B183** (1981) 384.

[47] O. Nachtmann, W. Wetzel, Nucl. Phys. **B187** (1981) 333;
S.A. Larin, Phys. Lett. **B303** (1993) 113; K.G. Chetyrkin, Phys. Lett. **B404** (1997) 161.

[48] J.A.M. Vermaseren, S.A. Larin, T. van Ritbergen, Phys. Lett. **B405** (1997) 327.

[49] R.K. Ellis, W.J. Stirling, B.R. Webber, *QCD and Collider Physics*, Cambridge University Press, Cambridge, 1996.

[50] F. Bloch and A. Nordsieck, Phys. Rev., **52** (1937) 54.

[51] T. Kinoshita, J. Math. Phys. **3** (1962);
T.D. Lee and M. Nauenberg, Phys. Rev. **B133** (1964) 1549.

[52] W. Bartel et al., Z. Phys. **C33** (1986) 23; S. Bethke et al., Phys. Lett. **B213** (1988) 235.

[53] N. Brown and N.J. Stirling, Phys. Lett. **B252** (1990) 657.

[54] L.A. Gribov, E.M. Levin, M.G. Ryskin, Phys. Rep. **100** (1983) 1.

[55] Yu.L. Dokshitzer, V.A. Khoze, A.H. Mueller, S.I. Troyan, *Basics of Perturbative QCD*, Edition Frontières, Gif-sur-Yvette, 1991.

[56] A. Bassetto, M. Ciafaloni, G. Marchesini, Phys. Rep. **100** (1983) 201.

[57] B.R. Webber, Ann. Rev. Nucl. Part. Sci. **36** (1986) 253.

[58] G. Altarelli, G. Parisi, Nucl. Phys. **B126** (1977) 298.

[59] X. Artru and G. Mennessier, Nucl. Phys. **B70** (1974) 93.

[60] B. Andersson, G. Gustafson, G. Ingelmann and T. Sjöstrand, Phys. Rep. **97** (1983) 31.

[61] B. Andersson and G. Gustafson, Z. Phys. **C3** (1980) 223.

[62] B. Andersson, G. Gustafson and B. Söderberg, Z. Phys. **C20** (1983) 317.

[63] M.G. Bowler, Z. Phys. **C11** (1981) 168.

[64] C. Peterson, D. Schlatter, I. Schmitt and P. Zerwas, Phys. Rev. **D27** (1983) 105.

[65] D. Amati and G. Veneziano, Phys. Lett. **B83** (1979) 87; G. Marchesini, L. Tretadue and G. Veneziano, Nucl. Phys. **B181** (1981) 335.

[66] CLEO Coll., S. Chen et al., Phys. Rev. Lett. **87** (2001) 251807;
CLEO Coll., D. Cronnin-Hennessy et al., Phys. Rev. Lett. **87** (2001) 251808;
CLEO Coll., R. Briere et al., hep-ex/0209024;
BABAR Coll., B. Aubert et al., hep-ex/0207084;

DELPHI Coll., Contributed paper for ICHEP 2002, 2002-071-CONF-605;
DELPHI Coll., Contributed paper for ICHEP 2002, 2002-071-CONF-604;
M. Batagglia et al., CERN-TH-2002-290, hep-ph/021031.

[67] II. Bigi et al., Phys. Rev. **D50** (1994) 2234;
M. Beneke, V.M. Braun, Nucl. Phys. **B426** (1994) 301.

[68] II. Bigi et al., Phys. Rev. **D56** (1997) 4017.

[69] R. Tarrach, Nucl. Phys. **B183** (1981) 384.

[70] N. Gray, D.J. Broadhurst, W. Grafe and K. Schilcher, Z. Phys. **C48** (1990) 673;
K.G. Chetyrkin and M. Steinhauser, DESY-99-174, [hep-ph/9911434];
M. Melnikov and T. van Ritbergen, SLAC-PUB-8321, [hep-ph/9912391].

[71] M. Spira, Fortsch. Phys. **46** (1998) 203.

[72] S. Narison, Nucl. Phys. Proc. Suppl. **86** (2000) 242.

[73] E. Gámiz et al., hep-ph/0212230.

[74] M. Eidemüller, IFIC/02-31, FTUV/02-0719 [hep-ph/0207237].

[75] A.X. El-Khadra, M. Luke, hep-ph/0208114. Submitted to Ann. Rev. Nucl. Part. Sci.

[76] L. Demortier et al., The top averaging group for CDF and D0 collaborations, FERMILAB-TM-2084, 1999.

[77] A.V. Manohar and H. Georgy, Nucl. Phys. **B234** (1984) 189.

[78] H. Leutwyler, Phys. Lett. **B378** (1996) 313.

[79] W.Bernreuther, A. Brandenburg, P.Uwer, Phys.Rev.Lett. **79** (1997) 189.

[80] P. Nason and C.Oleari, Phys. Lett. **B407** (1997) 57.

[81] S. Keller and E. Laenen, Phys. Rev. **D59** (1999) 114004.

[82] K. Hagiwara, T. Kuruma and Y. Yamada, Nucl. Phys. **B358** (1991) 80.

[83] D. Decamp et al., Nucl. Instr. and Meth. **A294** (1990) 121.

[84] P. Aarnio et al., Nucl. Instr. and Meth. **A303** (1991) 233.

[85] P. Abreu et al., Nucl. Instr. and Meth. **A378** (1996) 57.

[86] B. Adeva et al., Nucl. Instr. and Meth. **A289** (1990) 35.

[87] K. Ahmet et al., Nucl. Instr. and Meth. **A305** (1991) 275.

[88] *The LEP injector chain*, CERN LEP TH 83-29 (1983);
The LEP main ring, CERN LEP 84-01 (1984);
LEP 2, CERN AC 96-01 (1996).

[89] N. Bingefors et al., Nucl. Instr. and Meth. **A328** (1993) 447.

[90] V. Chabaud et al., Nucl. Instr. and Meth. **A368** (1996) 314.

[91] P. Abreu et al., Nucl. Phys. **B417** (1994) 3, erratum ibid., **B426** (1994) 244.

[92] P. Abreu et al., Nucl. Phys. **B418** (1994) 403;
D. Bardin et al., *Precision Determination of the Z Resonance Parameters*, DELPHI 94-114 PHYS 431, Contributed paper gls0301 to the 27th Interantional Conference on High Energy Physics, Glasgow (UK) 1994.

[93] DELPHI Collaboration, *High precision relative luminosity measurement with a Very Small Angle Tagger (VSAT) in DELPHI*, DELPHI 92-77 PHYS 188, Contributed paper to the Dallas Conference, 1992.

[94] *DELSIM User Manual*, DELPHI 87-96/PROG 99, 1989;
DELSIM Reference Manual, DELPHI 87-98/PROG 100, 1989.

[95] B.I. Ermolaev and V.S. Fadin, JETP Lett. **33** (1981) 269;
A.H. Mueller, Phys. Lett. **B104** (1981) 161;
A. Bassetto, M. Ciafaloni, G. Marchesini and A.H. Mueller, Nucl. Phys. **B207** (1982) 189;
G. Marchesini and B.R. Webber, Nucl. Phys. **B238** (1984) 1.

[96] E. Norrbin and T. Sjöstrand, Nucl. Phys. **B603** (2001) 297.

[97] A. Ballestrero et al., [hep-ph/0006259].

[98] A. Krzywicki, B. Petersson, Phys. Rev. **D6** (1972) 924;
J. Finkelstein, R.D. Pecceis, Phys. Rev. **D6** (1972) 2606;
F. Niedermayer, Nucl. Phys. **B79** (1974) 355;
A. Casher, J. Kogut, L. Susskind, Phys. Rev. **D10** (1974) 732.

[99] M. Weierstall, *Anpassung und Test von Fragmentierungsmodellen mit präzisen Ereignisform und Einteilchenverteilungen unter besonderer Berücksichtigung von identifizierten Teilchen*, WU B DIS 95-11 (1995).

[100] W.H. Press, B.P. Flannery, S.A. Teukolsky, W.T. Vetterling, Numerical Recipies, *The Art of Scientific Computing*, Cambridge University Press;
NAG Libary, MK16, NAG Ltd., Oxford, GB.

[101] S. Cantani, G. Marchesini and B.R. Webber, Nucl. Phys. **B349** (1991) 635.

[102] R.J. Hemingway, *An OPAL tune of HERWIG 6.1 using Z^0 data*, OPAL technical note TN652, 2000.

[103] U. Flagmeyer and K. Münich, *The program package* PROFESSOR.

[104] R. Akers et al., Z. Phys. **C61** (1994) 209.

[105] ALEPH Coll., ALEPH/2000-020, CONF/2000-017.

[106] K. Abe et al., Phys. Rev. Lett. **84** (2000) 4300.

[107] L. Lönnblad, Comput. Phys. Common. **71** (1992) 15;
I.G. Knowless et al., *QCD Event Generators*, [hep-ph/9601212], CERN 96-01, Vol. 2.

[108] G. Corcell, I.G. Knowles, G. Marchesini, S. Moretti, K. Odagiri, P. Richardson, M.H. Seymour and B.R. Webber, *Herwig 6.3 realeased note*, [hep-ph/0107071];
G. Corcell, I.G. Knowles, G. Marchesini, S. Moretti, K. Odagiri, P. Richardson, M.H. Seymour and B.R. Webber, *Herwig 6.4 realeased note*, [hep-ph/0201201];
G. Corcell, I.G. Knowles, G. Marchesini, S. Moretti, K. Odagiri, P. Richardson, M.H. Seymour and B.R. Webber, *Herwig 6.5 realeased note*, [hep-ph/0210213].

[109] S. Martí i Garcia, *Estudi de la dependència energètica de les diferéncies entre jets de quarks i gluons utilitzant el detector DELPHI de LEP*, PhD thesis, Universitat de València, 1995.

[110] A. De Rujula, H. Georgy, S.L. Glashow, Phys. Rev. **D12** (1975) 147.

[111] A. El-khadra and M. Luke, [hep-ph/0208114].

[112] S. Cabrera, *Determinación de la masa del quark b a la escala M_Z en el detector DELPHI*, PhD thesis, Universitat de València, 1999.

[113] S. Bethke, MPI-PhE-2002-17, [hep-ex/0211012].

[114] CLEO Coll., D. Cronin-Hennessy et al., Phys. Rev. Lett. **87** (2001) 251808.

[115] CLEO Coll., A.H. Mahmood et al., CLNS02-1810, [hep-ex/0212051].

[116] M. Battaglia et al., CERN-TH-2002-290, [hep-ph/0210319].

[117] DELPHI Coll. P. Abreu et al., Z. Phys. **C65** (1995) 555;
G.V. Borisov, C. Mariotti, Nucl. Instr. and Meth. **A372** (1996) 181.

[118] G. Borisov, Nucl. Instr. and Meth. **A417** (1998) 384.

[119] DELPHI Coll., J. Abdallah et al., Submitted to Eur.Phys.J. C. (2002).

[120] F. Martínez, *High precision measurement of* $\Gamma(Z \to b\bar{b})/\Gamma(Z \to \text{Hadrons})$ *with the* DELPHI *detector at LEP collider*, PhD thesis, Universitat de València, 1997.

[121] D. Brown, M. Frank, *Tagging B hadrons using track impact parameters*, ALEPH note 92-135.

[122] DELPHI Coll., E. Phys. J. **C10** (1999) 415.

[123] M.H. Seymour, Z. Phys. **C63** (1994) 99.

[124] M.H. Seymour, Nucl. Phys. **B436** (1995) 163.

[125] D.J. Miller and M.H. Seymour, Phys. Lett. **B435** (1998) 213.

[126] P. Abreu et al., Phys. Lett. **B405** (1997) 202.

[127] R. Barate et al., Phys. Lett. **B434** (1998) 437.

[128] P. Abreu et al., Phys. Lett. **B462** (1997) 202.

[129] K. Abe et al., Phys. Lett. **B507** (2001) 61.

[130] G. Abbiendi et al., Eur. Phys. J. **C18** (2001) 447.

[131] R. Barate et al., Eur. Phys. J. **C16** (2000) 597.

[132] M. Acciarri et al., Phys. Lett. **B476** (2000) 243.

[133] G. Abbiendi et al., Eur. Phys. J. **C13** (2000) 447.

[134] The LEP/SLD Heavy Flavour Working Group, LEPHF/2001-01.

[135] P. Abreu et al. Eur. Phys. J. **C10** (1999) 415.

[136] Jade Coll., W. Bartel et al., Z. Phys. **C33** (1986) 23.

[137] S. Bethke et al., Nucl. Phys. **B370** (1992) 310; erratum: *ibid.* **B523** (1998) 681.

[138] SLD Coll., K. Abe et al., Phys. Rev. **D59** (1999) 12002.

[139] R. Akers et al., Z. Phys. **C65** (1995) 17;
R. Akers et al., Z. Phys. **C63** (1994) 181.

[140] S. Brandt et al., Phys. Lett. **12** (1964) 57;
E. Fahri, Phys. Rev. Lett. **39** (1977) 1587.

[141] Mark J Collab., D. P. Barber et al., Phys. Rev. Lett. **43** 830 (1979);
Mark J Collab., D. P. Barber et al., Phys. Lett. 89b, 139 (1979).

[142] J.D. Bjorken, S. Brodsky, Phys. Rev. **D1** (1970) 1416.

[143] R.K. Ellis, D.A. Ross, A.E. Terrano, Nucl. Phys. **B178** (1981) 421;
G. Parisi, Phys. Lett. B74 (1978) 65;
J.F. Donohue, F.E. Low, S.Y. Pi, Phys. Rev. **D20** (1979) 2759.

[144] S. Catani, G. Turnock and B. R. Webber, Phys. Lett. **B295** (1992) 269.

[145] C. L. Basham et al., Phys. Rev. Lett. **41** (1978) 1585;
C. L. Basham et al., Phys. Rev. **D17** (1978) 2298